A STUDY OF THE REACTIONS
$K^+p \rightarrow K^-K^+K^+p$ AND $K^+p \rightarrow \bar{p}pK^+p$
AT 13 GeV/c

by

Douglas McLeod McFadzean

A thesis
presented to the University of Glasgow
in partial fulfillment of the
requirements for the degree of
Doctor of Philosophy
in the
Department of Natural Philosophy, University of Glasgow
June 1983

PREFACE

This thesis describes the work done by the author over the period October 1978 to October 1981 as a research student with the Experimental Particle Physics Group at the Department of Natural Philosophy, University of Glasgow. The author was present at CERN, Geneva, from October to December 1978 during the setting-up and data acquisition phases of an experiment performed in collaboration with groups from Birmingham and CERN. All subsequent processing and analysis work on the experiment was carried out at the University of Glasgow. The author was solely responsible for the analysis of the reaction channels discussed in this thesis.

Notes

1. The conventional units for momentum and mass/energy (GeV/c and GeV/c^2 respectively) are abbreviated to GeV throughout this thesis.
2. Reference numbers are enclosed in square brackets, eg. [17].

ACKNOWLEDGEMENTS

Many people have contributed to this thesis, both formally and informally, both consciously and unconsciously. In particular:

To the Science and Engineering Research Council, for financial support and the provision of computing facilities.

To the Department of Natural Philosophy, University of Glasgow, under the direction of Professor Sir J.C.Gunn, for the facilities provided and the hospitality extended.

To Professor I.S.Hughes, for the opportunity to carry out the research, and for his interest and guidance.

To Dr.R.M.Turnbull, for his help, advice and support as my supervisor.

To Drs.D.Frame, A.S.Thompson, J.G.Lynch and P.W.Minto, a special thanks for their friendship, encouragement, and help: David, for numerous ideas, discussions, and programs; Stan, for his humour, and not a few real ales; Jim, for help with the hardware; and Bill, for many a blether, and for fighting the good fight.

To our computer operators, for their cheerful assistance and many welcome cups of tea.

To Mrs.L.Y.Scott, and the systems staff, for their help with computing; especially to Lyn, for processing the data.

To Mr.C.N.Paterson, Mr.I.T.Wilkie, and other Glasgow research students, both past and present, for their camaraderie.

To Mrs.J.Gliori, for her help and patience as group secretary.

Finally,

To Christina, for listening and for having faith.

To my Mother and Father, for Home.

SYNOPSIS

Results are presented from a study of the reactions

$$K^+p \rightarrow K^-K^+K^+p$$

and

$$K^+p \rightarrow \bar{p}pK^+p$$

at an incident beam momentum of 13 GeV, using data recorded at the CERN Omega spectrometer. The data samples studied represent a significant improvement on existing statistics.

A description is given of the experimental apparatus, the electronic trigger system and the data acquisition process. Event reconstruction and the selection of three and four-prong events in the reactions of interest are also discussed.

After considering the geometrical acceptance of the spectrometer, a method of event simulation is adopted. Factors which account for various types of data losses are determined.

The production and decay characteristics of the $\bar{\Lambda}(1520)$ resonance are investigated in the reaction $K^+p \rightarrow \bar{p}pK^+p$. No narrow states are seen in $\bar{p}p$ or $\bar{\Lambda}(1520)p$.

$\phi(1020)$ and $f'(1515)$ production is studied in the reaction $K^+p \rightarrow K^-K^+K^+p$. A possible ϕ-like resonance is observed at a K^-K^+ mass of ~ 1.82 GeV.

Assuming diffractive production and t-channel helicity conservation, a spin-parity analysis of the ϕK^+ system shows a dominance of unnatural parity states, and in particular, dominance of the $J^P = 1^+$ wave. Evidence is presented for the existence of a 2^- resonance, possibly an L meson, at a mass of ~ 1.8 GeV. Small S and P-wave interference effects are observed in the K^-K^+ system.

CONTENTS

LIST OF FIGURES

Chapter I
INTRODUCTION

"Basic research is what I am doing when I don't know what I am doing."

Werner von Braun

1.1 MOTIVATION

The reactions

$$K^+p \rightarrow K^-K^+K^+p \qquad (1.1)$$

$$K^+p \rightarrow \bar{p}pK^+p \qquad (1.2)$$

at an incident beam momentum of 13 GeV have been studied in an experiment performed in 1978 using the Omega spectrometer [1] at the CERN super proton synchrotron. The motivation for such a study stemmed from the dearth of data on these reactions, and from the knowledge that the spectroscopy of the light quarks (u,d,s) is far from complete [2,3], partly because of the shift in emphasis of experimental particle physics towards heavy quark (c,b) spectroscopy following the discovery of charm in 1974.

The difficulty of producing a high-intensity kaon beam, and the low reaction cross-sections ($\sim 35\mu b$ and $\sim 3\ \mu b$ respectively) [4] relative to channels involving charged pions have prevented high statistics from being accumulated on reactions 1.1 and 1.2. In the present experiment, however, superconducting RF separators [5] were used to greatly enrich the K^+ content of the beam, and a trigger system which included a threshold Cherenkov counter was designed to select events with a fast forward K^- or $\bar{p}$ in the final state. (Such bubble chamber data as exist [6,7] indicate that the forward negative track is a characteristic feature of these reactions.)

We consider now some aspects of quark spectroscopy, and topics of particular interest in reactions 1.1 and 1.2.

1.2 SPECTROSCOPY

1.2.1 Mesons

For the SU(3) subgroup of quark flavours [8], containing u, d and s quarks, a quark and an antiquark can combine to form a bound mesonic state according to

$$q\bar{q} \equiv \{3\} \otimes \{3\} = \{1\} \oplus \{8\}$$

which defines a nonet (singlet plus octet) of particles all with the same spin-parity. If the $q\bar{q}$ system has spin J, orbital angular momentum L, and the quark and antiquark couple to give a spin S (0 or 1), then:

$$\underline{J} = \underline{L} + \underline{S}$$

The parity of a fermion-antifermion system is given by

$$P = (-1)^{L+1}$$

and charge conjugation applied to the neutral member of a multiplet yields:

$$C = (-1)^{L+S}$$

Hence,

$$CP = (-1)^{S+1}$$

so that all singlet states (S = 0) have CP = -1, and all triplet states (S = 1) have CP = +1. The resulting J^{PC} of the $q\bar{q}$ mesons allowed by SU(3) is therefore:

	S = 0	S = 1
L = 0	0^{-+}	1^{--}
L = 1	1^{+-}	0^{++}
		1^{++}
		2^{++}
L = 2	2^{-+}	1^{--}
		2^{--}
		3^{--}
⋮	⋮	⋮

with a nonet of states predicted for each J^{PC}. The series $J^P = \{0^+, 1^-, 2^+, \ldots\}$ with $P = (-1)^J$ and $J^P = \{0^-, 1^+, 2^-, \ldots\}$ with $P = (-1)^{J+1}$ will be referred to as the natural and unnatural spin-parity series respectively.

The current experimental status of SU(3) meson spectroscopy is summarised [2,3] in table 1.1. Confirmation of the ϕ-like and f'-like members of the natural spin-parity 3^{--} and 4^{++} nonets respectively is possible in the $K\bar{K}$ system; some evidence already exists [9,10] for a $\phi(1850)$ state. Progress on the unnatural spin-parity series has been slow, largely because an unnatural spin-parity state cannot decay to two pseudoscalar mesons (parity conservation), and therefore we must turn to the more complicated three-meson systems. Most three-meson data is derived from diffractive processes [11,12,13] which are difficult to interpret, although a qualitative description of some features is possible using Deck-type models [14,15]. Since the three-kaon system has been little studied in comparison with other three-meson systems, a detailed spin-parity analysis of $K^-K^+K^+$ or its two-body subsystems, for example $\phi(1020)K^+$, could contribute greatly to our understanding of unnatural spin-parity states containing strange quarks. Existing ϕK spin-parity analyses [16,17,18] have indicated possible resonant structure, but the results must be consolidated with higher statistics.

If radial excitations of the $q\bar{q}$ system are considered in addition to the orbital angular momentum excitations, further sets of resonant states are possible. Taking the ground state to have a radial quantum number n = 1, examples of n = 2 states do exist, such as the $\rho'(1600)$ and $\phi(1680)$ [2].

Various potential models of $q\bar{q}$ systems [19,20] successfully predict many of the experimentally observed states, but we note that agreement is poorer for light quark systems than for heavy quark systems.

1.2.2 Baryon-antibaryon states

The apparent observation of baryon-antibaryon resonances in several experiments stimulated much theoretical and experimental work on possible $qq\bar{q}\bar{q}$ states [eg. 21,22,23] which are 'exotic' with respect to the SU(3) scheme (not $q\bar{q}$ or qqq). Many theoretical models were devised to account for both the narrow ($\sim$ few MeV) and wide ($\sim$ few 100 MeV) $B\bar{B}$ or 'baryonium' states reported. For example, the states with narrow widths were thought to comprise a diquark and antidiquark separated by an angular momentum barrier. Such states would then be expected to have relatively high spin assignments.

However, many of the possible $B\bar{B}$ states could be interpreted as mesons, having a $q\bar{q}$ rather than a $qq\bar{q}\bar{q}$ configuration. Only $B\bar{B}$ states with manifestly exotic quantum numbers could unambiguously confirm the existence of a $qq\bar{q}\bar{q}$ state. Indeed, the original aim of the present experiment had been to confirm the existence of a narrow exotic state of mass 2.46 GeV observed [24] in $\bar{\Lambda}\Delta^{++}(1232)$ and $\bar{\Sigma}^{+}(1385)p$ combinations produced in the reactions

$$K^+p \rightarrow \bar{\Lambda}\Delta^{++}(1232)n, \quad \Delta^{++}(1232) \rightarrow p\pi^+$$
$$K^+p \rightarrow \bar{\Sigma}^{+}pn, \quad \bar{\Sigma}^{+} \rightarrow \bar{\Lambda}\pi^+$$

with $\bar{\Lambda} \rightarrow \bar{p}\pi^+$. The quantum numbers $Q = +2$ and $S = +1$ of the $\bar{\Lambda}p\pi^+$ combination uniquely define a $qq\bar{q}\bar{q}$ ($uu\bar{d}\bar{s}$) configuration. However, the existence of such a state was not confirmed in the present experiment [25].

With improved statistics on many of the possible baryonium candidates, the experimental evidence for narrow baryonium is now very weak. Only the $S(1935) \rightarrow \bar{p}p$ has retained some credibility as a resonance [2], but this state does not have an unambiguous $qq\bar{q}\bar{q}$ signature. Wide $\Lambda\bar{p}$ and $\bar{\Lambda}p$ states have been reported [26,27], but may have a simpler interpretation as K* resonances.

Reaction 1.2 allows a search for $B\bar{B}$ resonances with little complication from the production of other resonances in the final state, unlike similar processes with an

incident pion where the $\Delta^{++}(1232)$ is produced. The only known resonance produced is the narrow $\bar{\Lambda}(1520)$ decaying to $\bar{p}K^+$. Comparisons may be made between the $\bar{\Lambda}(1520)p$ and $\bar{\Lambda}p$ systems.

TABLE 1.1

Summary of SU(3) meson spectroscopy

J^{PC}	$^{2S+1}L_J$	I=1	I=0		I=1/2
0^{-+}	$^1S_0$	π	η	$\eta'(958)$	K
1^{--}	$^3S_1$	$\rho(770)$	$\omega(783)$	$\phi(1020)$	$K^*(892)$
1^{+-}	$^1P_1$	B(1235)	H(1190)		$Q_1(1280)$
0^{++}	$^3P_0$	$\delta(980)$	$\varepsilon(1300)$	$S^*(975)$	$\kappa(1350)$
1^{++}	$^3P_1$	$A_1(1270)$	D(1285)	E(1420)	$Q_2(1400)$
2^{++}	$^3P_2$	$A_2(1320)$	f(1270)	$f'(1515)$	$K^*(1430)$
2^{-+}	$^1D_2$	$A_3(1680)$			
1^{--}	$^3D_1$				
2^{--}	$^3D_2$				
3^{--}	$^3D_3$	g(1690)	$\omega(1670)$	$\phi(1850)$?	$K^*(1780)$
4^{++}	$^3F_4$	h(2040)			$K^*(2060)$

Chapter II
EXPERIMENTAL ARRANGEMENT

2.1 INTRODUCTION

The data to be discussed came from the CERN West Area experiment WA48 performed using the Omega spectrometer at the CERN super proton synchrotron (SPS) with a 13 GeV momentum RF separated beam of positive kaons incident on a liquid hydrogen target. Omega is a multi-user facility based on a ,superconducting magnet with a charged track detection system of optical spark chambers,[1] multiwire proportional chambers (MWPC's) and drift chambers [1]. A trigger system consisting primarily of two scintillation counter hodoscopes and a threshold Cherenkov counter placed downstream of the target was designed to select events where a fast forward $\bar{p}$ or K^- was produced.

2.2 THE OMEGA SPECTROMETER

The Omega magnet uses two superconducting coils, 3 m in diameter and 1.5 m apart, to maintain a field over a useful volume of 14 m^3, with a central field value of 1.8 T (figure 2.1). Inside the magnet, a cylindrical liquid hydrogen target 60 cm long and 2.6 cm in radius was surrounded by optical spark chambers. Forward charged secondary tracks were detected by a set of 7 spark chambers each with 10 x 1 cm spark gaps placed normal to the incident beam and downstream of the target (geometry 1). On either side of the target 4 spark chambers each with 8 x 1.2 cm spark gaps parallel to the beam detected slow charged secondaries (geometry 2). The spark chamber gaps could each provide one space point for track reconstruction, and were angled slightly in the vertical plane so that they could be viewed normally by stereo pairs of Plumbicon TV cameras (three pairs for geometry 1, one pair for geometry 2). Bars of

[1] Now replaced by the Omega' system of MWPC's.

fiducial lights mounted above the spark chambers provided a reference frame for the reconstruction of tracks in space. Spark positions and intensities were digitised and recorded on magnetic tape after each event, and fiducial digitisings were recorded after each beam burst. The spark chambers and associated readout are discussed in more detail in references 28 and 29.

High precision points on forward tracks were provided by 4 multiwire proportional chambers MWPC1-MWPC4 and 2 drift chambers. These chambers were also necessary for calibration work which corrected errors in the determination of track positions due to systematic effects in the spark chambers and TV camera system.

Figure 2.2 shows the layout of the counters in Omega for the experiment. A right-handed coodinate system for the spectrometer is defined by taking the origin at the centre of the magnet, the x,y-axes parallel to the plates of the spark modules in geometry 2 and geometry 1 respectively, and the z-axis vertical.

2.3 BEAM

The S1 beam line from the CERN SPS was used in conjunction with superconducting RF separators to provide a 13.02 GeV momentum positive beam enriched with kaons. The first stage of beam production involved a pulsed proton beam of momentum 200 GeV striking a 30 cm beryllium target. The resulting secondary particles were subjected to charge and momentum separation and focussing to produce a positive beam of the required momentum. Collimators were used to set the momentum spread to about 100 MeV. In order to greatly improve the K^+ content of the beam (approximately 1% at this stage), mass separation of the beam was done using two superconducting RF cavities (a special feature of this beam line [5]). The deviation of the momentum of individual beam particles from the nominal beam momentum was measured by a spectrometer in the beam line. Kaons in the beam were identified using a threshold Cherenkov counter and a 'CEDAR'

differential Cherenkov counter. The direction of beam particles as they entered the target was determined by 4 MWPC's B1-B4 situated just upstream of the target at the entry to Omega (figure 2.3).
Typical beam parameters were:

Burst frequency	:	0.1 Hz
Spill	:	2 seconds
Flux	:	$\sim 10^5$ K^+/burst (~50% of total beam flux)

2.4 TRIGGER

The spark chambers were fired only when the necessary trigger conditions were satisfied. The trigger logic was designed to select preferentially events with final states including a $\overline{\Lambda}$ by accepting only those K^+ interactions which had a fast forward $\bar{p}$. The trigger also accepted events with a K^- particle of momentum > 2.8 GeV originating in the target. The trigger required:

1. An identified K^+ incident on the target, as indicated by the beam Cherenkov counters, and by a set of scintillation counters S1-S4 located upstream of the target. The beam halo was vetoed by scintillation counters V2 and V4 around S2 and S4 respectively. Figure 2.3 shows the layout of these counters.
2. An interaction by a beam particle in the target. A downstream scintillation counter V0 vetoed beam particles which passed through the target without interacting. A 24 element cylindrical scintillation counter hodoscope TS surrounded the target, and was closed at the upstream end by the high precision (0.5 mm wire spacing) MWPC1 (see figure 2.2). The conditions imposed were:
   a) a beam interaction defined by $S1.S2.S3.S4.\overline{V2}.\overline{V4}.\overline{V0}$
   b) a charged particle multiplicity emerging from the target of
      either $\geq$ 1 hits in the TS hodoscope
      or $\geq$ 2 hits in MWPC1

3. Identification of a fast forward $\bar{p}$ or K^-. Two vertical scintillation counter hodoscopes were used in conjunction with a large threshold Cherenkov counter C placed between them (figures 2.2 and 2.4). The hodoscopes H1 and H2 consisted of 16 and 37 overlapping counters respectively, giving two arrays, 31 x 6 cm and 73 x 9 cm wide, of individually identifiable channels. The Cherenkov counter C had 32 optical cells, and was filled with Freon 114 at atmospheric pressure, giving Cherenkov radiation thresholds for pions, kaons and protons of 2.8, 9.9 and 18.8 GeV respectively. A matrix coincidence system was used to identify $\bar{p}$'s and K^-'s > 2.8 GeV which had passed through the downstream parts of the spectrometer by demanding correlated hits in the H1 and H2 arrays (31 x 31 channels used) with no light in the corresponding cells of the Cherenkov C (ie. $H1.H2.\bar{C}$). Particles from the target with momenta < 2.8 GeV were swept aside by the Omega magnetic field and could not traverse the Cherenkov counter.
4. More than 1 hit in the 'trigger' side of MWPC4. This reduced the number of spurious triggers caused by secondary interactions downstream of the target.
5. For the latter part of the experiment only, no forward π^0 signal. This condition was designed to reduce backgrounds by removing channels which included π^0's. Hodoscope H2 was used in conjunction with another scintillation counter hodoscope H3 (30 non-overlapping elements 20 cm wide) and a lead screen 1.1 cm thick to form a scintillator-lead-scintillator photon detector (see figures 2.2 and 2.4). The elements of each hodoscope were split up into 8 groups such that photons from a π^0 decay would pass undetected through a given H2 group into the lead, and there produce electrons which would be detected by the corresponding H3 group of elements (ie. $\overline{H2}.H3$).

The trigger signal formed may be expressed logically thus:

K^+ beam interaction	:	$(K^+.S1.S2.S3.S4.\overline{V2}.\overline{V4}.\overline{V0})$
multiplicity conditions	:	$.((TS \geq 1)+(MWPC1 \geq 2)).(MWPC4 \geq 1)$
fast forward $\bar{p}$ or K^-	:	$.(H1.H2.\overline{C})$
(no forward π^0	:	$.\overline{\pi^0})$

Table 2.1 lists some trigger counter specifications.

Two periods of data taking resulted in:

run 1 : 0.7 M triggers
without the π^0 veto condition in trigger
beam flux sensitivity for 100% acceptance = 3 ev/nb

run 2 : 1.7 M triggers
with the π^0 veto condition in trigger
beam flux sensitivity for 100% acceptance = 9 ev/nb

The author was present during the experimental setting up and data taking periods (October to December 1978). Responsibilities included the determination of trigger and beam counter positions relative to the Omega system, and the installation and testing of trigger elements.

2.5 DATA ACQUISITION

The Omega data acquisition system [30] recorded data from the Omega detectors onto magnetic tape and sampled data to permit the online monitoring of detector performance. The system (schematically shown in figure 2.5) was based on linked PDP11/34 and PDP11/40 mini-computers with CAMAC interfacing between the detector electronics and the computers. The data acquisition computer DAC buffered data onto tape; user computers U0 and U2 handled monitoring tasks; and the MUX computer managed computer linking. A CII 10070 computer was used for monitoring detector information offline.

2.5.1 Event Recording

Each trigger signal in a beam burst directed the DAC to transfer information from the detectors to an event data buffer via the CAMAC. At the end of each burst, the fiducial lights above the spark chambers were lit, and the Plumbicon cameras read out. The accumulated event data buffers for the beam burst were then written to tape, and for each event contained readout digitisings from: the spark chambers via the Plumbicon cameras; the MWPC's; the drift chambers; and the trigger counters. The Plumbicon digitisings of the fiducial lights were also recorded on tape for each beam burst. Typically, data from 30 triggers were recorded for each beam burst.

2.5.2 Online Monitoring

Online monitoring of the electronic information provided by the detectors was vital to ensure that any degradation in performance or failure in a detector was not biasing the data collected. A selection of monitoring programs running on the user computers U0 and U2 examined sample event records received from the DAC. U0 monitored information from the spark chambers, drift chambers and MWPC's, while U2 monitored information from the trigger counters. Insufficient statistics (usually a few hundred events) limited the use of these programs to detecting major hardware failures; more subtle effects were revealed by offline monitoring of a larger event sample.

Sparks and detector hits for sample events could be displayed graphically on a VDU screen by an online program (RAPIDE). Figure 2.6 shows an event with one negative track (the trigger track) and three positives. TS hodoscope hits are shown in the top left hand corner.

2.5.3 Offline Monitoring

To reveal slow variations in the performance of all detectors, a large monitoring program BUGHUNT was run offline on the CII 10070 computer, sampling typically one

event in ten stored on magnetic tape. Event samples of between one and two thousand events were accumulated and processed for comparison with subsequent data samples.

The data quality was further checked by studying the distributions of various parameters after processing samples of raw data with the Omega pattern recognition and geometry program ROMEO (see Chapter III) on the CERN main computers. The following parameters were studied:

1. the coordinates of primary and secondary vertices
2. the momentum of the fastest negative track
3. the mass of reconstructed V^0 (eg. K^0 and especially $\bar{\Lambda}$) particle decays
4. the multiplicity of hits at various planes in space

TABLE 2.1

Trigger Counters

Hodoscopes	H1	H2	H3	TS
scintillator slabs	16	37	30	24
slab dimensions (cm)	180x18x0.5	220x27x1	120x20x1	75x1x0.5
channels	31	73†	30	24
channel width (cm)	6	9	20	1

†31 channels used in H1.H2 correlation matrix

Cherenkov C	
cells	16 horizontal x 2 vertical
gas filling	Freon 114 (refractive index 1.00115)
gas pressure	1 atmosphere

MWPC1	
wire planes	2 x y-direction, 2 x z-direction
wires per plane	160
wire spacing (mm)	0.5

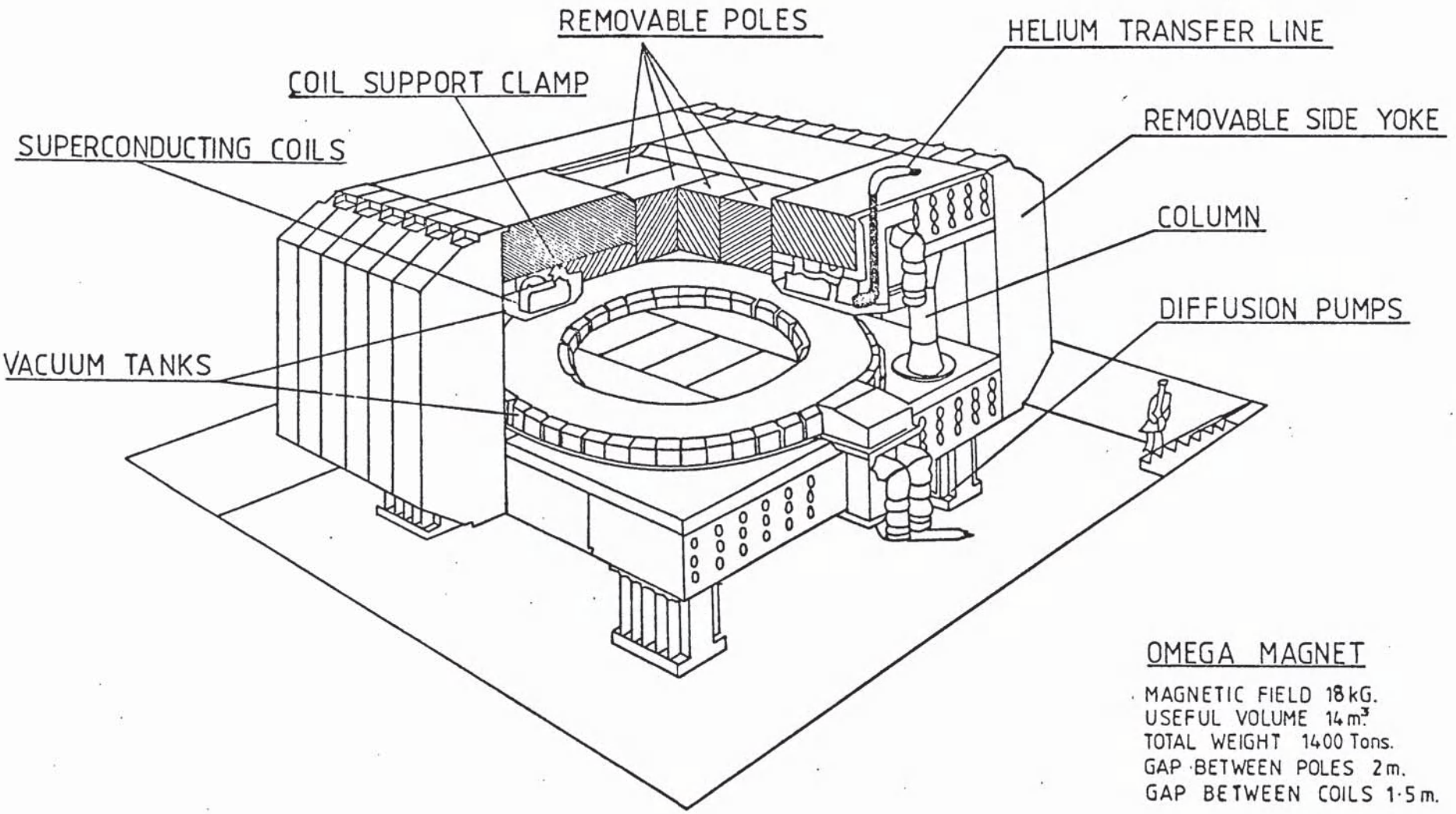

Figure 2.1: Omega magnet

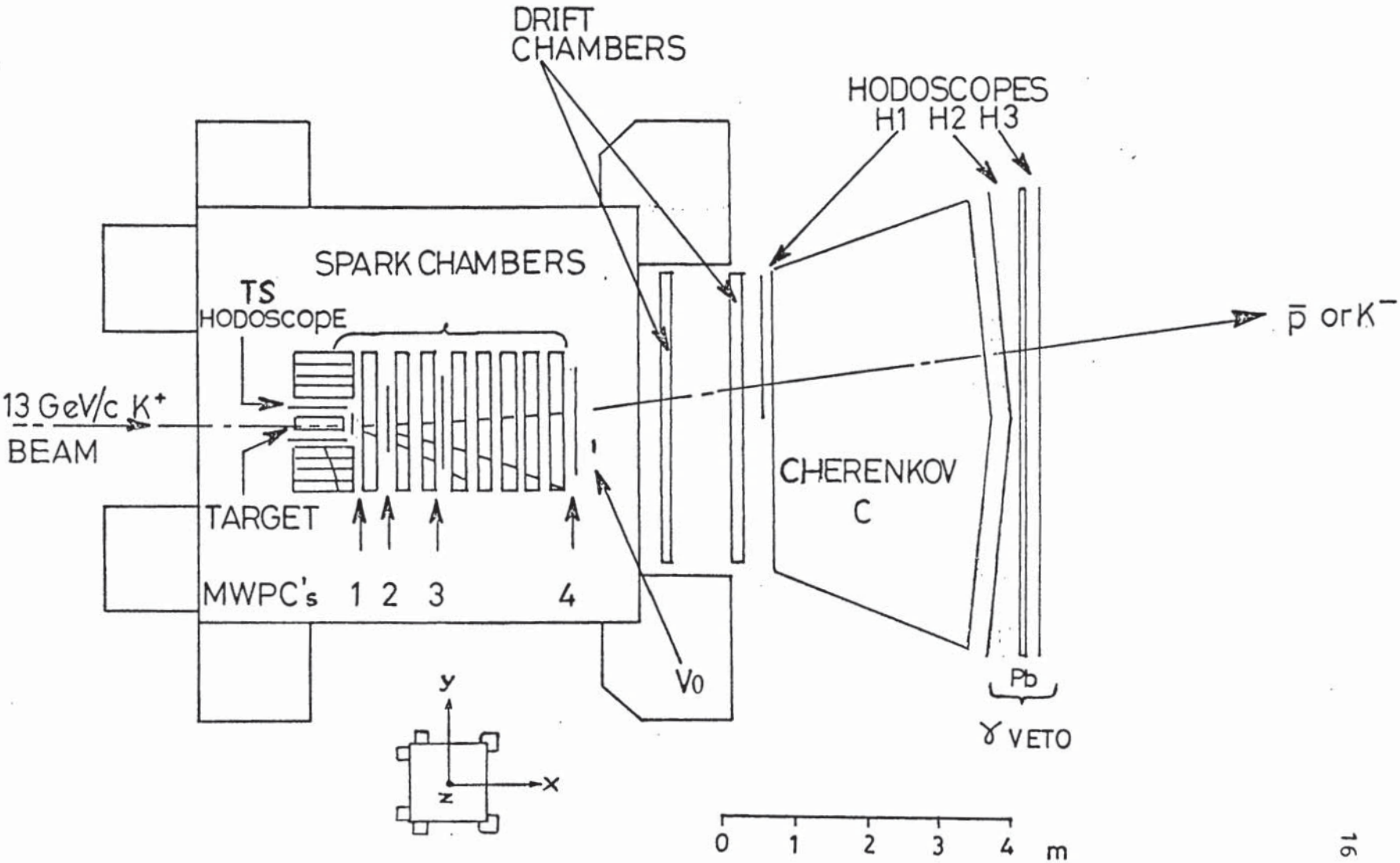

Figure 2.2: Detector layout

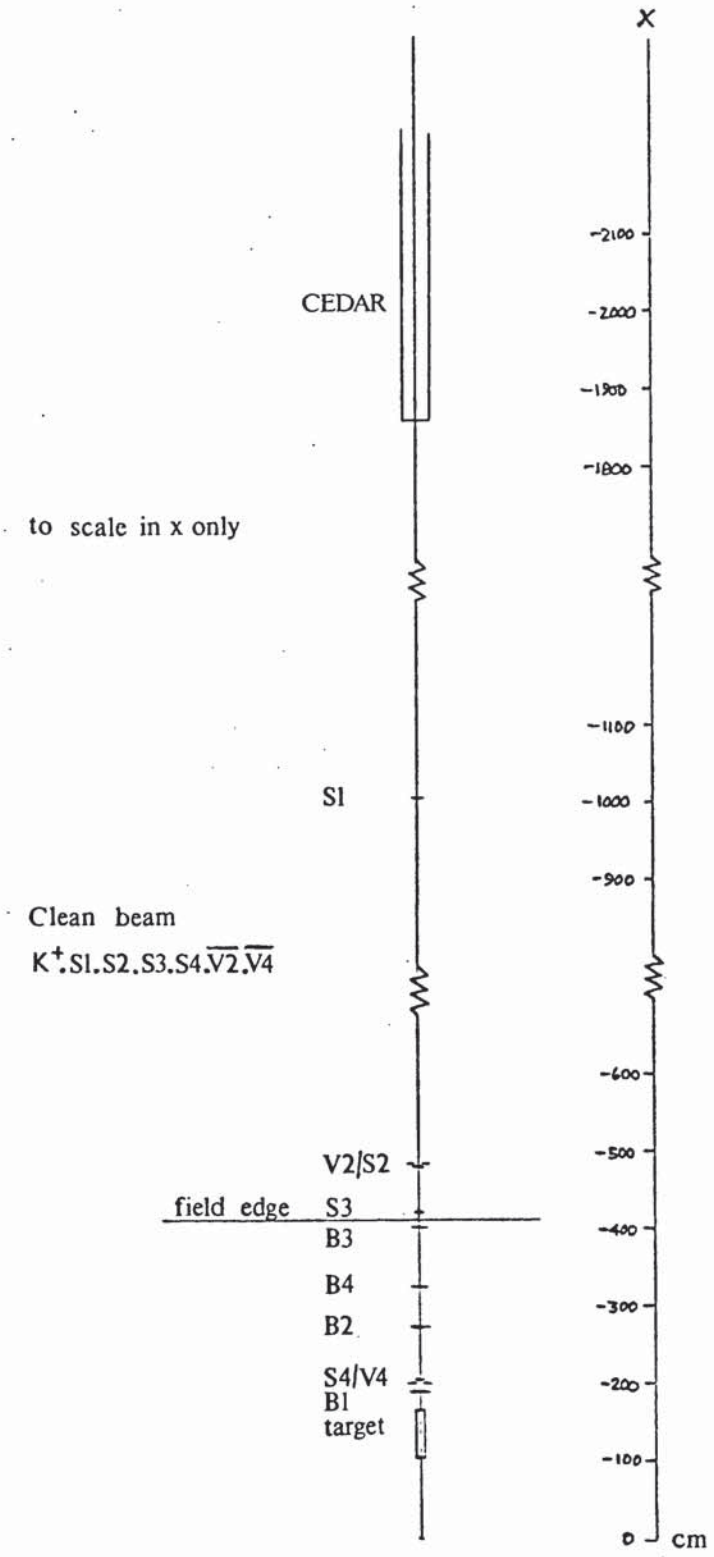

Figure 2.3: Beam counters

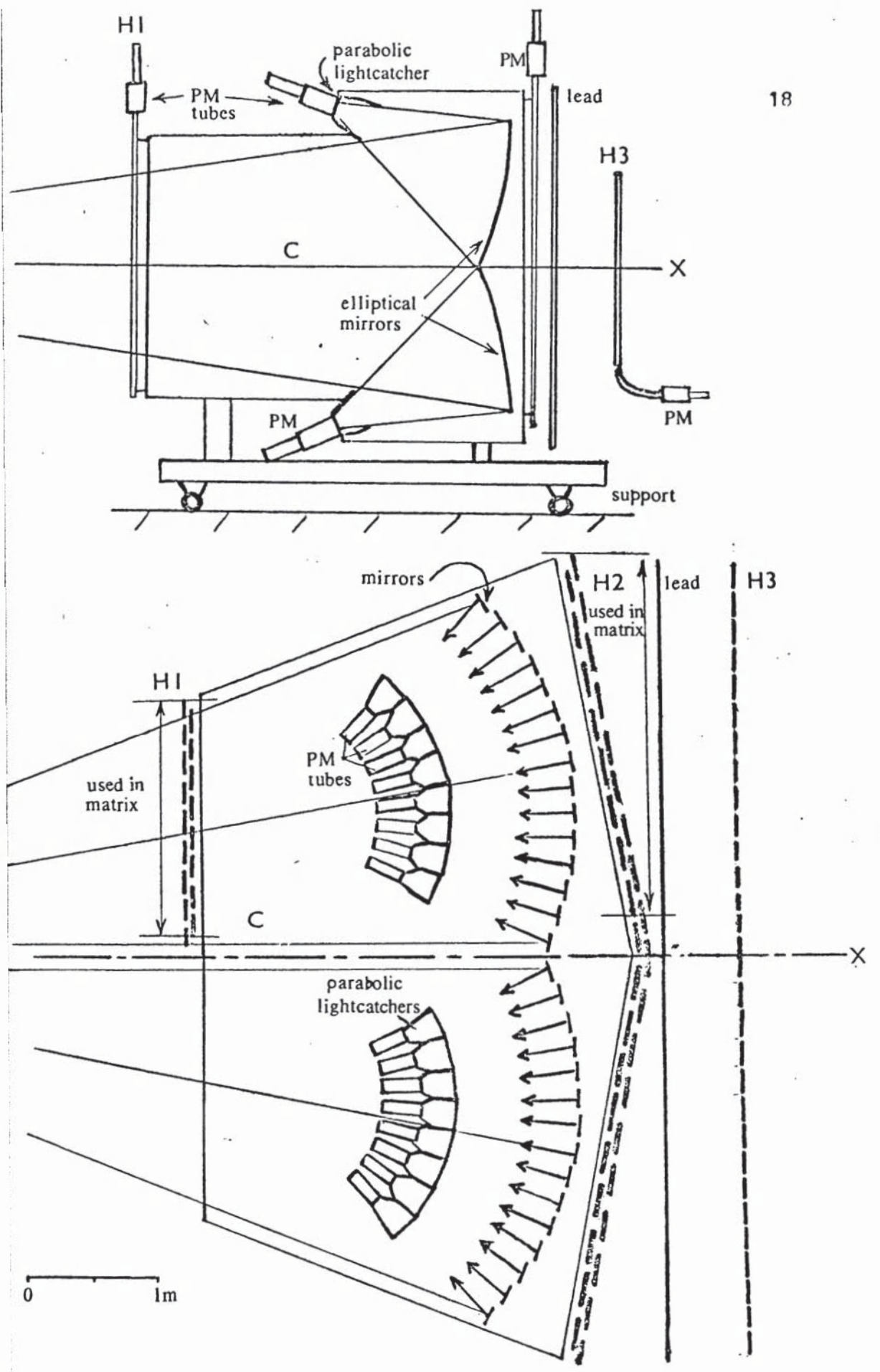

Figure 2.4: Downstream trigger counters

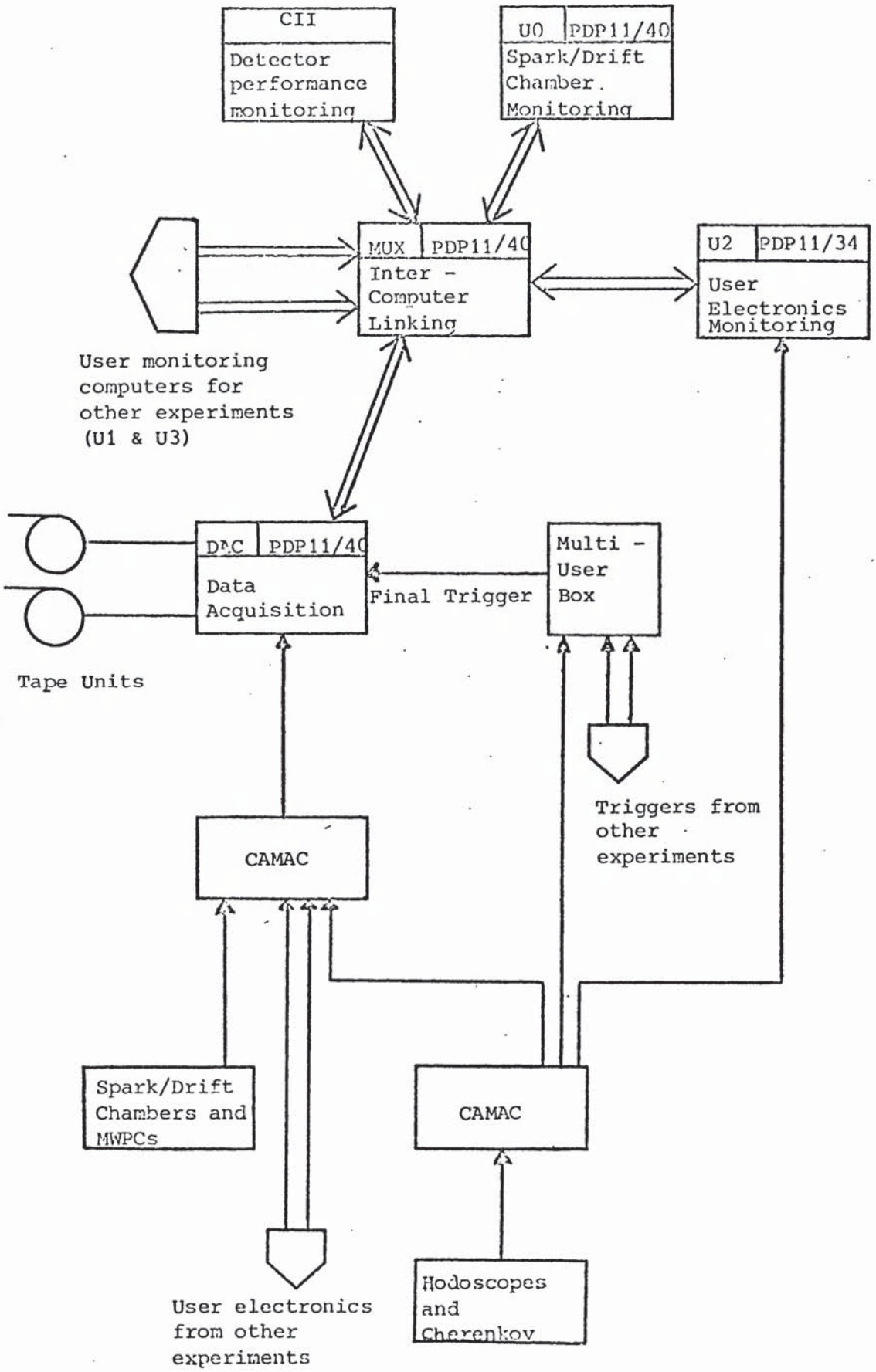

Figure 2.5: Data acquisition system

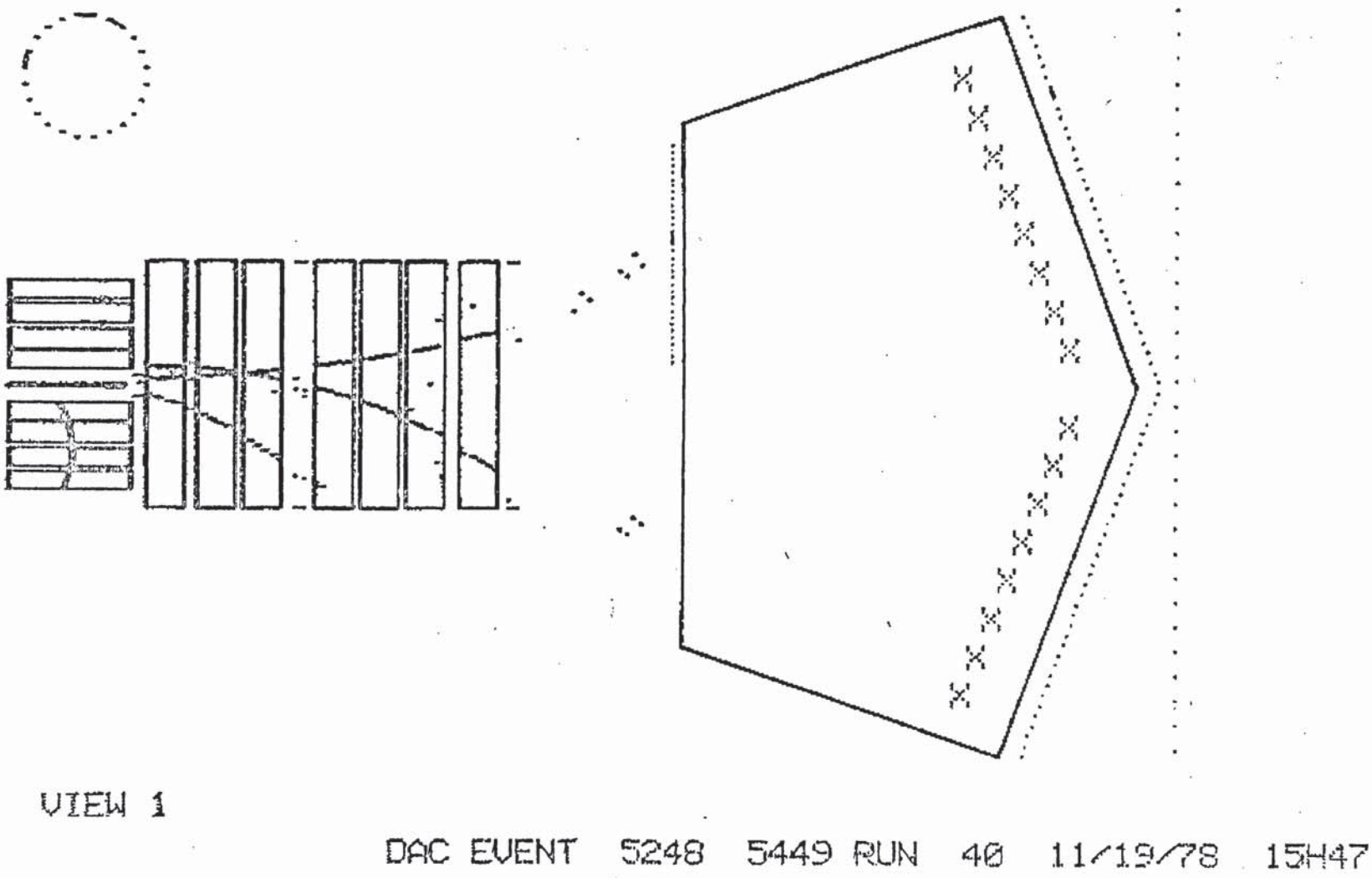

Figure 2.6: Online event display

Chapter III
DATA REDUCTION

3.1 EVENT RECONSTRUCTION

The raw data were processed at the Rutherford Appleton Laboratory using a version of the Omega pattern recognition and geometrical reconstruction program, ROMEO (see description in [28]). Pattern recognition for an event involved the combining of spark positions with space points from the MWPC's and drift chambers into tracks whose trajectories were known in the Omega system. Tracks in the spark chambers were found independently in each stereoscopic view and in each of the two sets of modules, Geometries 1 and 2. The track projections found were linked, and then matched with points from the MWPC's and drift chambers. Track momentum was determined by curvature in the Omega magnetic field. Geometrical reconstruction determined the topology of an event by fitting tracks to an interaction vertex in the target, the incident beam track having been reconstructed by the beam MWPC's. (Secondary vertices outside the target can also arise in the case of V^0 (eg. K^0 and $\bar{\Lambda}$) particle decays.) Tracks rejected from the vertex fit were labelled as 'extra tracks'. Geometry output from ROMEO for an event was written on magnetic tape and included vertex and track parameters, along with their covariance error matrices. In particular, the vertex coordinates were known, and the momenta of tracks at the vertex were given in terms of:

$1/p$: inverse momentum, signed by charge of track
λ : dip angle from x-y plane ($-\pi/2$ to $+\pi/2$)
Φ : azimuthal angle in x-y plane from x-axis (0 to 2π)

The author was responsible for reducing ROMEO geometry output to data summary tapes (DST's) for the events of interest, and for monitoring the quality of ROMEO processing.

3.2 PRELIMINARY SELECTIONS

Candidate events for the reactions

$$K^+p \rightarrow K^-K^+K^+p \qquad (3.1)$$

$$K^+p \rightarrow \bar{p}pK^+p \qquad (3.2)$$

were selected from ROMEO geometry output by requiring that each reconstructed event had:

1. Standard beam and trigger conditions.
2. A single vertex with an attached beam track inside the target volume defined to be a cylinder of radius 2.6 cm and length 60 cm aligned along the Omega x-axis and centred at x=-135 cm.
3. Three or four secondary tracks fitted to the vertex with charges -++ (three-prong) or -+++ (four-prong) respectively. The three-prong events arose when a positive track (usually slow) was not detected in the spark chambers either because it left too few sparks or had a trajectory which passed through the regions above and below the target.
4. A negative track which satisfied the trigger requirements. Each event was processed by a program[2] which compared the hodoscope hits recorded electronically with the hodoscope intersections predicted by extrapolating the negative track reconstructed in the spark chambers. Agreement was required within the errors on the track extrapolation through the Omega magnet field.

   Pion triggers were rejected by checking the Cherenkov condition from the electronic data, and by demanding that the negative track had a momentum of at least 3 GeV. The momentum cut was made higher than the nominal Cherenkov pion threshold of 2.8 GeV to allow for any inefficiencies in the Cherenkov counter.

---

[2] Courtesy of A.S. Thompson

For each event satisfying the above conditions the positive tracks were then ordered by the magnitude of their laboratory momenta before applying the selections described below.

3.3 THREE-PRONG EVENTS

For the three-prong events, the invariant (missing mass)^2 between the initial (beam + target) system and the final system of secondaries is defined by

$$(\text{missing mass})^2 = (\text{missing energy})^2 - (\text{missing momentum})^2 \quad (3.3)$$

and should correspond to the mass^2 of the missing particle within experimental error. Using the track momenta from ROMEO, and assigning sets of appropriate particle masses to the seen secondary tracks in turn, (missing mass)^2 distributions for reactions 3.1 and 3.2 have been investigated. The sets of mass assignments considered for the tracks were as follows:

$K^+p \rightarrow K^-K^+K^+p$: -ve = K^- / +ves = K^+K^+, pK^+, K^+p

$K^+p \rightarrow \bar{p}pK^+p$: -ve = $\bar{p}$ / +ves = K^+p, pK^+, pp

Significant peaks about the mass^2 of the missing particle were seen only for reaction 3.1 in the two cases corresponding to the hypotheses

$$K^+p \rightarrow K^-(p)K^+K^+ \quad (3.4)$$

$$\text{and} \quad K^+p \rightarrow K^-(K^+)pK^+ \quad (3.5)$$

where the latter signal has a very large background compared with the former. No missing particle signals were seen for reaction 3.2: this may reflect the order of magnitude reduction in cross-section anticipated for this channel relative to 3.1 [4]. Events were selected for

hypothesis 3.4 : $0.65 < (\text{missing mass})^2 < 1.10$ GeV^2

3.5 : $0.06 < (\text{missing mass})^2 < 0.42$ GeV^2

Figures 3.1 and 3.2 show the (missing mass)^2 distributions and selections corresponding to hypotheses 3.4 and 3.5

respectively. Events which lay inside both sets of cuts were treated as two separate events of combined weight unity, but with each individual event assigned an ambiguity weight derived from the relative peak/background ratios for the (missing mass)^2 distributions for the two hypotheses.

For events selected in this manner, the missing particle was assigned the missing momentum and the correct particle mass (proton or positive kaon) [2]. An investigation was also carried out on the selected events to determine whether any of the 'extra' (ie. unfitted to a vertex) tracks reconstructed by ROMEO could be attached to the three-prong vertex by fully extrapolating the extra (positive) tracks back to the closest point to the vertex. It was found that less than about 3% of events could be refitted as four-prongs.

3.4 FOUR-PRONG EVENTS

Firstly, the four-prong events were required to have small missing longitudinal and transverse momenta (denoted by Δp_L and $\Delta p_T = \sqrt{(\Delta p_y^2 + \Delta p_z^2)}$ respectively) between the initial and final states, measured in the laboratory system relative to the Omega axes:

$$|\Delta p_L| < 0.4 \text{ GeV} \qquad (3.6)$$

$$\Delta p_T < 0.2 \text{ GeV} \qquad (3.7)$$

The Δp_L, Δp_T distributions and cuts are shown in figures 3.3 and 3.4 with the effect of one cut on the other superimposed. For the mass assignments:

$K^+p \rightarrow K^-K^+K^+p$: -ve = K^- / +ves = pK^+K^+, K^+pK^+, K^+K^+p

$K^+p \rightarrow \bar{p}pK^+p$: -ve = $\bar{p}$ / +ves = pK^+p, ppK^+, K^+pp

a 'delta function' δ was calculated for the secondary tracks, where

$$\delta = (\text{mass(3 fastest)})^2 - (\text{missing mass against slowest})^2 \qquad (3.8)$$

Clear delta function peaks around zero were seen for the following hypotheses corresponding to reactions 3.1 and 3.2:

$$K^+p \rightarrow K^-pK^+K^+ \qquad (3.9)$$

$$K^+p \rightarrow K^-K^+pK^+ \qquad (3.10)$$

$$K^+p \rightarrow \bar{p}pK^+p \qquad (3.11)$$

$$K^+p \rightarrow \bar{p}ppK^+ \qquad (3.12)$$

Figures 3.5 to 3.8 show the delta functions for these hypotheses and the following selections which were made on the data:

hypothesis 3.9 : $|\delta| < 0.9$ GeV²

3.10 : $|\delta| < 0.9$ GeV²

3.11 : $|\delta| < 0.4$ GeV²

3.12 : $|\delta| < 0.4$ GeV²

The selections for hypotheses 3.11 and 3.12 were necessarily more restrictive to minimise contamination by the three kaon channel.

An attempt at redefining the delta functions using different permutations of the ordered tracks resulted in poorer separation of the different hypotheses. Events ambiguous between reactions 3.1 and 3.2 were assigned to the former because of the much larger cross-section expected [2]. Events internally ambiguous within a reaction were treated as two separate events of combined weight unity, but with each individual event assigned an ambiguity weight derived from the relative peak/background ratios for the δ distributions for the two hypotheses satisfied.

3.5 TRACK ADJUSTMENTS

3.5.1 Momentum Balance

Since the Δp_L distribution for four-prong events (figure 3.3) was found to peak at a value slightly shifted from zero, consideration was given as to whether exact momentum balance between beam and secondaries could be achieved by applying global shifts to beam track parameters. Four-prong events in the reaction

$$K^+p \rightarrow \phi(1020)K^+p, \quad \phi \rightarrow K^-K^+ \qquad (3.13)$$

selected by applying hypothesis 3.9 and cutting on

$$\phi \ : \ 1.01 < \text{mass}(K^-K^+) < 1.03 \text{ GeV}$$

were considered to yield the cleanest large data sample available to investigate momentum balance. Expressing the missing momentum components in terms of the ROMEO track parameters $p\ (=|p|), \lambda, \phi$ and taking differentials with respect to the beam parameters

$$d(\Delta p_x) = (p_x/p)\,dp - (p_z\,p_x/p\cos\lambda)\,d\lambda - (p_y)\,d\phi$$
$$d(\Delta p_y) = (p_y/p)\,dp - (p_z\,p_y/p\cos\lambda)\,d\lambda + (p_x)\,d\phi$$
$$d(\Delta p_z) = (p_z/p)\,dp + (p\cos\lambda)\,d\lambda$$

the shifts dp, $d\lambda$ and $d\phi$ on the beam parameters were calculated for each event, and the mean shifts for run 1 and run 2 determined. The global shifts applied to beam tracks in the selected data were:

run 1 : $dp = 35$ MeV, $d\lambda = 1.3$ mrad
2 : $dp = 29$ MeV, $d\lambda = 1.1$ mrad, $d\phi = 0.6$ mrad

(cf. ROMEO beam angle errors of about 0.4 mrad).

3.5.2 Energy Loss

Tracks were corrected for energy loss in passing through the liquid hydrogen target and the plastic scintillator of the TS counter. The length of a track in these media was calculated by intersecting a linear approximation to the track with two coaxial cylinders representing the target and the TS counter. Energy loss was calculated as a function of particle type and track momentum, using a parameterisation based on data from reference 2.

3.6 REMARKS

3.6.1 General

The momentum distribution of trigger tracks indicated that only a small fraction of events was lost by imposing a 3 GeV momentum cut rather than a 2.8 GeV cut. Figure 3.9 shows the trigger track momentum distribution for events selected in the three-kaon channel.

The reaction

$K^+p \rightarrow \pi^-\pi^+K^+p$

has a very large cross-section relative to reactions 3.1 and 3.2, and hence any Cherenkov counter inefficiencies could have resulted in serious data contamination. However, delta function and (missing mass)^2 distributions studied for this reaction hypothesis showed no peaking after the preliminary selections had been made.

3.6.2 $K^+p \rightarrow K^-K^+K^+p$

That the three-prong events corresponding to this reaction cover a particular kinematic region is illustrated by the low momentum distribution of the missing track (figure 3.10) and the angle of the missing track in the Omega y-z plane at the vertex. Figure 3.11 shows that the missing particle trajectory passed mostly through the regions above and below the target ($\pm\pi/2$), where tracks were not detected. The y-z plane angle for the slowest track from three-prong events (including the missing track) is also shown in figure 3.11, and should be compared with figure 3.12 which shows this angle for the slowest track from four-prong events. The distributions are largely complementary, and produce an angle for the combined three and four-prong events which is approximately isotropic (figure 3.13).

3.6.3 $K^+p \rightarrow \bar{p}pK^+p$

Possible contamination of this data by the three kaon channel was investigated by assigning kaon masses to the negative track and the two fastest positive tracks, and forming the mass combination of the negative track with each of the positives. The mass distribution (figure 3.14) shows no sign of the $\phi(1020)$ meson [2] which would be expected if contamination was present.

3.7 EVENT STATISTICS

Event statistics before channel selection were as follows:

reconstructed by ROMEO	- run 1	:	0.68 M
	- run 2	:	1.40 M
	- total	:	2.08 M
total with 1 -ve track > 3 GeV, 2 +ve tracks		:	0.17 M
total with 1 -ve track > 3 GeV, 3 +ve tracks		:	0.18 M
	- inside missing momentum cuts	:	35.1 K

The numbers of ambiguity weighted and unique events selected by (missing mass)^2 and delta function cuts for hypotheses 3.4, 3.5 and 3.9 - 3.12 are shown in figure 3.15. The total numbers of events in the reactions of interest were:

$K^+p \rightarrow K^-K^+K^+p$	:	50214	(44667 unique)
$K^+p \rightarrow \bar{p}pK^+p$	:	2093	(1788 unique)

3.8 OTHER REACTIONS

An attempt was made to identify events in the previously unreported reactions

$$K^+p \rightarrow \phi(1020)K^*(892)p, \quad \phi \rightarrow K^-K^+, \quad K^* \rightarrow K^+\pi^0 \qquad (3.14)$$

$$K^+p \rightarrow \phi(1020)K^+\pi^+n, \quad \phi \rightarrow K^-K^+ \qquad (3.15)$$

$$K^+p \rightarrow \bar{\Lambda}(1520)\Delta^{++}(1232)n, \quad \bar{\Lambda} \rightarrow \bar{p}K^+, \quad \Delta^{++} \rightarrow p\pi^+ \qquad (3.16)$$

by selecting events with four charged secondaries (-+++) which did not balance longitudinal and transverse momenta relative to the beam. Masses were then assigned to the tracks and the (missing mass)^2 against the charged tracks calculated for each set of assignments, in the hope of identifying the missing neutral pion or neutron as required. Also, the mass combinations of the negative track with each of the positive tracks were checked for indications of the $\phi(1020)$ or $\bar{\Lambda}(1520)$ resonances. It was found that only events in reaction 3.14 could be identified, and that the quality of data varied considerably with the cuts applied.

For events from run 1 identified with reaction 3.14, the $K^+\pi^0$ mass spectrum (showing the K*(892) resonance) is shown in figure 3.16, and the $K^*\phi$ mass spectrum in figure 3.17. The cuts applied to this data sample were

$$|\text{missing longitudinal momentum}| > 0.30 \text{ GeV}$$
$$|\text{missing transverse momentum}| > 0.07 \text{ GeV}$$
$$|(\text{missing mass against } K^-K^+K^+p)^2| < 0.05 \text{ GeV}^2$$
$$\phi : 1.01 < \text{mass}(K^-K^+) < 1.03 \text{ GeV}$$
$$K^* : 0.85 < \text{mass}(K^+\pi^0) < 0.93 \text{ GeV}$$

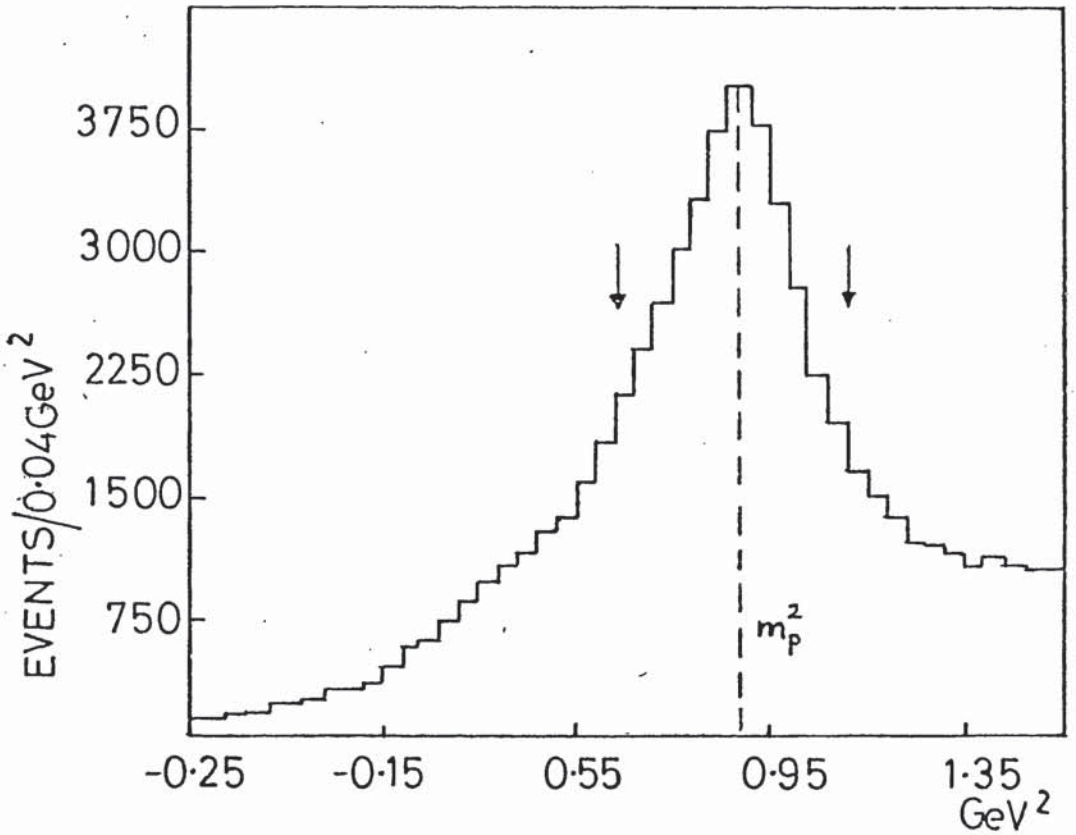

Figure 3.1: (Missing mass against K⁻K⁺K⁺)²

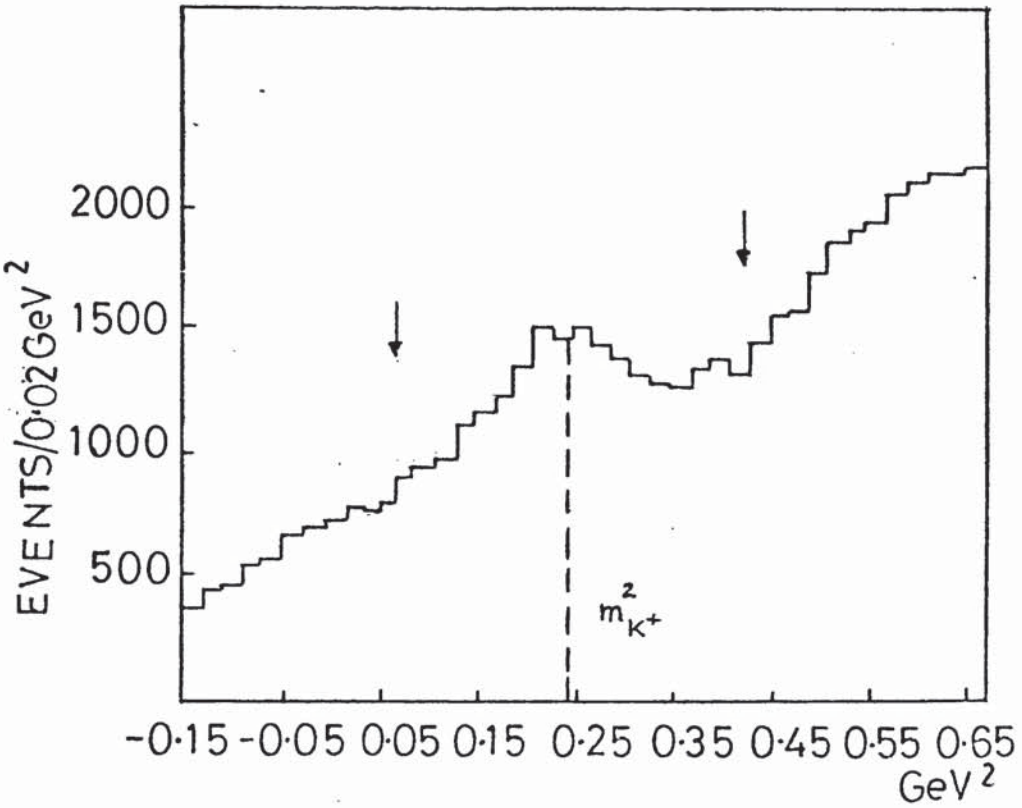

Figure 3.2: (Missing mass against K⁻pK⁺)²

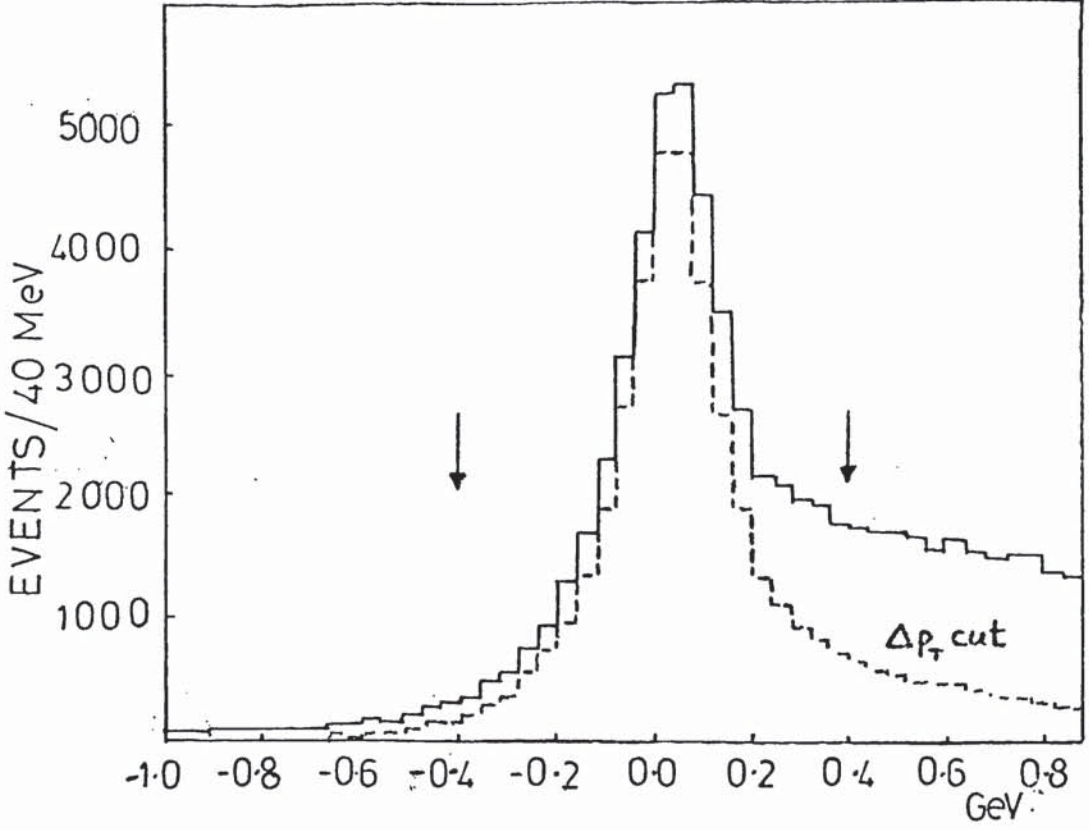

Figure 3.3: 4-prongs missing p_L

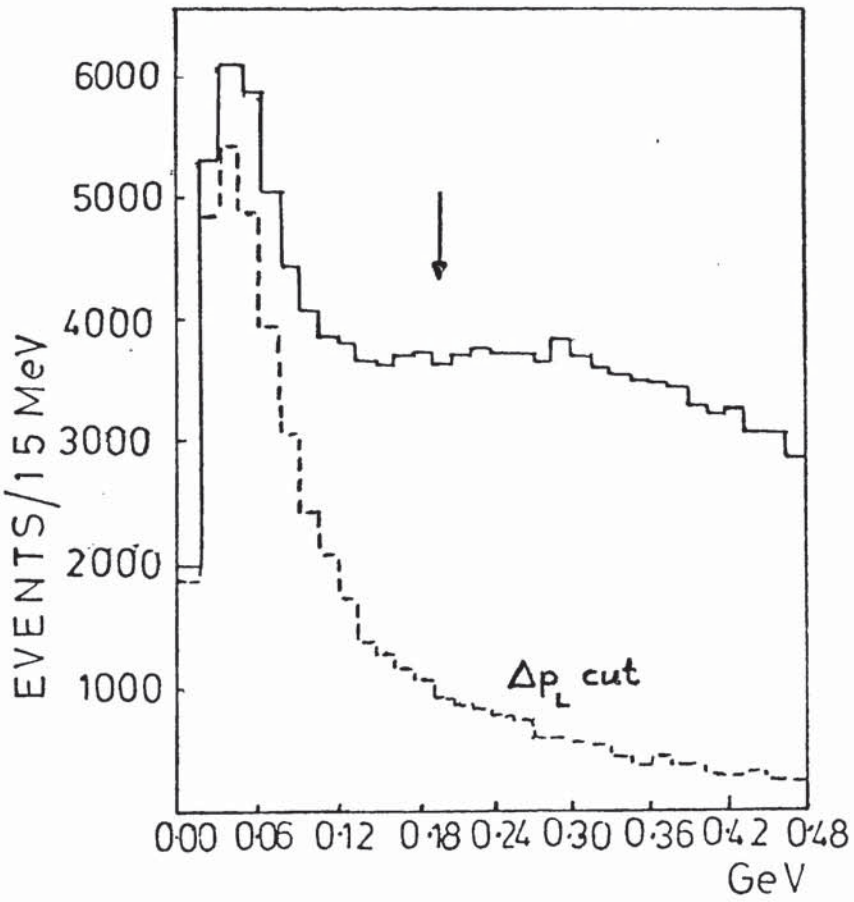

Figure 3.4: 4-prongs missing p_T

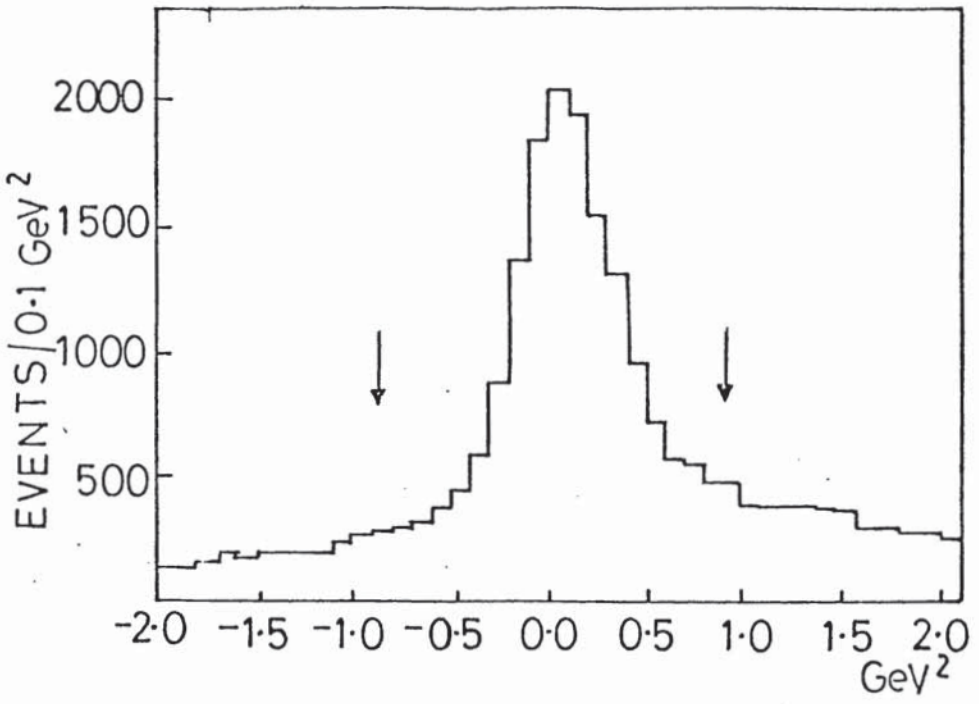

Figure 3.5:. $\delta(K^-pK^+K^+)$

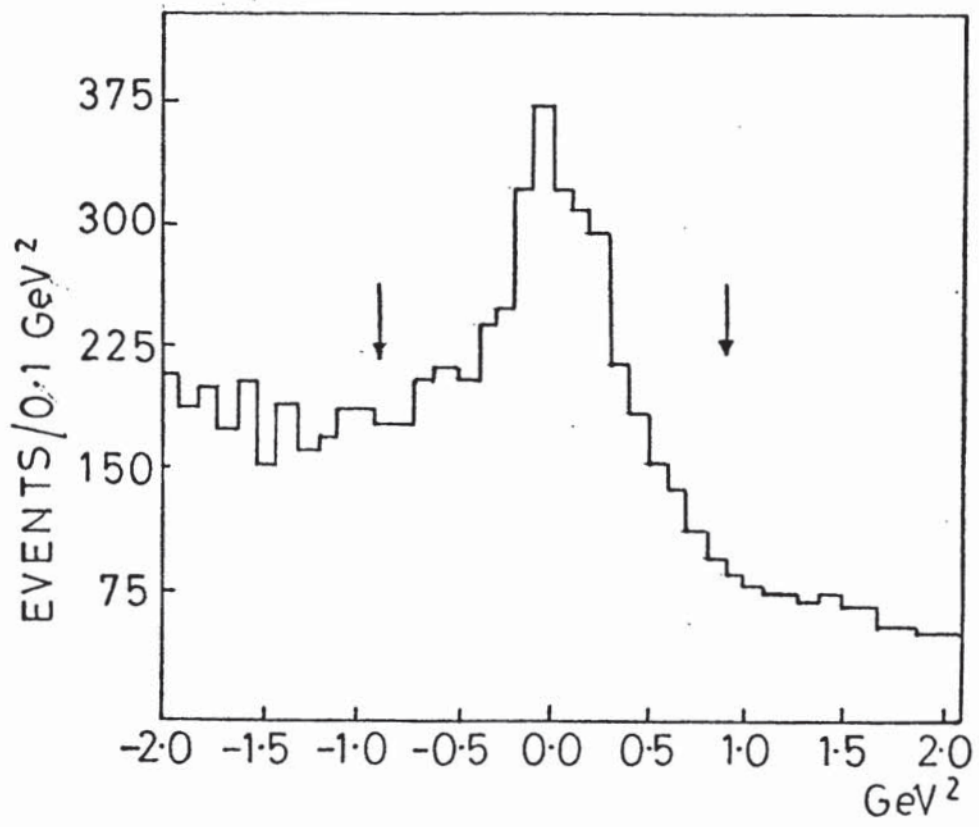

Figure 3.6: $\delta(K^-K^+pK^+)$

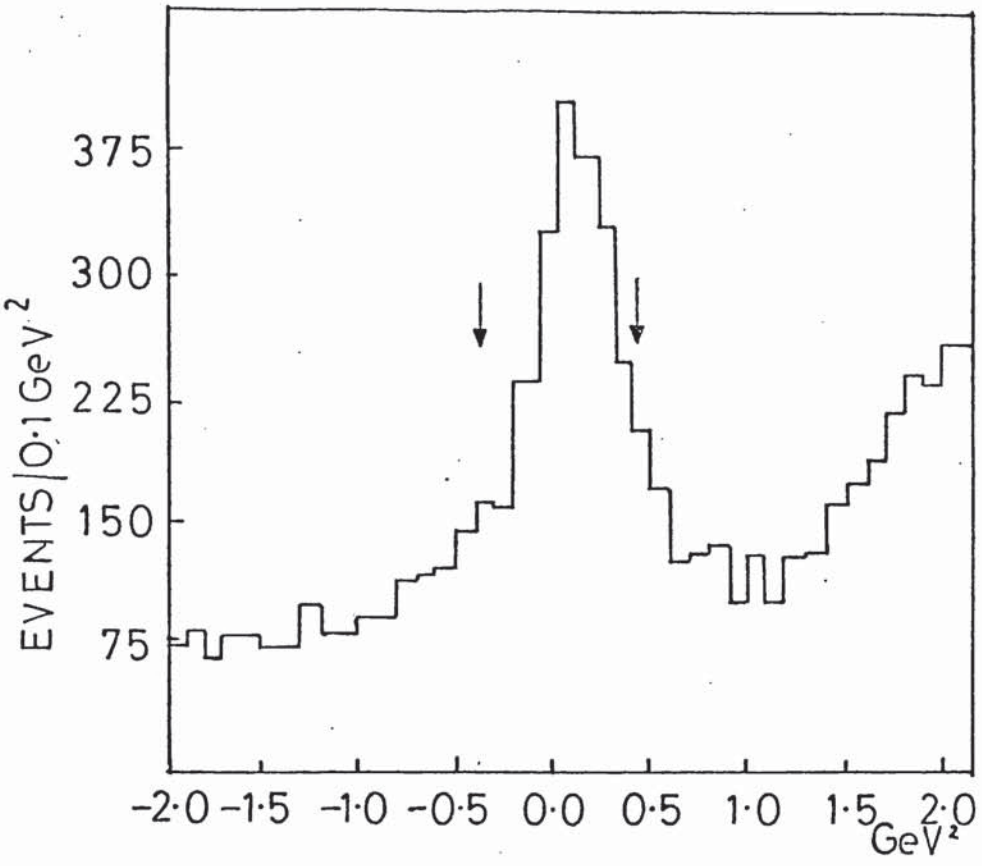

Figure 3.7: $\delta(\bar{p}pK^+p)$

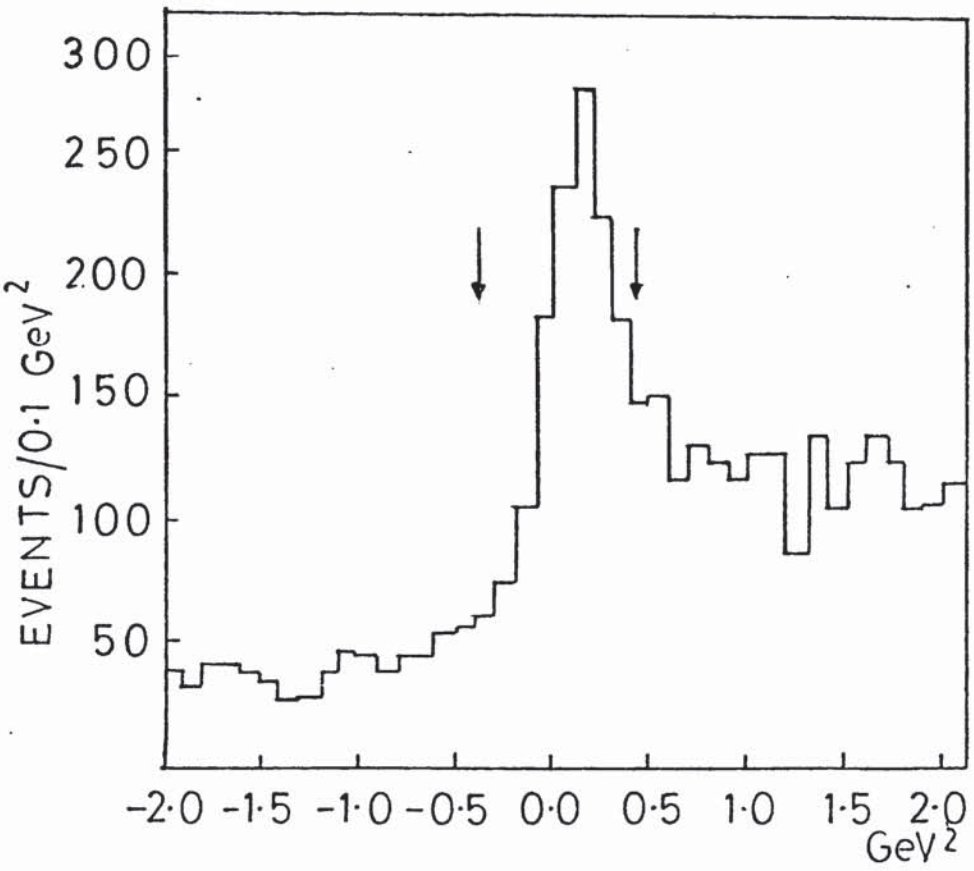

Figure 3.8: $\delta(\bar{p}pp\bar{K}^+)$

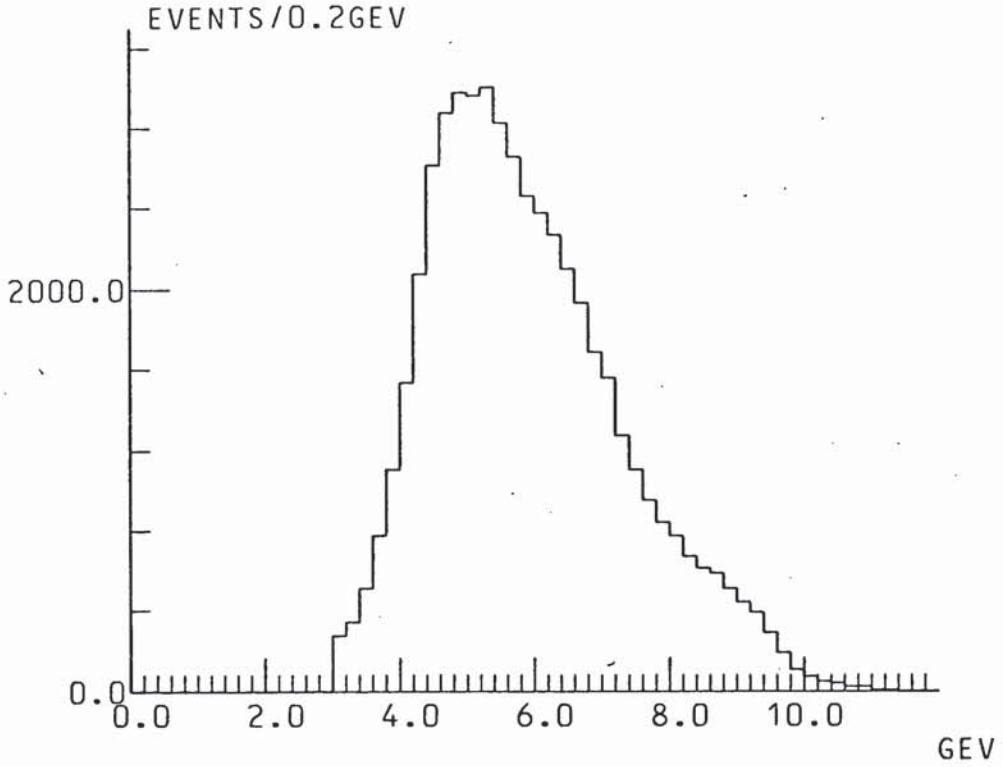

Figure 3.9: K⁻ trigger momentum

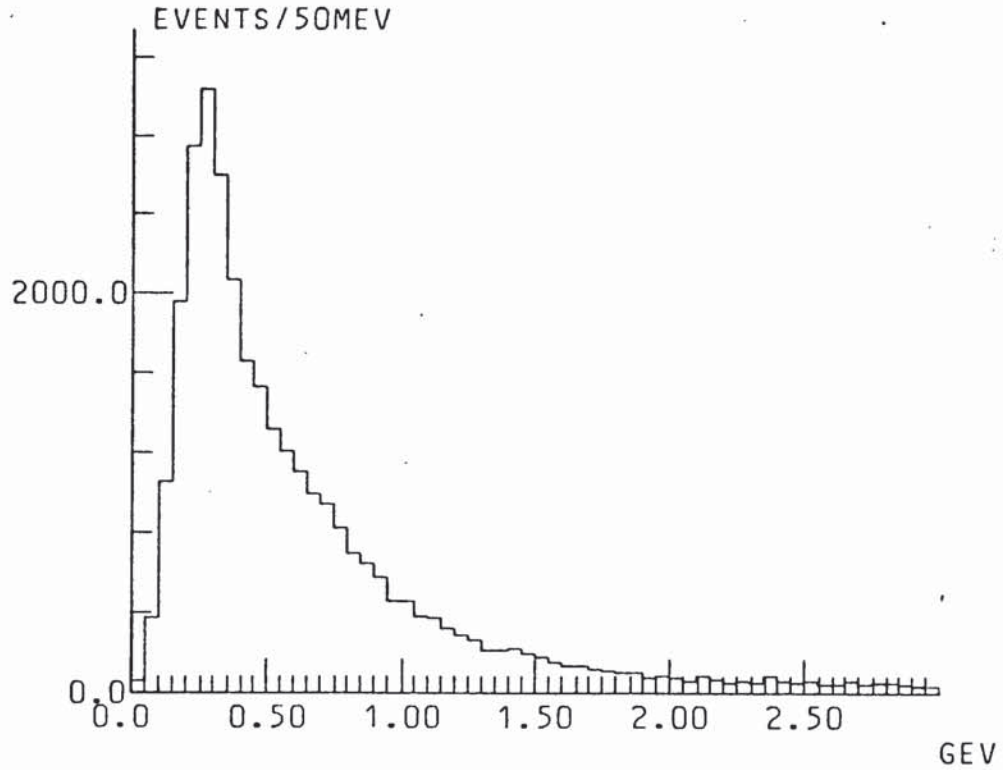

Figure 3.10: 3-prongs missing track momentum

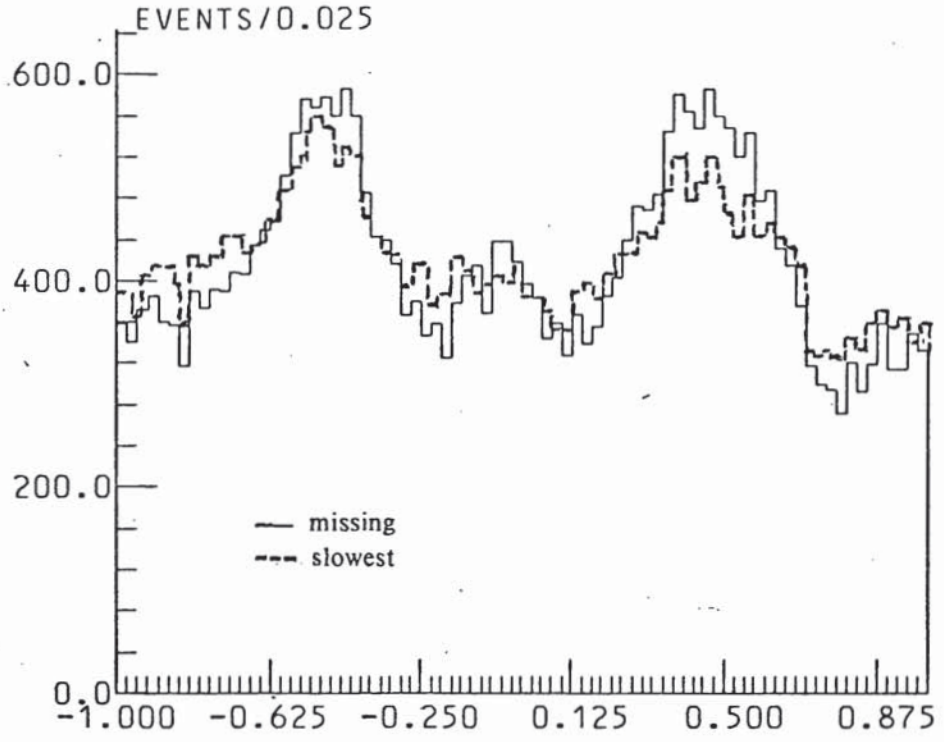

Figure 3.11: 3-prongs missing/slowest track y-z angle/π

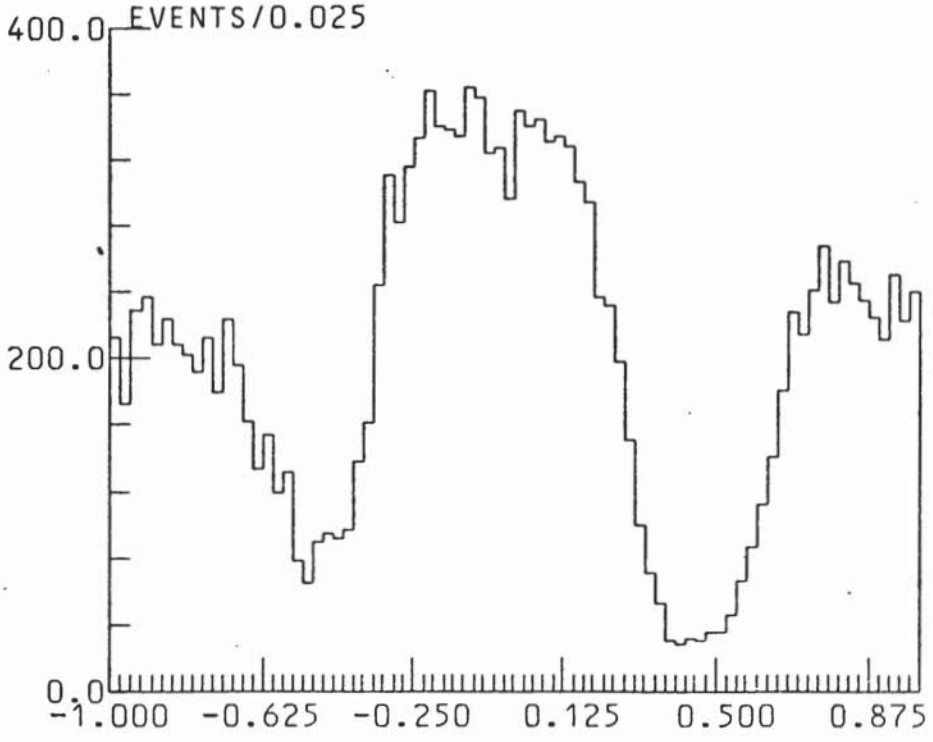

Figure 3.12: 4-prongs slowest track y-z angle/π

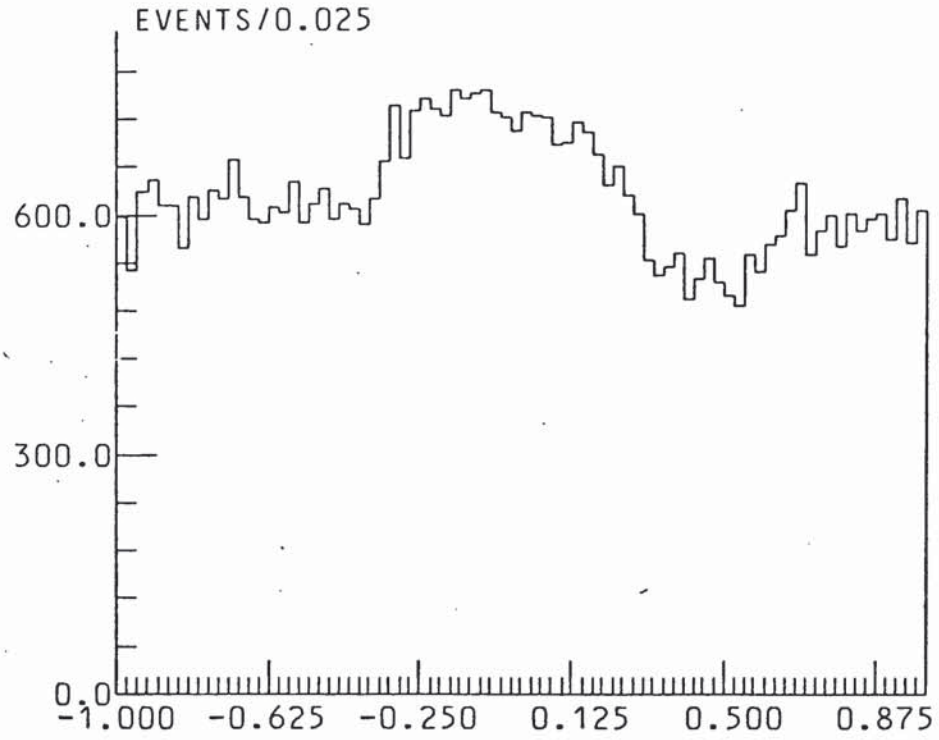

Figure 3.13: 3 and 4-prongs slowest track y-z angle/π

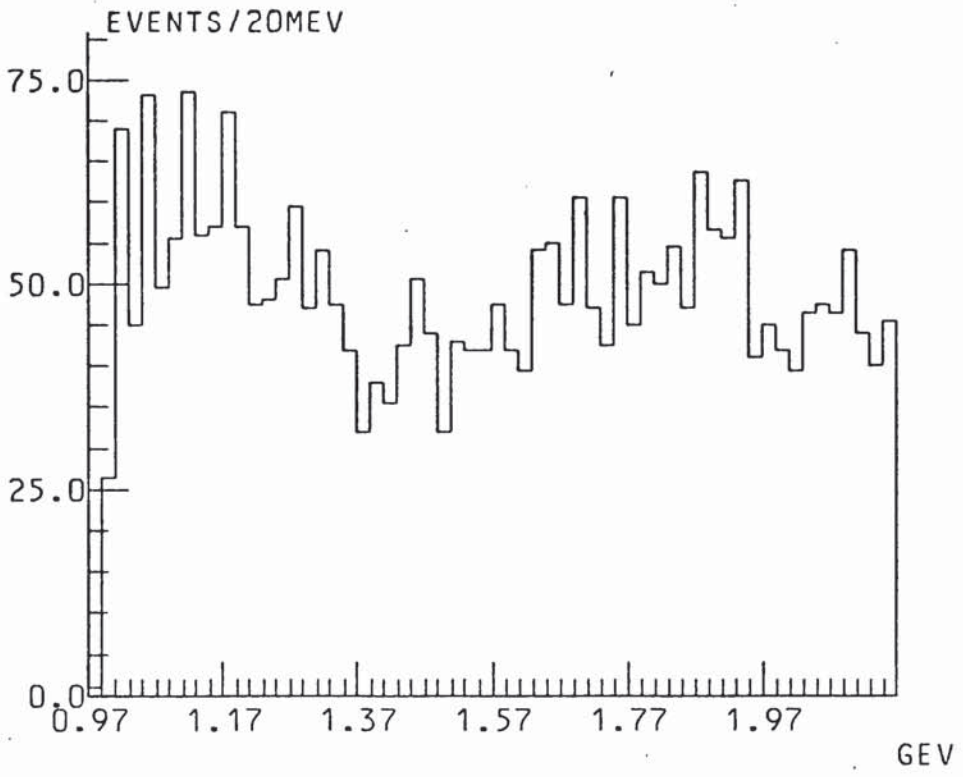

Figure 3.14: Mass("K-K+" combinations)

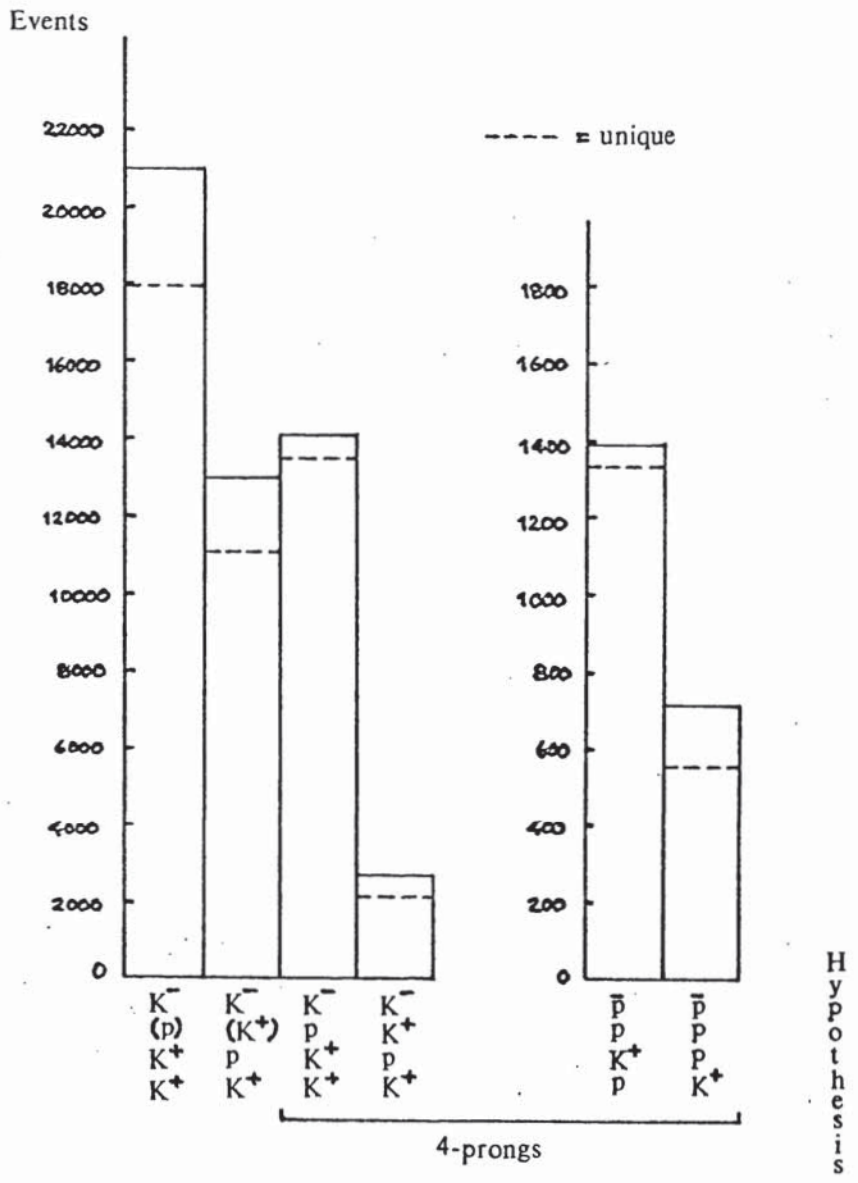

Figure 3.15: Events in each hypothesis

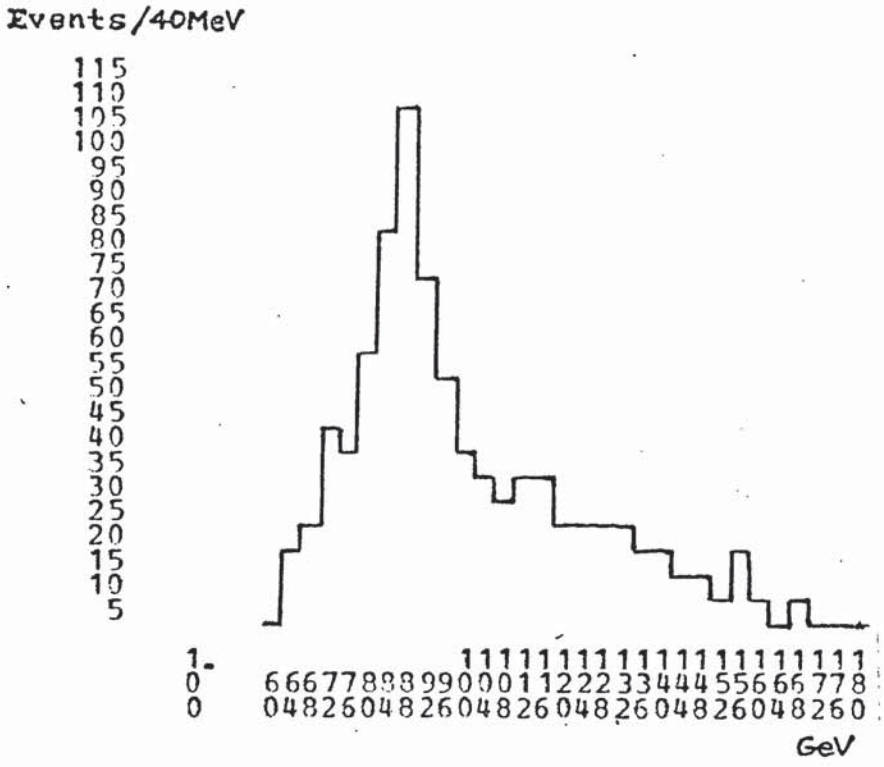

Figure 3.16: Mass $K^+\pi^0$

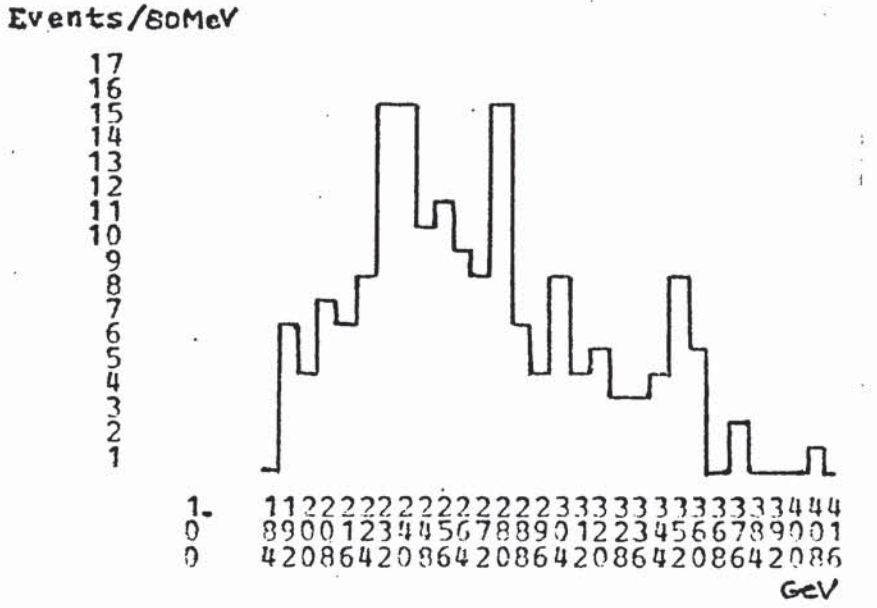

Figure 3.17: Mass $K^*(892)\phi(1020)$

Chapter IV
DETECTION LOSSES

4.1 INTRODUCTION

The imposition of a trigger on event recording in a spectrometer experiment is necessary to select preferentially the reactions of interest. Only those events are recorded whose configurations in space lie within the geometry of the trigger system. This has the effect of introducing biases into the data sample recorded. These biases must be studied as a function of the kinematic variables which are chosen to describe an event. Furthermore, some fraction of produced events which would be geometrically accepted by the spectrometer are not observed because of various detection and reconstruction inefficiencies.

Both the geometrical acceptance of the spectrometer and the correction factors necessary to take account of inefficiencies and other effects are discussed below, in addition to the method of calculating cross-sections.

4.2 ACCEPTANCE

The aim of any analysis is to:

a) reconstruct the original event distribution from the experimental data so that the underlying physical processes may be deduced

or b) test a theoretical model of the physical processes under study by comparing the experimental data with simulated data generated according to the model.

With regard to such an aim, we consider the final particle state and the limitations of acceptance biased data.

The description of an n body final state (ignoring spin) requires (3n-4) independent kinematic variables, where each

body has 3 degrees of freedom, and the final state is constrained by four-momentum conservation [31]. Hence, for a 4 body final state, the acceptance is completely defined if known as a function of 8 kinematic variables. However, in practice this is difficult to manage, since if each variable is divided into m bins, a total of m^8 bins is required to describe the acceptance function. Simplifying assumptions are therefore necessary to reduce the number of variables. It follows then that an event has a fractional probability of being accepted, rather than simply being accepted or not accepted. The reciprocal of this probability may be used to weight each observed event in order to reconstruct the original event distribution.

However, it may be found that there are regions of zero acceptance ('holes') in the space described by the chosen set of kinematic variables. The experimental data therefore can never yield any information on the physical processes which originally may have produced events in these regions. Weighting the observed events by the reciprocal of an acceptance probability can only reconstruct the original event distribution in regions of non-zero acceptance. Consequently, care must be exercised in interpreting results obtained from weighted data by integrating over kinematic variables. If a theoretical model is being tested by generating simulated data, the simplest model which produces results consistent with the observed data should be used.

To illustrate procedures a) and b) above, figure 4.1 shows event distributions as a function of some hypothetical final state space. Events in region A are always detected by the spectrometer, whilst events in region A' are never detected. The weighting procedure is shown in figure 4.1(1), and an iterative modelling procedure is shown in figure 4.1(2). Both techniques are discussed below.

4.2.1 Weighting

The primary trigger condition in WA48 was that of having a fast forward $\bar{p}$ or K^-. It is reasonable to assume that the overall acceptance was largely described by the acceptance for this particle in terms of its 3 kinematic variables. However, one further experimental bias must be considered: the effect of varying the position of the interaction vertex in the target. Since the target proton is unpolarised, one particle variable corresponding to rotation around the beam axis can be regarded as trivial. The final 3 variables used to describe the acceptance function were:

1. the transverse momentum p_T of the negative track relative to the beam direction.
2. the magnitude $|p|$ of the momentum of the negative track
3. the x-coordinate x of the interaction vertex in the target

A program was written by A.S.Thompson to calculate the acceptance for $\bar{p}$ and K^- tracks at points on a $(p_T, |p|, x)$ grid. For each point on the grid, tracks were generated around the beam direction at regular angular intervals. Each generated track was traced through the Omega magnetic field and the trigger system to determine whether the track was accepted or not. In the case of the acceptance for K^- tracks, each track was assigned a decay probability weight (see appendix A), since a μ^- or π^- from a K^- decay would have vetoed an event. The acceptance probability for a point on the $(p_T, |p|, x)$ grid was defined as:

$$\frac{\text{total weight of generated tracks accepted}}{\text{number of generated tracks}}$$

For the selected grid, figure 4.2 shows the percentage acceptance at every second point in the p_T and $|p|$ directions at x=-135 cm. Also, the $(p_T, |p|)$ distribution for the K^- trigger track from all data selected in the reaction $K^+p \rightarrow K^-K^+K^+p$ with $-135 < x < -125$ cm is shown in

figure 4.3. The numbers plotted represent the percentages of the total data lying within $(p_T, |p|)$ cells. The distribution of the data is such that a finer acceptance grid would be desirable, especially at low momentum.

Each event observed in the reactions 3.1 and 3.2 was weighted by a factor

$$w(p_T, |p|, x) = 1/a(p_T, |p|, x)$$

where the acceptance $a(p_T, |p|, x)$ of an event was interpolated from the computed acceptance grid for the trigger track.

The distributions of weighted events for various physically interesting parameters such as mass, production and decay angles, indicated that there were insufficient data in many regions of the final state space to make weighting a statistically valid procedure. It was decided therefore that priority should be given to developing a modelling method of analysis.

4.2.2 Modelling

Previous data [28, 12-34], though limited in statistics, have indicated that reactions 3.1 and 3.2 proceed largely in a diffractive manner, with the incident kaon dissociating into a forward three-body system, either directly:

$$K^+p \rightarrow (K^-K^+K^+)p \qquad (4.1)$$
$$K^+p \rightarrow (\bar{p}pK^+)p \qquad (4.2)$$

or indirectly via two-body sequential decay modes such as

$$K^+p \rightarrow (\phi(1020)K^+)p, \quad \phi(1020) \rightarrow K^-K^+ \qquad (4.3)$$
$$K^+p \rightarrow (\bar{\Lambda}(1520)p)p, \quad \bar{\Lambda}(1520) \rightarrow \bar{p}K^+ \qquad (4.4)$$

A characteristic feature of such reactions is the strong dependence of the slope of the $d\sigma/dt'$ distribution on the mass of the primary excited system, where $t' = |t - t_{min}|$ and t is the squared four-momentum transfer between the incident beam particle and the excited system. The quantity t' may also be expressed as

$$t' = 2|p_i||p_f|(1-\cos(\theta_p)) \qquad (4.5)$$

where: p_i, p_f are the momenta of the beam particle and excited system respectively

θ_p is the production angle of the excited system relative to the incident beam particle.

Assuming that the t' distribution may be described by a function of the form

$$d\sigma/dt' = A\exp(-Bt') \qquad (4.6)$$

the production of the excited system can be modelled, if the slope parameter B is known as a function of mass.

With a view to investigating the spin properties of the systems produced in processes such as 4.3 and 4.4, we shall model the sequential decays of two-body states:

$$\begin{array}{l} K^+ + p \rightarrow R + p \qquad (4.7) \\ \qquad\quad \Omega \hookrightarrow R_1 + R_2 \\ \qquad\qquad\quad \Omega' \hookrightarrow R_3 + R_4 \end{array}$$

where $\Omega = (\theta,\phi)$ and $\Omega' = (\theta',\phi')$ describe the decay angular distributions of resonances R and R_1 respectively.

Following a method originally devised by D.Frame [35], a program was written to generate events corresponding to the process 4.7, and to determine for each generated event whether the negative track (R_3) was accepted or rejected by the trigger system. With reference to figure 4.4, the scheme of event generation in the program was as follows:

1. A beam track was generated in the laboratory system (LS) within the experimentally observed distributions of momentum and divergence from the nominal beam direction. Normal distributions for momentum (mean 13.02 GeV, standard deviation 0.1 GeV) and divergence (standard deviation 4 mrad) were used. The beam track was then transformed into the centre-of-momentum system (CMS) of the beam (K^+) and target (p) particles.

2. An interaction point in the target was chosen, uniformly along the target length, across a radius, and in angle around the axis.
3. For a specific R mass, the energy and |momentum| of R were precisely determined in the CMS. A t'(beam/R) value was chosen within a distribution fitted to equation 4.6, and using equation 4.5, a production angle θ^{CMS} was determined for R. (Previous experience [35] of similar Omega data has shown that the slope parameters of t' distributions are largely unchanged by geometric acceptance. Therefore, data t' distributions fitted as a function of R mass were used in the first instance.) The angle of R around the beam axis ϕ^{CMS} was chosen uniformly. The momentum components of R were then calculated.
4. For a specific R_1 mass, the energy and |momentum| of R_1 were precisely determined in the R rest system. The beam was transformed into the R rest frame to define an axis, and decay angles (θ^R, ϕ^R) for R were chosen uniformly in solid angle. The momentum components of R_1 were then calculated.
5. The energy and |momentum| of R_3 were precisely determined in the R_1 rest frame. Decay angles $(\theta^{R_1}, \phi^{R_1})$ for R_1 were chosen uniformly in solid angle. The momentum components of R_3 were then calculated.
6. R_3 was transformed back into the laboratory system, assigned a negative charge, and then tracked from the vertex in the target through the Omega field to the hodoscopes H1 and H2. For speed, tracking was done by a routine (FOLLOW [36], accurate to about 10 cm at H2) which parameterised the field integral along the track length as a function of the vertex position and the initial track angles in Omega. If the track satisfied the following criteria, the event was accepted:

   a) |momentum| > 3 GeV

b) passed through H1 and H2 within the matrix correlation

c) did not pass through the beam veto counter V0

d) for a K^- track, did not decay to particles which then gave light in the Cherenkov counter C. The method of simulating K^- decays is described in appendix A.

7. For a specific process under study, any further selections necessary to simulate the real data were applied, and relevant physics quantities were calculated. If events were being generated within specific mass or decay angular distributions, the event was weighted according to the given distributions.

Muliplicity conditions were not incorporated into the simulation of the trigger since work on this topic by P.W.Minto [37] had shown that their effect on the overall acceptance was negligible.

The trigger simulation part of the program was tested using the experimental data which had been selected to lie in the reactions 3.1 and 3.2. Less than 0.3% of real events were rejected by the software trigger imposed.

4.3 CORRECTION FACTORS

Some fraction of events produced which would have been accepted by the geometry of the spectrometer were lost because of inefficiencies in the detectors or because the events could not be reconstructed adequately by the program ROMEO (see chapter III). Also, any beam flux losses or spurious vetoing by the forward π^0 detector would reduce the values of the cross-sections calculated. Whilst a proper study of the various inefficiencies and losses should take the configuration and kinematics of events into consideration, the investigation of these effects by simulation on an event by event basis was considered impractical. Consequently, global correction factors were applied to calculated cross-sections to take account of the

effects discussed below. Uncertainties have been quoted where practicable.

4.3.1 Beam Flux Corrections

The beam flux measured by the counters upstream of the target (figure 2.3) was modified to take account of the following effects:

1. Decays before target
   Using Monte-Carlo techniques similar to those described in appendix A, a program was written to simulate K^+ decays between the beam differential Cherenkov CEDAR and the target in order to estimate the probability of muon or pion decay products satisfying the clean beam signal.
2. Interactions in beam counters
   The probability of a beam particle interacting in the scintillation counter S4 or in the MWPC B1 was calculated, having assumed that the products of interactions upstream of these counters could not satisfy the the clean beam conditions. The interaction cross-section used was the K^+p total cross-section minus the elastic contribution [4].
3. Absorption in target
   The number of beam particles available for interaction decreases along the length of the target towards the downstream end. This 'beam absorption' effect was calculated using the total K^+p cross-section [4].
4. Decays in target
   The number of beam particles which would be expected to decay inside the target was calculated using the exponential decay law (see appendix A).

The combined correction factor for these effects was

$$f_{BEAM} = 1/0.97$$

4.3.2 Trigger Efficiency

Work done by P.J.Harper [39] on the determination of the efficiencies of hodoscopes H1 and H2, and the wire chamber MWPC1 (see figure 2.2), was used to estimate a trigger efficiency for three and four-prong events. The efficiencies of the above counters were determined by tracing tracks from the target through the Omega field to the counters, and comparing predicted hits with the actual electronic hits recorded. The tracks used were from data for which the trigger demanded only an interaction in the target.

Since the majority of three and four-prong events selected for analysis had three tracks which passed through MWPC1, the effects of inefficiencies in this counter were assumed to be of greater importance than those caused by the TS hodoscope (see chapter II). The probability of satisfying the multiplicity conditions required in MWPC1 ($\geq$ 2 tracks) and the probability of detecting hits both in H1 and H2 were combined to give a correction factor for the trigger efficiency

$$f_{TRIG} = 1/0.90$$

4.3.3 Spurious Vetoing

Consideration was given to the possibility of a forward charged particle from the target either directly, or indirectly through interaction, registering the electronic signal used to identify a forward π^0, and thereby vetoing an event (see chapter II). Work done by I.T.Wilkie [38] using tracks taken from data recorded with no π^0 veto in the trigger investigated whether

1. a track from the target could pass through an H3 group of elements without passing through the corresponding H2 group
2. the trajectories of particles produced in simulated interactions with material in the Cherenkov counter C, the hodoscope H2, and the lead sheet could pass

through an H3 group of elements without passing through the corresponding H2 group.

The correction factor obtained was

$$f_{\pi^o} = 1/0.99$$

4.3.4 Track Interactions

Consideration was given to the interaction of the outgoing tracks with the hydrogen in the target, and the interaction of the trigger track with material between the target and hodoscope H2. The mean momentum of each outgoing track in reactions 3.1 and 3.2 was determined from the experimental data, and the interaction cross-section for a given track taken to be the total cross-section minus the elastic contribution for the interaction of the track with a proton at the mean momentum. The probability of interaction along half the length of the target was calculated for the three fastest outgoing tracks. Using information from references 28, 2, 4, and 23, the total mass/unit area of the material contained in the spark chambers, MWPCs, drift chambers, Cherenkov C, and hodoscope H1, was calculated, and an interaction probability determined for a K^- or $\bar{p}$ trigger track.

The combined probabilities yielded correction factors

$$f_{INT}\ (K^-K^+K^+p) = 1/(0.88 \pm 0.02)$$
$$f_{INT}\ (\bar{p}pK^+p) = 1/(0.77 \pm 0.02)$$

4.3.5 Reconstruction Efficiency

In order to estimate an event reconstruction efficiency for the pattern recognition and geometrical reconstruction program ROMEO (see chapter III), spark chamber digitisings and ROMEO output records for 500 triggers from each of the two data-taking runs were studied. The raw digitisings were scanned for events with one negative track >3 GeV and two or

three positive tracks emanating from a single vertex in the target. If ROMEO was found to have reconstructed an event with topology 1-3+ as 1-2+ or 1-3+, or an event with topology 1-2+ as 1-2+, the program was deemed to have reconstructed the event adequately, ie. the event could be selected by the procedures described in chapter III. The correction factors determined were

$$f_{REC}\ (\text{run 1}) = 1/(0.63 \pm 0.07)$$
$$f_{REC}\ (\text{run 2}) = 1/(0.51 \pm 0.06)$$

4.3.6 Summary

Contributing Factors

Beam flux corrections		:	1/0.97
Trigger efficiency		:	1/0.90
Spurious vetoing		:	1/0.99
Track interactions	$K^+p \rightarrow K^-K^+K^+p$	:	$1/(0.88 \pm 0.02)$
	$K^+p \rightarrow \bar{p}pK^+p$	:	$1/(0.77 \pm 0.02)$
Reconstruction efficiency	run 1	:	$1/(0.63 \pm 0.07)$
	run 2	:	$1/(0.51 \pm 0.06)$

Total Factors

$K^+p \rightarrow K^-K^+K^+p$	run 1	:	$1/(0.48 \pm 0.05)$
	run 2	:	$1/(0.39 \pm 0.05)$
$K^+p \rightarrow \bar{p}pK^+p$	run 1	:	$1/(0.42 \pm 0.05)$
	run 2	:	$1/(0.34 \pm 0.04)$

4.4 METHOD OF CALCULATING CROSS-SECTIONS

The cross-section for a reaction is defined as the number of events occurring in the reaction per unit time per unit beam flux per target particle. This may be calculated as

$$\sigma = n/n_b \rho L N_A \qquad (4.8)$$

where: n = total number of events identified in the reaction
n_b = total number of beam particles incident on target
ρ = density of liquid hydrogen
L = length of target
N_A = Avogadro's number

The equivalent beam flux sensitivities s (= n/σ) for 100% detection efficiency, allowing for DST losses, were calculated from the above expression, giving

$s(K^+p \rightarrow K^-K^+K^+p)$ run 1 = 2.863
run 2 = 8.822, total = 11.685 events/nb

$s(K^+p \rightarrow \bar{p}pK^+p)$ run 1 = 2.863
run 2 = 9.333, total = 12.196 events/nb

Substituting appropriate values, and incorporating acceptance and correction factors into equation 4.8 yields

$$\sigma = cfn/n_b a \quad \mu b \qquad (4.9)$$

where: $c = 0.3908387 \times 10^6$

$f = f_{BEAM}\, f_{TRIG}\, f_{\pi^0}\, f_{INT}\, f_{REC}$ (total correction factor)

a = overall acceptance for the specific physics model of the reaction under study

The above expression (4.9) was used to calculate the cross-sections discussed in following chapters.

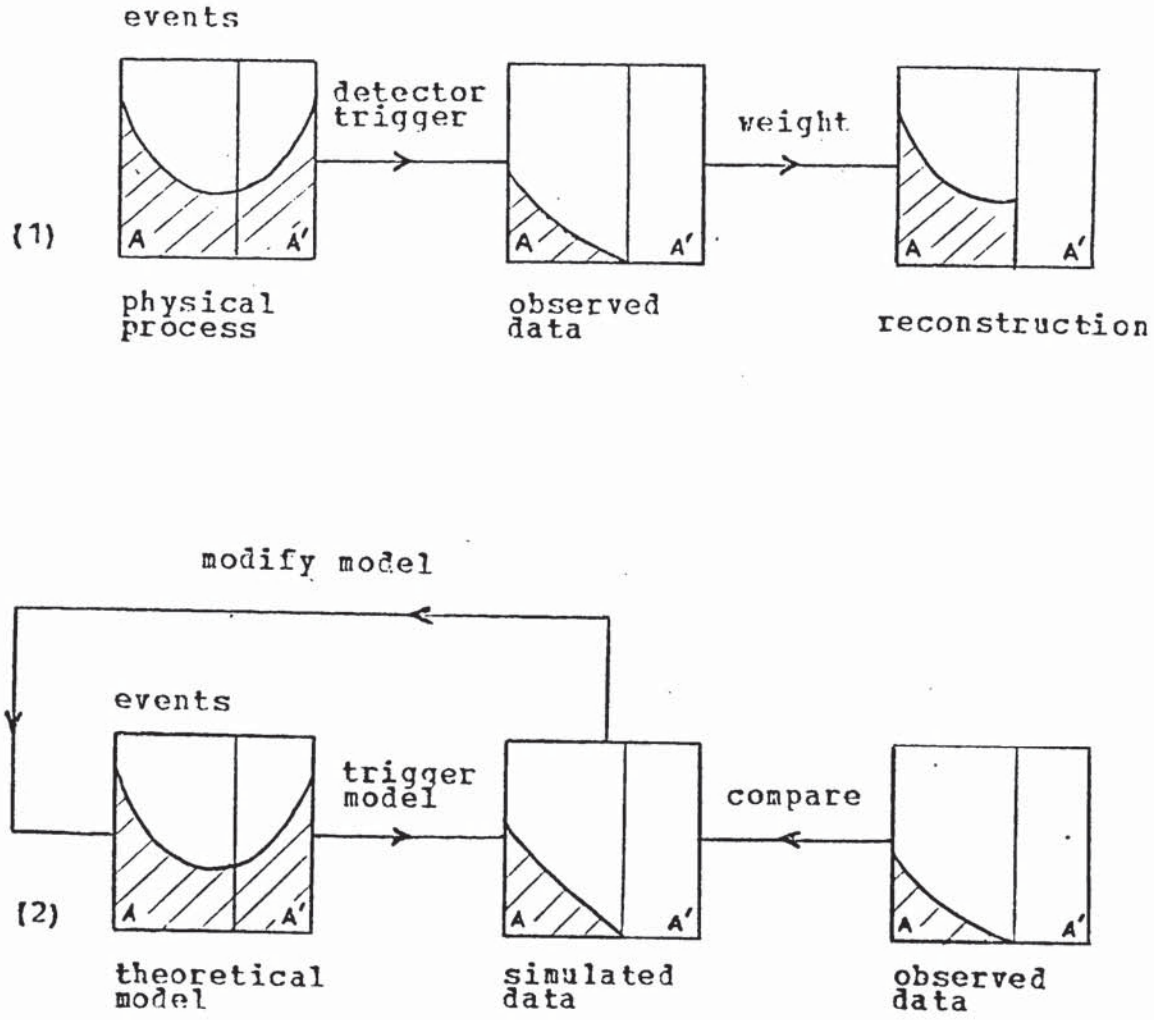

Figure 4.1: (1) Weighting (2) Modelling

x = -135 cm

p_T =	0.0	0.16	0.32	0.48	0.64	0.80	0.96	1.12	1.28	1.44	1.60 GeV
|p| = 2.8	0	0	0	0	9	8	7	0	0	0	0
3.6	0	0	14	20	14	11	9	1	0	0	0
4.4	72	42	37	34	20	15	10	8	0	0	0
5.2	76	76	76	55	29	19	14	13	0	0	0
6.0	79	79	79	79	65	28	17	15	1	0	0
6.8	81	81	81	81	81	55	27	11	2	0	0
7.6	83	83	83	83	83	83	51	19	3	0	0
8.4	84	84	84	84	84	84	61	33	11	0	0
9.2	86	86	86	86	86	86	80	43	22	6	0
10.0	87	87	87	87	87	87	75	54	34	15	8
10.8	88	88	88	88	88	85	73	66	39	26	22
11.6	88	88	88	87	83	80	64	62	46	28	24
12.4	89	88	79	82	82	71	68	55	54	31	22

GeV %

Figure 4.2: K^- trigger acceptance grid (p_T,|p|)

-135 < x < -125 cm

low edge p_T =	0.0	0.16	0.32	0.48	0.64	0.80	0.96	1.12	1.28	1.44	1.60 GeV
low edge |p| = 2.8	0	0	1	1	0	0	0	0	0	0	0
3.6	2	4	3	1	0	0	0	0	0	0	0
4.4	6	10	5	2	1	0	0	0	0	0	0
5.2	4	8	6	3	1	0	0	0	0	0	0
6.0	4	6	4	2	1	0	0	0	0	0	0
6.8	2	3	2	1	1	1	0	0	0	0	0
7.6	1	2	1	1	0	0	0	0	0	0	0
8.4	1	2	1	0	0	0	0	0	0	0	0
9.2	1	1	0	0	0	0	0	0	0	0	0
10.0	0	0	0	0	0	0	0	0	0	0	0
10.8	0	0	0	0	0	0	0	0	0	0	0
11.6	0	0	0	0	0	0	0	0	0	0	0
12.4	0	0	0	0	0	0	0	0	0	0	0

GeV %

Figure 4.3: Data K^- trigger (p_T,|p|) distribution

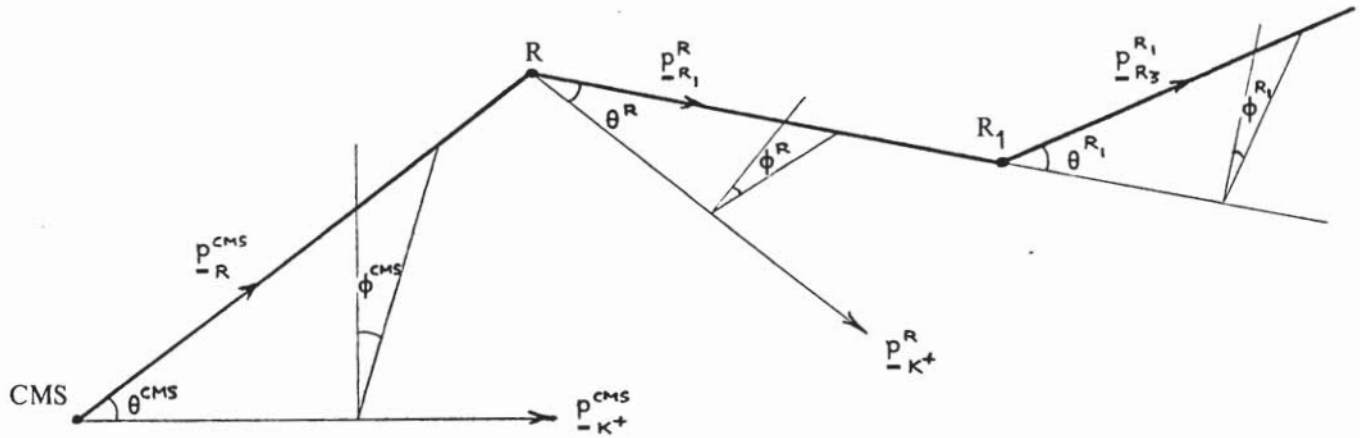

where: $\underline{p}^{\mu}_{\nu}$ is the momentum vector of particle ν in rest frame μ

$(\theta^{\mu}, \phi^{\mu})$ are the spherical polar generation angles in frame μ

Figure 4.4: Production and decay generation scheme

Chapter V

A STUDY OF THE REACTION $K^+p \rightarrow \bar{p}pK^+p$

5.1 INTRODUCTION

Few data exist [28,34,7] on the reaction

$$K^+p \rightarrow \bar{p}pK^+p$$

largely because of its low cross-section (a few μb) [4] relative to other four-body final states. The study of this process allows a search for resonances in the baryon-antibaryon system with little complication from the production of other resonances in the final state, unlike corresponding processes with an incident pion, where there is copious $\Delta^{++}(1232)$ production. The only well-recognised resonance produced is the narrow $\bar{\Lambda}(1520)$, which decays to $\bar{p}K^+$ [2]. The reaction mechanisms which produce the high rest mass final state are also of interest.

Previous data [34] at an incident beam momentum of 12 GeV showed a broad threshold enhancement in the $\bar{p}p$ mass spectrum, but no narrow enhancements, such as the S(1935) [2], were evident. For the reaction in which the $\bar{\Lambda}(1520)$ was not produced, a significant fraction of events was seen to have a backward K^+ in the CMS.

The data sample analysed in experiment WA48 represents a doubling of the previous best statistics, and comprises fully reconstructed (four-prong) events only. Reaction characteristics, the results of resonance searches, and the production and decay characteristics of the $\bar{\Lambda}(1520)$ resonance are discussed.

5.2 PRELIMINARY

The results presented are based on the data sample of 2093 events (1788 unique) selected and weighted for internal ambiguities by the techniques described in chapter III. Various sub-samples were also used to test the consistency of the results obtained. This involved:

1. separating run 1 and run 2 data samples
2. selecting unique events only
3. removing events with a -ve/+ve track combination which when assigned masses as K^-/K^+ had an effective mass in the region of the $\phi(1020)$ meson, viz. $1.00 < \text{mass}('K^-K^+') < 1.04$ GeV.

5.3 REACTION CHARACTERISTICS

The longitudinal momenta p_L of the secondary particles relative to the beam in the CMS are shown in figures 5.1 to 5.3. The $\bar{p}$ is seen to be produced forward (as required by the trigger), the K^+ largely forward, and the protons both forward and backward. The correlation between p_L of the slower proton and p_L of the faster proton in the laboratory system (figure 5.4) indicates that the protons may be distinguished as 'slower' (p_s) or 'faster' (p_f). The slower protons are produced entirely backward, and approximately a third of the faster protons are also backward.

The production of a forward $\bar{p}pK^+$ system against a recoiling backward proton suggests the importance of a beam fragmentation process in the reaction.

The fraction of events with a backward K^+ ($\sim 17\%$) is smaller than that anticipated from previous data [28], where almost half of the data were found to have a backward K^+. However, the previous data contained a large proportion ($\sim 25\%$) of three-prong events with a missing K^+. We recall that in the present experiment no delta function peak was seen for the four-prong hypothesis with the K^+ as the slowest track in the laboratory system (hence backward in the CMS), and that no missing kaon signal was seen in the three-prong data (see chapter III).

5.4 MASS SPECTRA

5.4.1 $\bar{p}K^+$

The $\bar{p}K^+$ effective mass distribution shown in figure 5.5, and in figure 5.6 in finer detail, exhibits a clear peak corresponding to the $\bar{\Lambda}(1520)$ resonance. The resonance region is well fitted by a Breit-Wigner function superimposed on a quadratic background (see appendix B). The fitted mass and width, uncorrected for experimental resolution, are

$$m = 1.520 \pm 0.001 \text{ GeV}$$
$$\Gamma = 0.021 \pm 0.003 \text{ GeV}$$

respectively. After considering the minimum resolution function width Γ_r of 2 MeV obtained from the experimental errors on mass (see appendix C), these resonance parameters are consistent with Particle Data Group (PDG) values [2]. The $\bar{\Lambda}(1520)$ pp data sample will be discussed later.

No higher mass $\bar{\Lambda}$ states are seen.

5.4.2 $\bar{p}p$ and $\bar{p}pp$

Figure 5.7 shows the mass distribution for $\bar{p}p$ combinations (two combinations per event). Two broad enhancement regions are seen, corresponding to the $\bar{p}p_f$ (lower mass) and $\bar{p}p_s$ (higher mass) combinations. The $\bar{p}p_f$ combination, expected to be kinematically more favourable for resonance production, is shown superimposed on the figure, and is responsible for producing a threshold enhancement peaking around 2 GeV with a steep leading edge. No narrow structures are evident,[3] and in particular, there is no evidence for the production of the narrow ($\Gamma \lesssim 10$ MeV) S(1935) resonance, which is not well-established at present [2]. A resolution of 1.5 MeV in the threshold $\bar{p}p_f$ mass region was derived from the experimental errors. The $\bar{p}p$ system is discussed in more detail later.

---

[3] To be regarded as significant, a signal was required to rise at least 3 standard deviations from the background. See discussion in reference 66.

The $\bar{p}pp$ mass spectrum is shown in figure 5.8. Again, there is no evidence for any resonant states. The narrow ($\Gamma \sim 40$ MeV) enhancement at 3.755 GeV suggested by the very limited statistics $\pi^+p \rightarrow \pi^+pp\bar{p}$ data of Ehrlich et al. [40] is not seen. As has already been noted by D.Frame [28], any resonant effect in $\bar{p}pp$ would probably be produced by target fragmentation, and the resulting slow $\bar{p}$ would not be accepted by the forward trigger geometry in the present experiment.

5.4.3 pK^+, pp and $\bar{p}pK^+$

The mass spectra of the exotic combinations pK^+ and pp are shown in figures 5.9 and 5.10 respectively. No significant enhancements are seen in either distribution, although a dip exists in the pp spectrum in the region 2.5 - 2.6 GeV. This dip was found to be a kinematic effect produced by the addition of the two pp mass spectra corresponding to the hypotheses with positive track ordering ppK^+ (lower mass spectrum) and pK^+p (higher mass spectrum).

Figure 5.11 shows the mass distribution for $\bar{p}pK^+$ combinations (two combinations per event). Two broad enhancement regions are seen, corresponding to the $\bar{p}p_f K^+$ (lower mass) and $\bar{p}p_s K^+$ (higher mass) combinations. No significant enhancements are seen in the total mass spectrum, or in the mass spectra of the individual combinations.

5.5 THE REACTION $K^+p \rightarrow \bar{\Lambda}(1520)pp$

5.5.1 Production characteristics

A sample of 487 (428 unique) events corresponding to the reaction

$$K^+p \rightarrow \bar{\Lambda}(1520)pp, \quad \bar{\Lambda}(1520) \rightarrow \bar{p}K^+ \qquad (5.1)$$

was selected by requiring a $\bar{p}K^+$ mass in the range 1.50 - 1.54 GeV.

Although data distributions may be distorted by the trigger acceptance and the selection of only four-prong

events, the characteristics of this reaction are evident from the Van Hove plot (see appendix B) of $\bar{\Lambda}(1520)\,p_f\,p_s$ shown in figure 5.12, and the associated ω angle (figure 5.13). In the CMS, the $\bar{\Lambda}(1520)$ is produced forward, the slower proton backward, and the faster proton either forward or backward, but largely forward. This, and the high t' slope parameter ($B \sim 2.5$ GeV^{-2}) for t'(beam/$\bar{\Lambda}(1520)\,p_f$) fitted from the data, suggest that an important reaction process is the diffractive excitation of the incident K^+ to a state which decays to $\bar{\Lambda}(1520) + p_f$.

The observed behaviour is similar to that of the reaction

$$K^+p \rightarrow \bar{\Lambda}pp$$

which has been studied in the present experiment [23,22]. Bubble chamber data [41,42] on this reaction at 10 GeV and 12.7 GeV, with few acceptance biases, also supports a diffractive interpretation.

5.5.2 Mass spectra

The $\bar{\Lambda}(1520)\,p$ mass spectrum which is shown in figure 5.14 comprises two broad enhancement regions, the lower mass enhancement being produced by the $\bar{\Lambda}(1520)\,p_f$ combination (shown superimposed). No significant structures are seen to suggest the presence of, for example, high mass K* mesons decaying via this mode.

5.5.3 Decay of $\bar{\Lambda}(1520)$

The $\cos\Theta$ and ϕ distributions describing the decay $\bar{\Lambda}(1520) \rightarrow \bar{p}K^+$ in the t-channel helicity (TCH) frame (see appendix B) are shown in figures 5.15 and 5.16 respectively. The $\cos\Theta$ distribution appears to show structure, whilst the ϕ distribution is approximately isotropic. The TCH frame has been used since the $\bar{\Lambda}(1520)$ appears to be beam-like in the reaction 5.1. Since the $\bar{\Lambda}(1520)$ is known [2] to have spin 3/2, the decay angular distribution $W(\Theta,\phi)$ is of the form given by equation B.8 in appendix B, and depends on three independent density matrix elements ρ_{33}, $Re\rho_{31}$ and

$Re\rho_{3-1}$. In order to estimate the values of these parameters, the following analysis was carried out:

1. Using the modelling program described in chapter IV, events were generated according to the processes:

$$K^+ + p \rightarrow (\bar{\Lambda}(1520)\, p_f) + p_s$$
$$\hookrightarrow \bar{\Lambda}(1520) + p_f$$
$$\hookrightarrow \bar{p} + K^+$$

assuming isotropic decay of the $\bar{\Lambda}(1520)\, p_f$ system, and the $\bar{\Lambda}(1520)$ decay according to $W(\theta,\phi)$ for a given set of $\{\rho_{33}, Re\rho_{31}, Re\rho_{3-1}\}$.

$\bar{\Lambda}(1520)\, p_f$ masses were chosen according to the $\bar{\Lambda}(1520)\, p_f$ mass spectrum weighted for acceptance. (An approximate acceptance as a function of $\bar{\Lambda}(1520)\, p_f$ mass was obtained after initial estimates of the density matrix elements had been made from a study of the $\cos\theta$ and ϕ projections.) Production angles in the CMS were generated according to the $t'(\text{beam}/\bar{\Lambda}(1520)\, p_f)$ distribution described by the fitted experimental slope parameter.

$\bar{p}K^+$ masses were chosen according to the Breit-Wigner peak plus polynomial background fitted to the data $\bar{p}K^+$ mass spectrum in the $\bar{\Lambda}(1520)$ region. The $\bar{p}K^+$ system was decayed according to $W(\theta,\phi)$, or isotropically, depending on whether the event lay in the peak or background regions.

Events generated which satisfied the experimental selection criteria for the final state $K^-K^+K^+p$ were rejected.

2. For various $\underline{\rho} = \{\rho_{33}, Re\rho_{31}, Re\rho_{3-1}\}$ (the ρ's being varied within their allowed range of values in 0.1 steps) 10 x number of real events were simulated, and the resulting acceptance modified 2-dimensional angular distributions in $(\cos\theta,\phi)$ then compared with the data. Since there were regions of zero acceptance in $(\cos\theta,\phi)$ for $\cos\theta < 0$, only the forward $\cos\theta$ region was used, this being split into

4 cosΘ x 4 ϕ cells. The values of the density matrix elements were determined for which the chi-squared function given by

$$\chi^2(\underline{\rho}) = \sum_{\substack{\text{cells} \\ k}} \chi^2_k(\underline{\rho}) = \sum_{\substack{\text{cells} \\ k}} ((s_k - n_k)/\sqrt{n_k})^2 \quad (5.2)$$

where: n_k = number of real events in cell k
s_k = number of simulated events in cell k

was a minimum.

3. Errors on the density matrix elements $\{\rho_i, \rho_j, \ldots\}$ which minimised the χ^2 function were estimated by evaluating [43]:

$$\partial^2\chi^2/\partial\rho_i\partial\rho_j \simeq \sum_k 2(\partial\chi_k/\partial\rho_i)(\partial\chi_k/\partial\rho_j), \quad \text{with}$$

$$(\partial\chi_k/\partial\rho_i) \simeq (\chi_k(\rho_i + d\rho_i) - \chi_k(\rho_i - d\rho_i))/2d\rho_i$$

The second derivative matrix thus calculated could then be inverted to yield the covariance matrix. Increments $d\rho_i$ of 0.05 on the density matrix elements were used.

The best fit (confidence level ~73%) was obtained with each of $Re\rho_{31}$, $Re\rho_{3-1}$, and, in particular, ρ_{33} set to zero. The error calculated on ρ_{33} was ± 0.03. Figure 5.15 shows the forward cosΘ projection from this fit superimposed on the data cosΘ distribution.

Within experimental error, the $\bar{\Lambda}(1520)$ was found therefore to be produced entirely with helicity ±1/2 in the t-channel helicity frame ($\rho_{11} = \rho_{-1-1} = 1/2$). The vertex formed by the $\bar{\Lambda}(1520)$ (helicity 1/2), the incident K^+, and some exchange particle e in the rest frame of the $\bar{\Lambda}(1520)$ is shown [44] in figure 5.17. Conservation of baryon number and the component of angular momentum along the quantisation axis (z) indicates that the simplest exchange particle into the vertex is an antiproton. This, together with the apparently diffractive LPS characteristics, is consistent with the production diagram (see figure 5.18) suggested by Armstrong et al. [34], in which a 'Deck' type mechanism

[14,11] elastically scatters the faster proton at the bottom vertex.

An overall acceptance of 0.53 for a $\bar{\Lambda}(1520)$pp final state was determined using the above model with the best estimates of the $\bar{\Lambda}(1520)$ density matrix elements.

The distribution in the Van Hove plot of events simulated by the above method corresponded closely with the real data distribution. An alternative model which generated events according to the t'(beam/$\bar{\Lambda}(1520)$) distribution, $W(\theta,\phi)$, and isotropic decay of the $p_f p_s$ system, was unable to reproduce the real data distributions.

5.6 DATA EXCLUDING $\bar{\Lambda}(1520)$

In order to study the remainder of the channel, events with a $\bar{p}K^+$ mass in the range 1.50 - 1.54 GeV were removed from the data sample. For the remaining events, the mass combination formed by the $\bar{p}$ and each of the positive tracks assigned as a K^+ showed no signal for the $\bar{\Lambda}(1520)$. The mass spectra studied for these data was therefore not complicated by $\bar{\Lambda}(1520)$ reflections caused by internally ambiguous positive track assignments. As mentioned previously, no $\phi(1020)$ signal was seen when the $\bar{p}p$ combinations were treated as K^-K^+. (For example, the $\phi(1020)$ and $\bar{\Lambda}(1520)$ would reflect as peaks at $\sim$1.907 GeV and $\sim$1.962 GeV respectively in the $\bar{p}p$ mass spectrum.)

The pp, $\bar{p}pp$ and $\bar{p}pK^+$ effective mass spectra for the data sample excluding the $\bar{\Lambda}(1520)$ are similar to those for the total data sample and are not discussed further since they show no significant structures. The $\bar{p}p$ and pK^+ systems are, however, considered in more detail below.

5.6.1 $\bar{p}p$

The $\bar{p}p_f$ and $\bar{p}p_s$ mass spectra shown in figure 5.19 are very similar to those of the data sample including $\bar{\Lambda}(1520)$ events. No significant narrow enhancements are seen. Treating the $\bar{p}p_f$ combination as a single particle, the Van Hove plot and the corresponding ω angle distribution for the reaction

$$K^+p \rightarrow (\bar{p}p_f)K^+p_s$$

are shown in figures 5.20 and 5.21 respectively. The distribution of events falls essentially in two sectors, corresponding to forward $\bar{p}p_f$ production with forward or backward K^+ production. The former sector suggests a beam fragmentation process, whilst the latter is indicative of both beam and target fragmentation (see sector diagrams in figure 5.20). Backward K^+ events account for approximately a quarter of the data sample.

The $\bar{p}p_f$ mass spectra for both sectors (figures 5.22 and 5.23) appear as threshold enhancements, the spectrum for the backward K^+ sector being narrower and peaking at a lower mass. Although a possible shoulder is seen on the falling edge of both spectra, there is no statistically significant evidence for the production of narrow resonant states.

The $\bar{p}p_f$ decay angular distribution in the t-channel helicity frame was not found to show any significant effects when studied as a function of mass and Van Hove plot sector.

5.6.2 pK^+

Figures 5.24 and 5.25 show the mass spectra of the exotic (B=+1, S=+1, Q=+2) combinations p_sK^+ and p_fK^+ in the LPS sectors corresponding to forward $\bar{p}p_f$ production with forward or backward K^+ production. The p_sK^+ spectrum for events with a backward K^+ exhibits a significant ($\sim 5\sigma$ background $\rightarrow$ peak) signal in the 1.70 - 1.74 GeV mass bin. The peak region is shown in figure 5.26, and is well-fitted by a Breit-Wigner function plus a quadratic background. The fitted mass and full width were:

$$m = 1.721 \pm 0.004 \text{ GeV}$$
$$\Gamma = 0.039 \pm 0.015 \text{ GeV}$$

The lower limit to the width of the resolution function in this mass region, determined from the track errors, was ~ 6 MeV, giving a maximum true width to the peak of $\sim 33 \pm 15$ MeV by subtraction from the observed width.

The authenticity of the peak as an effect in the data is confirmed by its presence in the spectrum of the missing mass recoiling against the $\bar{p}p_f$ combination (figure 5.27). The reduced significance of the signal is consistent with the degradation in resolution estimated for this missing mass combination. Also, no resonance was known which could reflect a narrow spurious peak in the pK^+ mass spectrum around 1.72 GeV as a consequence of track mis-assignment.

The $p_s K^+$ decay angular distribution in the t-channel helicity frame has been studied in the following $p_s K^+$ mass ranges which were used to define the peak and control regions on either side of the peak:

Peak	:	1.68 - 1.76 GeV
Low guard band	:	< 1.68 GeV
High guard band	:	1.76 - 1.89 GeV

The $\cos\Theta$ and ϕ projections of the angular distributions for these regions are shown in figures 5.28 and 5.29. (Note that the Θ angle has been defined by taking p_s as the decay analyser and the target proton direction as the TCH frame z-axis.) The $\cos\Theta$ distribution shows little variation between the peak and guard band regions, whilst the ϕ distribution appears to change significantly with increasing mass only. Therefore, within the limited statistics available, the interpretation of the $p_s K^+$ peak as a resonance cannot be confirmed by the decay angular distribution.

If the $p_s K^+$ peak at 1.72 GeV is interpreted as a resonance, its exotic quantum numbers imply a $q^4\bar{q}$ ($uudu\bar{s}$) state, with isospin $I \geq 1$. With reference to [2] and [45], there is little evidence for Breit-Wigner type Z^* (S=+1 baryon) resonances, although KN amplitude analyses have suggested the existence of states such as the $Z_0(1780)$, $Z_0(1865)$ (both with I=0), and $Z_1(1900)$ (I=1), with widths of a few hundred MeV. The signal observed in the present experiment clearly cannot correspond to any of these Z^* states.

The final state $K^-K^+K^+p$ also provides an opportunity for detecting any possible resonant effects in pK^+: the analysis of this channel will be discussed in the following chapter.

5.7 CROSS-SECTIONS

Since the data sample consisted only of four-prong events, any cross-section calculated (by the methods described in Chapter IV) should be regarded as a lower cross-section limit. However, in order to provide a better estimate of the true cross-section, the 3/4-prong event ratio for events selected in the final state $K^-K^+K^+p$ has tentatively been assumed for the $\bar{p}pK^+p$ channel also. The ratio, $r_{3/4} \sim 2.2$, was calculated for events within (missing mass)^2 or delta function peaks after background subtraction.

5.7.1 $K^+p \rightarrow \bar{\Lambda}(1520)pp$

Using the acceptance of 0.53 determined previously, and the number of events found within $m_o \pm 3\Gamma$ of the fitted $\bar{\Lambda}(1520)$ Breit-Wigner peak above the observed background, the following lower limit was set:

$$\sigma(K^+p \rightarrow \bar{\Lambda}(1520)pp,\ \bar{\Lambda}(1520) \rightarrow \bar{p}K^+) \geq 0.22 \pm 0.03\ \mu b$$

The true cross-section was estimated to be $0.7 \pm 0.1\ \mu b$ using $r_{3/4}$. This is in good agreement with the only published value [34] of $0.54 \pm 0.15\ \mu b$.

5.7.2 $K^+p \rightarrow \bar{p}pK^+p$

An estimate of the total reaction cross-section was obtained by using $r_{3/4}$, and the $\bar{\Lambda}(1520)pp$ acceptance as an average acceptance for the channel. The number of events observed above background was estimated from the delta function peaks for the channel. The cross-section estimated:

$$\sigma(K^+p \rightarrow \bar{p}pK^+p) = 3.1 \pm 0.5\ \mu b$$

agrees well with the only known published value [7] of $3.0 \pm 0.5\ \mu b$ from bubble chamber data, and is consistent with the lower limits set by the data of reference 34.

5.7.3 Upper limit for S(1935) → $\bar{p}p$

Normalising to an estimated cross-section for the channel excluding $\bar{\Lambda}(1520)$ production:

$$\sigma(K^+p \rightarrow \bar{p}pK^+p, \text{ no } \bar{\Lambda}(1520) \rightarrow \bar{p}K^+) = 2.4 \pm 0.5 \ \mu b$$

and allowing for the mass resolution of the $\bar{p}p_f$ system in the S(1935) region, the upper limit determined for the production of the S(1935) decaying to $\bar{p}p$ was:

$$\sim 50 \pm 10 \text{ nb}$$

at 3 standard deviations confidence level.

5.7.4 pK^+ peak

The cross-section lower limit for the production of the peak (Z) seen at 1.72 GeV in the p_sK^+ mass spectrum was calculated to be:

$$\sigma(K^+p \rightarrow \bar{p}p_f Z(1.72), Z(1.72) \rightarrow p_s K^+) \geq 28 \pm 3 \text{ nb}$$

where events within $m_o \pm 3\Gamma$ of the fitted Breit-Wigner shape were taken, and the $\bar{\Lambda}(1520)$ acceptance was assumed. Using $r_{3/4}$, the true cross-section was estimated to be 88 ± 13 nb.

5.8 RESUME

The reaction $K^+p \rightarrow \bar{p}pK^+p$ at 13 GeV has been studied with the best statistics known. Strong $\bar{\Lambda}(1520)$ production is seen in $\bar{p}K^+$, and the $\bar{\Lambda}(1520)p_f$ system is found to be produced in a manner consistent with diffractive dissociation of the incident K^+. No narrow resonances are found in the baryon-antibaryon spectra, but a possible narrow exotic state is seen in pK^+. Cross-sections have been estimated for the complete channel and for the subreaction $K^+p \rightarrow \bar{\Lambda}(1520)pp$. An upper limit has been determined for the production of S(1935) decaying to $\bar{p}p$.

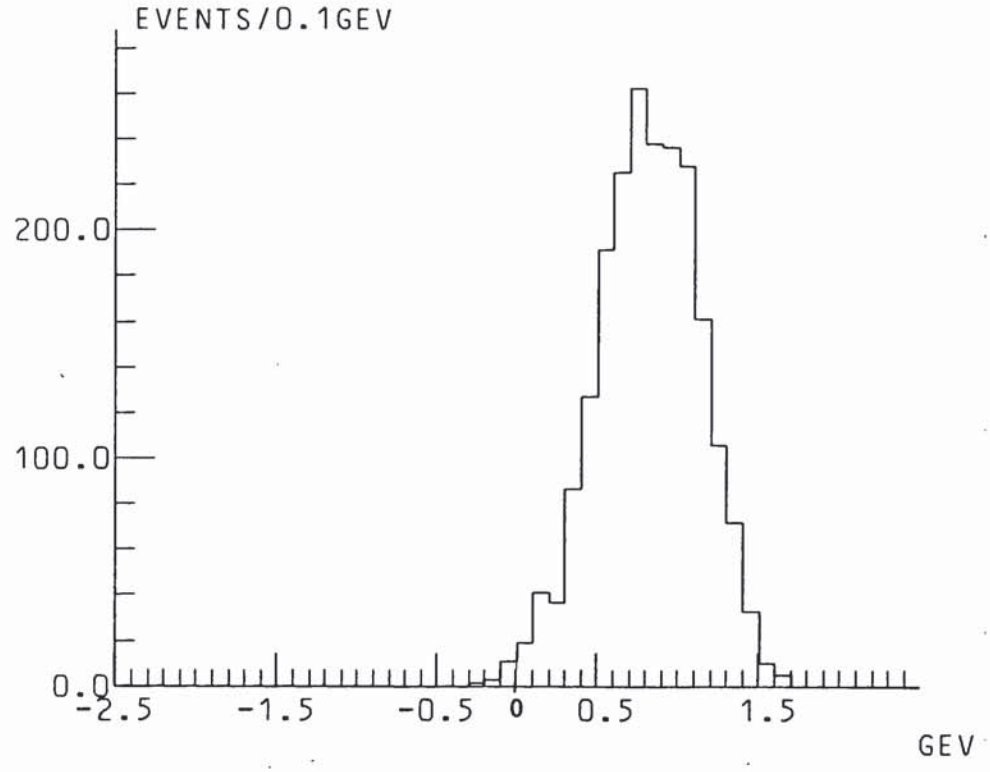

Figure 5.1: $\bar{p}$ **CMS longitudinal momentum**

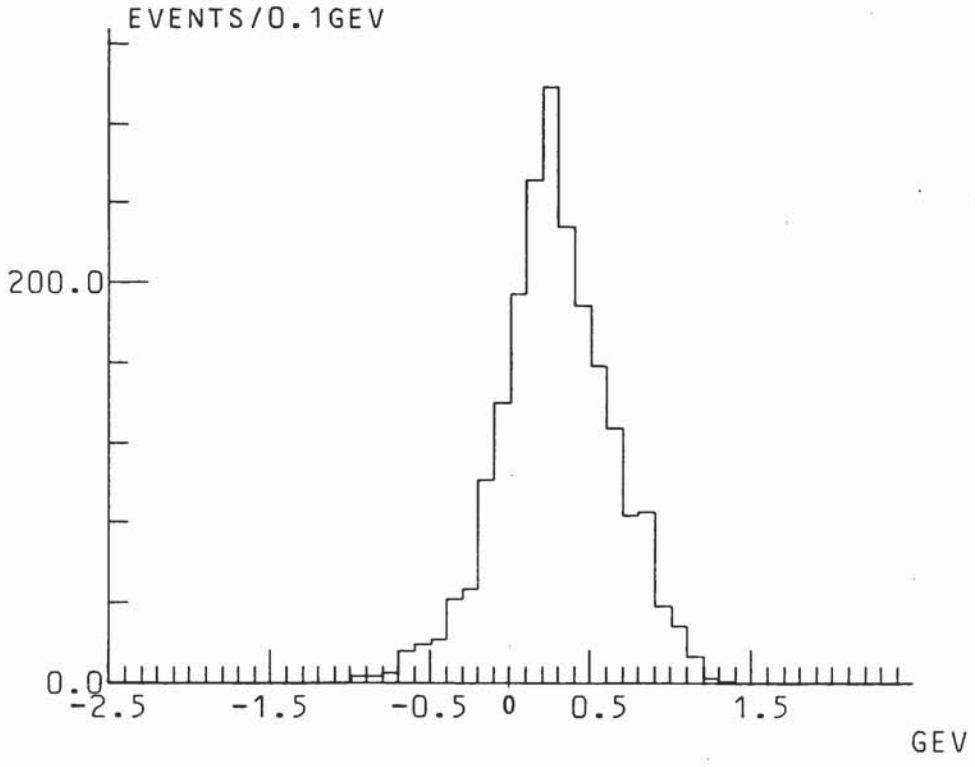

Figure 5.3: K^+ **CMS longitudinal momentum**

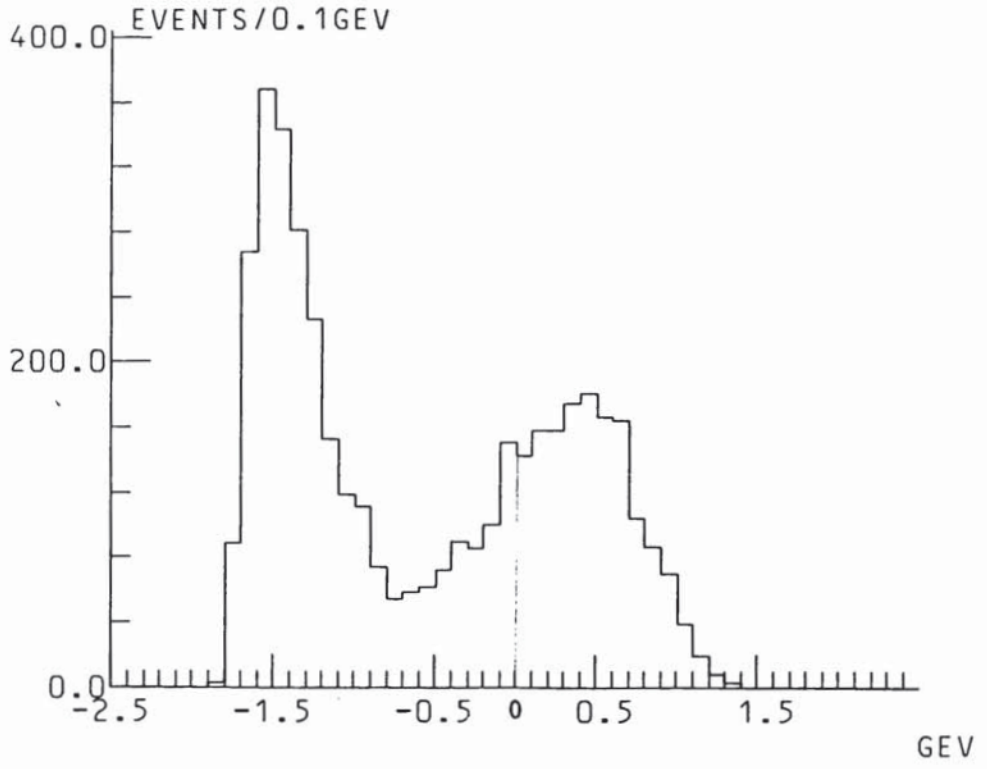

Figure 5.2: p CMS longitudinal momentum

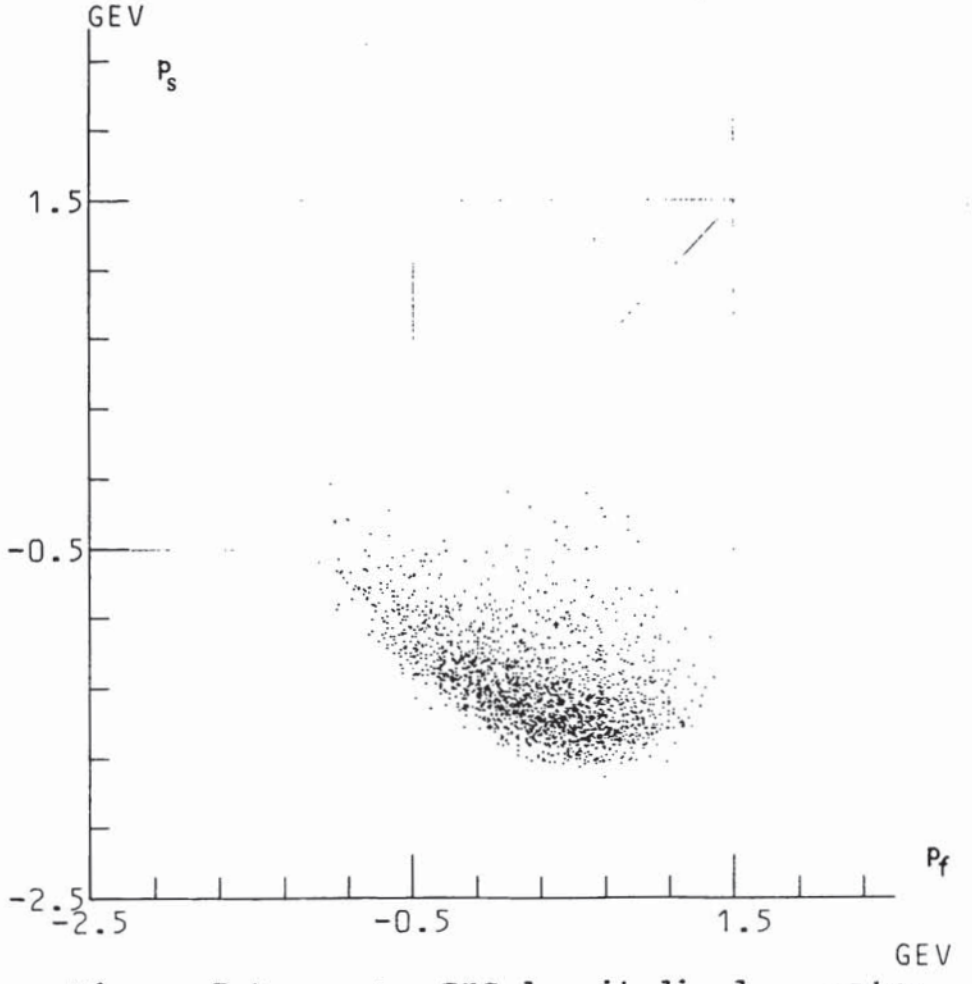

Figure 5.4: p_f / p_s CMS longitudinal momentum

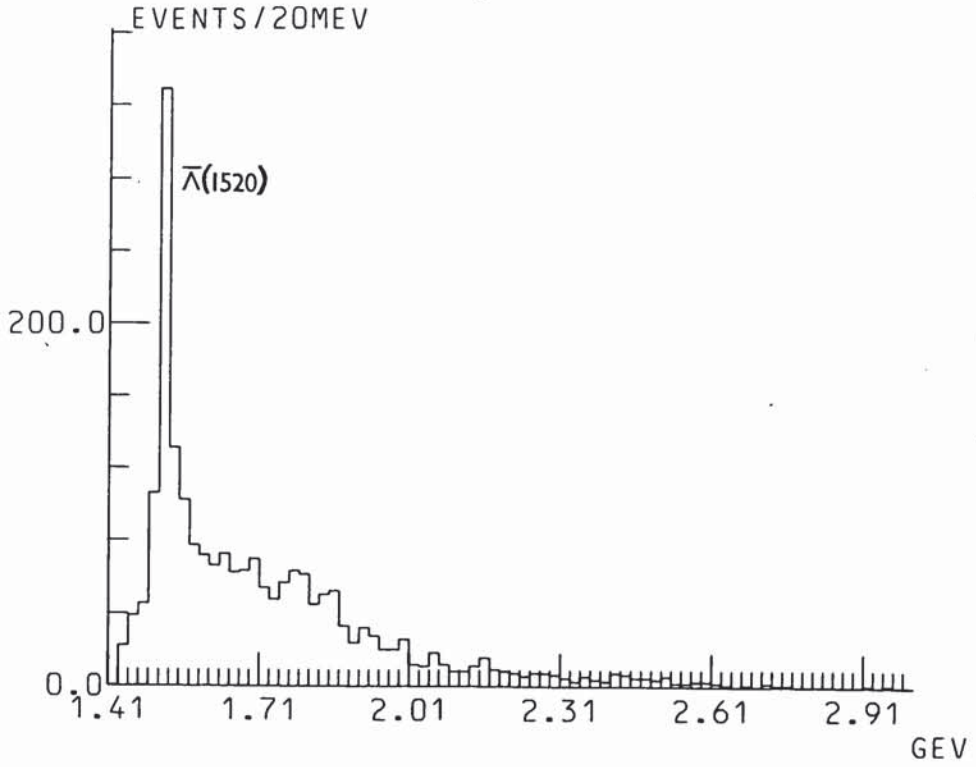

Figure 5.5: Mass $\bar{p}K^+$

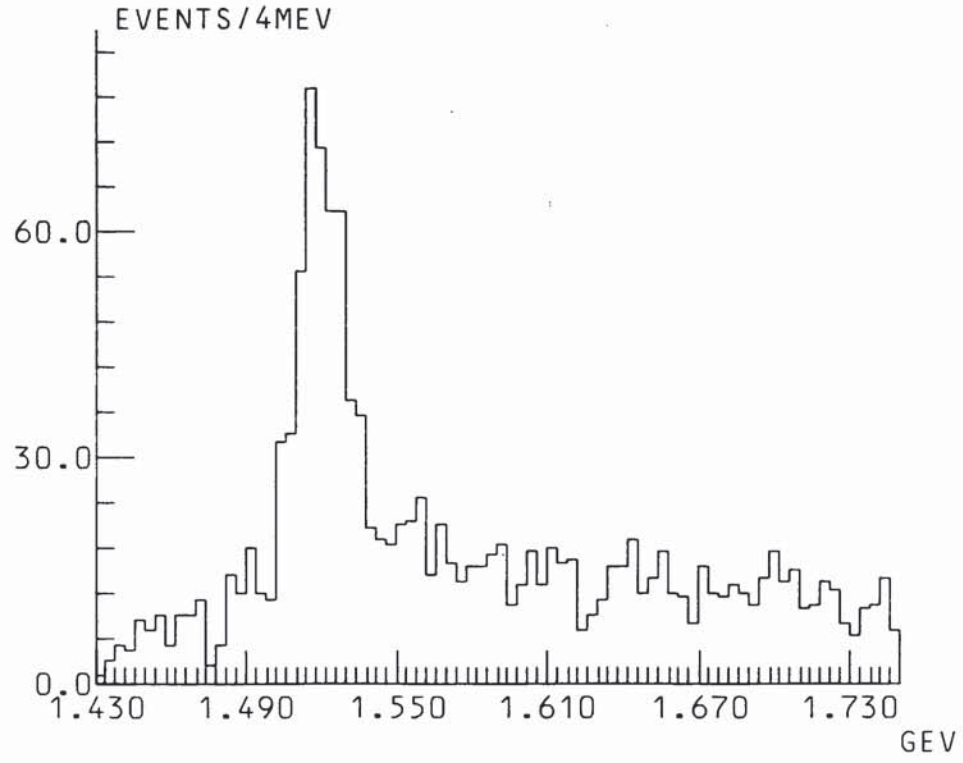

Figure 5.6: Mass $\bar{p}K^+$ in $\bar{\Lambda}$(1520) region

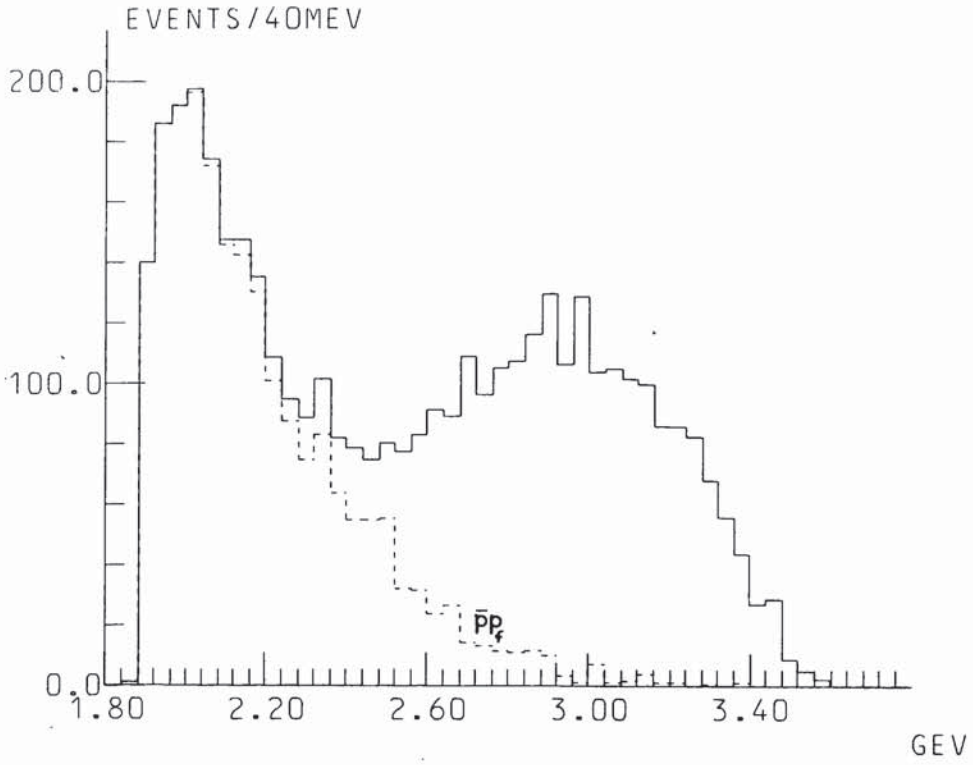

Figure 5.7: Mass $\bar{p}p$ and mass $\bar{p}p_f$

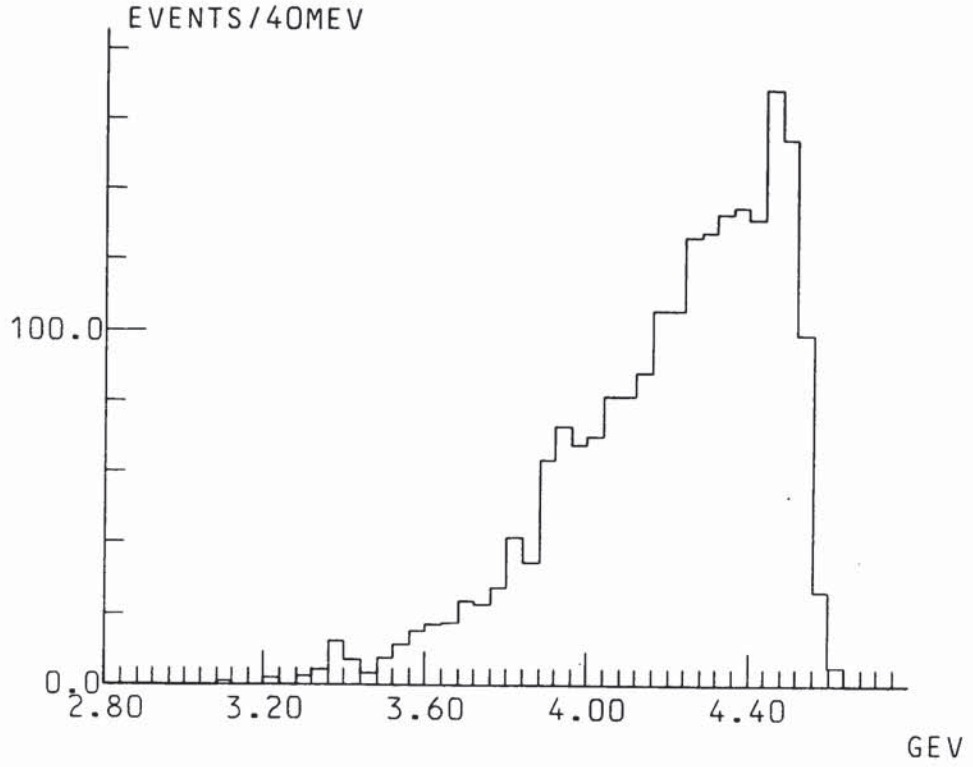

Figure 5.8: Mass $\bar{p}pp$

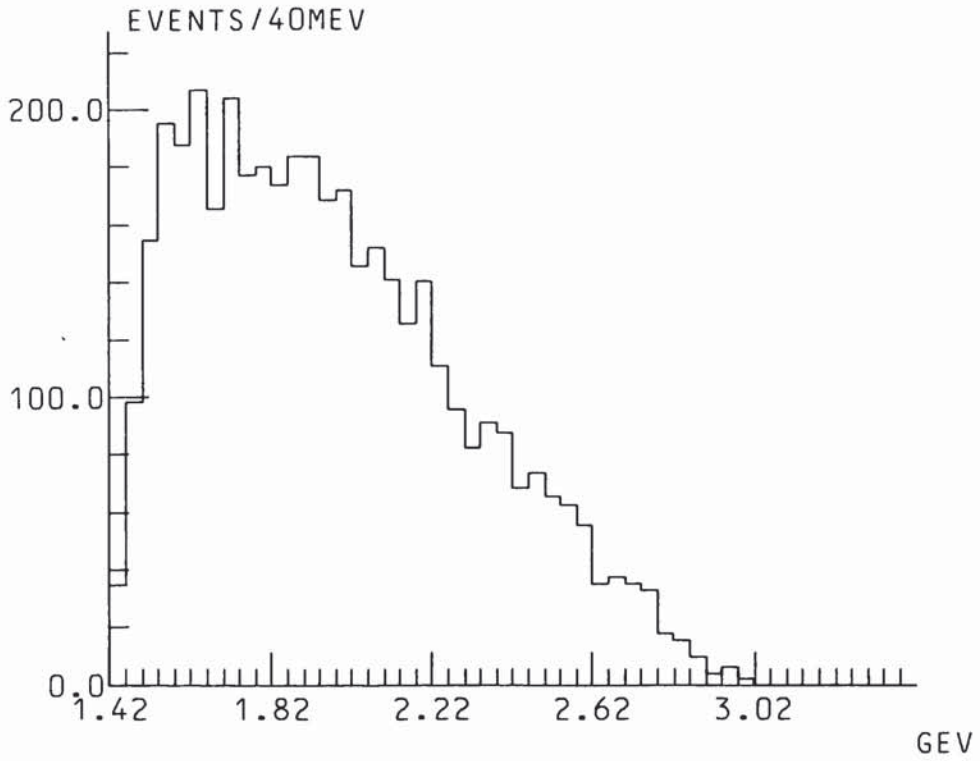

Figure 5.9: Mass pK^+

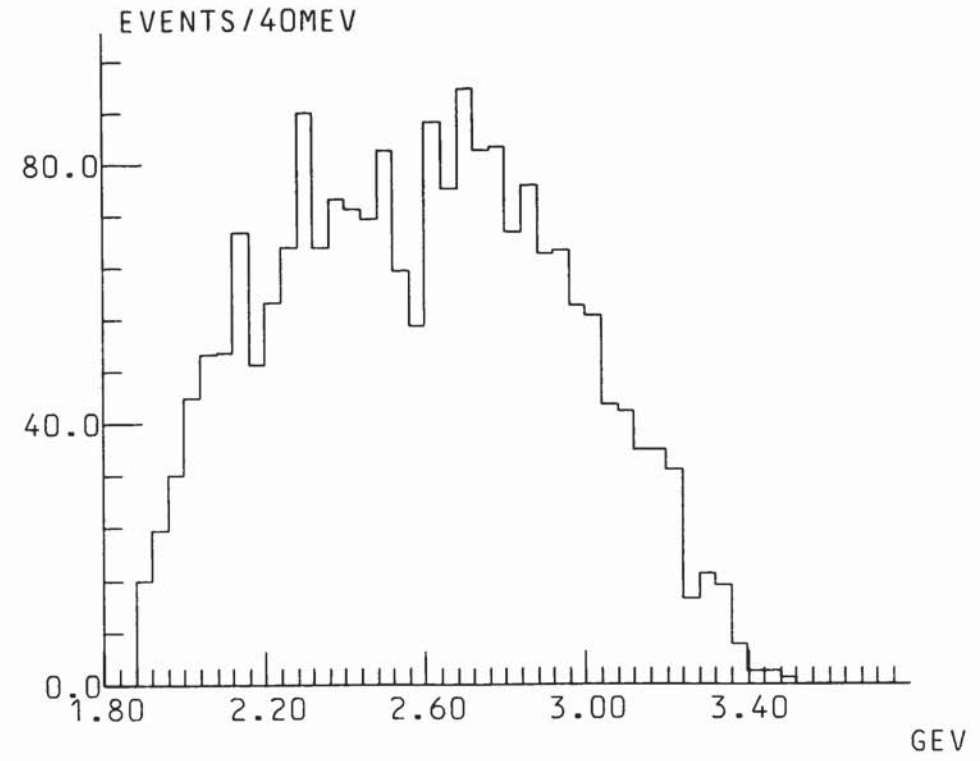

Figure 5.10: Mass pp

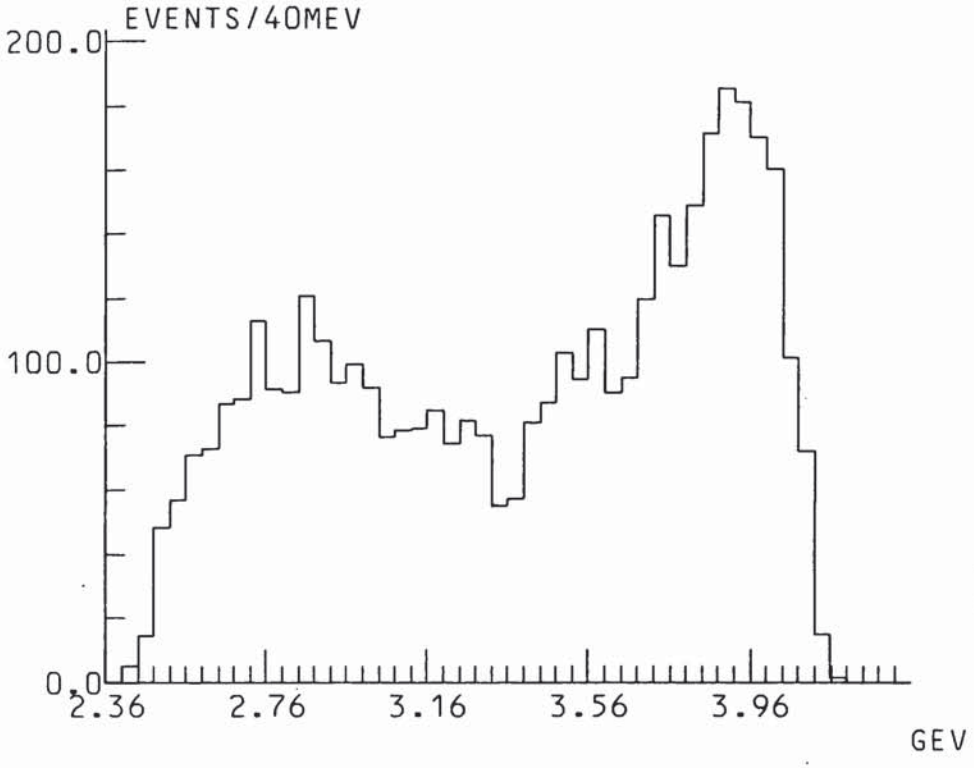

Figure 5.11: Mass $\bar{p}pK^+$

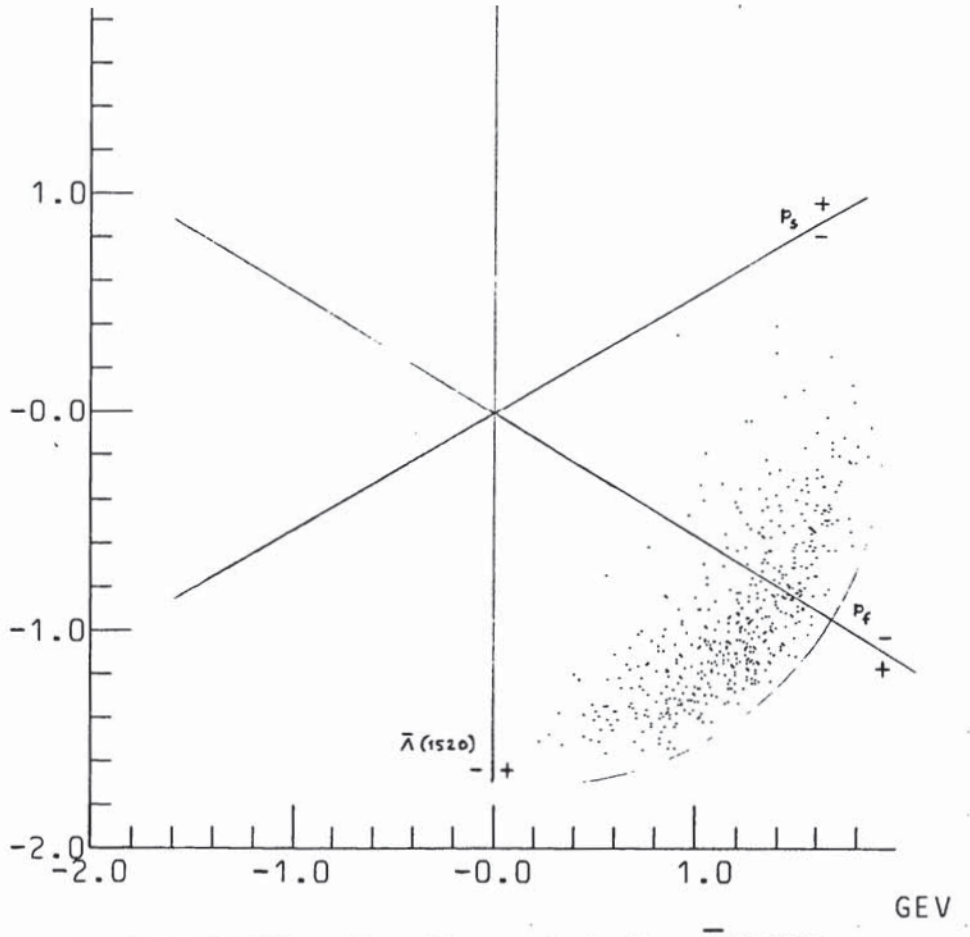

Figure 5.12: Van Hove plot for $\bar{\Lambda}(1520)\, p_f\, p_s$

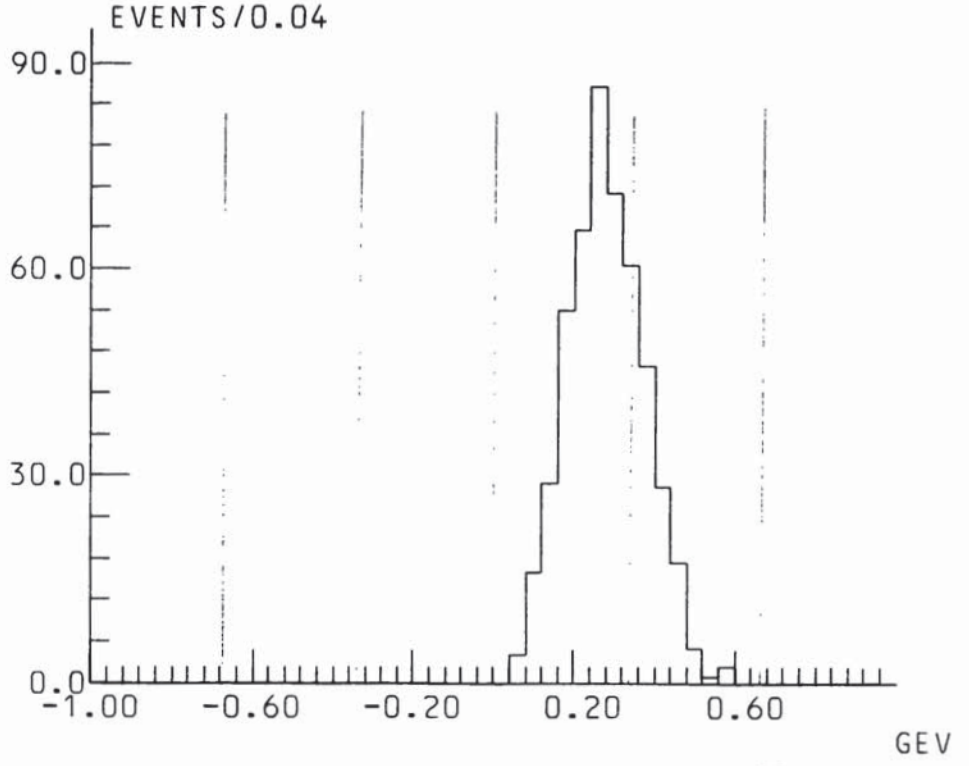

Figure 5.13: Van Hove ω angle/π for $\bar{\Lambda}(1520)\, p_f\, p_s$

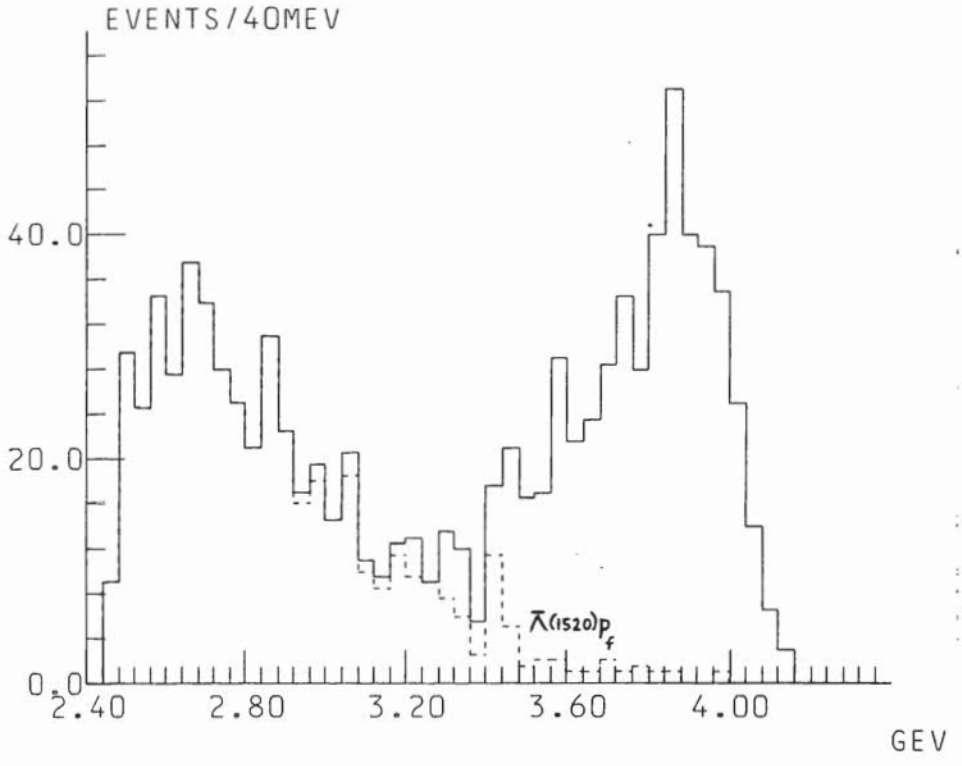

Figure 5.14: Mass $\bar{\Lambda}(1520)p$ and mass $\bar{\Lambda}(1520)p_f$

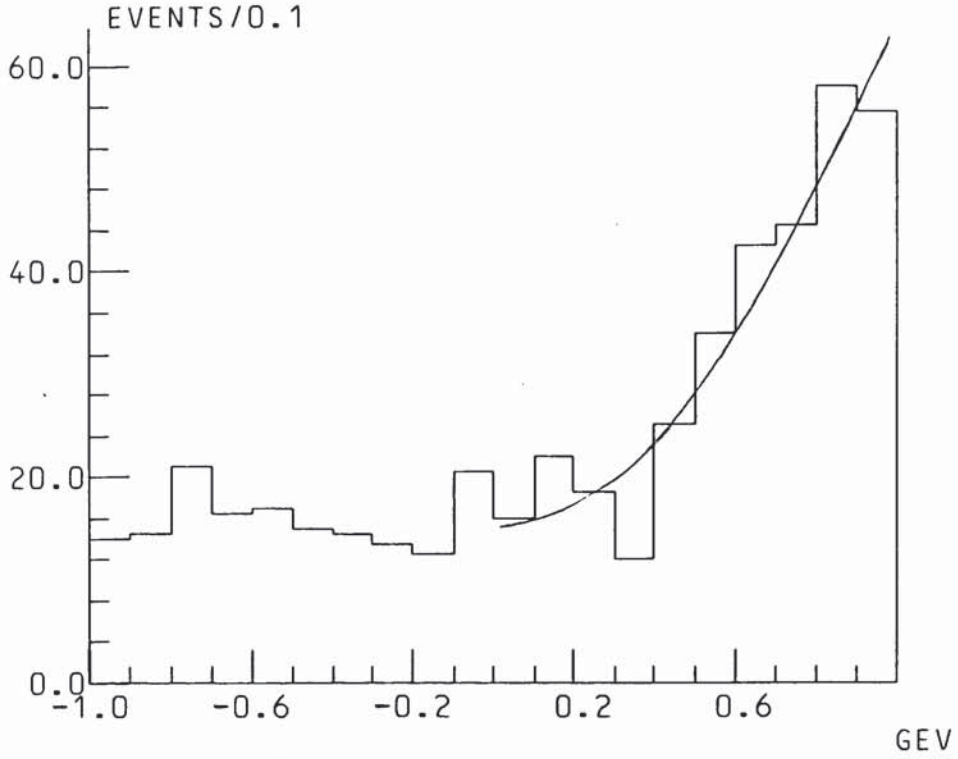

Figure 5.15: $\bar{\Lambda}(1520)$ decay TCH $\cos\theta$ + 2-D fit projection

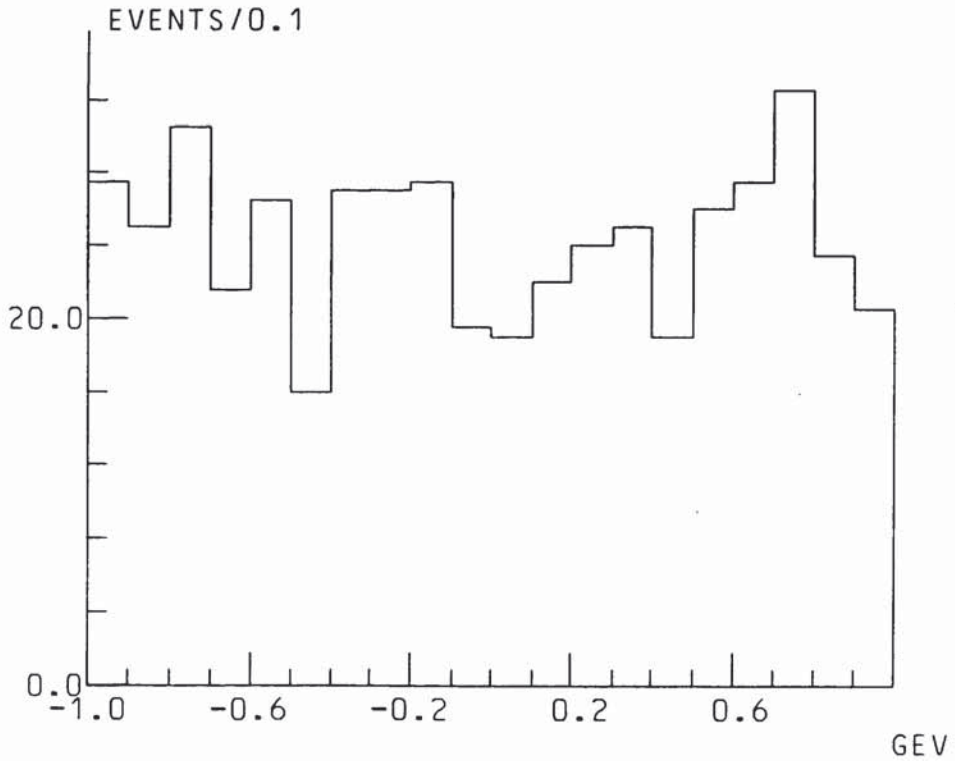

Figure 5.16: $\bar{\Lambda}(1520)$ decay TCH ϕ/π

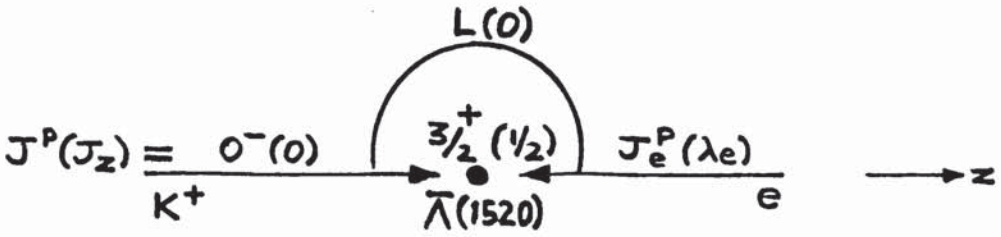

Figure 5.17: $\bar{\Lambda}(1520)$ production vertex

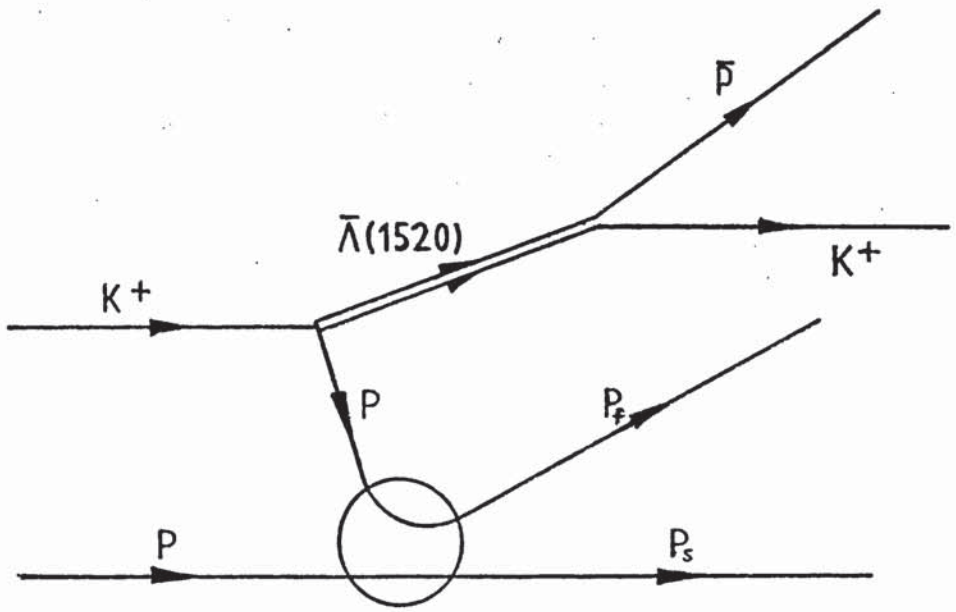

Figure 5.18: Deck type diagram for $\bar{\Lambda}(1520)\, p_f\, p_s$

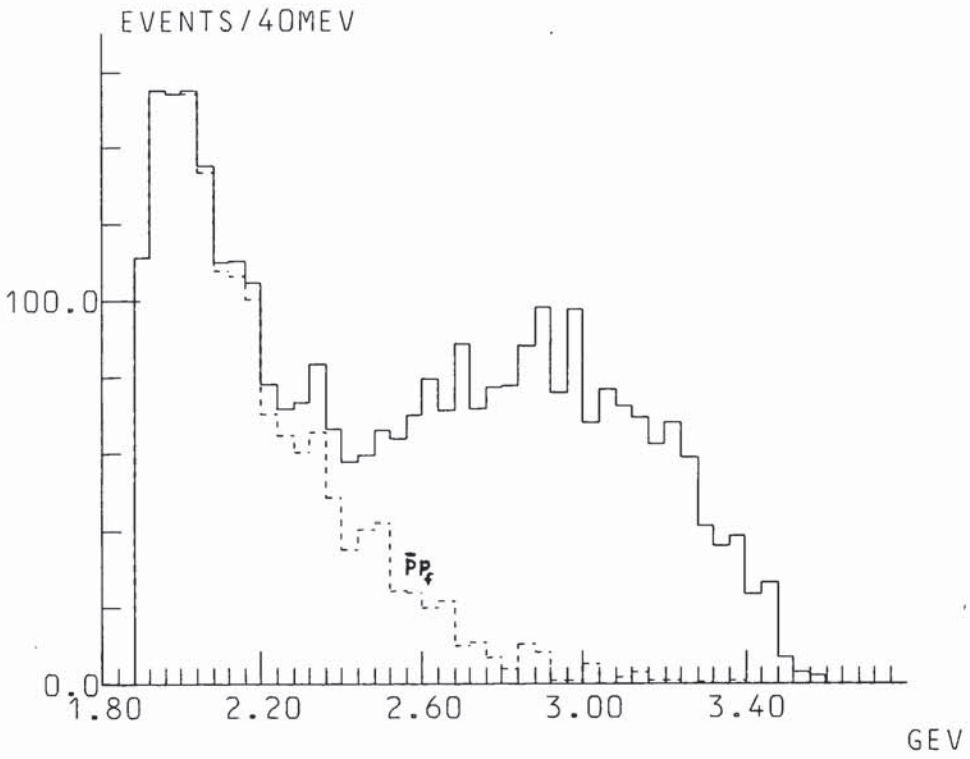

Figure 5.19: Mass $\bar{p}p$ and mass $\bar{p}p_f$ (no $\bar{\Lambda}(1520)$)

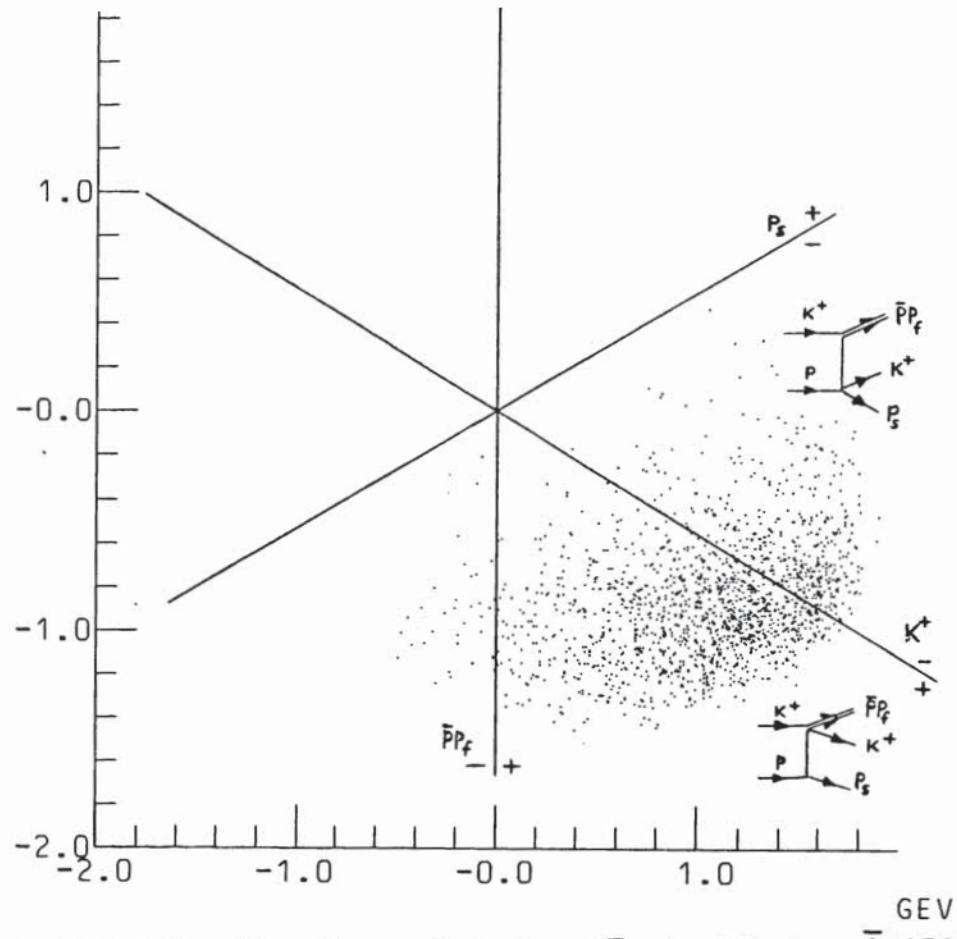

Figure 5.20: Van Hove plot for $(\bar{p}p_f)\,p_s\,K^+$ (no $\bar{\Lambda}(1520)$)

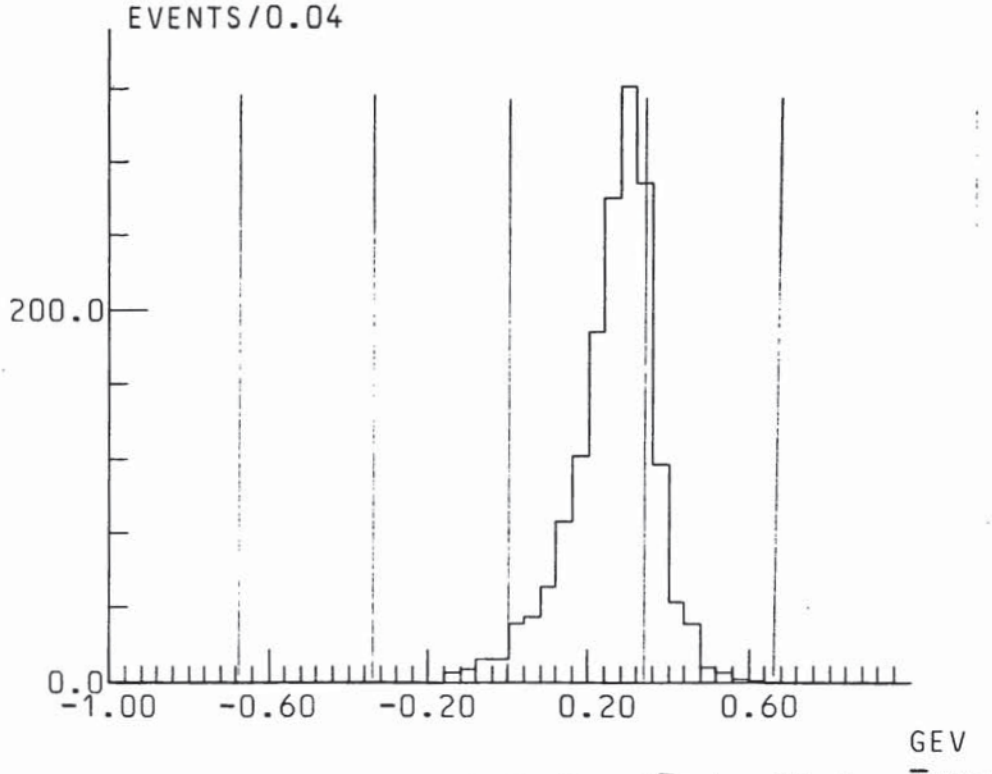

Figure 5.21: Van Hove ω angle/π for $(\bar{p}p_f)\,p_s\,K^+$ (no $\bar{\Lambda}(1520)$)

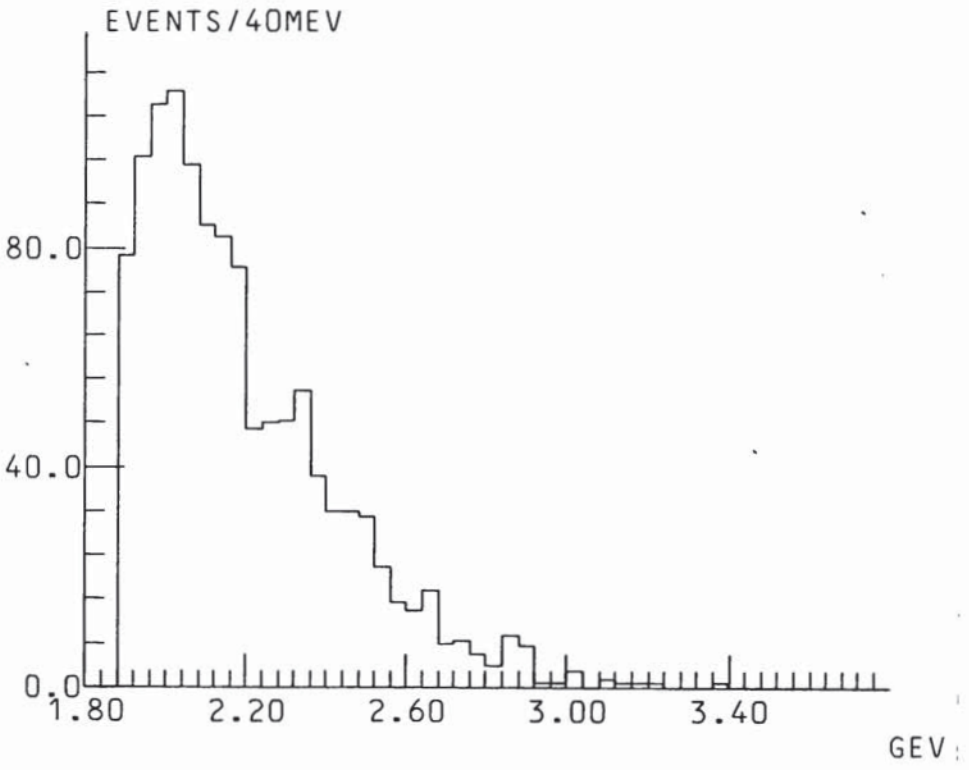

Figure 5.22: Mass $\bar{p}p_f$ (no $\bar{\Lambda}(1520)$, K^+ forward)

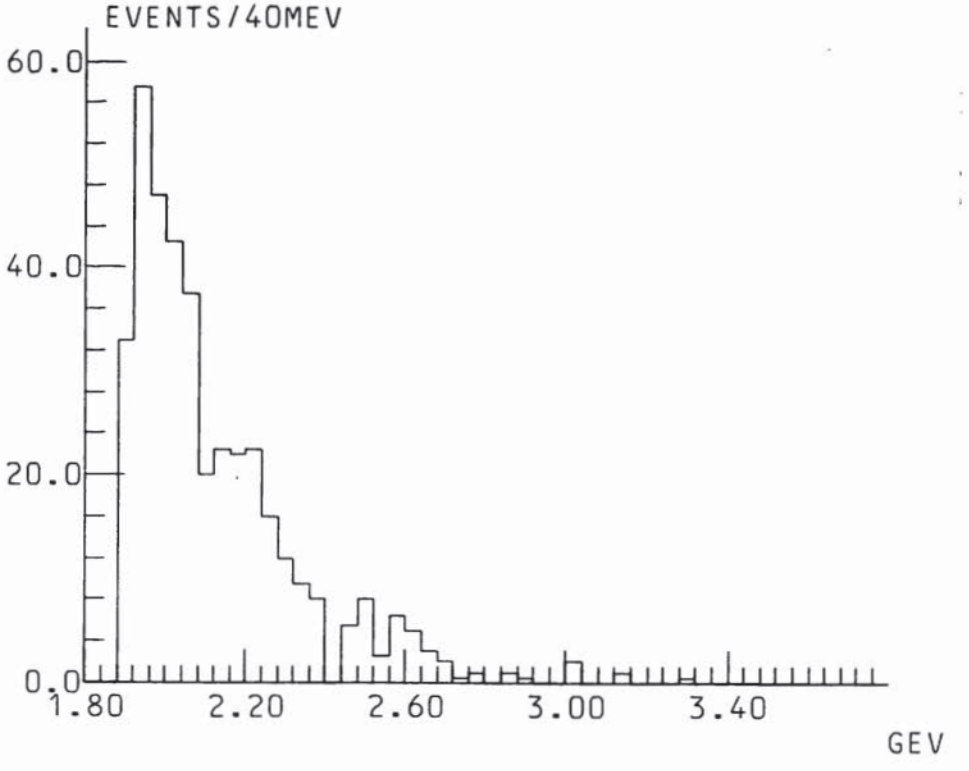

Figure 5.23: Mass $\bar{p}p_f$ (no $\bar{\Lambda}(1520)$, K^+ backward)

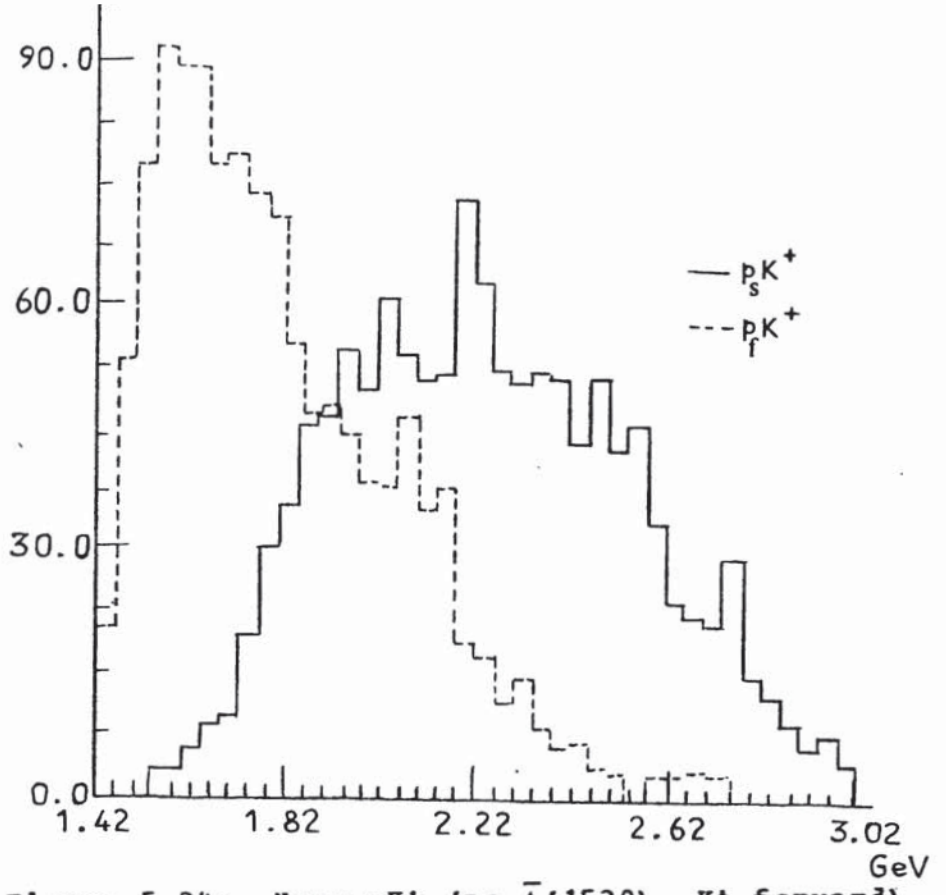

Figure 5.24: Mass pK+ (no $\bar{\Lambda}(1520)$, K+ forward)

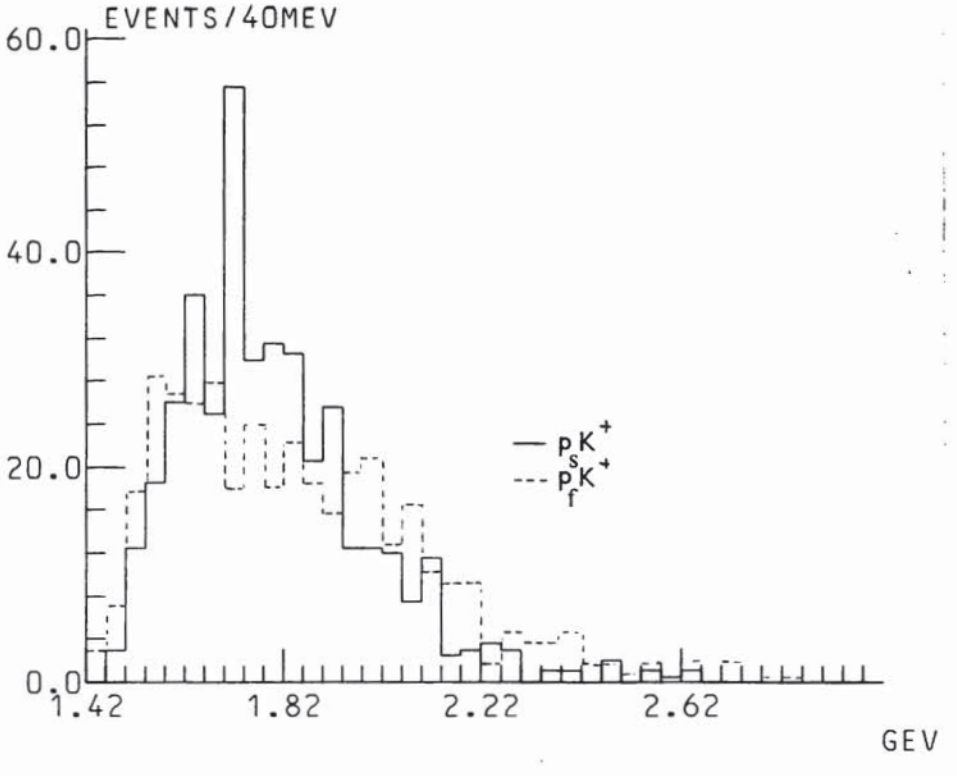

Figure 5.25: Mass pK+ (no $\bar{\Lambda}(1520)$, K+ backward)

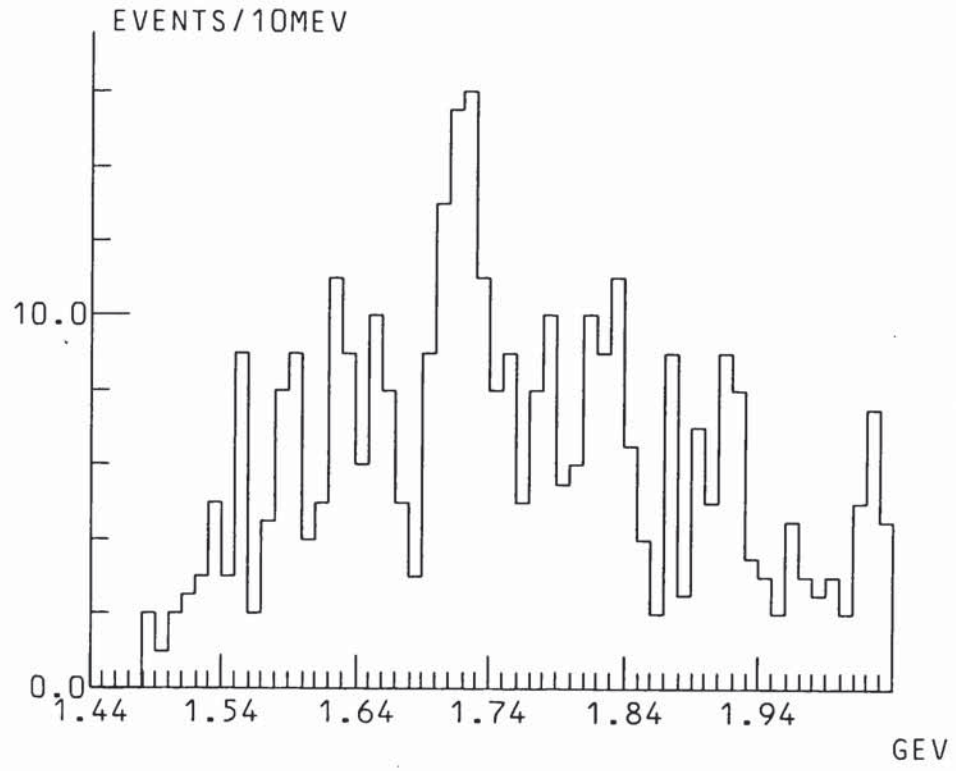

Figure 5.26: Mass $p_s K^+$ in peak region

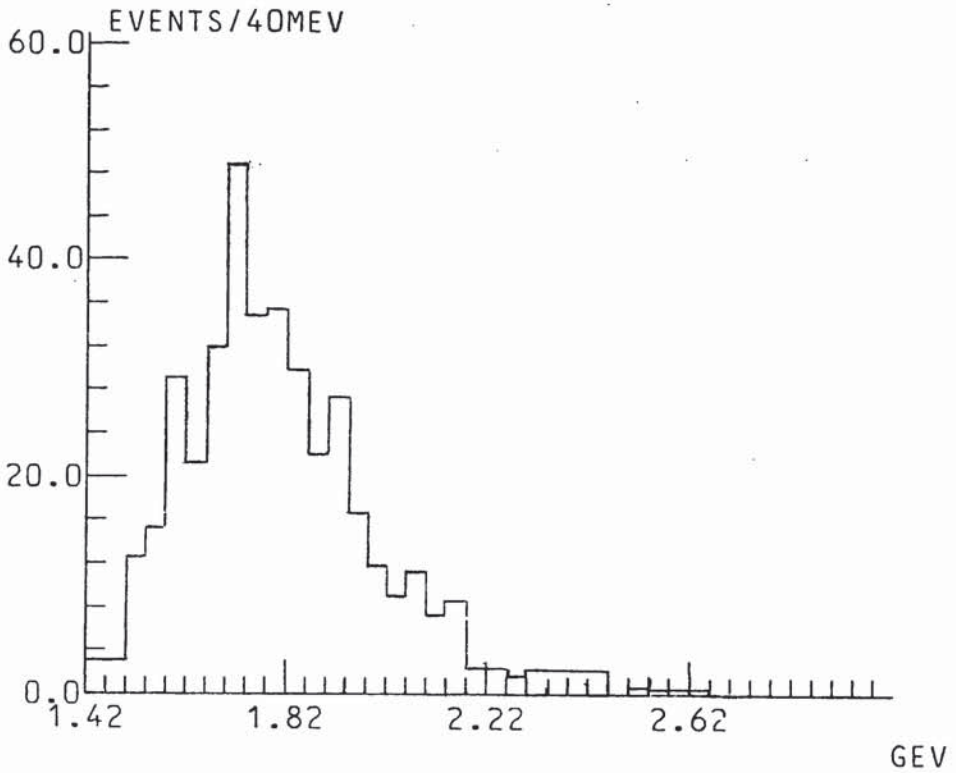

Figure 5.27: Missing mass to $\bar{p}p_f$ (no $\bar{\Lambda}(1520)$, K^+ backward)

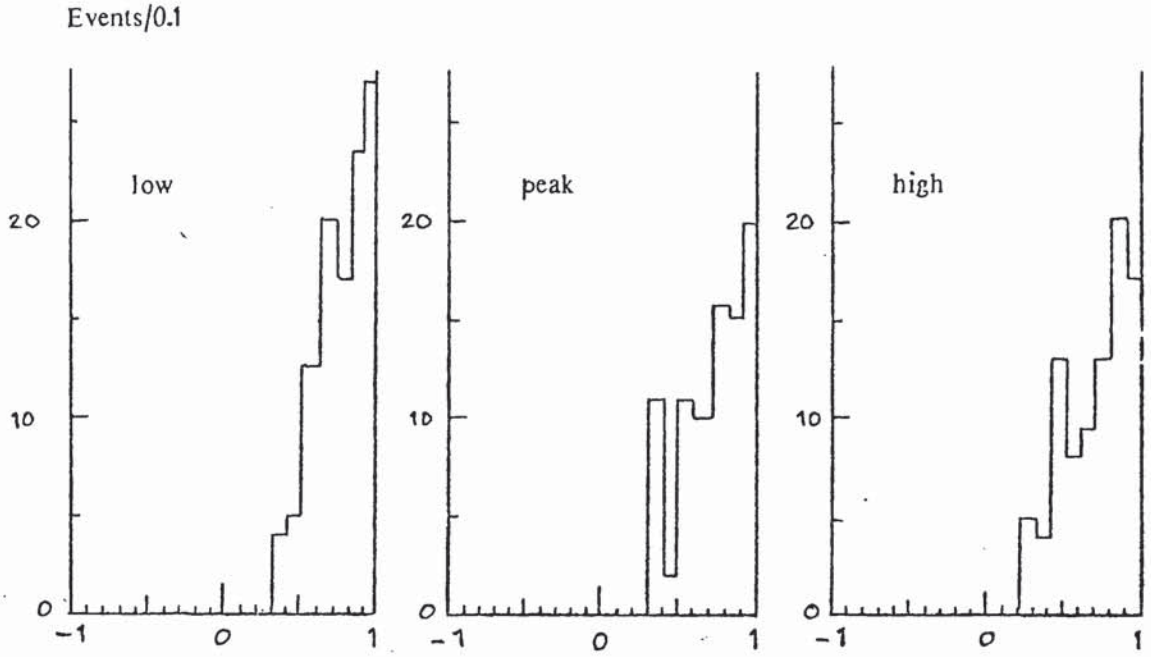

Figure 5.28: $p_s K^+$ TCH $\cos\theta$ in peak and guard bands

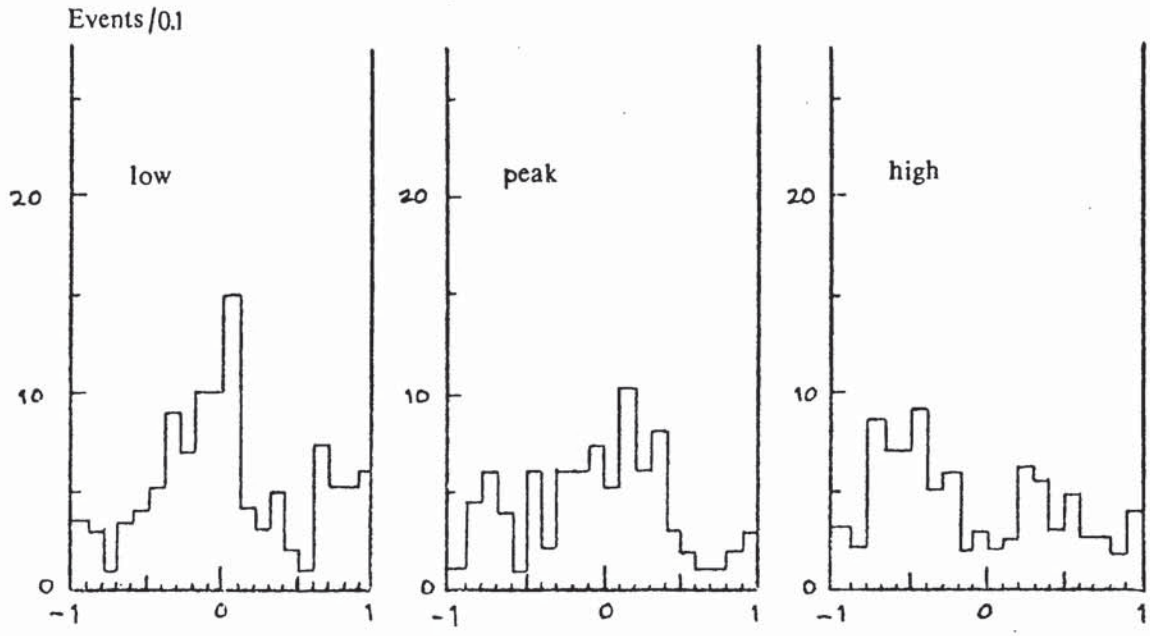

Figure 5.29: $p_s K^+$ TCH ϕ/π in peak and guard bands

Chapter VI

A STUDY OF THE REACTION $K^+p \rightarrow K^-K^+K^+p$

6.1 INTRODUCTION

The reaction

$$K^+p \rightarrow K^-K^+K^+p \qquad (6.1)$$

permits a study of the behaviour of strange quarks via the K^-K^+ and $K^-K^+K^+$ systems. The $\phi(1020)$ and $f'(1515)$ resonances, which decay predominantly to $K\bar{K}$ [2], are the octet-like isosinglets of the $J^{PC}=1^{--}$ and $J^{PC}=2^{++}$ nonets respectively in the SU(3) representation [8]. The $\phi(1020)$ is well-established [6,33,28,16] in the above reaction, and is of particular interest because of its existence as an almost pure $s\bar{s}$ state [2], with quark configuration $^{2S+1}L_J = {}^3S_1$. Data on the $^3P_2$ state $f'(1515)$ with incident K^+ are rather limited [6], and some uncertainty remains about the resonance parameters. Recent literature [9,10,3] has speculated that an enhancement of mass 1.85 GeV and width ~ 100 MeV seen in $K\bar{K}$ from the reaction $K^-p \rightarrow K\bar{K}(\Lambda/\Sigma^0)$ is the ϕ-like member of the $J^{PC}=3^{--}$ nonet (L=2), with the other members being the $K^*(1780)$, $g(1690)$ and $\omega(1670)$. Radially excited $s\bar{s}$ states such as the $\phi'(1680)$ [2] have been observed decaying to $K\bar{K}$ in e^+e^- collisions and in photoproduction, but have not been seen in hadronic interactions. Various $q\bar{q}$ potential models [47,19,20] predict further $s\bar{s}$ states which should be evident in the $K\bar{K}$ spectrum.

The three-kaon system, and its association with $\phi(1020)K$ and $f'(1515)K$, has been little studied [32,33,28,46,16]. Such data as exists, and the results from recent spin-parity analyses of the $\phi(1020)K^-$ system produced in the reaction $K^-p \rightarrow \phi K^-p$ at 8.25 GeV and 18.5 GeV [18,17], indicate that the three-kaon system is produced essentially in a diffractive manner with unnatural spin-parity. The ϕK

system has been reported to show resonant structure, especially in the region of the L(1770) meson(s) [2], but the system is complicated and existing results are of limited statistical significance. A detailed study of the $K^-K^+K^+$ system would complement existing knowledge of three-meson systems, which is largely based on the results from diffractively produced $\pi\pi\pi$, $K\pi\pi$ and $KK\pi$ systems [eg. 11,13,48].

The data sample in the present experiment improves existing statistics on reaction 6.1 [33] by an order of magnitude. In addition to studies of the reaction characteristics and the K^-K^+, $K^-K^+K^+$ mass spectra, the data permitted a spin-parity analysis of the $\phi(1020)K^+$ system to be undertaken. The $\phi(1020)K^+$ analysis will be discussed in the following chapter. A limited angular analysis of the high mass K^-K^+ system was also possible.

6.2 PRODUCTION CHARACTERISTICS

Notwithstanding the effects of the trigger acceptance, the data exhibit features which are consistent with diffractive production of the $K^-K^+K^+$ system. The $K^-K^+K^+$ system is produced with relatively low mass and low four-momentum transfer from the incident beam particle, as the Chew-Low plot of t(beam/$K^-K^+K^+$)/mass($K^-K^+K^+$) shows in figure 6.1. The slope parameter B of the fitted experimental t' distribution ($\propto \exp(-Bt')$), though possibly distorted by acceptance, was found to fall (approximately linearly) with increasing $K^-K^+K^+$ mass: a characteristic feature of a diffractive process according to reference 12.

The longitudinal momentum distribution of the recoil proton in the CMS is shown in figure 6.2, and displays a large, very backward peak. The two K^+ particles could not be meaningfully distinguished since no strong correlation was observed between their longitudinal momenta. For convenience only, the slower and faster K^+ in the laboratory system will be labelled as K^+_s and K^+_f respectively.

6.3 MASS SPECTRA

6.3.1 K^-K^+

The effective mass distribution for all K^-K^+ combinations (two combinations per event) is shown in figure 6.3. The spectrum is dominated by the production of the $\phi(1020)$, but the $f'(1515)$ is also evident. The individual $K^-K^+_s$ and $K^-K^+_f$ spectra also clearly show these resonances. The $\phi(1020)$ region, the intermediate mass region and the $f'(1515)$ region are shown in more detail in figures 6.4, 6.5 and 6.6 respectively. No other significant ($\geq 3\sigma$) enhancements are seen, and in particular, there is no indication of structure in the region above the $f'(1515)$. The high mass region will be discussed in more detail later.

The $\phi(1020)$ region was fitted using a P-wave Breit-Wigner function superimposed on a linear background to yield the following mass and width, uncorrected for experimental resolution:

$$m = 1.0209 \pm 0.0002 \text{ GeV}$$
$$\Gamma = 0.0089 \pm 0.0003 \text{ GeV}$$

Difficulty was experienced in fitting this region, especially over the range 1.027 - 1.037 GeV. The fit (probability $\lesssim 5\%$) was not significantly improved by using higher background polynomials, different angular momenta, or by convoluting the Breit-Wigner function with a normal resolution function ($\sigma \sim 2.3$ MeV). The possibility of S/P-wave interference in this region resulting from the the presence of the $S^*(975)$ resonance [2] is discussed in the next chapter. The best fitted ϕ mass is 1.3 ± 0.2 MeV higher than the accepted PDG value, and the observed width indicates a resolution Γ_r of ~ 5 MeV by subtraction of the PDG width.

The region of the $f'(1515)$ in the total K^-K^+ mass spectrum is well fitted by a D-wave Breit-Wigner plus a quadratic background. The parameters of the observed resonance are:

$$m = 1.522 \pm 0.002 \text{ GeV}$$
$$\Gamma = 0.116 \pm 0.005 \text{ GeV}$$

where the fitted mass is in good agreement with the PDG value. An average resolution of $\sim$10 MeV in the f'(1515) region was derived from the experimental mass error spectrum, indicating an upper limit of $\sim$106 $\pm$ 5 MeV for the true width of the f'(1515) in the total K^-K^+ spectrum. Although this width is greater than the PDG value of 75 $\pm$ 10 MeV, a fit to the four-prong $K^-K^+_f$ spectrum yielded a more consistent value (see later).

6.3.2 $\underline{K^-K^+K^+}$

The $K^-K^+K^+$ mass spectrum was studied for the following subsamples of data:-

1. figure 6.7: all events
2. figure 6.8: events with at least one K^-K^+ combination ($K^-K^+_s$ or $K^-K^+_f$) in the ϕ(1020) mass region defined by

   $$\phi(1020) \quad : \quad 1.00 < \text{mass}(K^-K^+) < 1.04 \text{ GeV}$$

3. figure 6.8: events with at least one K^-K^+ combination in the f'(1515) mass region defined by

   $$f'(1515) \quad : \quad 1.42 < \text{mass}(K^-K^+) < 1.60 \text{ GeV}$$

4. figure 6.9: events where no ϕ(1020) or f'(1515) was produced in either K^-K^+ combination within the selections given above.

Threshold enhancements are seen in the $K^-K^+K^+$ mass spectrum for each of the above subsamples. The shape of the $K^-K^+K^+$ spectrum for all events is consistent with that observed in previous data [32,33]. A small enhancement at high mass is associated with the contribution from events corresponding to the three-prong hypothesis $K^-(K^+)pK^+$.

The $\phi(1020)K^+$ and $f'(1515)K^+$ spectra appear as similarly shaped threshold enhancements of width $\sim$450 MeV, peaking at $\sim$1.7 GeV and $\sim$2.2 GeV respectively.

The $K^-K^+K^+$ spectrum excluding events where a $\phi(1020)$ or $f'(1515)$ is produced shows an enhancement of width ~300 MeV, centred at ~1.8 GeV, and apparently sitting on some background distribution. The peak seen, although obviously enhanced by the removal of $\phi(1020)K^+$ and $f'(1515)K^+$ events, corresponds to the enhancement which is evident at low mass in the total $K^-K^+K^+$ spectrum. As has been already noted [33,28], this enhancement has a mass and width consistent with those of the $J^P=2^-$ L(1770) meson(s) seen in diffractively produced $K\pi\pi$ systems [2]. However, since the spin-parity of existing three-kaon data has only been analysed in terms of two-body (or quasi two-body) states, the possibility of a pure three-body decay mode of the L(1770) awaits further investigation.

6.3.3 Other combinations

The effective mass spectra of all other 2 and 3-particle combinations were studied and found to show no significant enhancements. As expected, no $\Lambda(1520)$ signal was seen in the pK^- mass spectrum since the combination of a forward K^- and a backward proton is kinematically unfavourable for resonance production.

The pK^+_S spectrum was studied in various data subsamples and LPS sectors for indications of the narrow enhancement at 1.72 GeV seen in the backward pK^+ system in the reaction $K^+p \rightarrow \bar{p}pK^+p$ (see chapter V). The search for such a signal is greatly complicated by the production of resonances in the K^-K^+, and possibly the $K^-K^+K^+$, systems. The mass spectrum of the backward pK^+_S system in four-prong events where no $\phi(1020)$ or $f'(1515)$ is produced in the $K^-K^+_S$ combination (within the selections described previously) is shown in figure 6.10. No narrow enhancement is seen. This spectrum was also studied as a function of $K^-K^+_f$ mass, and although some peaking was observed at high $K^-K^+_f$ mass (see figure 6.10 for $1.48 < \text{mass}(K^-K^+_f) < 1.58$ GeV), the existence of a narrow pK^+ state at 1.72 GeV cannot be confirmed in the reaction $K^+p \rightarrow K^-K^+K^+p$.

6.4 ESTIMATE OF CROSS-SECTION

Without a full understanding of the physical processes governing reaction 6.1, an overall acceptance for the channel could not be calculated by the simulation of events. However, the author had access to bubble chamber data on reaction 6.1 taken at an incident beam momentum of 10.12 GeV (the data of [6]). This data should have relatively few acceptance biases. For the 462 bubble chamber events, the longitudinal momenta of tracks in the CMS were boosted according to the higher beam momentum of the present experiment. The events were then passed through the WA48 trigger simulation programs (see chapter IV), with each event being rotated 10 times in regular angular steps around the beam direction.

The following cross-section was calculated using the acceptance obtained by the above method, and taking the estimated number of WA48 events in the relevant (missing mass)^2 and δ-function peaks above background:

$$\sigma(K^+p \rightarrow K^-K^+K^+p) = 33 \pm 4\ \mu b$$

The result agrees well with the published values [4] of $36 \pm 6\ \mu b$ and $35 \pm 4\ \mu b$ for 10 and 16 GeV incident momenta respectively.

6.5 THE REACTION $K^+p \rightarrow \phi(1020)K^+p$

The production characteristics of the reaction

$$K^+p \rightarrow \phi(1020)K^+p, \quad \phi(1020) \rightarrow K^-K^+$$

are illustrated by the Van Hove plot and associated ω angle shown in figure 6.11. For events with a $\phi(1020)$ produced in both K^-K^+ combinations ($\sim 5\%$ of events with at least one ϕ), the $K^-K^+_f$ combination has been taken to form the $\phi(1020)$. The peaking of the ω angle distribution clearly shows that the dominant process is the peripheral production of a forward $\phi(1020)$ and K^+, with the proton recoiling backwards. This behaviour is consistent with that observed in previous data [33,28].

The essentially diffractive-like production of the $\phi(1020)K^+$ system, together with the knowledge that the $\phi(1020)$ is narrow and has little background in K^-K^+, suggests that the $\phi(1020)K^+$ system is a good subject for a spin-parity analysis using a moments technique [49]. Such an analysis has been carried out, and will be discussed in the following chapter.

6.6 THE REACTION $K^+p \rightarrow f'(1515)K^+p$

6.6.1 Production characteristics

The Van Hove plot for the reaction

$$K^+p \rightarrow f'(1515)K^+p, \quad f'(1515) \rightarrow K^-K^+$$

is shown in figure 6.12. For events with a f'(1515) produced in both K^-K^+ combinations ($\sim$10% of events with at least one f'(1515)), the $K^-K^+_f$ combination has been taken as the f'(1515). The ω angle distribution again suggests a beam fragmentation process, and should be compared with the ω distribution for $\phi(1020)K^+p$. We recall, however, that the f'(1515) is relatively wide ($\sim$ 100 MeV), and that the K^-K^+ background is high (signal/background $\sim$0.6 from the total K^-K^+ mass spectrum).

6.6.2 Decay of f'(1515)

Using the simulation program described in Chapter IV, an attempt was made to confirm the spin 2 assignment [2] for the f'(1515), and to estimate the values of the density matrix elements for the resonance in the t-channel helicity (TCH) frame. It was assumed that the f'(1515) was produced only with helicity 0 or $\pm$1, leaving three independent density matrix elements ρ_{00}, ρ_{1-1} and $Re\rho_{10}$ to be determined (see appendix B). The mass spectrum of the $K^-K^+_f$ combination (see figure 6.6) was found to show a clear f'(1515) peak with a lower signal/background ratio than that for the total K^-K^+ spectrum. Consequently, the 2-dimensional ($\cos\Theta$,ϕ) TCH decay angular distribution for $K^-K^+_f$ was used for fitting, with the fit being restricted to forward $\cos\Theta$ only because

of regions of zero acceptance at backward $\cos\Theta$ angles. A grid of 5 $\cos\Theta$ x 10 ϕ cells were fitted by minimising the χ^2 function for the difference between the simulated and real cell contents (see equation 5.2). Events were generated according to:

$$K^+ + p \rightarrow (f'(1515)K_s^+) + p$$
$$\hookrightarrow f'(1515) + K_s^+$$
$$\hookrightarrow K^- + K_f^+$$

where isotropic decay of the $f'(1515)K_s^+$ system was assumed, and the $f'(1515)$ (ie. the $K^-K_f^+$ combination lying in the $f'(1515)$ region) was decayed with some angular distribution dependent on a given set of values of $\{\rho_{00}, \rho_{1-1}, Re\rho_{10}\}$. A $f'(1515)K_s^+$ mass was chosen according to the experimental $f'(1515)K_s^+$ mass spectrum weighted for the approximate acceptance, and its CMS production angle chosen according to the experimental $t'(beam/(f'(1515)K_s^+))$ distributions fitted as a function of mass (slope parameter $B \sim 10.4 - 2.6$ x mass).

Two methods were used to take a non-resonant $K^-K_f^+$ background into account:

1. With respect to the Breit-Wigner $f'(1515)$ peak plus polynomial background fitted to the observed $K^-K_f^+$ mass spectrum, the peak was assumed to have spin 2, and the background was assumed to consist of an incoherent mixture of spin 0 and spin 1 in a zero helicity state ($\rho_{00}=1$). The mass of a $K^-K_f^+$ combination in the $f'(1515)$ region was chosen according to the fitted $K^-K_f^+$ spectrum, and decay angles $(\cos\Theta,\phi)$ were chosen uniformly. Each event was assigned a decay weight $W(\Theta,\phi)$ consisting of spin 0, spin 1 and spin 2 contributions according to the peak/background ratio at the selected $K^-K_f^+$ mass and the spin 0/spin 1 background mixture. For various sets of values of spin 2 density matrix elements and various background mixtures, 10 x number of real events were simulated.

2. A background subtraction was performed on the observed f'(1515) $(\cos\Theta,\phi)$ distribution by using the following $K^-K^+_f$ mass regions:

Peak	:	1.43 - 1.60 GeV
Low guard band	:	1.35 - 1.40 GeV
High guard band	:	1.63 - 1.70 GeV

The combined guard bands were normalised to the background under the fitted f'(1515) Breit-Wigner shape in the peak region. Events were generated with a $K^-K^+_f$ mass chosen according to the fitted f'(1515) peak, and with a decay angular distribution $W(\Theta,\phi)$ for a specific spin (J=0,1,2,3 used) with a given set of density matrix elements.

The results obtained using both methods were rather poor, with fit probabilities being of the order of a few percent. However, the best fits were consistent, and were achieved for a spin 2 f'(1515) with density matrix elements

$$\{\rho_{00}, \rho_{1-1}, \mathrm{Re}\rho_{10}\} = \{0.7, -0.1, 0\}$$

The first method suggests that the background in the f'(1515) region is largely in a spin 1 state. A more qualitative approach to the f'(1515) spin assignment is discussed later.

6.6.3 Cross-section

An overall acceptance of 0.25 for the reaction was determined using a spin 2 f'(1515) and the above values of the density matrix elements. Following the example of Colley et al. [6], the cross-section was estimated from the number of K^-K^+ combinations seen in the fitted Breit-Wigner f'(1515) peak for all K^-K^+ pairs:

$$\sigma(K^+p \rightarrow f'(1515)K^+p,\ f'(1515) \rightarrow K^-K^+) = 6 \pm 1\ \mu b$$

This result is consistent with the only published value [6] of $4 \pm 1\ \mu b$.

6.7 FURTHER STUDY OF THE HIGH MASS K⁻K⁺ SYSTEM

6.7.1 Mass spectrum

Whilst studying the K^-K^+ mass spectrum for various data subsamples, an enhancement was seen at $\sim$1.8 GeV in the $K^-K^+_f$ combination for four-prong events (see figure 6.13). The signal was not significantly improved by selecting data in particular LPS regions. In order to gauge the significance of the enhancement, the mass spectrum was fitted with a D-wave Breit-Wigner for the f'(1515) plus a quadratic background. The result of the fit is represented by the dotted curve shown superimposed on the data in figure 6.14, and yields the following parameters for the f'(1515):

$$m = 1.516 \pm 0.003 \text{ GeV}$$
$$\Gamma = 0.082 \pm 0.009 \text{ GeV}$$

These values are consistent with the accepted PDG values [2]. After subtraction of the fitted background, the 1.8 GeV enhancement region appears as shown in the inset of figure 6.14. The enhancement may reasonably be identified with the $K\bar{K}$ structures (labelled ϕ(1850) [2]) of mass 1.85 GeV and 1.87 GeV reported[4] in the reaction $K^-p \rightarrow K\bar{K}(\Lambda/\Sigma^0)$ at 8.25 GeV and 18.5 GeV respectively [9,10]. The approximate Breit-Wigner parameters of the enhancement are:

$$m = 1.82 \pm 0.01 \text{ GeV}$$
$$\Gamma = 0.06 \pm 0.02 \text{ GeV}$$

where the width is consistent with that found in the data of [9]. A fit to the mass spectrum with two Breit-Wigner functions corresponding to the f'(1515) and the observed bump gave a higher fit probability than a fit with a single f'(1515) Breit-Wigner, but the statistical significance is limited by the low statistics and the large number of parameters for a two Breit-Wigner fit. The lower limit to the resolution function width for the $K^-K^+_f$ combination

---

[4] The data of reference 6 also showed an enhancement at $\sim$1.82 GeV, but event statistics were low and the effect was not remarked upon.

($\sim$5 MeV) was found to be $\sim$3 MeV smaller than that for the $K^-K^+_s$ combination. This may indicate why the observed enhancement is present in $K^-K^+_f$ and not in $K^-K^+_s$, but better estimates of the true resolution would clearly be desirable.

Assuming that the enhancement is the missing ϕ-like member of the $J^{PC}=3^{--}$ nonet, with other members being the K*(1780), g(1690) and ω(1670), an octet-singlet mixing angle Θ can be calculated using the Gell-Mann-Okubo mass formulae:

$$\tan^2\Theta = (m_\phi^2-m_8^2)/(m_8^2-m_\omega^2), \quad m_8^2 = (4m_{K^*}^2-m_g^2)/3$$

Taking the PDG particle masses [2], and the above mass of the $K^-K^+_f$ enhancement, a mixing angle

$$\Theta = 22^0 \pm 5^0$$

is obtained, which, when compared with the ideal mixing angle of 35.3°, indicates that the ϕ(1820) is largely octet ($s\bar{s}$).

The following cross-section for the (background subtracted) enhancement was calculated using the f'(1515) acceptance and the f'(1515) (total K^-K^+/4-prong $K^-K^+_f$) event ratio:

$$\sigma(K^+p \rightarrow \phi(1850)K^+p,\ \phi(1850) \rightarrow K^-K^+) \sim 350 \pm 50 \text{ nb}$$

6.7.2 Moments of the decay distribution

The limited statistics in the $K^-K^+_f$ high mass region prevents a detailed analysis of the decay angular distribution, but a study of the experimental moments [63] of the decay as a function of mass may indicate possible spin structure. The angular distribution for the parity-conserving decay of a system with mixed spin into two spin 0 particles is given by the following summation over spin-parity states $A=J^P$ and helicities Λ:

$$W(\theta,\phi) = \sum_{\substack{AA' \\ \Lambda\Lambda'}} \frac{\sqrt{(2J+1)(2J'+1)}}{4\pi}\ \rho^{AA'}_{\Lambda\Lambda'}\ D^{J}_{\Lambda 0}{}^{*}(\phi,\theta,0)\ D^{J'}_{\Lambda' 0}(\phi,\theta,0) \qquad (6.2)$$

where: $\rho^{AA'}_{\Lambda\Lambda'}$ are the elements of the spin density matrix [64]

$D^{J}_{\Lambda 0}$ are the elements of the rotation matrix [65]

Θ,ϕ are the decay angles

Defining the moments H(LM) as the experimental averages of the D-functions:

$$H(LM) = \sum_{\substack{\text{events} \\ k}} w_k D^L_{M0}(\phi_k,\Theta_k,0) \propto \langle D^L_{M0}(\phi,\Theta,0)\rangle$$

where w_k is the ambiguity weight for event k, the angular distribution may also be expanded as a series of D-functions:

$$W(\Theta,\phi) = \sum_{LM} \left(\frac{2L+1}{4\pi}\right) H(LM)\ D^{L}_{M0}{}^{*}(\phi,\Theta,0) \qquad (6.3)$$

with $L \leq 2J_{max}$ and $|M| \leq J$. Comparing coefficients with those in equation 6.2 then gives [50] the moments H(LM) in terms of the density matrix elements $\rho^{\lambda\lambda'}_{M'} = \mathrm{Re}\rho^{\lambda\lambda'}_{\lambda\lambda'}$. H(00) is simply the event distribution.

The (unnormalised) experimental moments H(LM) = ReH(LM) of the $K^-K^+_f$ system in the t-channel helicity frame were calculated for the total data sample, and a selection of the moments is shown in figures 6.15 and 6.16 for 50 MeV wide mass bins. Variances on the H(LM) were estimated (after [51]) by calculating:

$$V(H(LM)) = \sum_{\substack{\text{events} \\ k}} w^2_k \left(\mathrm{Re}D^L_{M0}(\phi_k,\Theta_k,0)\right)^2$$

The features evident in the moments will be discussed bearing in mind that the moments are uncorrected for acceptance and that acceptance effects can produce spurious moments, especially if the acceptance is varying rapidly with mass.

The moments with L=6 should show structure only for resonances with spin ≥3. H(62) and H(64) are structureless within error, but H(60) is seen to peak around the 1.85 GeV region, and possibly to dip just below the f'(1515). H(60) is therefore consistent with a spin 3 assignment for the ϕ(1850), and is a measure of

only $\rho_{\Lambda\Lambda}^{33}$ if no higher spin contributions are present. A striking signal for the f'(1515) is seen in H(40). This, together with the effects seen in lower moments (eg. H(20)) around the f'(1515) mass, suggests the accepted spin 2 assignment for the f'(1515). The moment H(50), being a measure of $\rho_{\Lambda\Lambda}^{23}$, can indicate interference between a spin 2 f'(1515) and a spin 3 ϕ(1850). However, the only significant effect seen is a slight peaking around the f'(1515) mass.

To conclude, the observed moments are consistent with a spin 2 f'(1515), and, within the limited statistics, suggest a spin 3 assignment for the ϕ(1850).

6.8 SUMMARY

The present experiment has studied the reaction $K^+p \rightarrow K^-K^+K^+p$ at 13 GeV with significantly improved statistics. Production of the ϕ(1020) dominates the K^-K^+ spectrum, but the f'(1515) is also evident. The $K^-K^+K^+$ system, and the associated $\phi(1020)K^+$ and $f'(1515)K^+$ systems appear to be produced diffractively. A possible spin 3 resonance in K^-K^+ at 1.82 GeV is observed, consistent with that found in data with incident K^-. Cross-sections estimated for the overall reaction and for the $K^+p \rightarrow \phi(1020)K^+p$ and $K^+p \rightarrow f'(1515)K^+p$ subreactions are found to be consistent with accepted values.

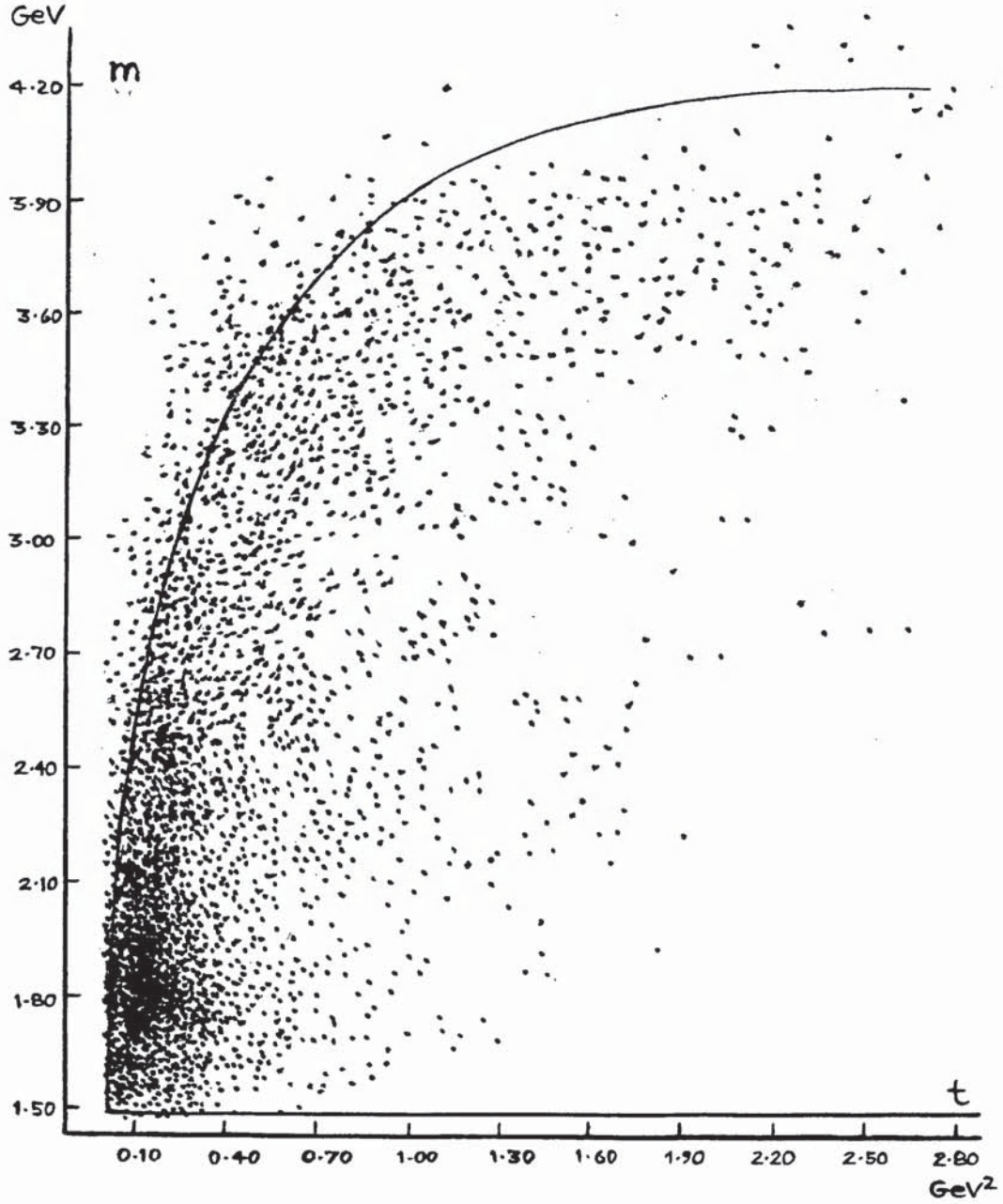

Figure 6.1: Chew-Low plot for $K^-K^+K^+$

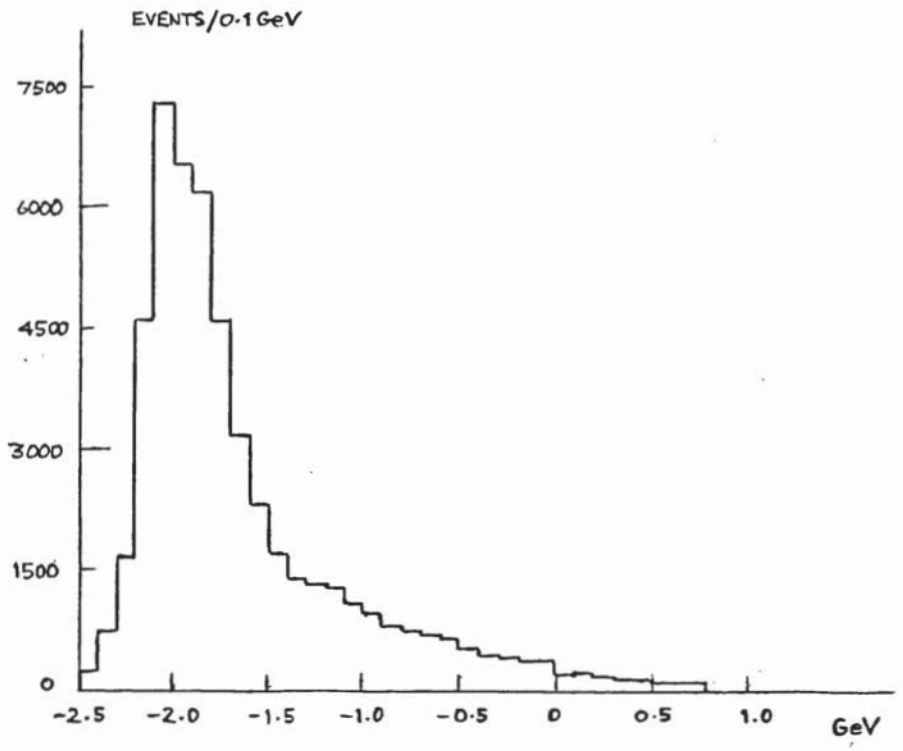

Figure 6.2: Longitudinal momentum of proton in CMS

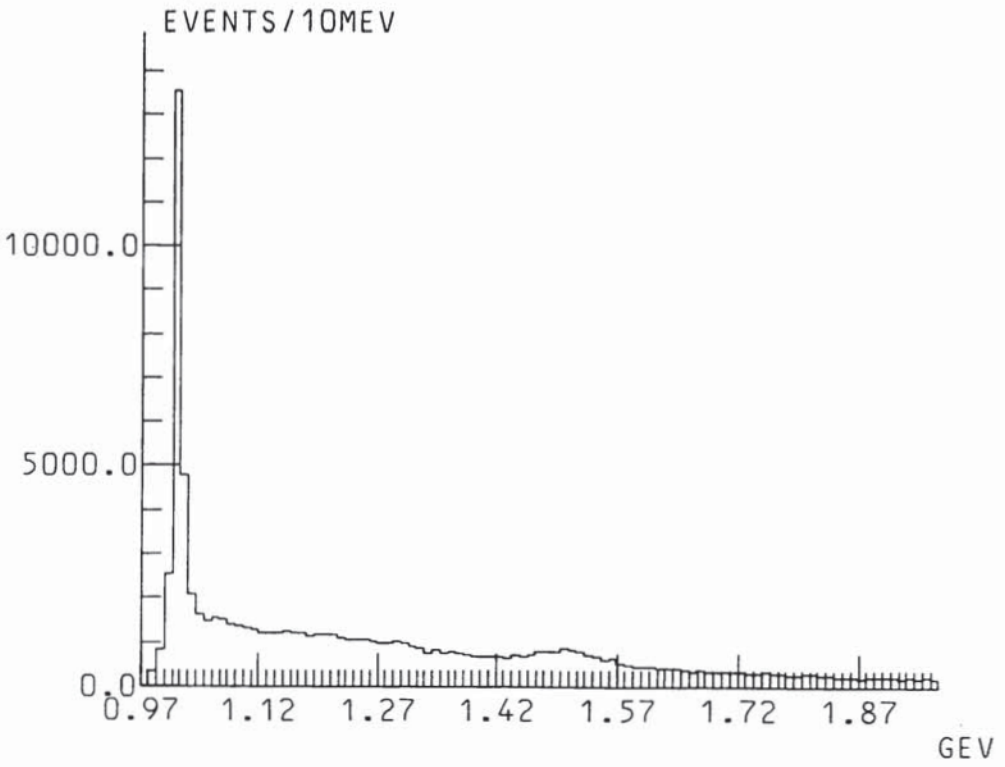

Figure 6.3: Mass K^-K^+

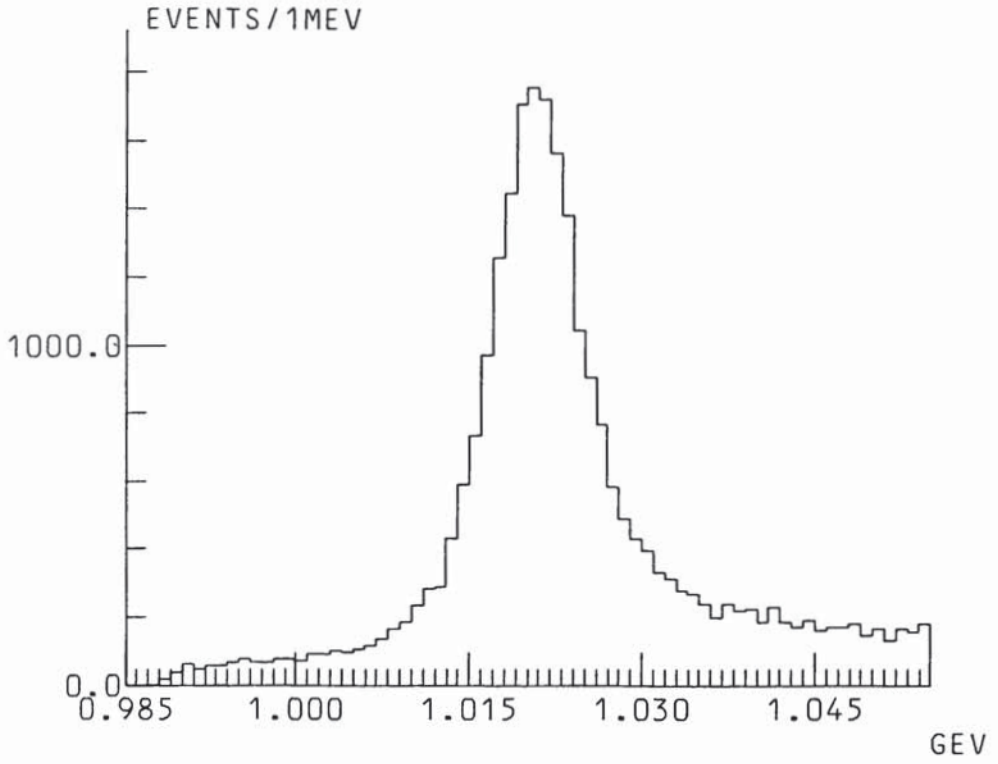

Figure 6.4: Mass K⁻K⁺ in ϕ(1020) region

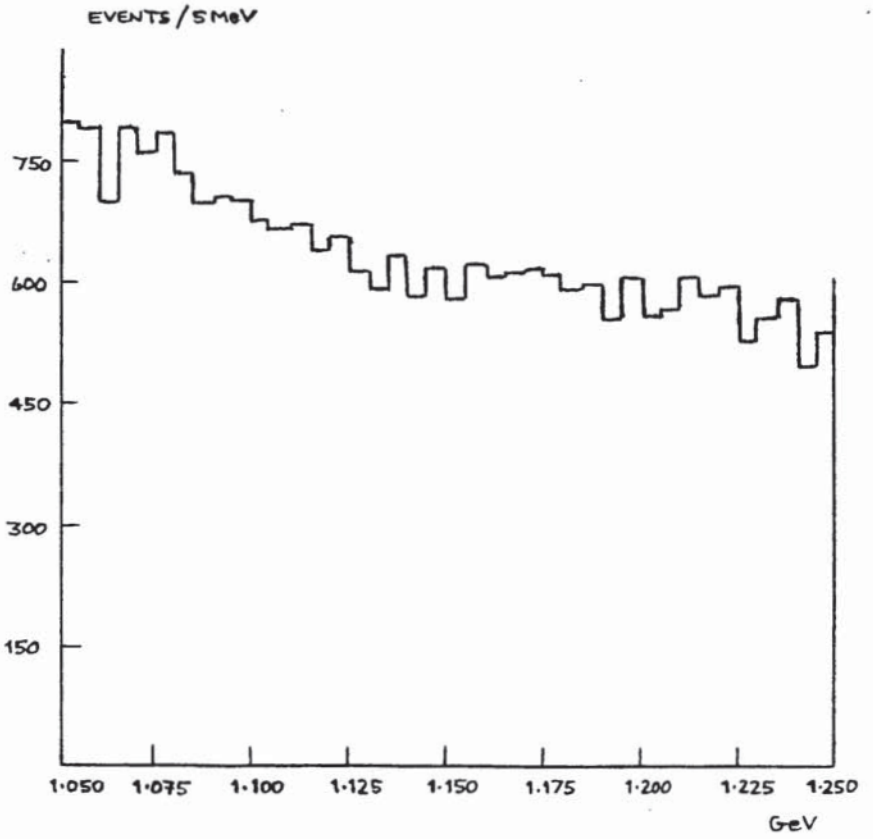

Figure 6.5: Mass K⁻K⁺ in intermediate mass region

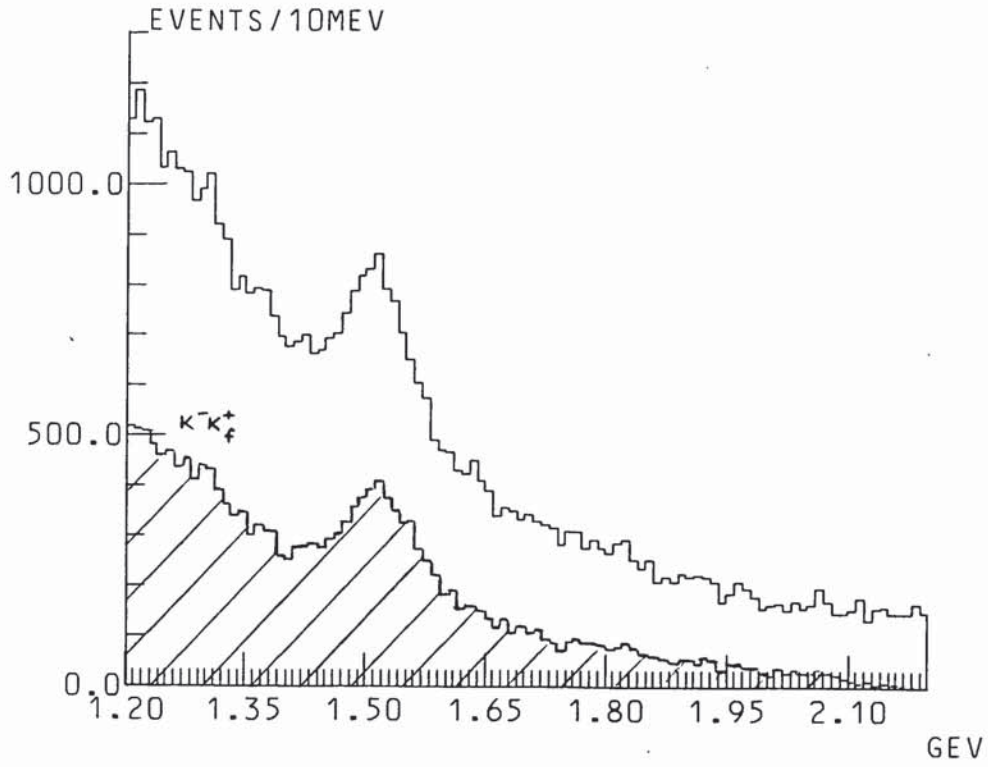

Figure 6.6: Mass K-K+ and mass $K^-K^+_f$ in f'(1515) region

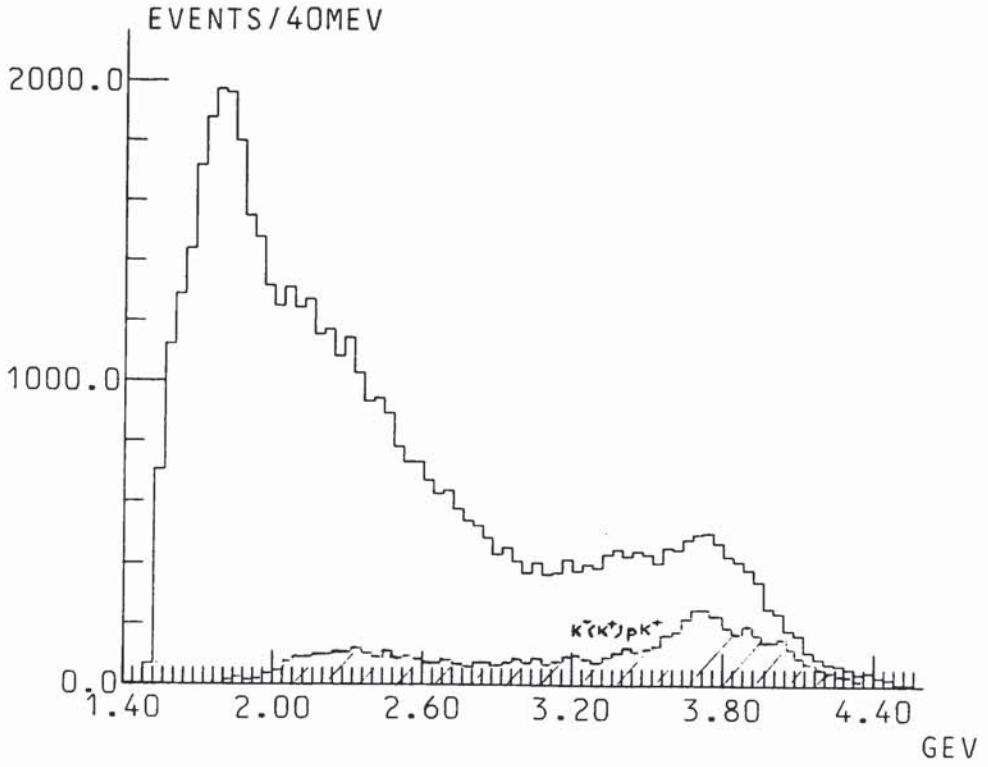

Figure 6.7: Mass K-K+K+ for all data and $K^-(K^+)pK^+$ hypothesis

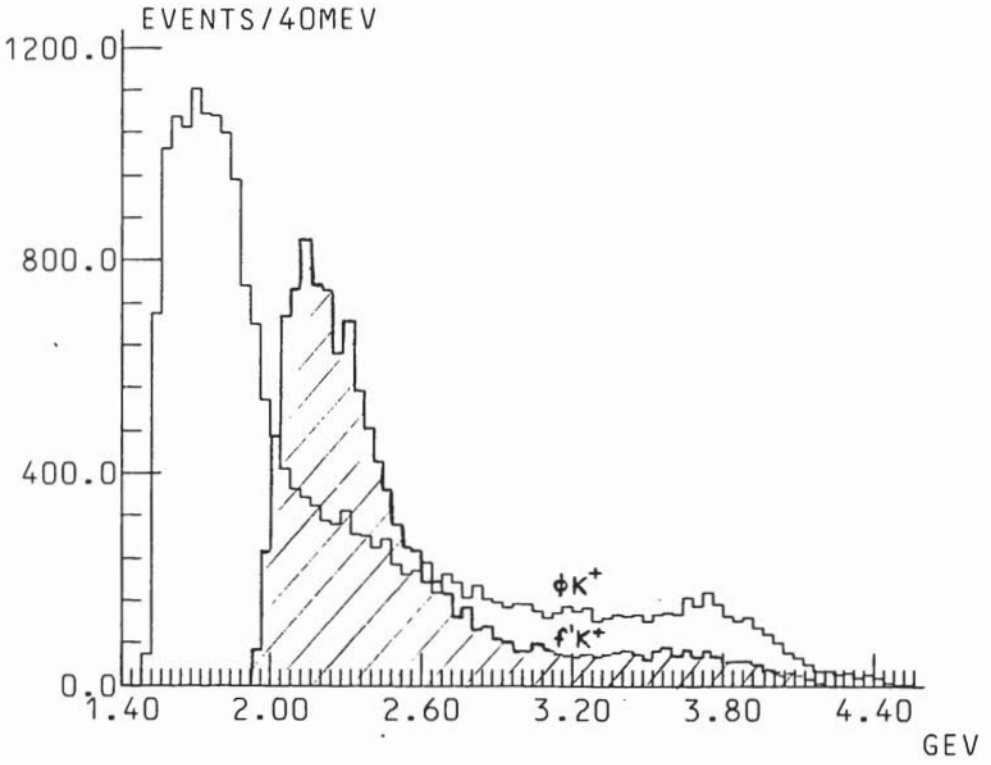

Figure 6.8: Mass $\phi(1020)K^+$ and mass $f'(1515)K^+$

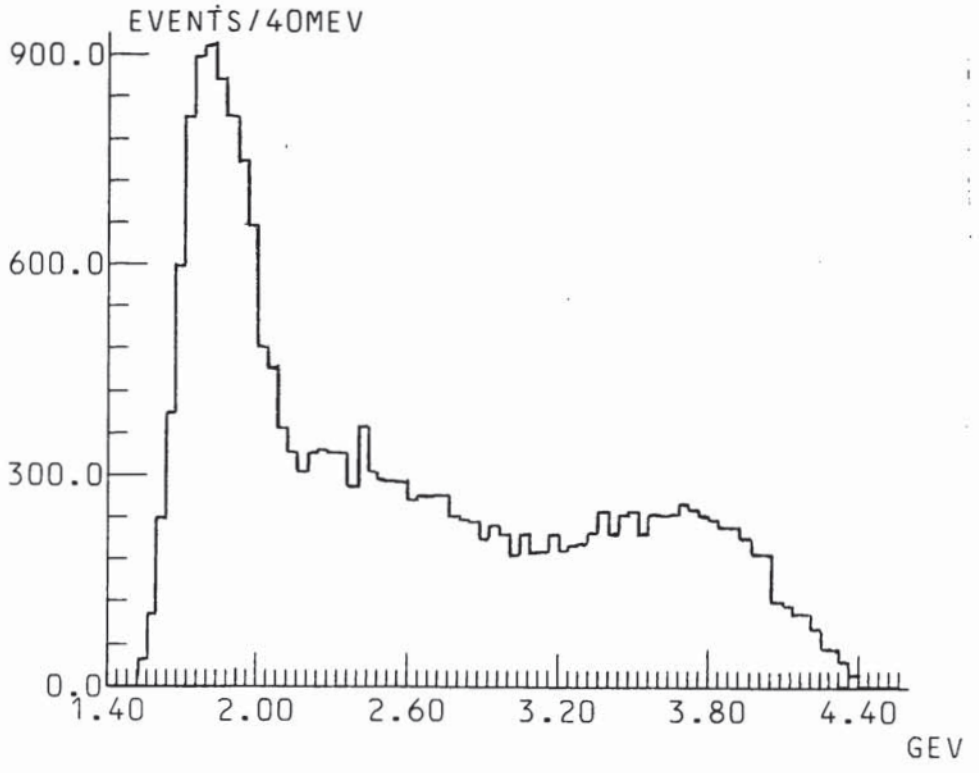

Figure 6.9: Mass $K^-K^+K^+$ excluding $\phi(1020)K^+$ and $f'(1515)K^+$

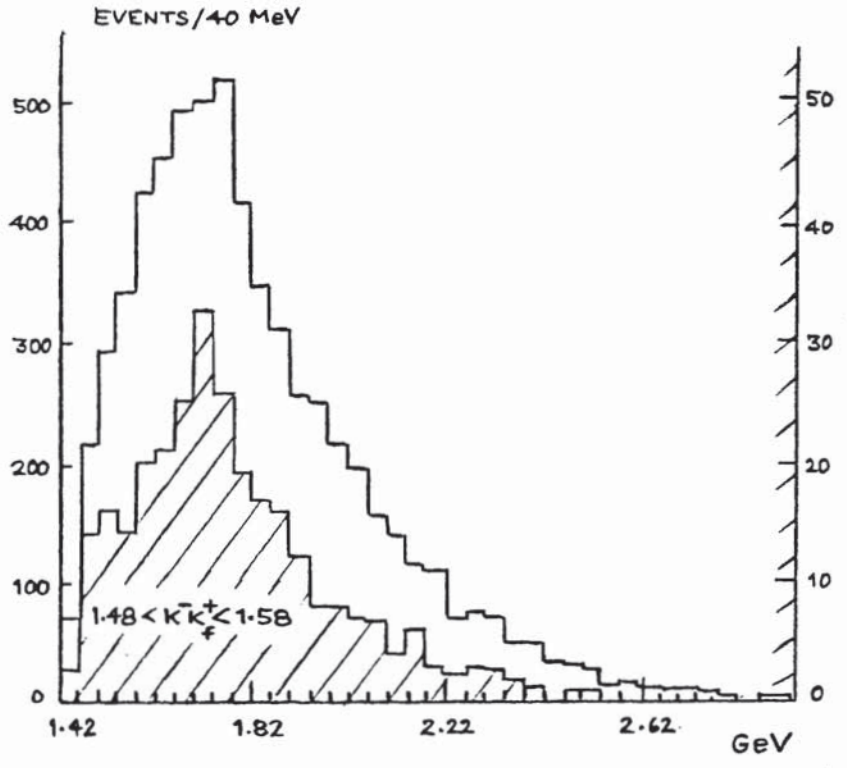

Figure 6.10: Mass pK^+_S excluding $K^-K^+_S$ in $\phi(1020)$ or $f'(1515)$

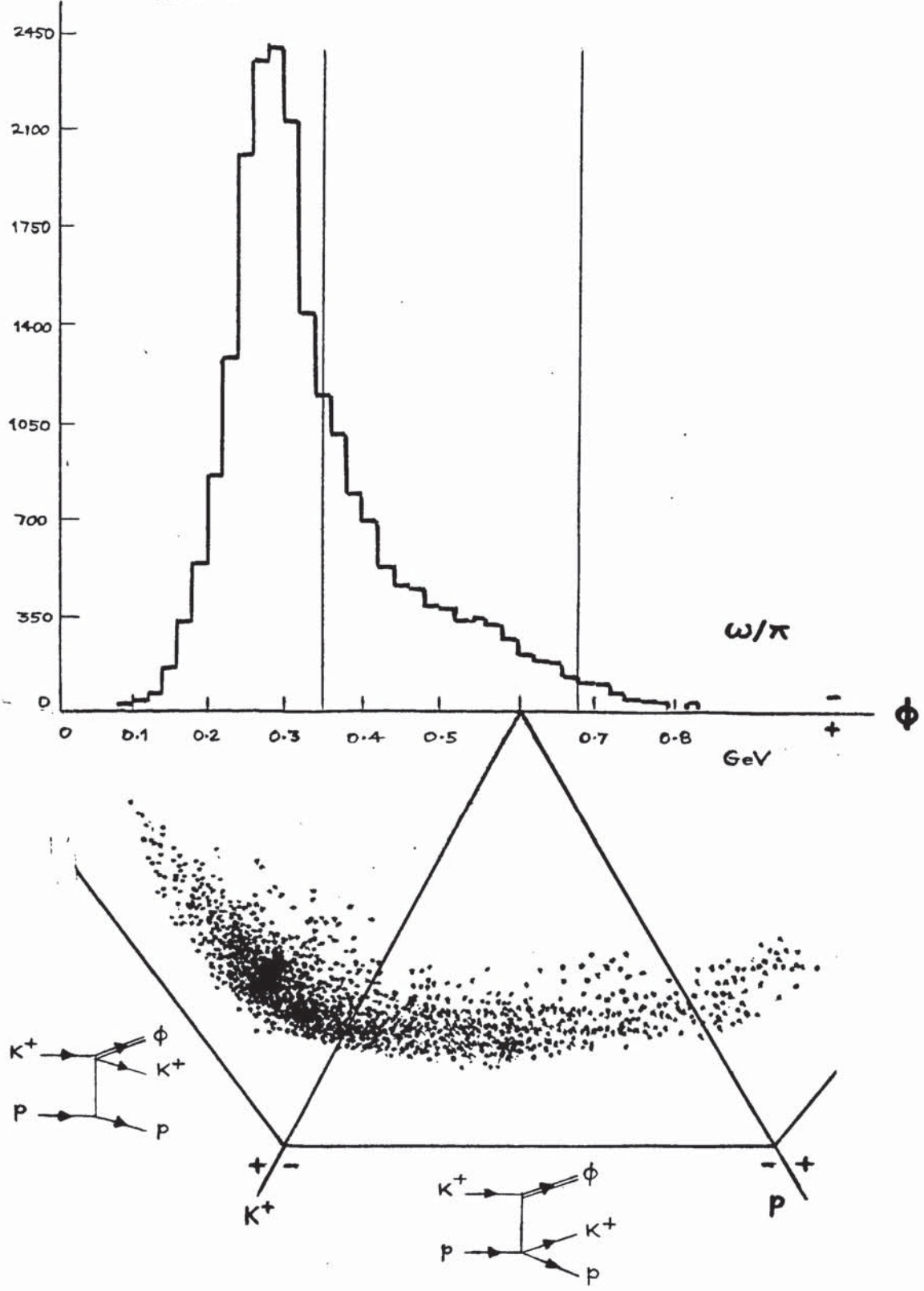

Figure 6.11: Van Hove plot for $\phi(1020)K^+p$

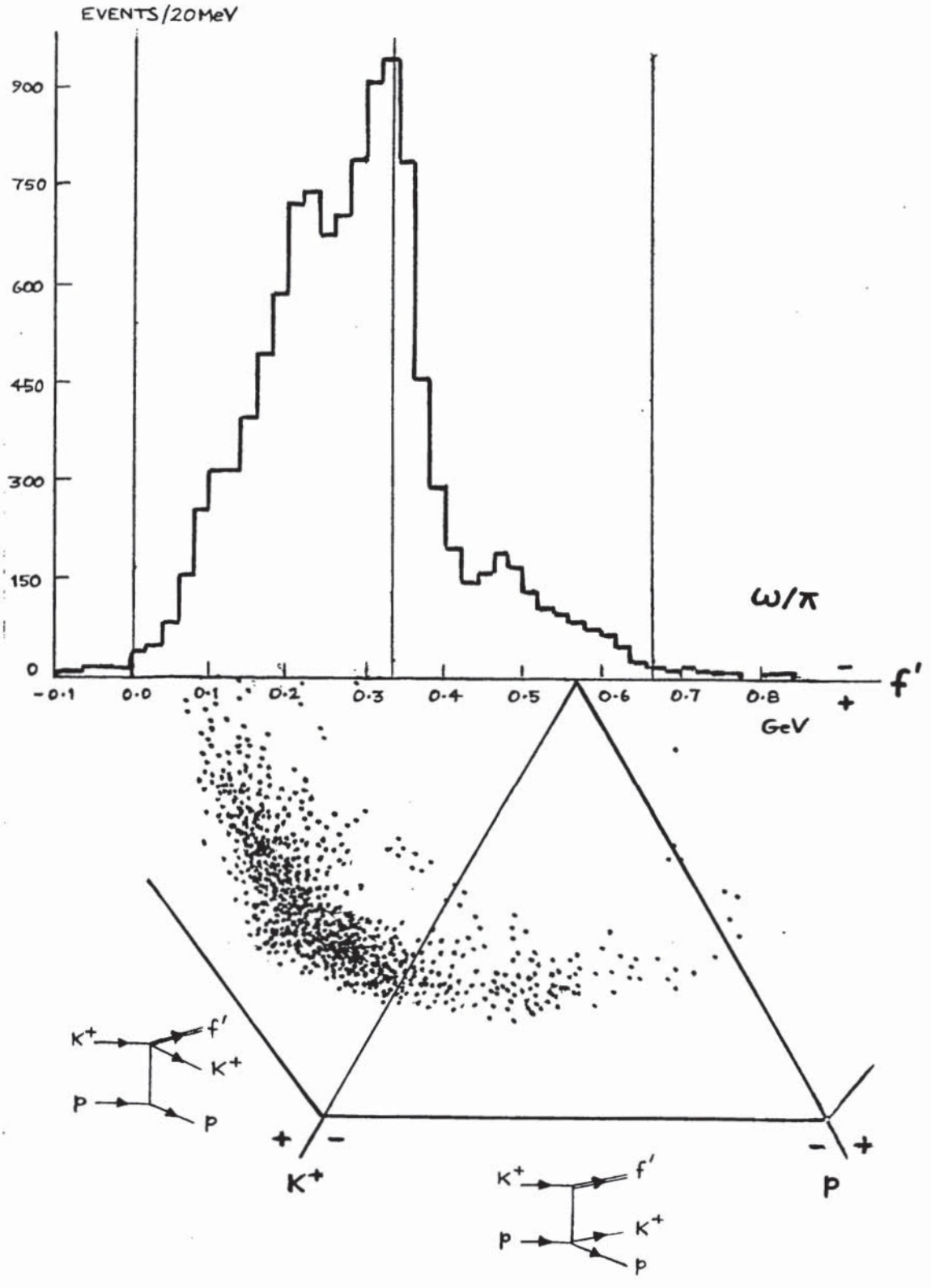

Figure 6.12: Van Hove plot for $f'(1515)K^+p$

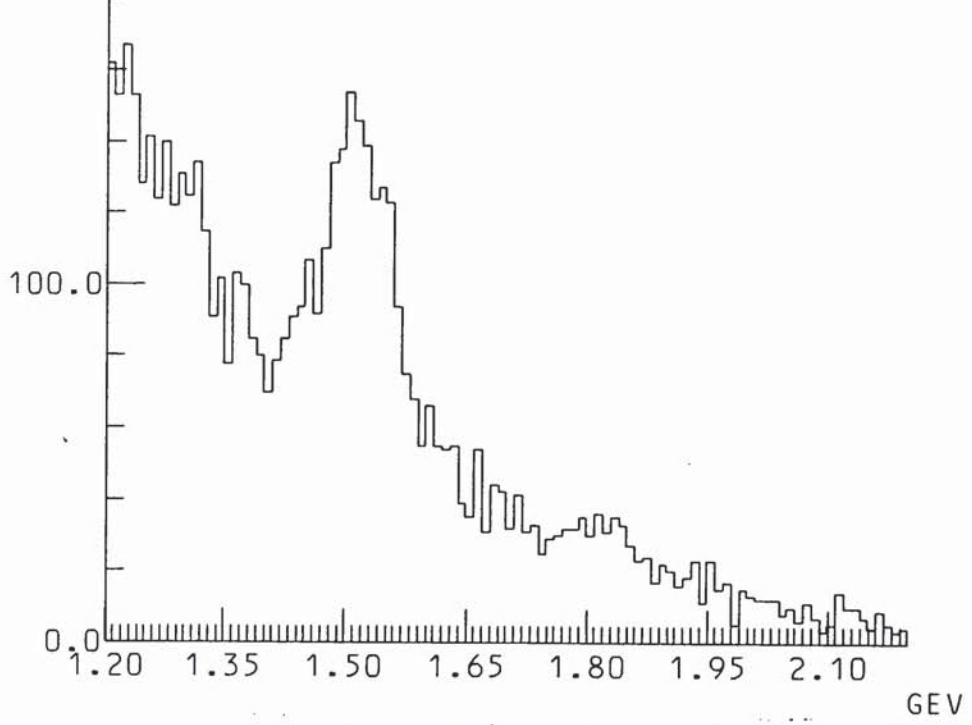

Figure 6.13: Mass $K^-K^+_f$ in $f'(1515)$ region for 4-prong data

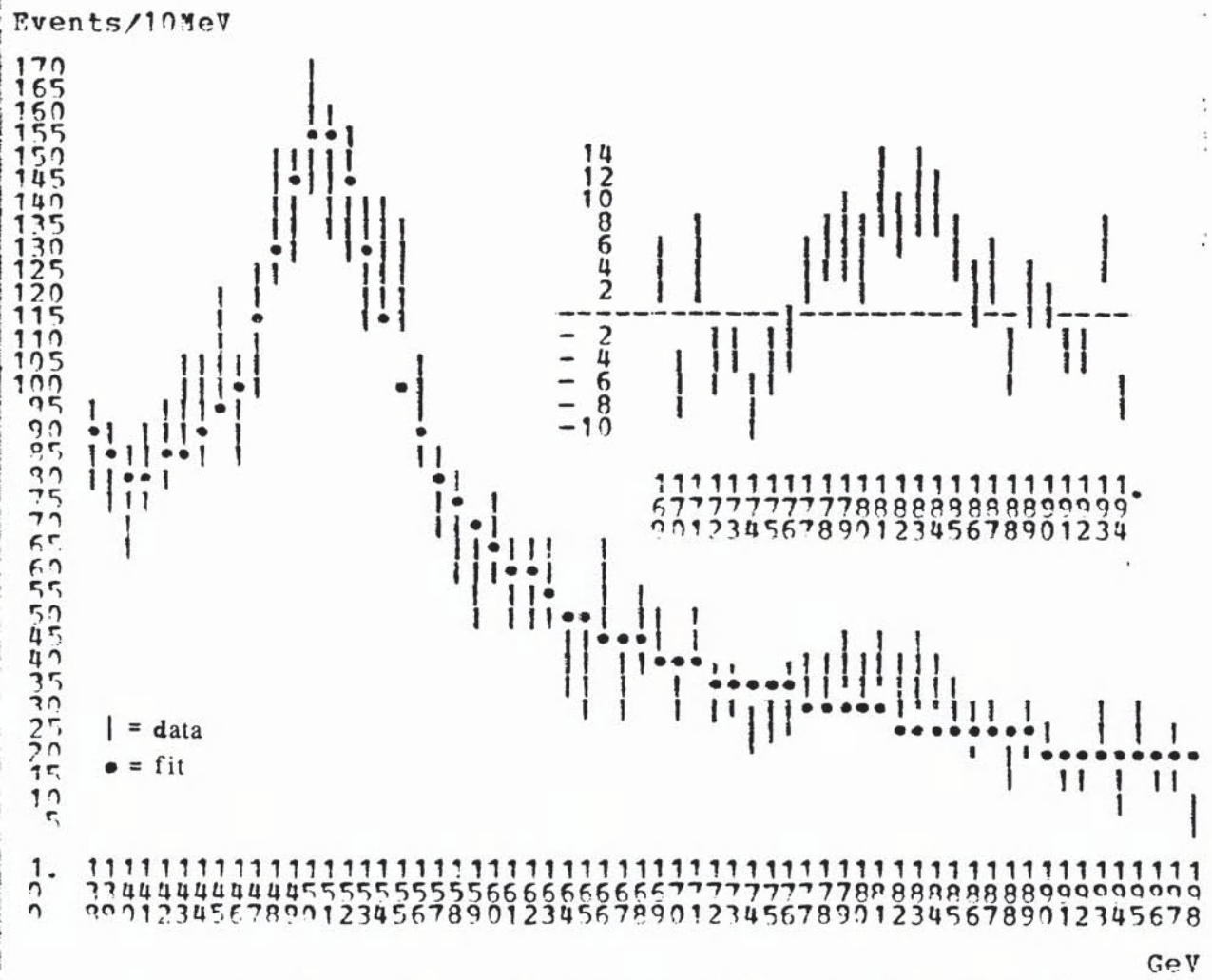

Figure 6.14: Fit to high mass $K^-K^+_f$ and (inset) with background subtraction

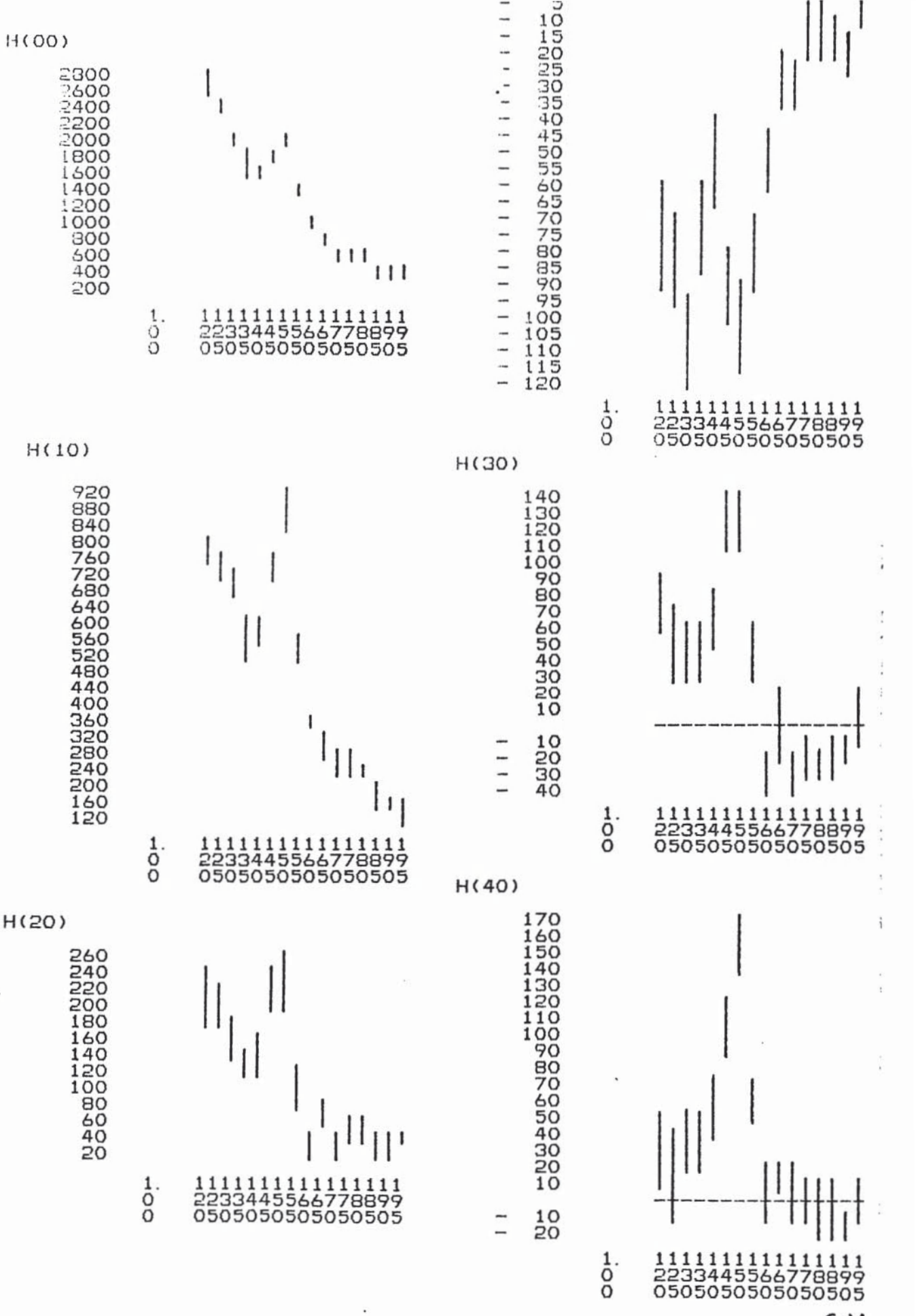

Figure 6.15: H(LM) as a function of mass $K^-K^+_f$

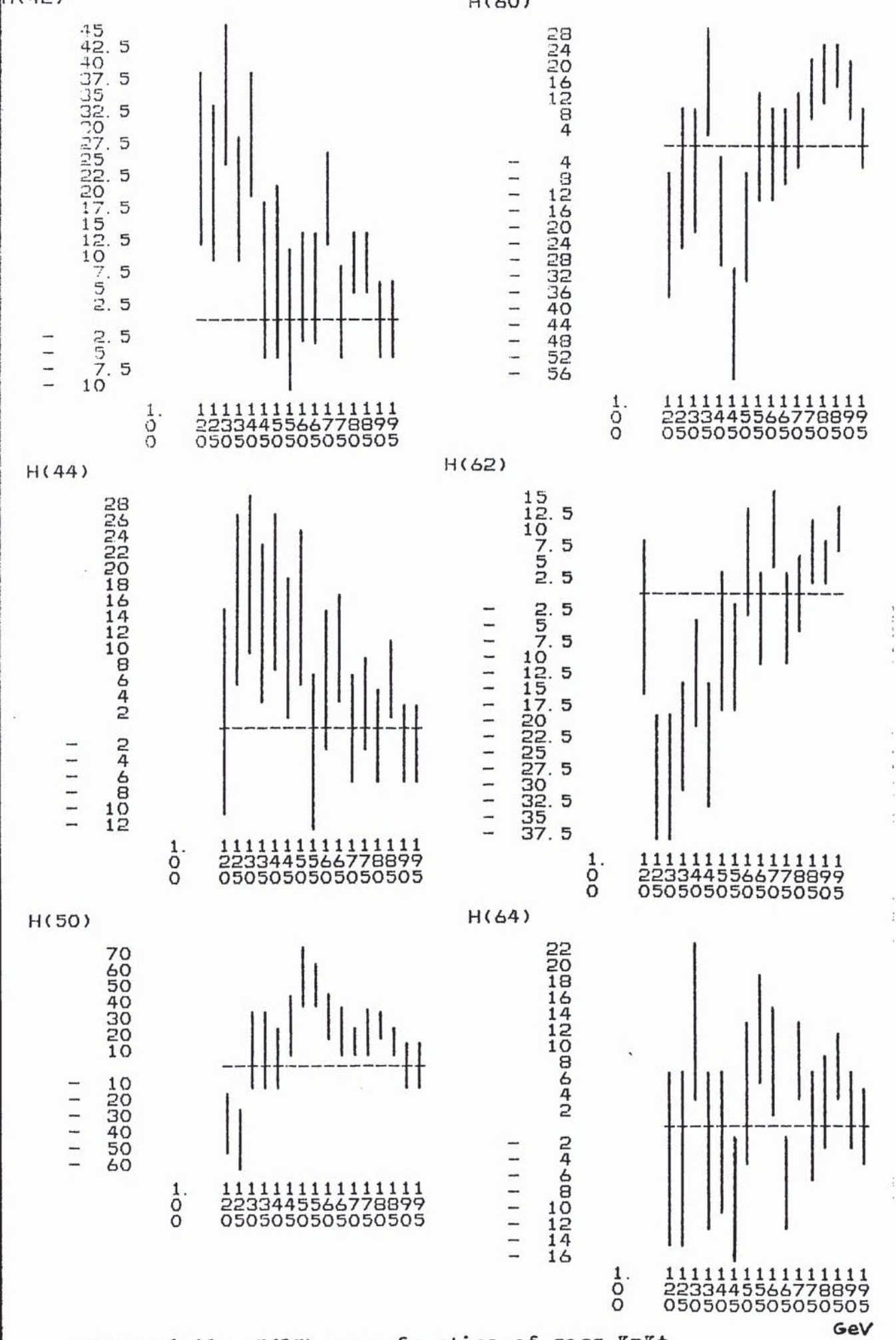

Figure 6.16: H(LM) as a function of mass $K^-K^+_f$

Chapter VII

A SPIN-PARITY ANALYSIS OF THE ϕK^+ SYSTEM

"A clock is placed on a rotating table. As the speed of rotation is increased, the clock flies to pieces. Discuss the angular distribution of the fragments and show how this allows one to calculate the spin and parity of the clock."

H.J.Lipkin, A Random Walk in Science

7.1 INTRODUCTION

The diffractive dissociation of the pion and the kaon in the processes $\pi \rightarrow \pi\pi\pi$ and $K \rightarrow K\pi\pi$ has been extensively studied [11,12,13], and detailed results on other diffractively produced systems, such as $K\bar{K}\pi$ and $\Lambda\bar{p}$, are now available [48,26,27]. Natural parity exchange is found to dominate these diffractive channels, preferentially producing unnatural spin-parity states ($P = (-1)^{J-1}$) which are approximately t-channel helicity conserving (TCHC), or, in the case of the ρK and ωK systems, approximately s-channel helicity conserving (SCHC) [12,15,52]. Conclusive evidence exists [13,2] for unnatural parity resonance production, the 1^+ $Q_1(1280), Q_2(1400)$ and the 2^- $L(1770)$ being examples of strange mesons seen in $K\pi\pi$ systems.

The partial wave decomposition of the KKK system, however, has been little studied [32,46], although recent analyses [16,17,18] of the diffractive $\phi(1020)K$ subsystem have greatly improved existing knowledge and have indicated possible resonant structure. Table 7.1 summarises existing data which have yielded information on the spin-parity of the ϕK system. Note that in the partial wave analyses of the total KKK system performed using the Illinois method [53,54], the data are analysed in terms of quasi two-body states, with ϕK being one such state included. The more recent analyses of the ϕK system have used the double moments [63,49] of the ϕK and ϕ decay angular distributions, where the ϕ is assumed to be in a well-defined 1^-

spin-parity state. All existing analyses have described the ϕK decay in terms of spin-orbit (LS) angular momentum couplings. The analyses agree that the $J^P L = 1^+S$ wave is dominant in the low mass region, producing a broad threshold enhancement around 1.7 GeV. The observed behaviour of this wave is essentially non-resonant, and is characteristic of a Deck mechanism [14,11], where a secondary kaon is (off-shell) elastically scattered on the target proton. The 2^-P wave is found to be weaker, but important, apparently showing resonant behaviour in the double moments analyses. The observed 2^- signal has been tentatively identified with the L(1770) meson(s), of mass ~ 1.8 GeV and width ~ 0.2 GeV [2], but the resonance parameters are poorly defined, largely because of inadequate statistics. The analyses performed using the Illinois technique have too few data to investigate resonance production in any detail, but Carney et al. [32] have reported that there is no evidence for a $K^-K^+K^+$ decay mode of a 2^- L meson in the mass range 1.6 - 1.9 GeV.

The KKK system is therefore not well understood, and requires further investigation. The dominance of the $\phi(1020)$ in $K\bar{K}$ suggests that an extensive high statistics study of the ϕK subsystem would contribute greatly to our understanding of the total KKK system. The ϕK^+ system produced in the reaction

$$K^+p \rightarrow \phi(1020)K^+p, \quad \phi(1020) \rightarrow K^-K^+ \qquad (7.1)$$

is of particular interest because of the dearth of existing data, and, since the pK^+ combination is exotic, the channel is not complicated by the production of the $\Lambda(1520)$ resonance decaying to pK^- which occurs in data taken with incident K^-. Assuming a diffractive production model, the spin-parity of the ϕK^+ system has been investigated in the present experiment over the mass range 1.5 - 2.2 GeV. The analysis data sample of 10429 (ambiguity weighted) events represents a threefold improvement on the best existing ϕK^+ statistics, and a significant improvement on ϕK^- data. The

spin-parity analysis was performed using a double moments technique, and helicity, rather than LS, amplitudes were used to describe the decay of the ϕK^+ system.

7.2 FORMALISM

The helicity formalism and notation used will closely follow that of Chung et al. [55,63,56], with further reference to Martin et al. [65,49]. We require to describe the production and subsequent decay of the ϕK^+ system in the following sequence of processes:

$$\begin{array}{l} K_i^+ + p_i \rightarrow R[J^P(\Lambda)] + p_f \\ \qquad\quad \Omega \hookrightarrow \phi[1^-(\lambda)] + K^+ \\ \qquad\qquad\quad \Omega_1 \hookrightarrow K^- + K_1^+ \end{array} \qquad (7.2)$$

where:

K_i^+	is the incident beam K^+
p_i / p_f	is the target/recoil proton
$R[J^P(\Lambda)]$	denotes the ϕK^+ system in a spin-parity state J^P with helicity Λ
$\phi[1^-(\lambda)]$	denotes the ϕ in a spin-parity state 1^- with helicity λ
$\Omega = (\Theta,\Phi)$	is the R decay angular distribution
$\Omega_1 = (\Theta_1,\Phi_1)$	is the ϕ decay angular distribution

Figure 7.1 illustrates the above processes, assuming diffractive dissociation of the incident kaon. Since approximate t-channel helicity conservation (TCHC) is anticipated [12,15], the primary decay $R \rightarrow \phi K^+$ will be described in the t-channel helicity (Jackson) frame. The angles $\Omega = (\Theta,\Phi)$ give the direction of the ϕ in the rest frame of R, with reference to axes defined such that the z-axis is along the beam direction, and the y-axis is normal to the production plane. The helicity angles $\Omega_1 = (\Theta_1,\Phi_1)$ for the secondary decay $\phi \rightarrow K^- K_1^+$ describe the direction of the K^- in the ϕ rest frame, with reference to axes defined such that z_1 is along the ϕ direction and y_1 is along $\underline{z} \times \underline{z}_1$ in the R rest frame. The reference frames used to define the decay angles are shown in figure 7.2.

7.2.1 Decay angular distribution

The joint decay angular distribution is given by

$$W(\Omega,\Omega_1) = d^2\sigma/d\Omega\, d\Omega_1 \sim \sum_{\substack{AA' \\ \Lambda\Lambda' \\ \lambda\lambda'}} M_{fi} M'^{*}_{fi}$$

where several spin-parities $A \equiv J^P$ are present, and M_{fi} represents the overall transition amplitude between the initial and final states. Assuming factorisation of production and decay amplitudes, M_{fi} may be expressed as

$$M_{fi} \sim \underset{(1)}{\langle A\Lambda|T|i\rangle}\ \underset{(2)}{\langle\Omega\lambda|F|A\Lambda\rangle}\ \underset{(3)}{\langle\Omega_1|f|\lambda\rangle}$$

where:

(1) is the amplitude for producing R in a spin-parity state A with helicity Λ. This amplitude defines the generalised density matrix elements

$$\rho^{AA'}_{\Lambda\Lambda'} \sim \langle A\Lambda|T|i\rangle \langle A'\Lambda'|T|i\rangle^{*}$$

which we consider to depend only on the mass of R.

(2) is the R decay matrix element, which, when transformed to an angular momentum basis yields

$$\langle\Omega\lambda|F|A\Lambda\rangle = \sqrt{\frac{2J+1}{4\pi}}\, D^{J}_{*\Lambda\lambda}(\Omega)\, F^{A}_{\lambda}$$

where F^A_λ is the helicity amplitude describing the decay $R \to \phi K^+$ from a spin-parity state A, and $D^J_{\Lambda\lambda}(\Omega)$ is a rotation matrix element [65]. If the state A has natural parity ($P = (-1)^J$), then $F^A_0 = 0$.

(3) is the $\phi \to K^-K^+_1$ decay matrix element, which similarly may be written

$$\langle\Omega_1|f|\lambda\rangle = \sqrt{\frac{3}{4\pi}}\, D^{1}_{*\lambda 0}(\Omega_1)$$

where the ϕ has spin-parity 1^-.

Hence,

$$W(\Omega,\Omega_1) = \sum_{\substack{AA' \\ \Lambda\Lambda' \\ \lambda\lambda'}} \rho^{AA'}_{\Lambda\Lambda'} \left(\frac{3}{4\pi}\right) \frac{\sqrt{(2J+1)(2J'+1)}}{4\pi} D^{J}_{\Lambda\lambda}(\Omega)\, D^{J'}_{\Lambda'\lambda'}(\Omega)\, D^{1}_{\lambda 0}(\Omega_1)\, D^{1}_{\lambda' 0}(\Omega_1)\, F^{A}_{\lambda} F^{A'}_{\lambda'} \qquad (7.3)$$

gives the decay angular distribution in terms of density matrix elements $\rho^{AA'}_{\Lambda\Lambda'}$ and helicity decay amplitudes F^{A}_{λ}. For a normalised distribution

$$\int W(\Omega,\Omega_1)\, d\Omega\, d\Omega_1 = 1$$

we impose the conditions

$$\sum_{A} \sum_{\Lambda} \rho^{AA}_{\Lambda\Lambda} = 1, \qquad \sum_{\lambda} |F^{A}_{\lambda}|^2 = 1 \qquad (7.4)$$

Parity conservation in the production and decay of R leads respectively to

$$\rho^{AA'}_{\Lambda\Lambda'} = PP'(-1)^{J-J'}(-1)^{\Lambda-\Lambda'} \rho^{AA'}_{-\Lambda-\Lambda'} \qquad (7.5)$$

$$F^{A}_{\lambda} = P(-1)^{J-1} F^{A}_{-\lambda} \qquad (7.6)$$

Furthermore, hermiticity and positivity conditions on the density matrix give respectively

$$\rho^{AA'}_{\Lambda\Lambda'} = \rho^{*A'A}_{\Lambda'\Lambda} \quad \text{and} \quad |\rho^{AA'}_{\Lambda\Lambda'}|^2 \leq \rho^{AA}_{\Lambda\Lambda}\, \rho^{A'A'}_{\Lambda'\Lambda'} \qquad (7.7)$$

7.2.2 Double moments

The double moments [55,63] of the decay angular distribution $W(\Omega,\Omega_1)$ are the experimental averages of the product of two D-functions:

$$H(LMlm) = \langle D^{L}_{Mm}(\Omega)\, D^{l}_{m0}(\Omega_1) \rangle = \int W(\Omega,\Omega_1)\, D^{L}_{Mm}(\Omega)\, D^{l}_{m0}(\Omega_1)\, d\Omega d\Omega_1 \qquad (7.8)$$

with normalisation $H(0000) = 1$. The angular distribution may then be expanded in terms of the double moments thus:

$$W(\Omega,\Omega_1) = \sum_{LM1m} \left(\frac{2L+1}{4\pi}\right)\left(\frac{2l+1}{4\pi}\right) H(LM1m)\, D^{L}_{Mm}(\Omega)\, D^{1}_{m0}(\Omega_1) \qquad (7.9)$$

with $0 \leq L \leq 2J_{max}$, $|M| \leq L$, $l = 0$ or 2 and $|m| \leq 1$.

By comparing equations 7.3 and 7.9, and by using the D-function coupling relations [65], the moments may be expressed alternatively as

$$H(LM1m) = \sum_{AA'} H^{AA'}(LM1m) = \sum_{AA'} t^{AA'}_{LM}\, f^{AA'}_{L1m} \langle 1010|10\rangle \qquad (7.10)$$

where:
$$t^{AA'}_{LM} = \sqrt{\frac{2J'+1}{2J+1}} \sum_{\Lambda\Lambda'} \rho^{AA'}_{\Lambda\Lambda'} \langle J'\Lambda' LM|J\Lambda\rangle \qquad (7.11)$$

$$f^{AA'}_{L1m} = \sum_{\lambda\lambda'} F^{A}_{\lambda} F^{A'}_{\lambda'} \langle J'\lambda' Lm|J\lambda\rangle \langle 1\lambda' 1m|1\lambda\rangle \qquad (7.12)$$

$\langle 1010|10\rangle$ represents a Clebsch-Gordon coefficient of the form $\langle j_1 m_1 j_2 m_2|JM\rangle$ (7.13)

Each interference moment $H^{AA'}(LM1m)$ is therefore the product of three factors which depend on the production of R, the decay $R \rightarrow \phi K^+$, and the decay $\phi \rightarrow K^-K^+$, respectively. The symmetries given in equations 7.5 - 7.7 for the density matrix elements $\rho^{AA'}_{MM'}$ and the decay helicity amplitudes F^{A}_{λ} impose symmetries on $t^{AA'}_{LM}$ (the generalised multipole parameters) and $f^{AA'}_{L1m}$, leading to the following symmetries in $H^{AA'}(LM1m)$ [56,63]:

$$H^{AA'}(LM1m) = PP'(-1)^{L+M} H^{AA'}(L-M1m) \qquad (7.14)$$

$$H^{AA'}(LM1m) = PP'(-1)^{L+1} H^{AA'}(LM1-m) \qquad (7.15)$$

$$H^{AA'}(LM1m) = (-1)^{M} H^{*A'A}(L-M1-m) \qquad (7.16)$$

$$H^{AA'}(LM1m) = (-1)^{1} H^{*A'A}(LM1m) \qquad (7.17)$$

with 7.17 ensuring that the decay angular distribution $W(\Omega,\Omega_1)$ is real. We note, in particular, that $H^{AA}(LM1m)$ is also real.

7.3 METHOD OF ANALYSIS

The plausibility of TCHC ϕK^+ production and the existence of regions of zero acceptance in the experimental decay angular distributions suggested that the simplest method of determining the ϕK^+ spin-parity decomposition was to compare the data double moments with simulated double moments (ie. modified by acceptance) for a given ϕK^+ spin-parity model with $\rho^{MM'}_{M'}$ and F^{A}_{λ} as input parameters. The various stages of a ϕK^+ spin-parity analysis based on such a modelling technique are described below.

7.3.1 Experimental moments

Events were selected from the total $K^-K^+K^+p$ data sample if either the $K^-K^+_s$ or the $K^-K^+_f$ effective mass combination lay in the $\phi(1020)$ region (see figure 6.4) defined by:

$$1.01 < \text{mass}(K^-K^+) < 1.03 \text{ GeV}$$

In the small fraction of data ($\sim 4\%$) where both the $K^-K^+_s$ and $K^-K^+_f$ combinations satisfied the above selection, the combination nearest the central $\phi(1020)$ mass of 1.0196 GeV [2] was taken to form the ϕ. The ϕK^+ effective mass distribution for the events selected is shown in figure 7.3. Events with an ambiguous ϕ assignment were found to lie almost entirely in the region < 1.6 GeV. The ϕK^+ mass spectrum was studied as a function of the squared four-momentum transfer t between the incident beam K^+ and the outgoing ϕK^+ system. The t distribution is shown in figure 7.4. As might be anticipated from the total $K^-K^+K^+$ Chew-Low plot of figure 6.1, it was found that the threshold enhancement in the ϕK^+ mass spectrum was associated with low momentum transfer. Therefore, a cut of $t < 0.7$ GeV^2 was imposed to enhance the diffractive-like component of the data. The effect of this t cut on the ϕK^+ mass spectrum (shown in figure 7.3) was largely to remove the three-prong events corresponding to the hypothesis $K^-(K^+)pK^+$. We recall that these events were responsible for producing the high mass contribution seen in figure 6.7.

The data sample was divided into mass bins of width 100 MeV, starting at 1.5 GeV. To ensure an adequate statistical sample in each bin, only the mass region <2·2 GeV was considered for the spin-parity analysis. The final data sample then consisted of 10429 ambiguity weighted events, almost entirely (93%) corresponding to the $K^-(p)K^+K^+$ and $K^-pK^+K^+$ hypotheses for three and four-prong events respectively (see chapter III). The sample breakdown, with unique event numbers in parentheses, was as follows:

hypothesis				
	$K^-(p)K^+K^+$	: 6012	(5913)	events
	$K^-(K^+)pK^+$	: 706	(706)	
	$K^-pK^+K^+$	: 3711	(3708)	
	total	: 10429	(10327)	

The experimental double moments with

$$0 \leq L \leq 12$$
$$0 \leq M \leq \text{smaller of } L \text{ and } 4$$
$$0 \leq l \leq 2$$
$$0 \leq m \leq 1$$

were calculated for each mass bin in the following manner:

$$H(LMlm) = \sum_{\substack{\text{events} \\ k}} w_k \, D^{L}_{Mm}(\phi_k, \Theta_k, 0) \, D^{l}_{m0}(\phi_{1_k}, \Theta_{1_k}, 0) \qquad (7.18)$$

where w_k represents the ambiguity weight for an event. Variances on the moments [51] were estimated by calculating:

$$V((LMlm)) = \sum_{\substack{\text{events} \\ k}} w_k^2 \{\mathrm{Re}(D^{L}_{Mm}(\phi_k, \Theta_k, 0) \, D^{l}_{m0}(\phi_{1_k}, \Theta_{1_k}, 0))\}^2 \qquad (7.19)$$

The data moments were studied to indicate possible resonant structure, and to suggest a maximum spin content and dominant ϕK^+ helicity amplitude. In order to emphasise any structure, the moments were normalised to the H(0000) moment, thereby removing the dependence on the shape of the mass distribution. It was found that essentially only the moments with $L \leq 4$ were non-zero within error, and that the

M = 0 moments were dominant. The real parts of the normalised experimental moments with $L \leq 4$ and M = 0 are shown as a function of mass in figures 7.5 to 7.8. Other significant non-zero moments with M = 1 (H(1100) and H(2100)) are also shown. The imaginary parts of the moments were largely consistent with being zero.

Clear structure of width $\sim$ 300 MeV centred on the 1.8 - 1.9 GeV mass bin is evident throughout the moments, the existence of a strong signal for L = 4 suggesting a spin 2 effect. The dominance of the M = 0 moments indicate in turn that the ϕK^+ helicity $\Lambda = 0$ amplitudes dominate: an observation which is consistent with the moments of previous data [17,16] and with the results of some simulation work in the present experiment (see later).

7.3.2 Assumptions and simplifications

The assumptions and the simplifications made for a diffractive ϕK^+ production model are discussed below, without regard to the effects of acceptance on the double moments.

1. The $K^-K^+_1$ system in the 1.01 - 1.03 GeV mass range is assumed to be entirely in the 1^- spin-parity state of the $\phi(1020)$, and consequently [63], since the ϕ decay conserves parity, only the moments with l = 0 or 2 are non-zero. Although the background under the observed ϕ Breit-Wigner signal (see figure 6.4) is low ($\lesssim 5\%$), spin 0/spin 1 interference effects have been detected in the ϕ region [57]. This topic will be discussed in more detail later.
2. The density matrix elements $\rho^{AA'}_{MM'}$ are considered to be a function of ϕK^+ mass only. In particular, the $\rho^{AA'}_{\Lambda\Lambda'}$ are assumed to be independent of the momentum transfer t to the ϕK^+ system and of the initial and final helicity states of the target proton.
3. TCHC is assumed ie. that the ϕK^+ system is produced from the incident kaon with helicity $\Lambda = 0$ in the t-channel helicity frame. The expectation and

consequences of approximate TCHC is discussed in detail in references 15 and 49. Existing results on ϕK confirm that the $M = 0$ moments, and hence the $\Lambda = 0$ amplitudes, are dominant. We note [49] that the omission of $\Lambda = 1$ terms from the density matrix is a good approximation as the $\Lambda = 1$ amplitudes enter quadratically into the $M = 0$ moments. Also, if ϕK^+ is produced with helicity zero by natural parity exchange (anticipated to be dominant [49]), then unnatural parity ($P = (-1)^{J-1}$) ϕK^+ states will be preferred.

The fundamental sets of ϕK^+ moments and spin-parity states are therfore considered to be $H(L0lm)$ and $J^P = \{0^-, 1^+, 2^-, \ldots\}$ respectively. If $M = 0$ and $l = 0$ or 2 then equations 7.16 and 7.17 give the symmetries:

$$H^{AA'}(L0lm) = H^{AA'}(L0l-m)$$

$$H^{AA'}(L0lm) = H^{*A'A}(L0lm)$$

which imply that the $H(L0lm)$ are real, and that only $m \geq 0$ need be considered. Assuming TCHC, and $L \leq 4$, $M = 0$, $l = 0$ or 2 and $0 \leq m \leq 1$, a total of 17 independent moments describe the ϕK^+ system. This restricted set of moments will be denoted by $\underline{H}(L0lm)$.

7.3.3 Programs

7.3.3.1 Calculation of moments and angular distribution

A program was written by the author, after some original ideas by J.B.Dainton,[5] to calculate the double moments and angular distribution resulting from an interfering mixture of ϕK^+ spin-parity states. The parameters input to the program are the generalised density matrix elements $\rho^{AA'}_{MM'}$ (which may be normalised as required) and the decay helicity amplitudes F^{Λ}_{λ} for each spin-parity state present. The

---

[5] Acknowledgements also to J.V.Morris and C.N.Paterson.

moments H(LM1m) are calculated according to equation 7.10 via 7.11, 7.12 and 7.13, thereby permitting the decay angular distribution $W(\Omega,\Omega_1)$ to be calculated by the moments expansion of equation 7.9. The angular distribution can also be predicted directly as in equation 7.3 by summation over all ϕK^+ spin-parity states A, ϕK^+ helicities Λ and ϕ helicities λ. The program can accommodate up to six different spin-parities and ϕK^+ helicity $|\Lambda| \leq 1$.

7.3.3.2 Event simulation

The general modelling program described in detail in chapter IV was adapted to simulate events corresponding to the production and decay processes of reaction 7.2 for a given ϕK^+ spin-parity model. The simulation of an event in the program was as follows:

1. For a given R (ϕK^+) mass bin, an R mass was chosen uniformly within the bin. Using this mass, and selecting a t'(beam/R) value according to the fitted experimental t'(beam/R) distribution for the bin, a CMS production angle for R was defined. (The t' distributions as a function of R mass were refitted after preliminary J^P models, hence acceptances, had been obtained, and were found to yield slope parameters $\lesssim 5\%$ higher than those fitted in the data, where $B \sim 12.1 - 3.8 \times$ mass. However, the spin-parity decompositions were not found to change significantly when acceptance corrected slope parameters were used.)
2. A $K^-K^+_1$ mass in the range 1.01 - 1.03 GeV was chosen according to a Breit-Wigner resonance shape with parameters corresponding to the $\phi(1020)$ signal observed in the data (see chapter VI).
3. Decay angles $\Omega = (\theta,\phi)$ and $\Omega_1 = (\theta_1,\phi_1)$ for R and the ϕ respectively were chosen uniformly in solid angle, with the ϕ and the K^- being taken as decay analysers.
4. Tracks were Lorentz transformed into the laboratory system and, if the K^- track satisfied the trigger

conditions (see chapters III and IV), the decay angles Ω and Ω_1 were recalculated using the decay reference frames shown in figure 7.2. The event was then weighted according to the theoretical angular distribution $W(\Omega,\Omega_1)$ for a given R spin-parity model and the contribution to the moments summation (equation 7.18) calculated as required.

Preliminary models

For the first three ϕK^+ mass bins ($1.5 < \text{mass} < 1.8$ GeV), simulations of unnormalised double moments were carried out for each of the following pure spin-parity states:

$$A \equiv J^P = 0^-,\ 1^-,\ 1^+,\ 2^- \text{ and } 2^+$$

for various values of the helicity decay amplitudes F^A_λ. (Recall that $F^{0^-}_1 = 0$ and $F^{1^-}_0, F^{2^+}_0 = 0$.) The only non-zero density matrix element ρ^{AA}_{00} was scaled to the number of events in each mass bin such that the simulated and data H(0000) moments agreed. The sets of moments $\underline{H}$(L0lm) for the simulated events and the data were then compared by eye. It was found that, in general, each spin-parity state produced a sufficiently distinctive set of moments to justify the inclusion or exclusion of the state from a partial wave decomposition. In particular, it was apparent that the 1^+ state was dominant, and that a 2^-, and possibly a 2^+, contribution was also required. The amounts of 0^- and 1^- present were clearly small.

Simple incoherent mixtures of spin-parities were then constructed, producing simulated moments and decay angular distributions in reasonable agreement with the data (using a 1^+, 2^- and 2^+ model). The addition of helicity 1 diagonal density matrix elements (ρ^{AA}_{11}) did not significantly improve the matching of the moments. In general, satisfactory results could be obtained by taking the decay helicity amplitudes to be real.

The results obtained from these simple models therefore supported the conjectures of unnatural spin-parity state

dominance and approximate t-channel helicity conservation. However, the computing overheads for event-by-event simulation were considerable, and an alternative technique for simulating moments which was devised is described below.

7.3.4 Acceptance correlation matrix technique

A technique was required for manipulating an experimental acceptance function which was zero in regions of angular decay space. That the acceptance can produce spurious effects in the observed moments is illustrated by figure 7.9 which shows the unnormalised moments $\underline{H}(L0lm)$ in the ϕK^+ mass range 1.6 - 1.7 GeV for the data and for simulated events where the ϕK^+ and ϕ systems were decayed isotropically. Following the method of reference 58 for single moments, the acceptance function will be described below in terms of correlation matrix elements. Using the abbreviations:

ν = LMlm

c_ν = $(\frac{2L+1}{4\pi})(\frac{2l+1}{4\pi})$

$A(\Omega,\Omega_1)$ = experimental acceptance function

$W^t(\Omega,\Omega_1)$ = theoretical angular decay distribution

$D_\nu(\Omega,\Omega_1) = D^L_{Mm}(\Omega)\ D^l_{m0}(\Omega_1)$

H^e_ν = experimental moment H(LMlm)

H^t_ν = theoretical moment H(LMlm)

consider the following definition of the experimental moments:

$$H^e_\nu = \int A(\Omega,\Omega_1)\ W^t(\Omega,\Omega_1)\ D_\nu(\Omega,\Omega_1)\ d\Omega d\Omega_1$$

$$= \sum_{\nu'} c_{\nu'} H_{\nu'} \int D_\nu(\Omega,\Omega_1)\ A(\Omega,\Omega_1)\ D^*_{\nu'}(\Omega,\Omega_1)\ d\Omega d\Omega_1$$

since $$W^t(\Omega,\Omega_1) = \sum_{\nu'} c_{\nu'} H_{\nu'} D^*_{\nu'}(\Omega,\Omega_1).$$

Defining the acceptance correlations

$$A_{\nu\nu'} = \int D_{\nu}(\Omega,\Omega_1)\ A(\Omega,\Omega_1)\ D^*_{\nu'}(\Omega,\Omega_1)\ d\Omega d\Omega_1 \qquad (7.20)$$

we then have

$$H^e_{\nu} = \sum_{\nu'} c_{\nu'}\, A_{\nu\nu'}\, H^t_{\nu'} \qquad (7.21)$$

which in an obvious matrix notation gives $H^e = A'H^t$, where $A' = cA$.

For each ϕK^+ mass bin, the acceptance correlations $A_{\nu\nu'}$ defined by equation 7.20 were calculated by generating events uniformly in the solid angles corresponding to Ω and Ω_1 and evaluating:

$$A_{\nu\nu'} = \frac{16\pi^2}{N_G} \sum_{\substack{\text{events}\\ k=1}}^{N_G} D_{\nu}(\Omega_k,\Omega_{1_k})\ a(\Omega_k,\Omega_{1_k})\ D^*_{\nu'}(\Omega_k,\Omega_{1_k})$$

where N_G denotes the number of events generated (before acceptance), and $a(\Omega_k,\Omega_{1_k})$ is 1 or 0 depending on whether event k is accepted or not accepted. In general, sufficient events were generated such that $\gtrsim 5$ x (number of real events in bin) remained after acceptance losses. An acceptance correlation matrix of dimension 24 x 24 was thus formed for each mass bin, with elements for $L \leq 4$, $M = 0$, $1 = 0,2$ and $-1 \leq m \leq 1$, assuming negligible contributions from higher terms (see also figure 7.9). Given such a matrix and a theoretical set of moments for a particular ϕK^+ spin-parity model, the moments after acceptance modification could be calculated simply by matrix multiplication, without the need for time-consuming event-by-event simulation.

As a check on the accuracy of the acceptance matrix method, simple J^P models were used to yield sets of theoretical moments and decay angular distributions. The 'experimental' moments predicted by the correlation matrix technique were then compared with the moments obtained from event-by-event simulations by using equation 7.18. The two

methods were found to give consistent results: we assume therefore that the restricted range of acceptance matrix elements chosen sufficed to describe the main features of the experimental acceptance function.

7.3.5 Fitting of moments

The reduction in computing overheads resulting from the description of the acceptance by a correlation matrix permitted the fitting of model-predicted moments to the unnormalised data moments (shown in figures 7.10 - 7.12). The CERN program MINUIT [59] was used to minimise for each ϕK^+ mass bin the chisquared function defined by:

$$\chi^2 = \sum_{\nu} (H_\nu^d - H_\nu^p)^2 / V_\nu^d$$

where: ν = L01m, with values as for $\underline{H}$(L01m)

H_ν^d = unnormalised data moment

H_ν^p = unnormalised moment predicted by J^P model after acceptance modification

V_ν^d = variance of data moment

Each mass bin was fitted independently, with final minimisation in each case being achieved by convergence of the MIGRAD [59] minimiser. The fit parameters were chosen bearing in mind the results from previous data and from the preliminary event-by-event simulations. Assuming that the 1^+ state was dominant and largely non-resonant, the helicity decay amplitudes F_λ^A for unnatural parity states were expressed in the form:

$$F_0^A = |F_0^A| \exp(i\delta_0^A)$$

$$F_1^A = |F_1^A| \exp(i\delta_1^A), \quad \text{where} \quad |F_1^A| = \sqrt{(1-|F_0^A|^2)/2}$$

with all decay phases δ^{A}_{λ} being measured with respect to the F^{1+}_{0} phase, defined to be zero. For natural parity states, $F^{A}_{1} = 1/\sqrt{2}$ was assumed. Since unnormalised moments were being fitted, the parameters corresponding to the density matrix elements $\rho^{AA'}_{\lambda\lambda'}$ were scaled to the number of events N originally produced before acceptance losses. Only interference terms involving the 1^+ state were considered, since condition 7.7 applies, and simple incoherent mixtures of states had been found previously to provide an adequate description of the data moments. During the course of this analysis, evidence for a 3^+ contribution to the ϕK^+ spin-parity decomposition was presented in reference 16. Figure 7.13 shows our experimental unnormalised moments for L = 6 and M = 0. Whilst these moments are consistent with being zero within error for most mass bins, we consider that a 3^+ contribution might reasonably be expected at higher mass, and note that this wave will also contribute to the lower moments. Parameters corresponding to the presence of a 3^+ state were therefore tentatively included in the fits. The final 21 parameters considered for fitting were:

1) $N\rho^{0^-0^-}_{00}$	2) $N\rho^{1^+1^+}_{00}$	3) $N\rho^{2^-2^-}_{00}$	4) $N\rho^{3^+3^+}_{00}$
5) $N\rho^{1^-1^-}_{00}$	6) $N\rho^{2^+2^+}_{00}$	7) $N\mathrm{Re}\rho^{0^-1^+}_{00}$	8) $N\mathrm{Im}\rho^{0^-1^+}_{00}$
9) $N\mathrm{Re}\rho^{1^+2^-}_{00}$	10) $N\mathrm{Im}\rho^{1^+2^-}_{00}$	11) $N\mathrm{Re}\rho^{1^+3^+}_{00}$	12) $N\mathrm{Im}\rho^{1^+3^+}_{00}$
13) $\lvert F^{1^+}_{0}\rvert$	14) $\lvert F^{2^-}_{0}\rvert$	15) $\lvert F^{3^+}_{0}\rvert$	16) $\delta^{0^-}_{0}$
17) $\delta^{1^+}_{1}$	18) $\delta^{2^-}_{0}$	19) $\delta^{2^-}_{1}$	20) $\delta^{3^+}_{0}$
21) $\delta^{3^+}_{1}$			

Preliminary minimisations for each mass bin were carried out with parameters 5), 6), 7), 8) and 16) fixed at zero, assuming the dominance of unnatural parity states and a small 0^- contribution. For subsequent minimisations, parameters were fixed at zero if they were persistently consistent with being zero within one standard deviation. If the diagonal density matrix element ($N\rho^{AA}_{00}$) corresponding to a particular spin-parity state was set to zero, then that state was completely removed from the model. Parameters (such as 5) and 6) for natural parity states) were released

and fitted according to the number of degrees of freedom available. The following observations were made during fitting:

1. The parameters for 1^+ and 2^- were found to be largely insensitive to the initial assumptions input to the fit. The parameters for these waves appeared to be tightly constrained by the data.
2. The amount of 0^- present was generally consistent with zero. If 0^- was re-introduced to the model after final minimisation, any contribution was still too small to be fitted reasonably.
3. The dominant natural parity wave was 2^+. Although the 2^+ contribution was not large, the wave was necessary to produce good fits. The 1^- content was always found to be small.
4. A fairly substantial contribution from 3^+ was found to significantly improve the fits obtained, although the interference and decay parameters for this wave were rather poorly defined.

The final fitted moments are shown superimposed on the experimental moments in figures 7.10 - 7.12. The quality of fit is seen to be generally good; fit probabilities were in the range 1% - 76%.

Using the fitted spin-parity model for each mass bin, two sets of event-by-event simulations were performed, with the decay angular distribution in one case being calculated directly as in equation 7.3, and in the other case via the restricted set of moments $\underline{H}(L0lm)$, applying equations 7.10 and 7.9. The projections (θ,ϕ) and (θ_1,ϕ_1) of the angular distribution after acceptance modification were then compared with the data, and the agreement found to be good. Figure 7.14 shows the results from the former set of simulations superimposed on the data. Whilst the θ, θ_1 and ϕ_1 projections always agreed closely, the ϕ projection was seen to be less peaked in the simulations than in the data. Notwithstanding this effect, which was investigated but not

understood, we conclude that the fitted models serve as a good basis for a description of the spin-parity of the ϕK^+ system. Little information seems to have been lost by fitting only the restricted set of moments $\underline{H}(L0lm)$.

The theoretical unnormalised moments (before acceptance) for the final model fitted in each bin are shown in figures 7.15 - 7.17, and may be compared directly with bubble chamber data [17] or acceptance corrected data [eg. 16].

7.4 RESULTS

The final values of the fitted parameters are presented as a function of ϕK^+ mass in figures 7.18 - 7.21. A full analysis of the errors on the parameters was not completed, and consequently the errors presented are simply the parabolic fitting errors determined by the MIGRAD minimiser.

The number of events originally produced in each spin-parity state contributing to the final model is given by the parameters $N\rho_{00}^{AA}$ shown in figure 7.18. Note that any 0^- contributions are not shown, being essentially consistent with zero, and that the 1^- contribution could not be determined for two bins. Recall that if $N\rho_{00}^{AA}$ for a particular state was consistent with zero, then that state was removed from the model for the mass bin under study.

Before studying the results in detail, the quantities described below were calculated from the fitted parameters.

Coherences and production phases

The magnitude

$$|\varepsilon| = |\rho^{AA'}| / \sqrt{\rho^{AA}\,\rho^{A'A'}}$$

of the coherence ε measures the extent to which the states A and A' interfere (see also condition 7.7). If the density matrix elements are expressed [11] in terms of production amplitudes R and phases γ, then

$$\rho^{AA} = |R^{A}\exp(i\gamma^{A})|^2 = R^{A2}$$

$$\rho^{A'A'} = |R^{A'}\exp(i\gamma^{A'})|^2 = R^{A'2}$$

and $\rho^{AA'} = \varepsilon R^{A}\exp(i\gamma^{A})[R^{A'}\exp(i\gamma^{A'})]^* = \varepsilon R^{A}R^{A'}\exp[i(\gamma^{A} - \gamma^{A'})]$

Hence, if the interference is coherent $\varepsilon \sim 1$ and the phase $(\gamma^{A} - \gamma^{A'})$ gives the relative phase between the production amplitudes for the states A and A'. The calculated magnitudes of the coherences $\varepsilon_{\infty}^{1^+2^-}$ and $\varepsilon_{\infty}^{1^+3^+}$ are shown in figure 7.19, and although the errors are rather large, the coherence is consistent with unity for 1^+2^- and in bins 2 - 5 for 1^+3^+. We have therefore assumed $\varepsilon \sim 1$ and have determined the relative production phases

$$\tan(\gamma_{00}^{AA'}) = \arg(N\rho_{00}^{AA'}) = NIm\rho_{00}^{AA'} / NRe\rho_{00}^{AA'}$$

which are shown in figure 7.20. For a simple Breit-Wigner resonance in state A', the phase $\gamma^{A'}$ will change by $\pi/2$ in passing through the resonance peak. However, since we can only measure the phase $(\gamma^{A} - \gamma^{A'})$ relative to the state A, any variation in γ^{A} will distort the phase change observed.

Decay phases

If the state A' is resonant, time-reversal invariance applied to the scattering process $\phi K^+ \rightarrow \phi K^+$ in the s-channel implies [63] that the phase of F_{λ}^{A} is independent of λ. Hence the relative phase $(\delta_0^{A'} - \delta_1^{A'})$ between the helicity 0 and helicity 1 decay amplitudes should be zero as we pass through the central value of the resonance. The differences between the helicity 0 and helicity 1 phases relative to $F_0^{1^+}$ have been calculated and are shown in figure 7.22.

7.4.1 Discussion

The 1^+ spin-parity state is dominant, peaking in the 1.6 - 1.7 GeV mass bin and accounting for $\sim 70\%$ of the cross-section in this region. Above 2.1 GeV however, the 1^+ contribution falls to zero. The 2^- wave appears as a peak,

centred at ~ 1.8 GeV, and falling to zero at the edges of the mass range studied. A substantial 3^+ contribution is seen to increase slowly with mass, becoming the most important wave above 2 GeV. The dominant natural parity state is 2^+, with the 1^- contribution probably consistent with zero. A peak centred on the 1.8 - 1.9 GeV bin is seen in 2^+, apparently sitting on some background which increases with mass.

The magnitudes $|F_0^A|$ of the helicity zero decay amplitudes for 1^+ and 2^- dip strongly in the 3rd and 4th mass bins respectively, with the 2^- dip being the more pronounced. $|F_0^{3^+}|$ peaks slightly in the 4th mass bin.

The relative production phase between 1^+ and 2^- falls by $\sim 140^\circ$ between bins 2 and 3, and rises by $\sim 120^\circ$ between bins 3 and 4. The phase between 1^+ and 3^+ is consistent with being zero within the large errors. The relative phase between the helicity 0 and helicity 1 decay amplitudes for 1^+ dips to become negative in the 1.7 - 1.8 GeV mass bin. In the same region, the relative decay phase $(\delta_0^{2^-} - \delta_1^{2^-})$ for 2^- rises by ~ 0.7 through zero. The behaviour of the 3^+ relative decay phase is somewhat erratic.

Possible resonant states

The most striking candidate for a resonant state is 2^-, with both the relative production and decay phases changing significantly in the region of the peak seen in the intensity distribution. The decay phase variation $(\delta_0^{2^-} - \delta_1^{2^-})$ is regarded as especially significant as it is independent of the behaviour of the other waves. We also note the greatly increased preference for a helicity 1 ϕ configuration in the peak region. The 2^- intensity was fitted to a Breit-Wigner function (without spin dependence) to yield the following estimates of the resonance parameters:

$$m \sim 1.81 \pm 0.02 \text{ GeV}$$
$$\Gamma \sim 0.14 \pm 0.04 \text{ GeV}$$

Figure 7.18 shows the fitted Breit-Wigner function superimposed on the 2^- intensity distribution. The 2^- signal is therefore compatible with the enhancements suggested by previous ϕK analyses, and may reasonably be identified with the L(1770) meson(s) seen [13] in $K\pi\pi$ systems such as $K^*\pi$ and fK produced from an incident K^-.

Whilst the 2^+ intensity shows a clear peak with similiar Breit-Wigner parameters to the 2^- signal, the absence of phase information prevents interpretation of this enhancement. We note, however, that the 2^+D waves of references 16 and 18 also exhibit small enhancements consistent with that observed in the present experiment.

Interpretation of the total 1^+ threshold enhancement as a resonance is unlikely, assuming a 2^- resonance at ~ 1.8 GeV and considering the relative production phases. However, the dip seen in $|F_0^{1^+}|$ and the decay phase $\delta_1^{1^+}$ may indicate an effect centred on the 1.7 - 1.8 GeV region. Armstrong et al. [18] have investigated the 1^+ wave in their data by using a Deck [14] model, according to Berger and Donohue [15]. The result of this study was a satisfactory Deck description of the 1^+S wave, if some contribution from a 1^+ resonance of width ~ 0.25 GeV at ~ 1.84 GeV was assumed. Daum et al. [13] have already discussed the possibility of a 1^+ resonance at ~ 1.8 GeV decaying to $\pi\pi\pi$ and $K\pi\pi$ systems. Although a Deck-type analysis was considered beyond the scope of this thesis, the effects observed in the present experiment cannot exclude the possibility of some contribution from a 1^+ resonance in the 1.7 - 1.8 GeV region.

7.4.2 Cross-sections

The final spin-parity models were used to calculate angular distributions via equation 7.3, and hence by performing event-by-event simulations, the acceptance as a function of mass (shown in figure 7.23) was determined. The particular subsample of events used in the spin-parity analysis represents a cross-section contribution of $5.9 \pm 0.9\ \mu b$,

and this may be regarded as a lower cross-section limit for the reaction 7.1. By allowing for the cuts made on the data, and by approximately extrapolating the acceptance to higher masses, the following estimate of the true reaction cross-section (background subtracted) was obtained:

$$\sigma(K^+p \rightarrow \phi K^+p, \quad \phi \rightarrow K^-K^+) \quad = \quad 13 \pm 3 \ \mu b$$

This value is consistent with the $11 \pm 3 \ \mu b$ of reference 6 measured at an incident beam momentum of 10 GeV.

The estimated true cross-section for the production of the possible 2^- L resonance at 1.81 GeV is:

$$\sigma(K^+p \rightarrow L(1810)p, \ L(1810) \rightarrow \phi K^+, \ \phi \rightarrow K^-K^+) \sim 0.7 \pm 0.1 \ \mu b$$

7.5 INVESTIGATION OF K^-K^+ BACKGROUND IN ϕ REGION

Fitting of the $K^-K^+_1$ mass spectrum[6] in the $\phi(1020)$ region indicated that $\lesssim 5\%$ of events in the range 1.01 - 1.03 GeV lay beneath the ϕ Breit-Wigner resonance form. Evidence exists [2] for $j^{pc} = 0^{++}$ states (notably the S*(975) and $\delta(980)$) which decay to $K\bar{K}$ in this region, and small but significant S-P wave interference effects in K^-K^+ have been reported [57].

The $K^-K^+_1$ background in the ϕ region has been investigated in the present experiment by studying the available ϕK^+ double moments which depend only on the decay of the $K^-K^+_1$ pair. The (real parts of the) experimental unnormalised double moments H(0000), H(0010), and H(0020) were calculated as a function of $K^-K^+_1$ mass for each of the ϕK^+ spin-parity analysis mass bins. These moments may be written [50] in terms of a density-matrix formalism for S and P-wave $K^-K^+_1$ thus:

$$H(0000) = \rho^{00}_{00} + \rho^{11}_{00} + 2\rho^{11}_{11} = 1 \qquad (7.22)$$

$$H(0010) = (2/\sqrt{3})\rho^{01}_{10} \qquad (7.23)$$

$$H(0020) = (2/5)(\rho^{11}_{00} - \rho^{11}_{11}) \qquad (7.24)$$

---

[6] ie. the spectrum of the $K^-K^+_1$ combination which lay closest to the central mass of the $\phi(1020)$.

where $H = ReH$, and $\rho^{jj'}_{\lambda\lambda'} = Re\rho^{jj'}_{\lambda\lambda'}$ is the density matrix element describing interference between spin states j and j' with $\lambda(\lambda')$ the helicity of the $K^-K^+_1$ system in the spin states $j(j')$. The H(0010) moment is of particular interest in that it is a direct measure of any interference between the S and P-waves. Expressing the density matrix elements in terms of an amplitude A and phase γ for each wave gives [11]:

$$\rho^{00}_{00} = |A_0 \exp(i\gamma_0)|^2 = A_0^2 \qquad (7.25)$$

$$\rho^{11}_{00} = |A_1 \exp(i\gamma_1)|^2 = A_1^2 \qquad (7.26)$$

$$\rho^{01}_{00} = \varepsilon A_0 A_1 \exp(i(\gamma_0 - \gamma_1)) \qquad (7.27)$$

$$= \sqrt{\rho^{00}_{00}\rho^{11}_{00}}\cos(\gamma_0 - \gamma_1) \quad \text{taking real parts and} \qquad (7.28)$$

ε = coherence ~ 1

The data H(0010) moment as a function of $K^-K^+_1$ mass is shown in figures 7.24 and 7.25 for each of the $K^-K^+K^+$ mass bins used in the ϕK^+ spin-parity analysis. For $K^-K^+K^+$ mass < 1.8 GeV the final fitted ϕK^+ spin-parity models were used in conjuction with the detector model to simulate events and predict the H(0010) moment after acceptance modification. The predicted moments are shown superimposed on the data moments in figure 7.24, and are suggestive of an inadequate model for the $K^-K^+_1$ system.

In order to obtain a rough estimate of the amount of S-wave $K^-K^+_1$ present in the ϕ region, the experimental H(0010) moment for $K^-K^+K^+$ mass < 1.6 GeV was fitted [59] to equation 7.28 using a constant S-wave and a Breit-Wigner P-wave with the observed ϕ mass and width. The fitted moment is shown superimposed on the data moment in figure 7.26. (This moment was chosen for fitting since the effect of acceptance appeared to be uniform over the $K^-K^+_1$ mass range.) The corresponding data H(0000) and H(0020) moments for this $K^-K^+K^+$ bin are also shown in figure 7.26.

The results from the fit, used in conjuction with equation 7.22, indicate a S/P-wave intensity ratio of $(1.0 \pm 0.5)\%$ at the central ϕ mass (cf. an estimated $(9 \pm 7)\%$ in reference 57 for $K^-p \rightarrow K^-K^+\Lambda$ at 4.2 GeV

incident momentum). Furthermore, an estimated (2 ± 1)% of events with $K^-K_1^+$ mass in the range 1.01 - 1.03 GeV decay via an S rather than P-wave (ϕ) $K^-K_1^+$ state.

7.6 SUMMARY

The data presented constitute a significant improvement on existing ϕK^+ statistics. With some justification from the data, a TCHC diffractive production model has been assumed for the ϕK^+ system. Based on this model, a spin-parity analysis of ϕK^+ in the mass range 1.5 - 2.2 GeV has indicated a high unnatural spin-parity state content, with 1^+ being the dominant wave. Evidence exists for a 2^- resonance at $\sim$1.8 GeV, consistent with being one of the L mesons reported in $K\pi\pi$ data. The 1^+ wave appears largely non-resonant, but the possibility of a resonant contribution around 1.8 GeV is not excluded. The estimated reaction cross-section for the ϕK^+p final state is consistent with the accepted value. Indications of small K^-K^+ interference effects are observed in the ϕ region.

CHANNEL, SYSTEM ANALYSED	BEAM MOMENTUM (GeV)	TYPE OF EXPERIMENT	NUMBER OF EVENTS JP ANALYSED	MASS RANGE (GeV)	ANALYSIS TECHNIQUE	POSSIBLE RESONANCES OBSERVED (GeV)	REFERENCE
$K^+p \to \underline{K^-K^+K^+}p$	combined 8·2, 10, 16	BUBBLE CHAMBER	~660	1·6 – 2·4	ILLINOIS	—	32
$K^-p \to \underline{K^+K^-K^-}p$	combined 10, 16	BUBBLE CHAMBER	298	1·6 – 2·4	ILLINOIS	—	46
$K^+p \to \underline{\phi K^+}p$ $\hookrightarrow K^-K^+$	50	SPECTROMETER	~3340	1·5 – 2·0	DOUBLE MOMENTS	1^+ ? 2^- { M = 1·84 ± 0·02, Γ = 0·16 ± 0·04	16
$K^-p \to \underline{\phi K^-}p$ $\hookrightarrow K^0\bar{K}^0$	8·25	BUBBLE CHAMBER	838	1·5 – 2·5	DOUBLE MOMENTS	2^- { M ~ 1·80, Γ ~ 0·25	17
$K^-p \to \underline{\phi K^-}p$ $\hookrightarrow K^-K^+$	18·5	SPECTROMETER	7524	1·5 – 2·1	DOUBLE MOMENTS	0^- { M ~ 1·83, Γ ~ 0·25 1^+ { M ~ 1·84, Γ ~ 0·25 ? 2^- { M ~ 1·73, Γ ~ 0·22	18

TABLE 7.1

Existing ϕK spin-parity analyses

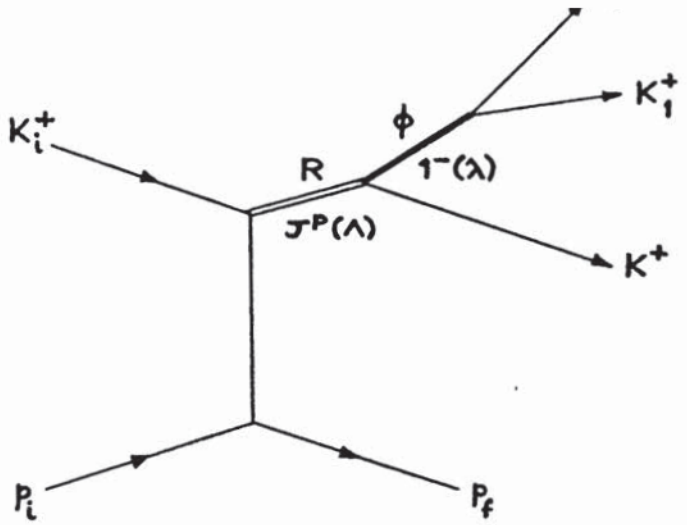

Figure 7.1: ϕK^+ diffractive production and decay

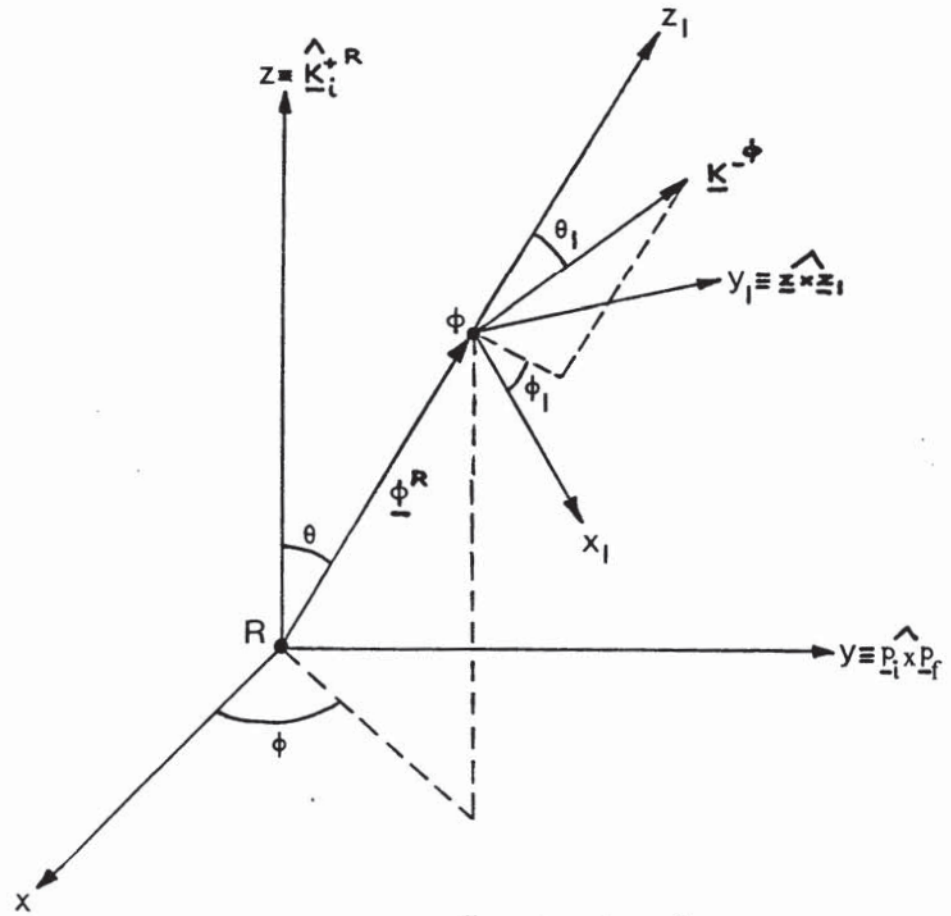

$\underline{\alpha}^{\mu}$ = momentum of α in μ rest frame

Figure 7.2: ϕK^+ decay reference frames and angles

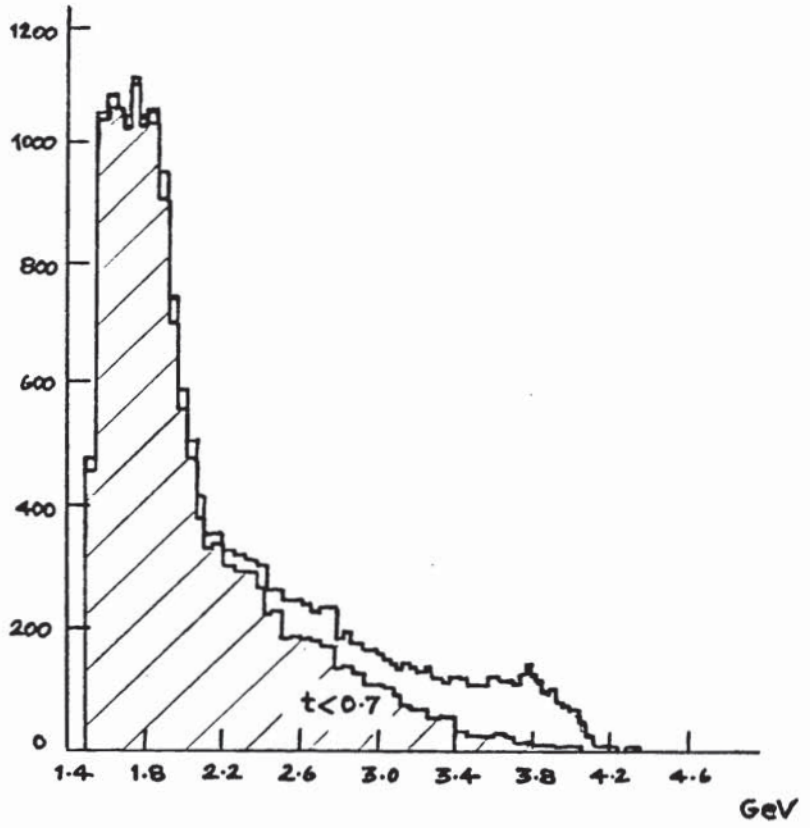

Figure 7.3: Mass ϕK^+ (with effect of t cut)

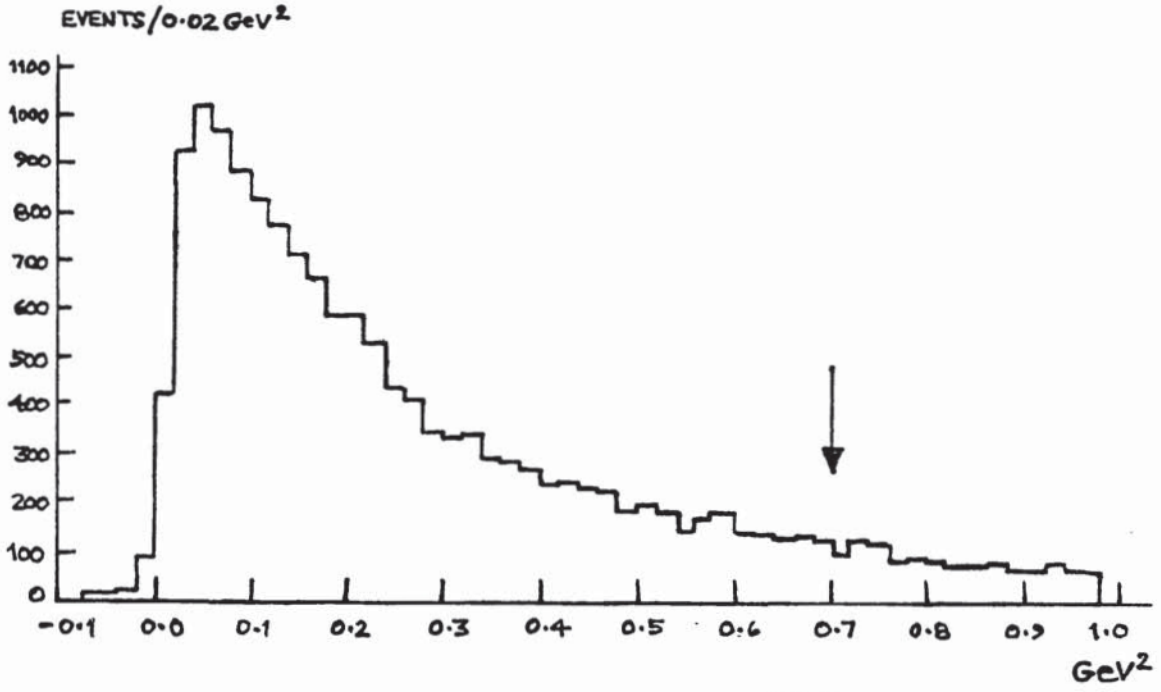

Figure 7.4: t(beam/ϕK^+)

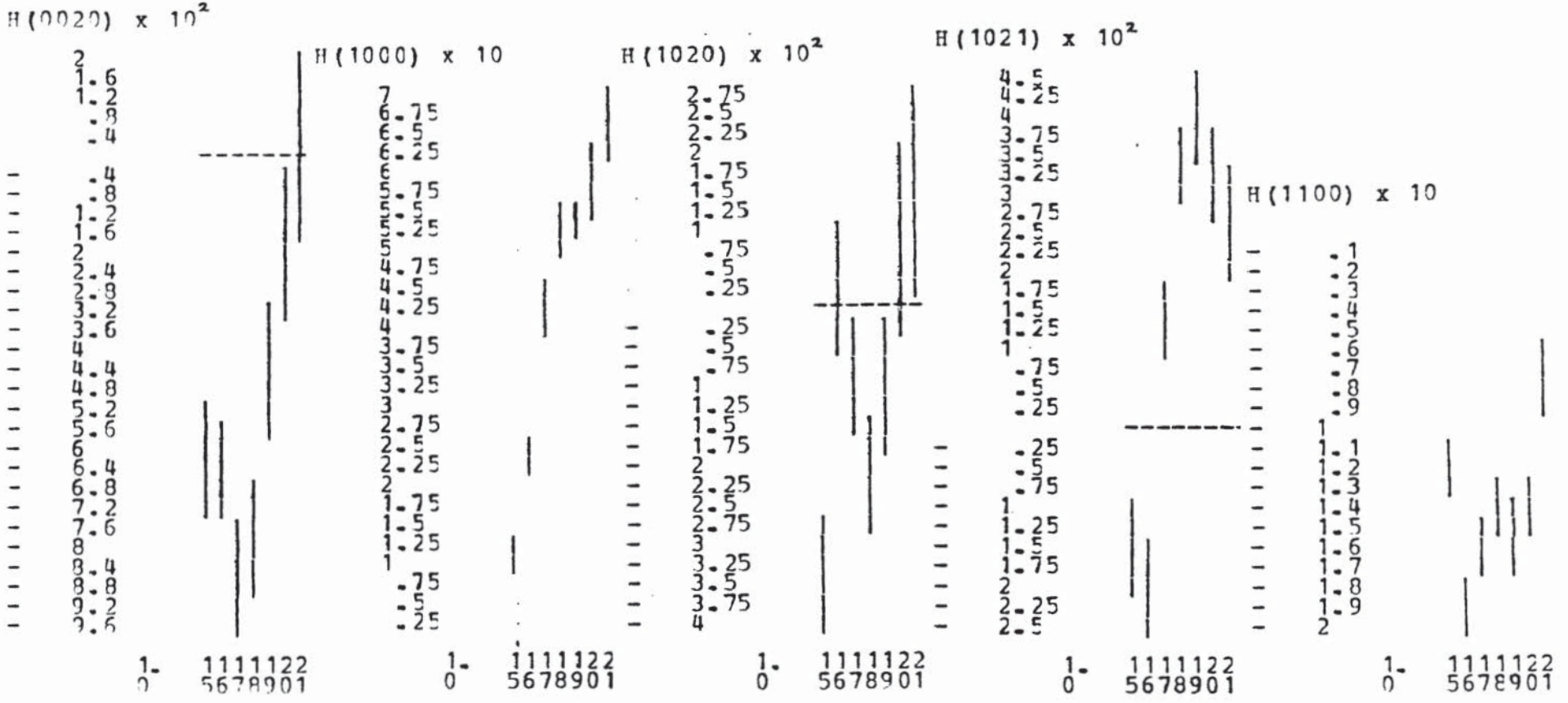

Figure 7.5: Experimental normalised H(0020) - H(1100)

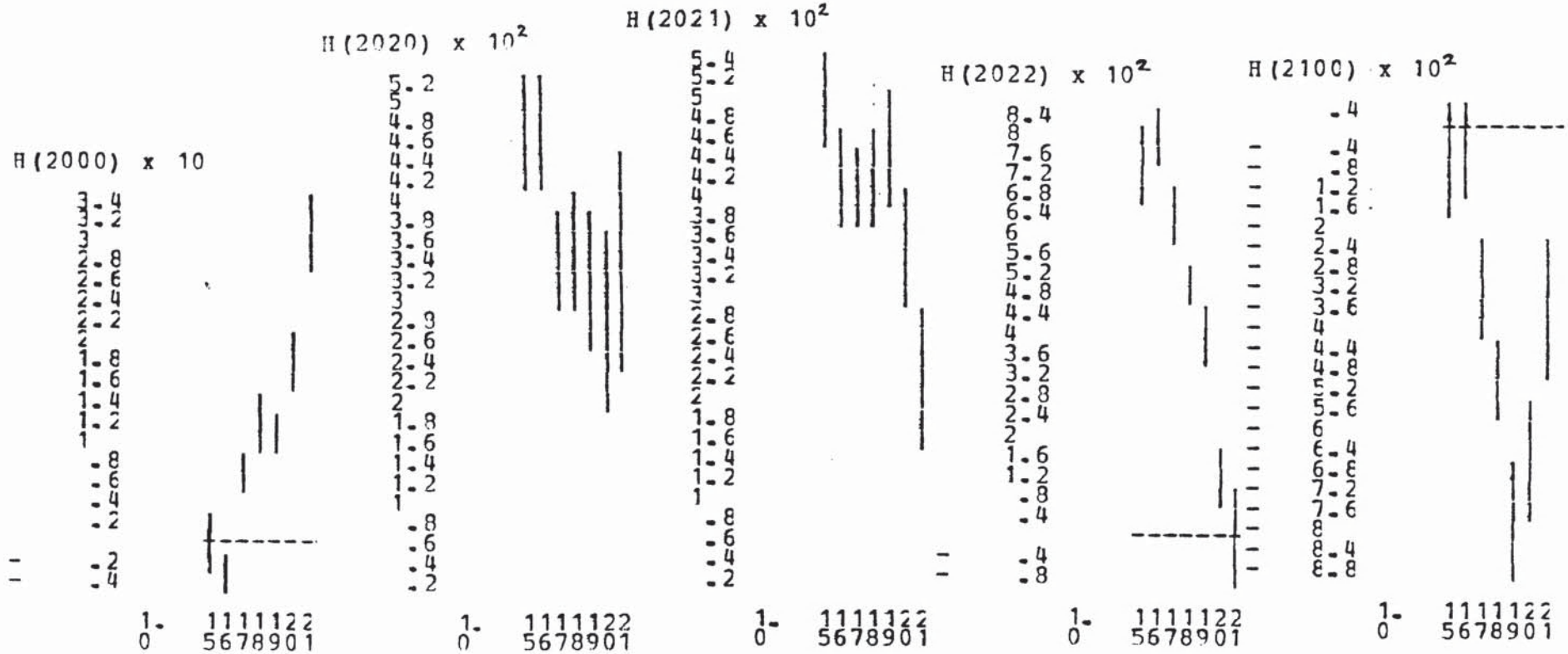

Figure 7.6: Experimental normalised H(2000) - H(2100)

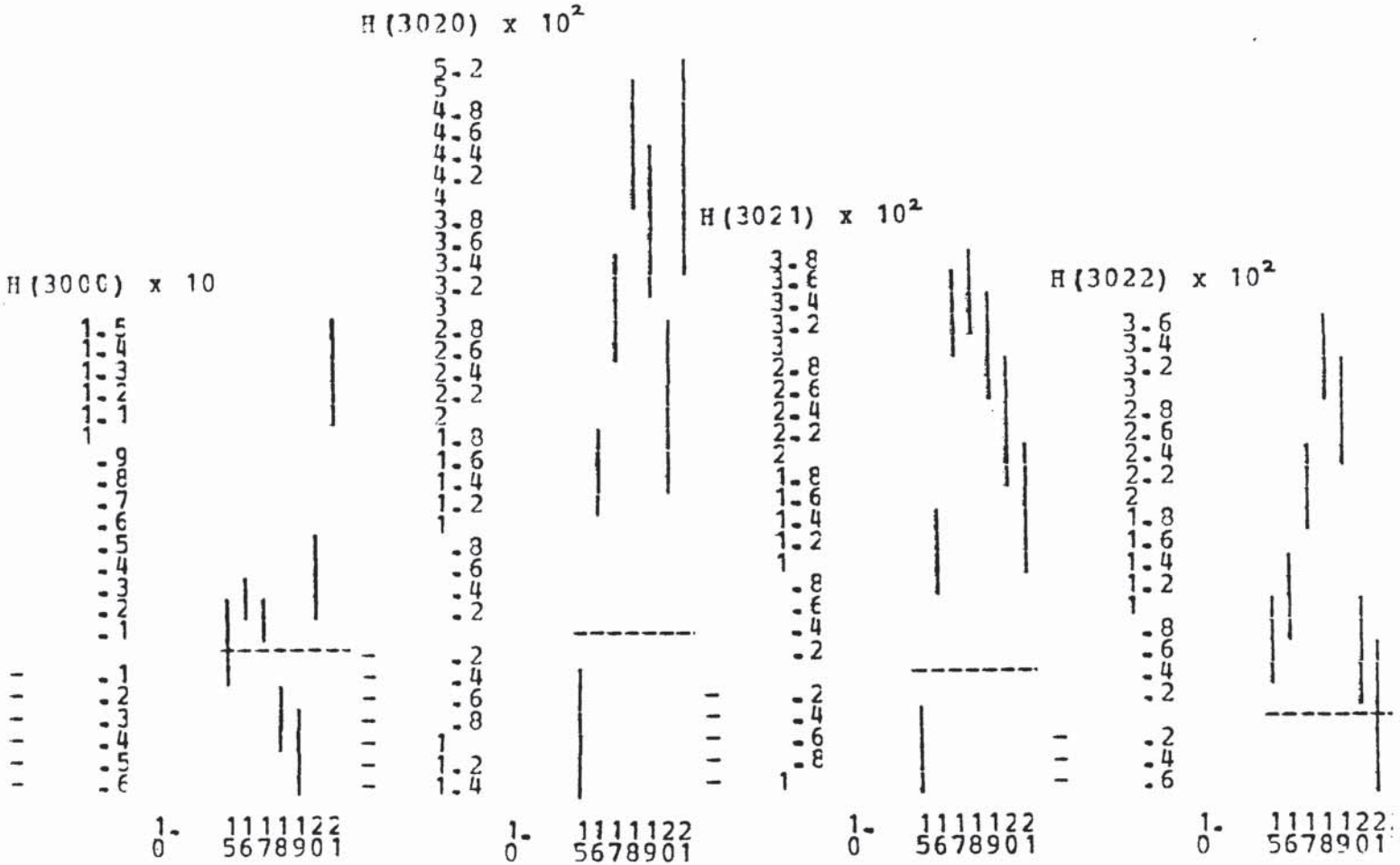

Figure 7.7: Experimental normalised H(3000) - H(3022)

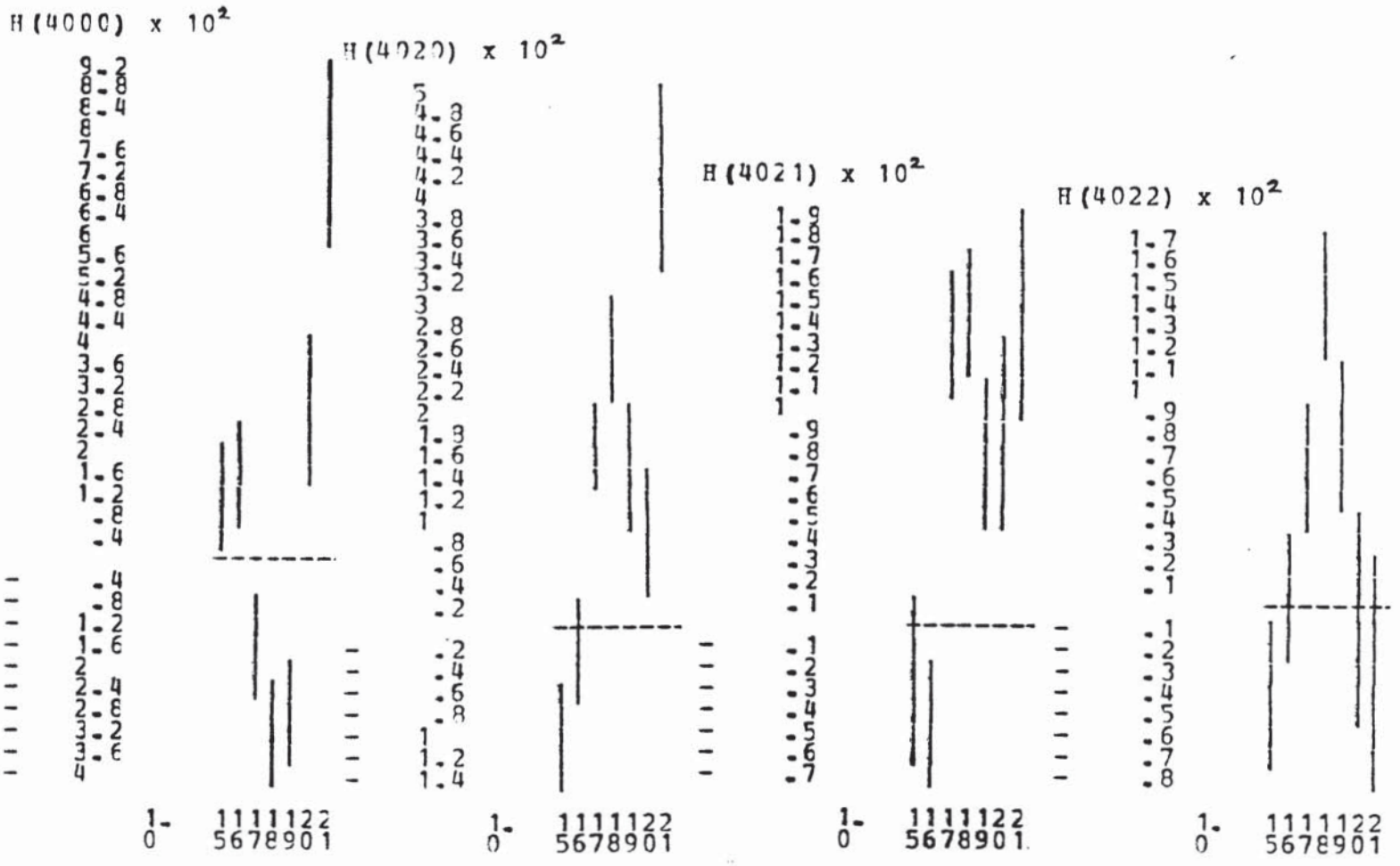

Figure 7.8: Experimental normalised H(4000) - H(4022)

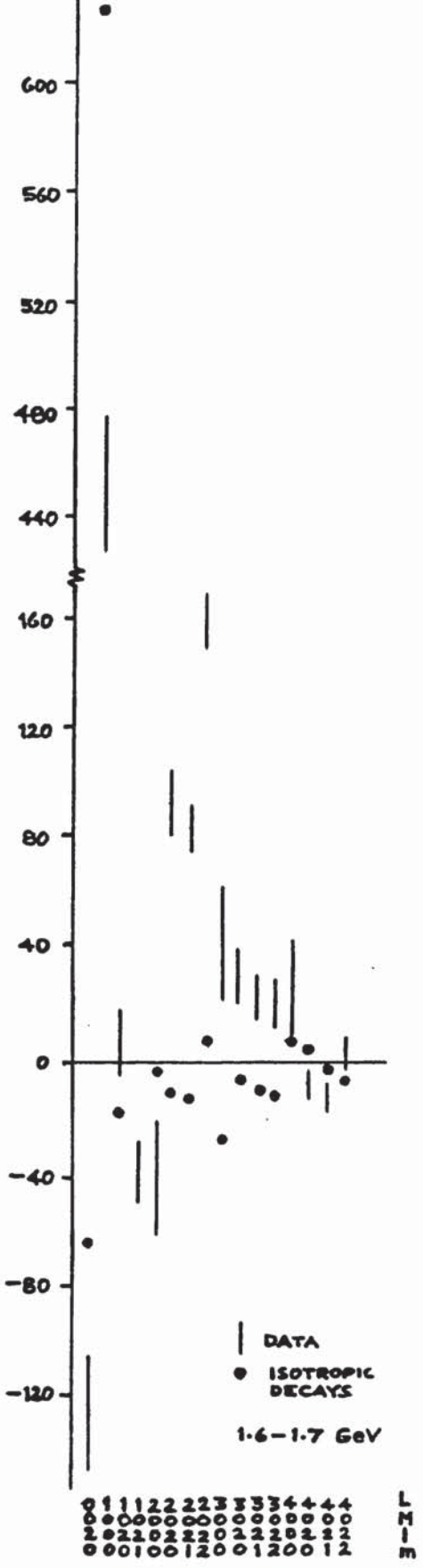

Figure 7.9: Data and acceptance induced moments for mass 1.6 - 1.7 GeV

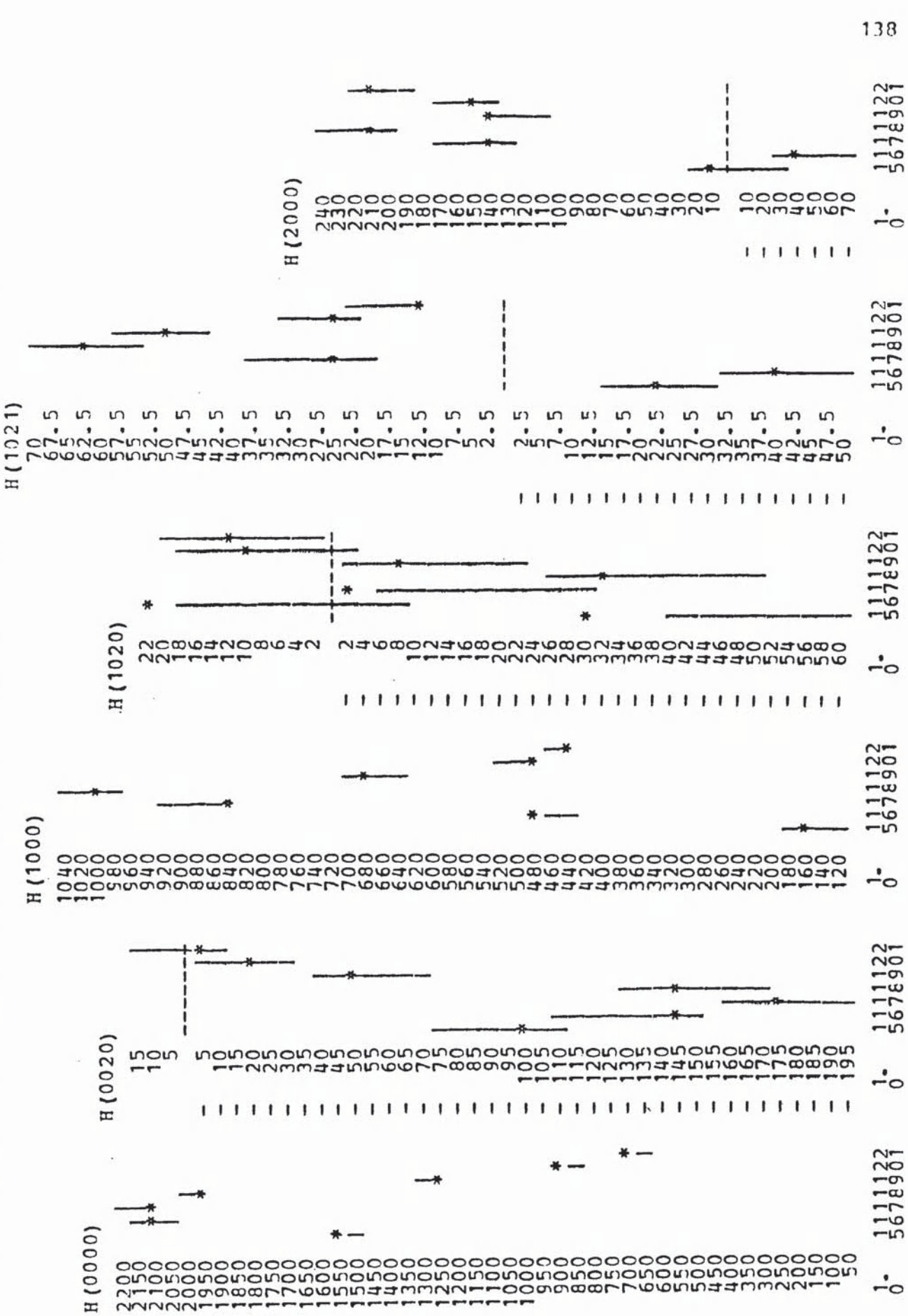

Figure 7.10: Experimental $H(0000) - H(2000)$ + fitted (*) unnormalised

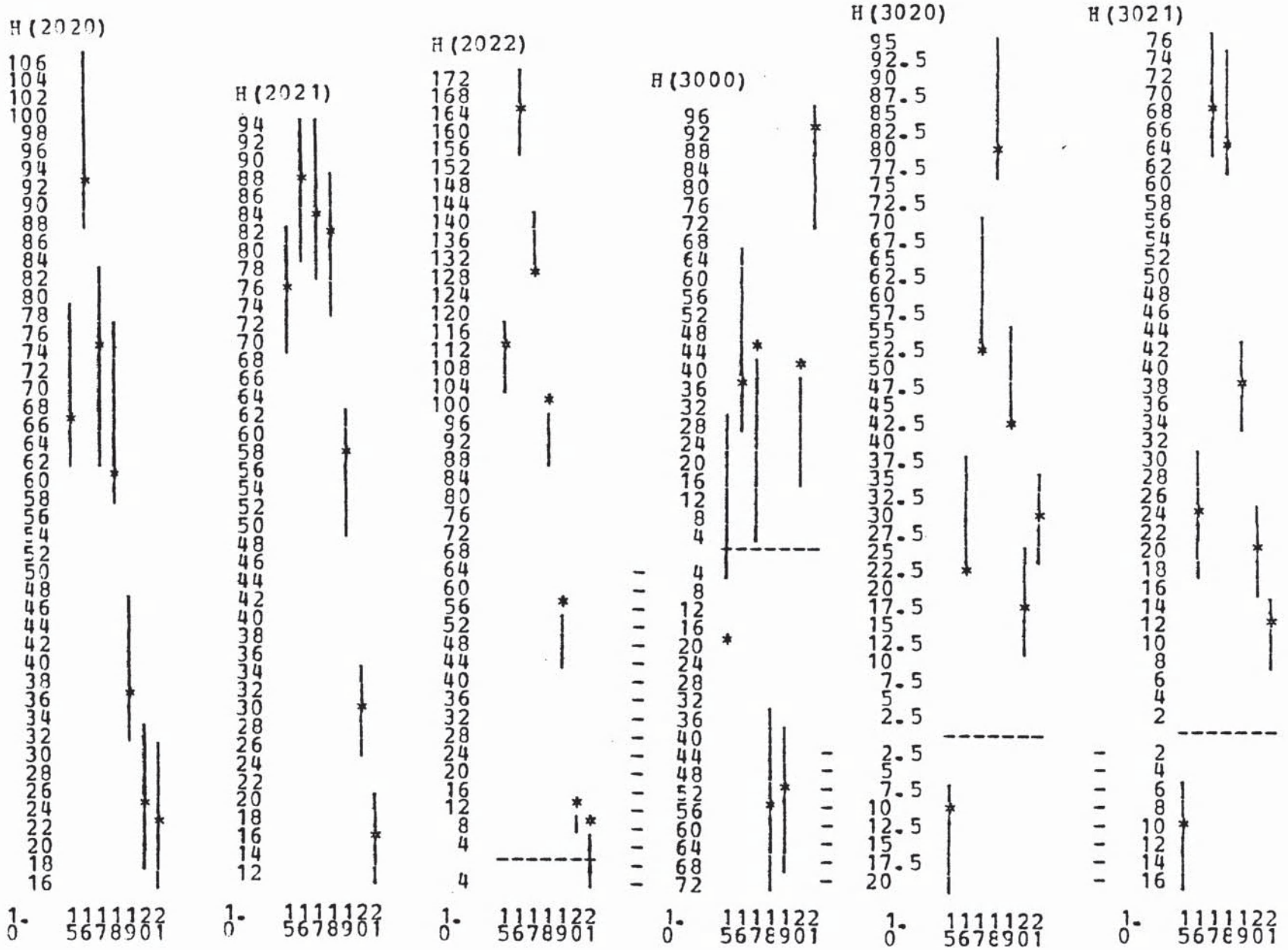

Figure 7.11: Experimental (I) + fitted (*) unnormalised H(2020) - H(3021)

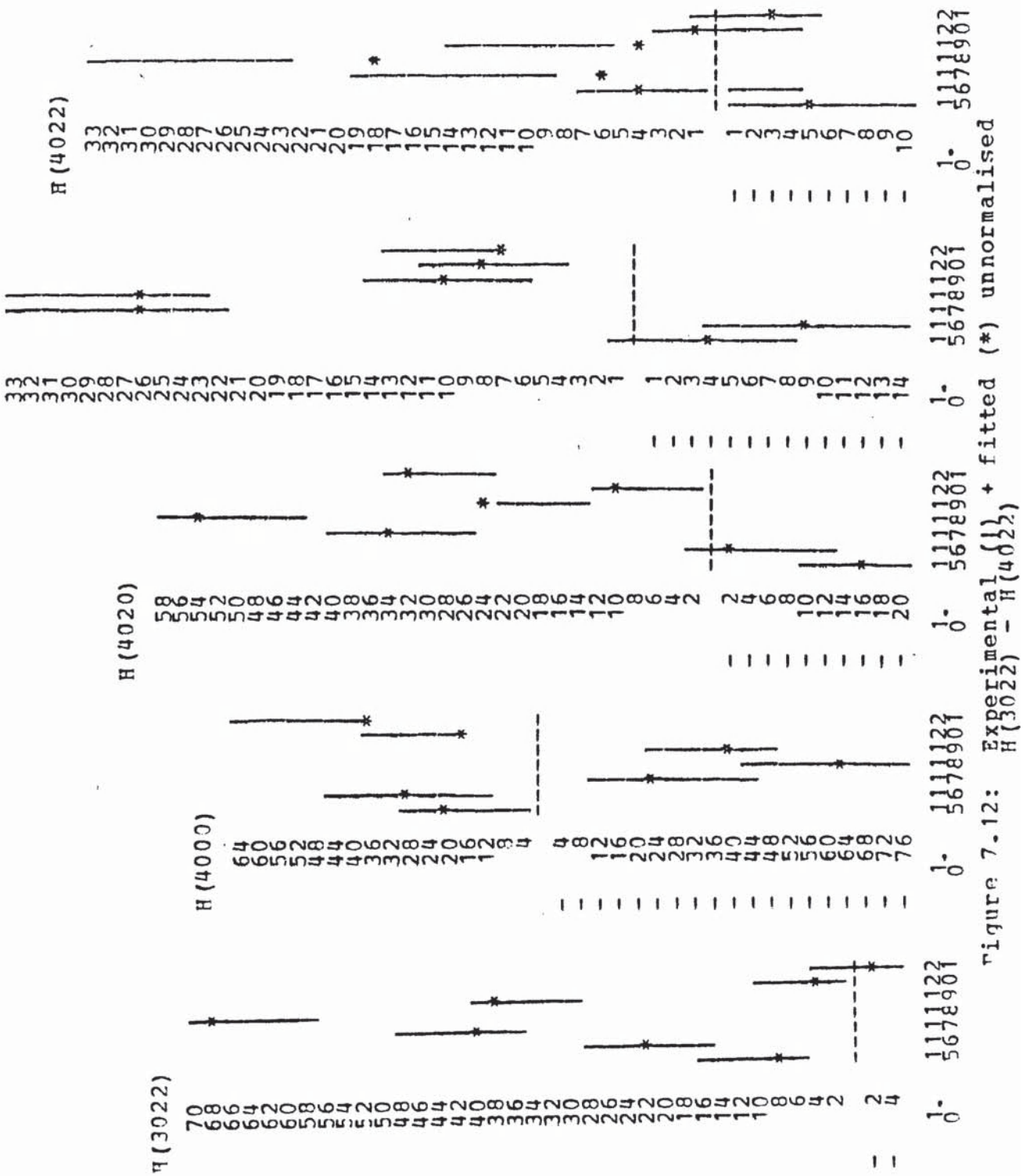

Figure 7.12: Experimental $H(11)$ + fitted (*) unnormalised $H(3022) - H(4022)$

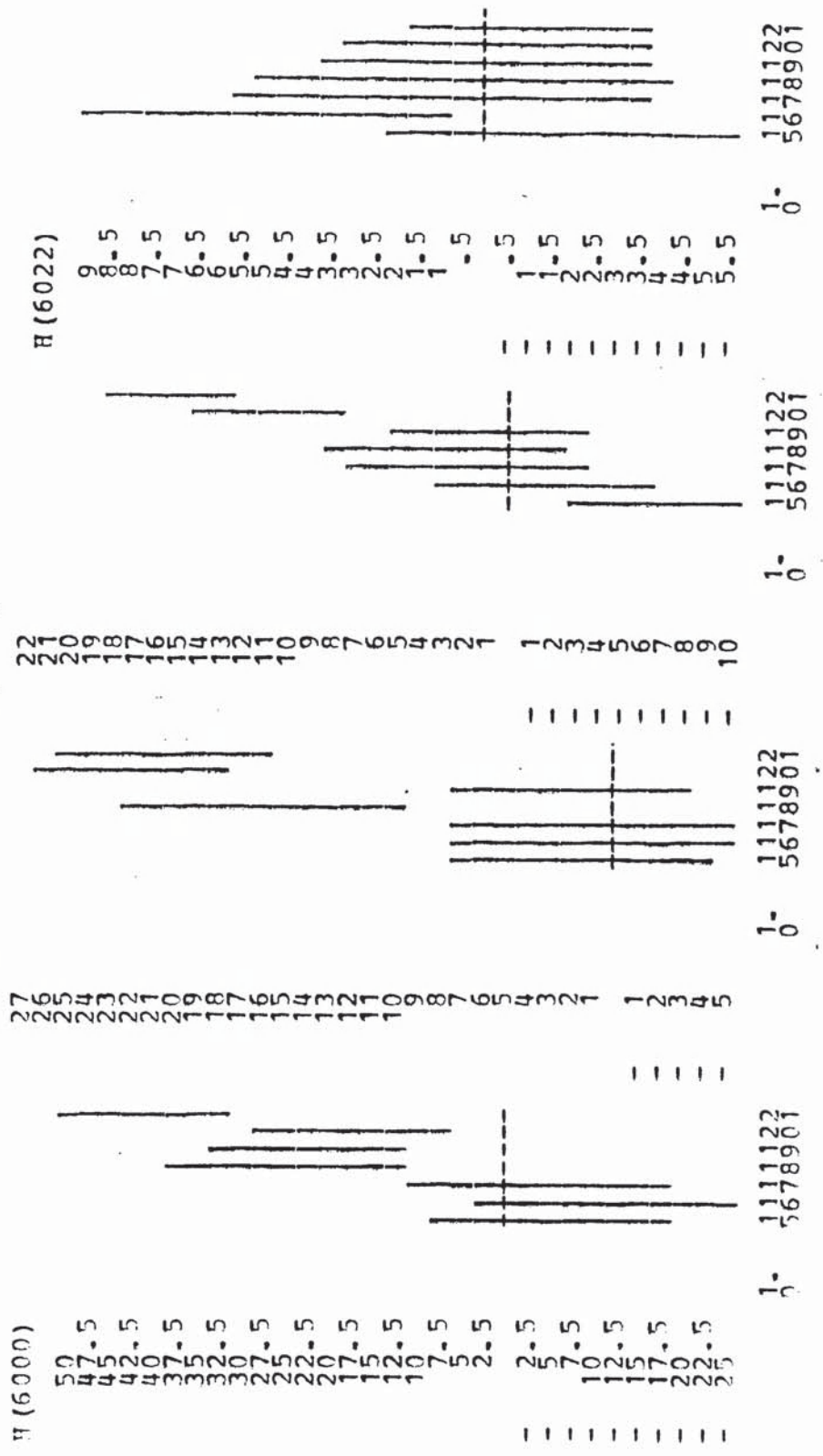

Figure 7.13: Experimental unnormalised H(6000) - H(6022)

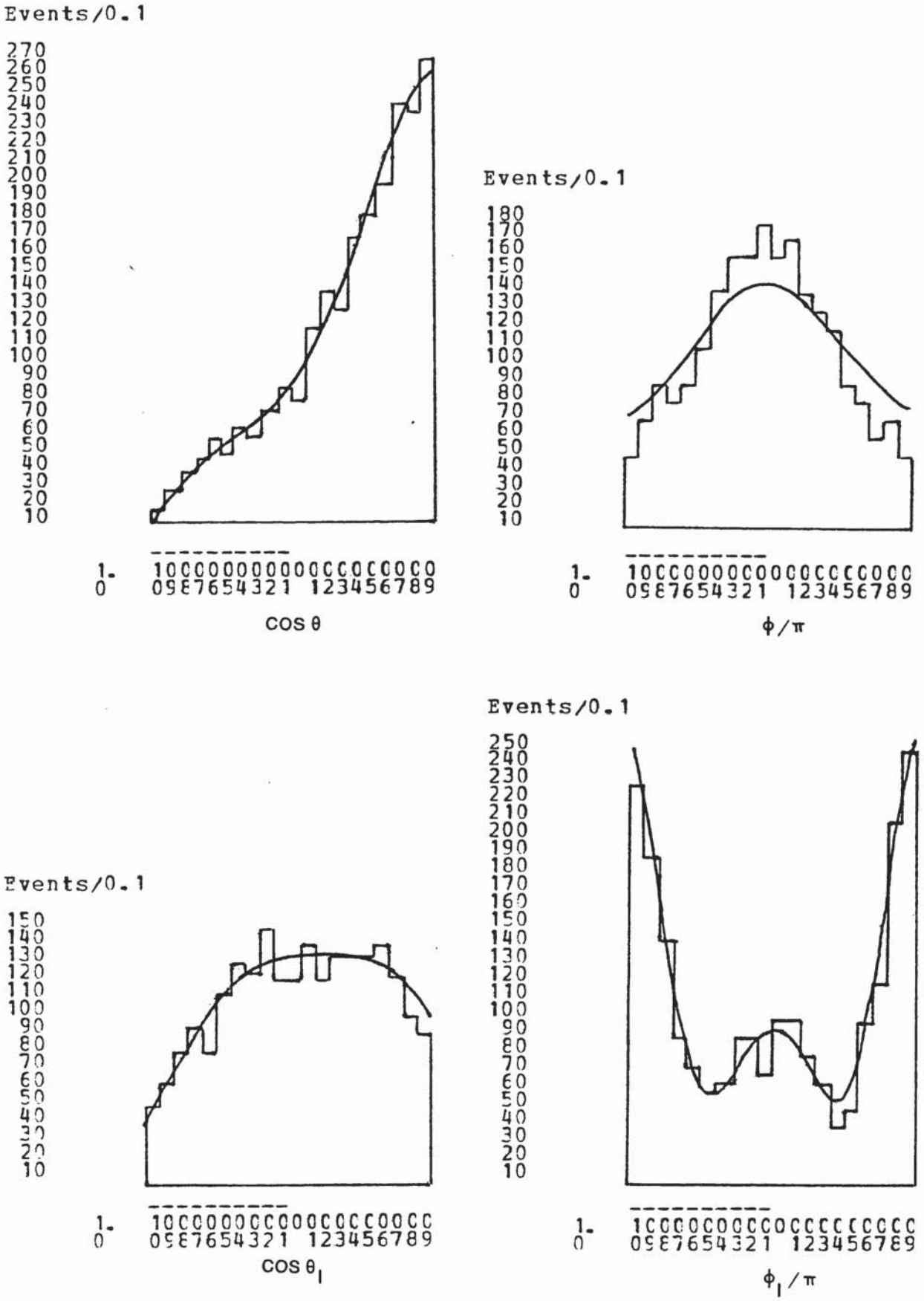

Figure 7.14: Data + simulated decay angles for mass 1.7 - 1.8 GeV

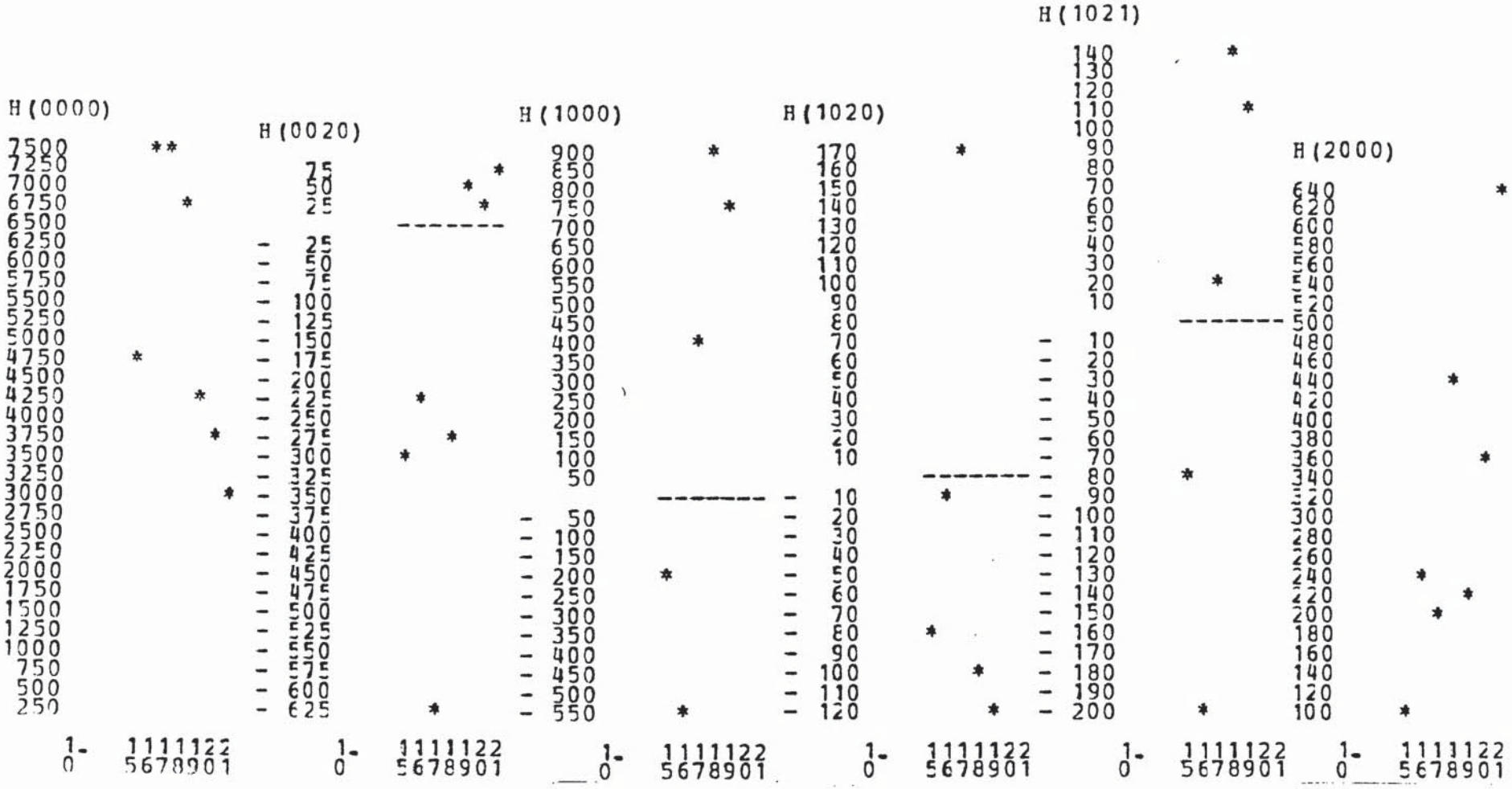

Figure 7.15: Theoretical unnormalised H(0000) - H(2000)

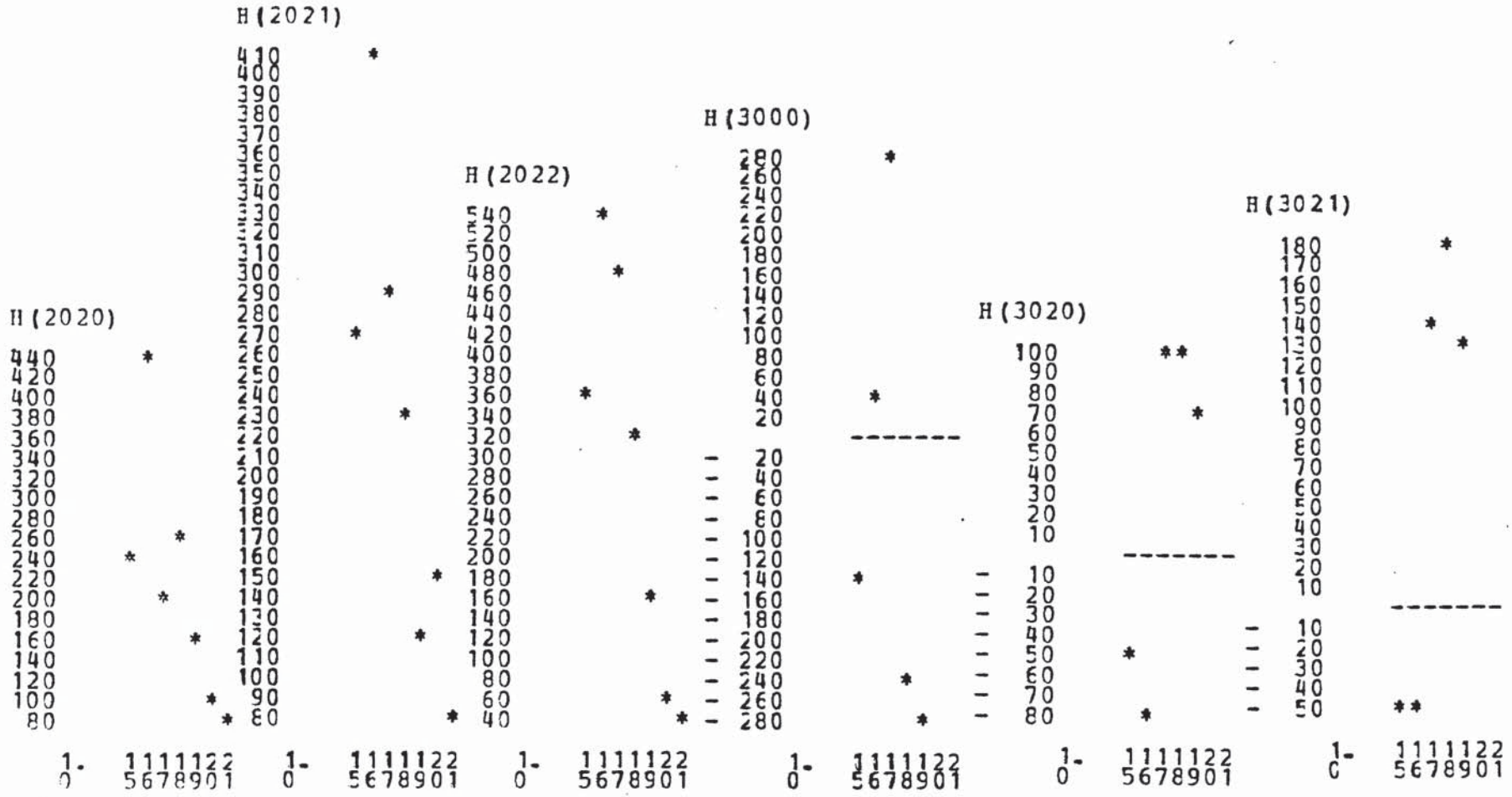

Figure 7.16: Theoretical unnormalised H(2020) - H(3021)

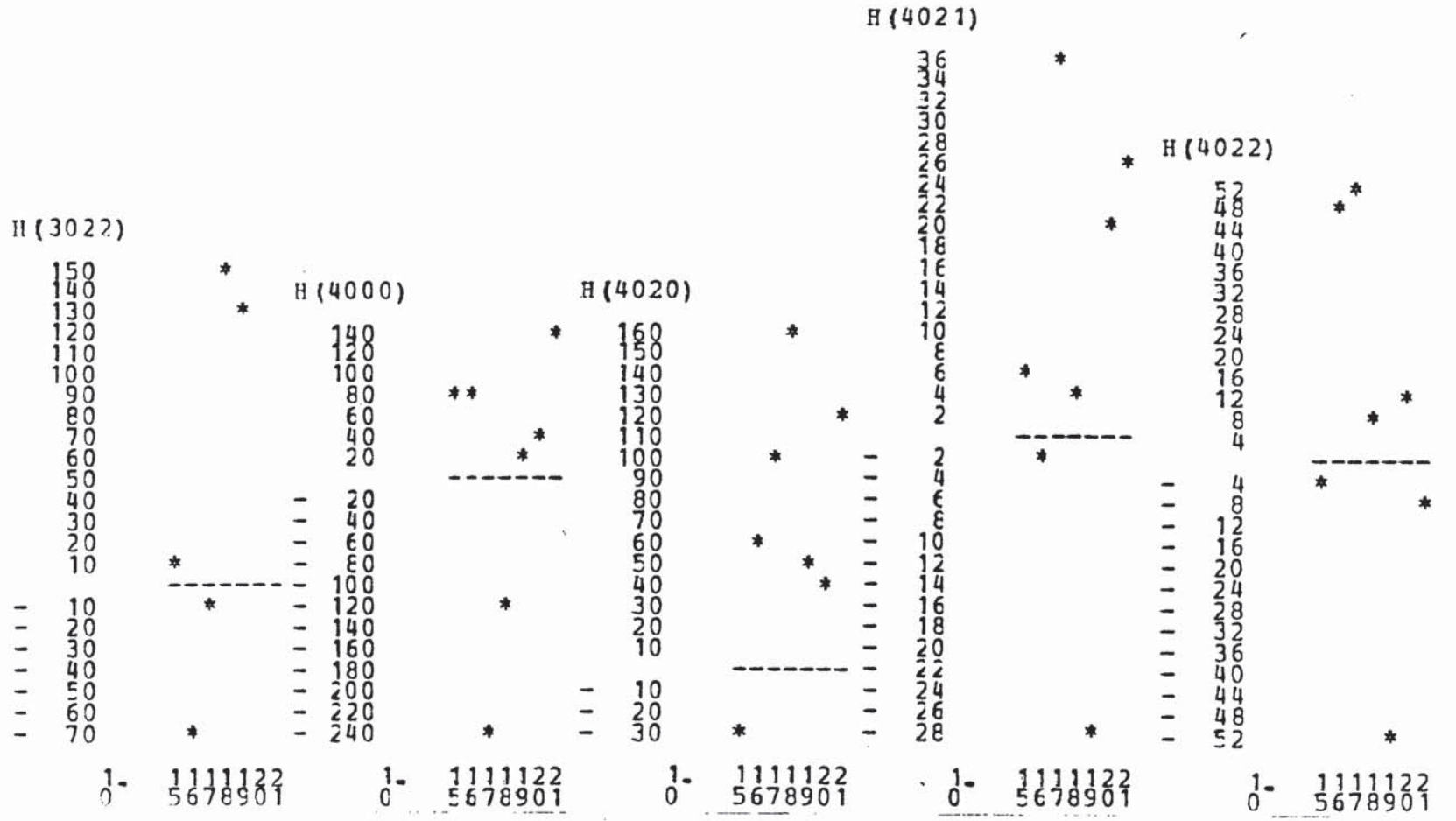

Figure 7.17: Theoretical unnormalised H(3022) - H(4022)

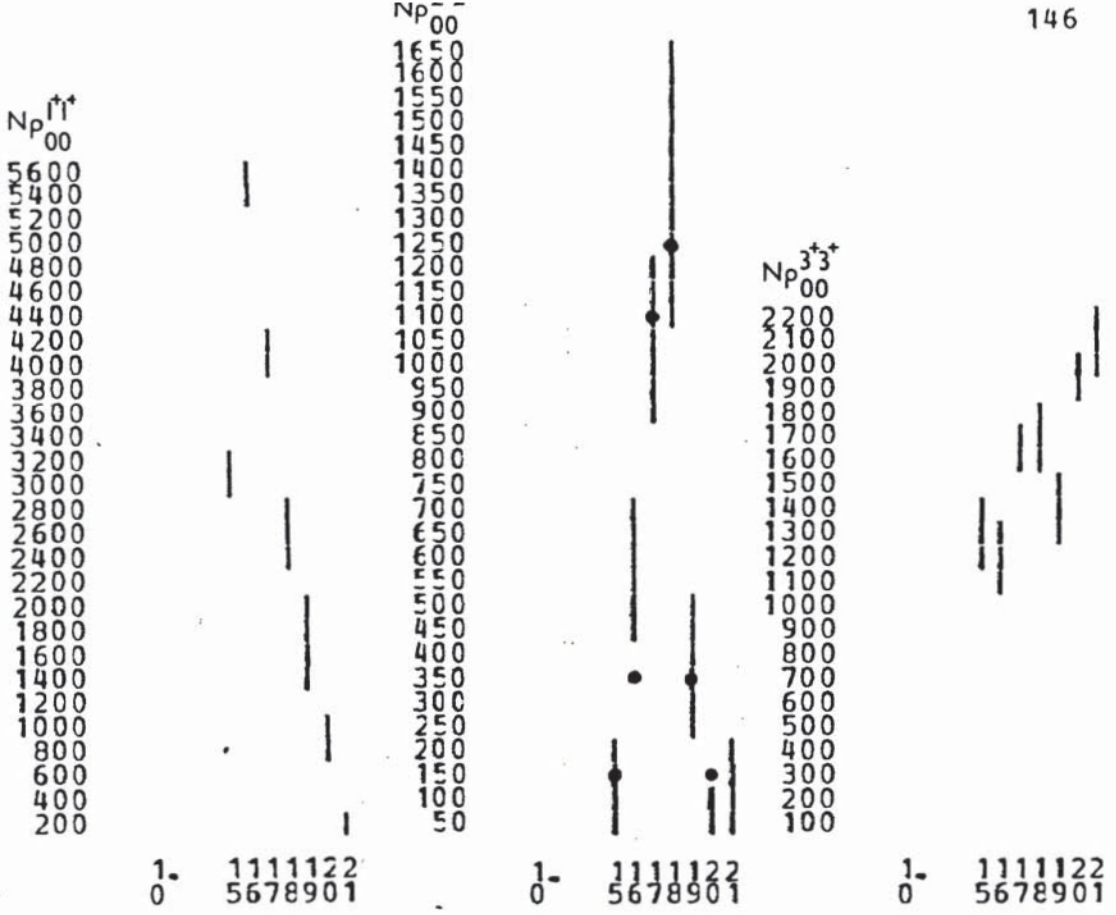

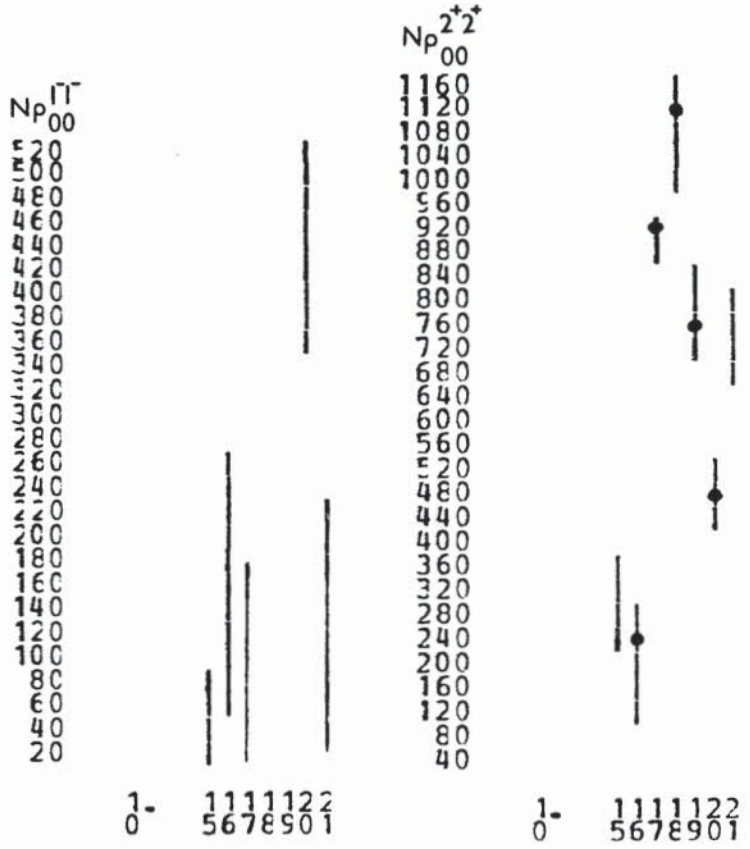

Figure 7.18: Fitted parameters $Np_{00}^{1^+1^+}$ - $Np_{00}^{2^+2^+}$ and fitted Breit-Wigners (•)

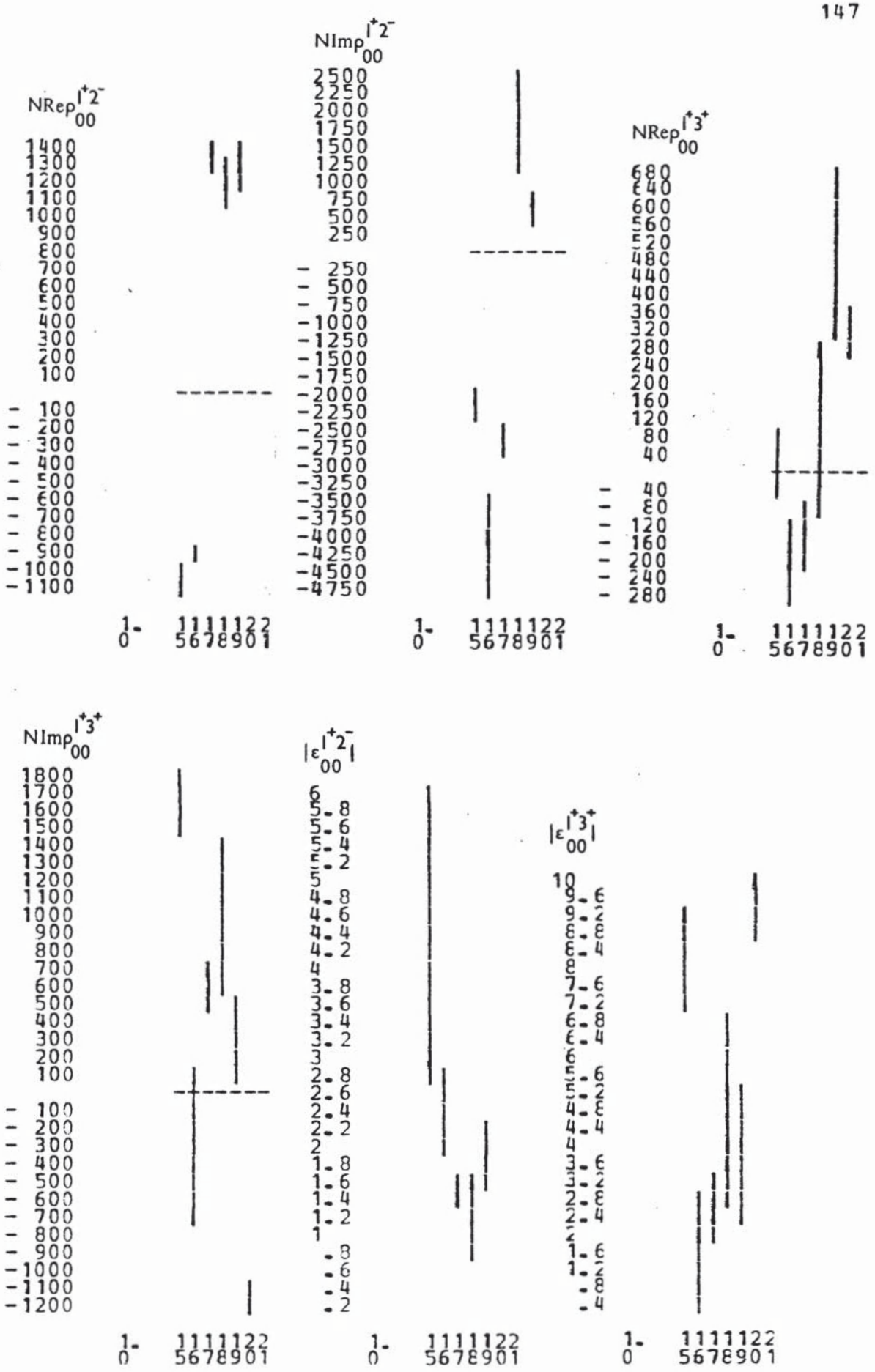

Figure 7.19: Fitted parameters NRe$\rho_{00}^{1^+2^-}$ - NIm$\rho_{00}^{1^+3^+}$ and coherences

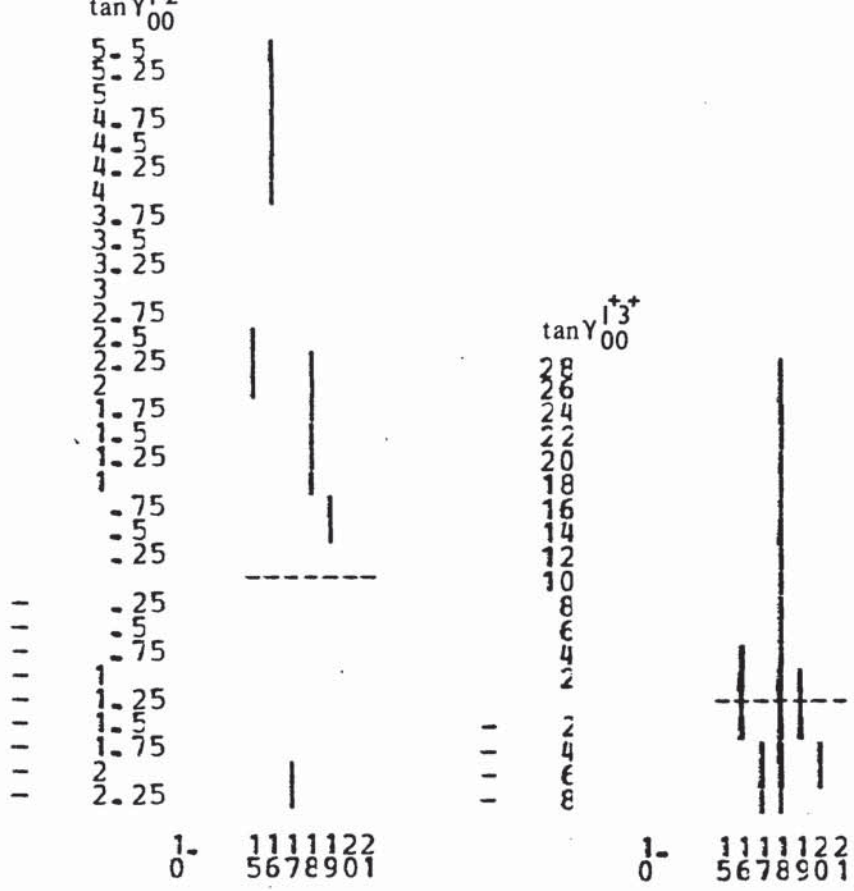

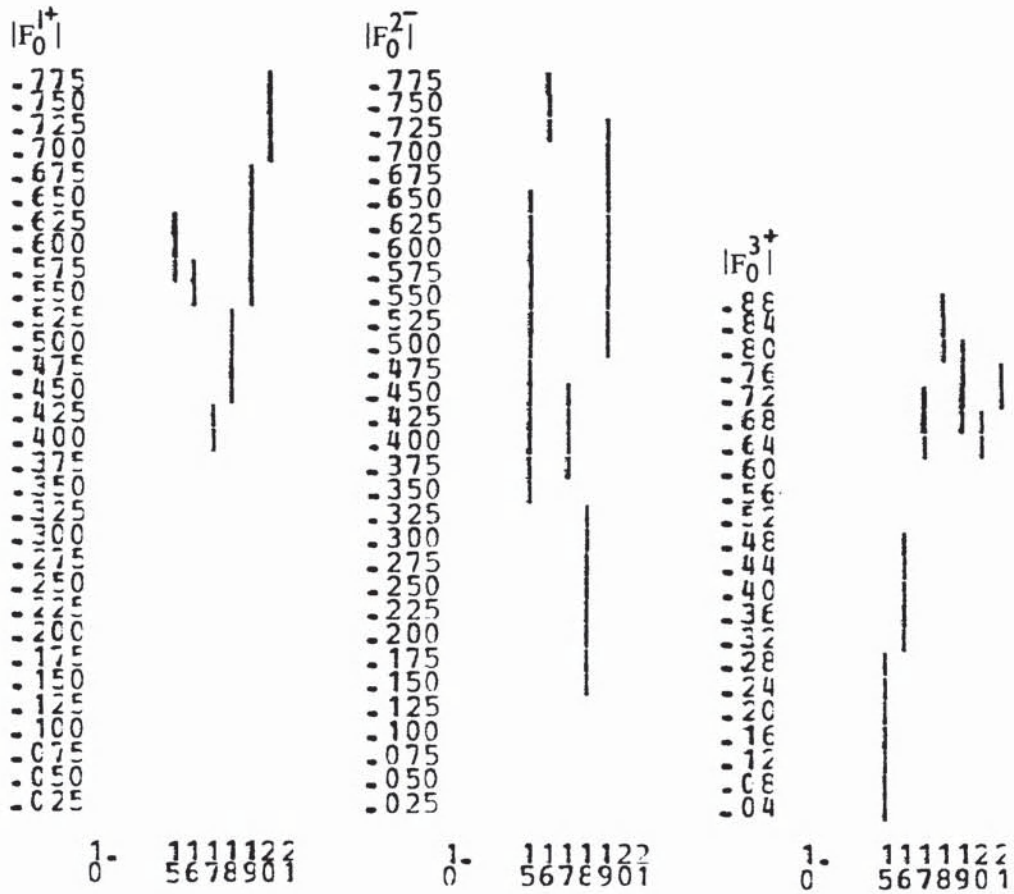

Figure 7.20: Fitted parameters $|F_0^{1+}|$ - $|F_0^{3+}|$ and production phases

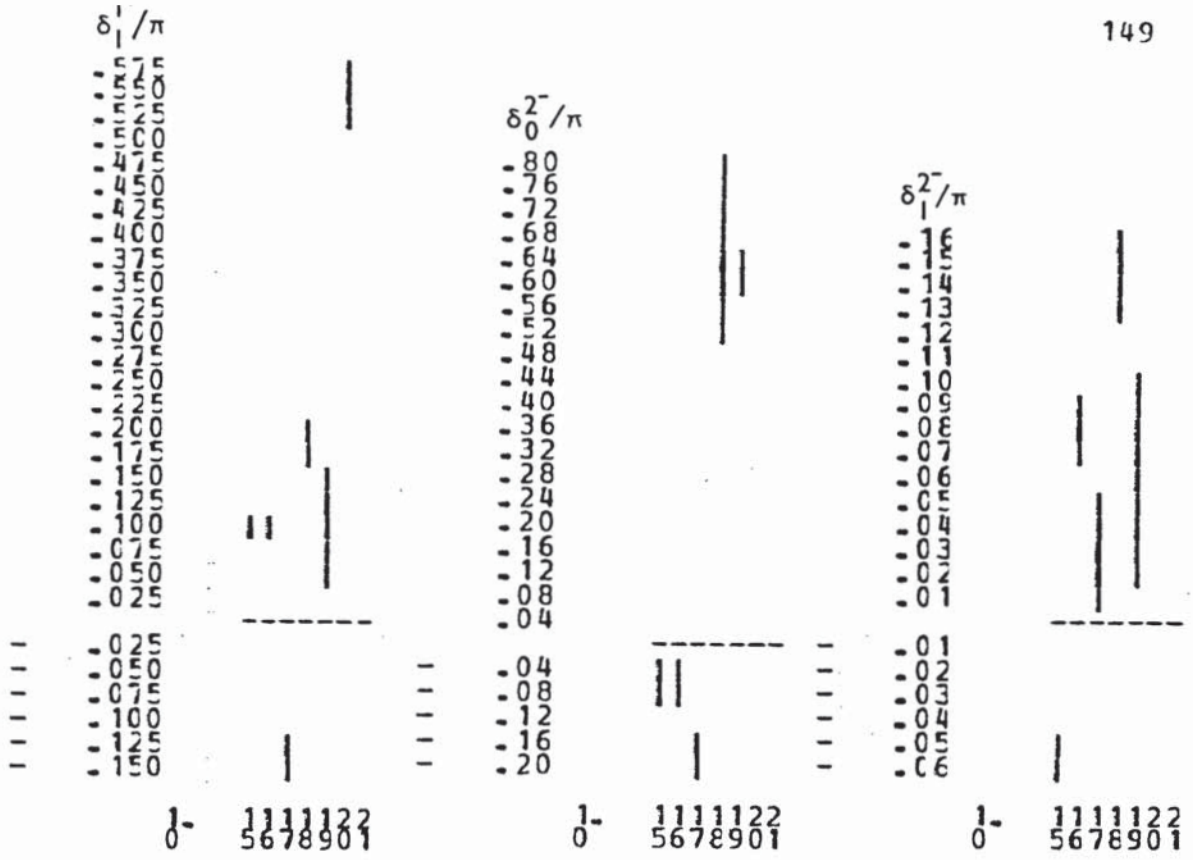

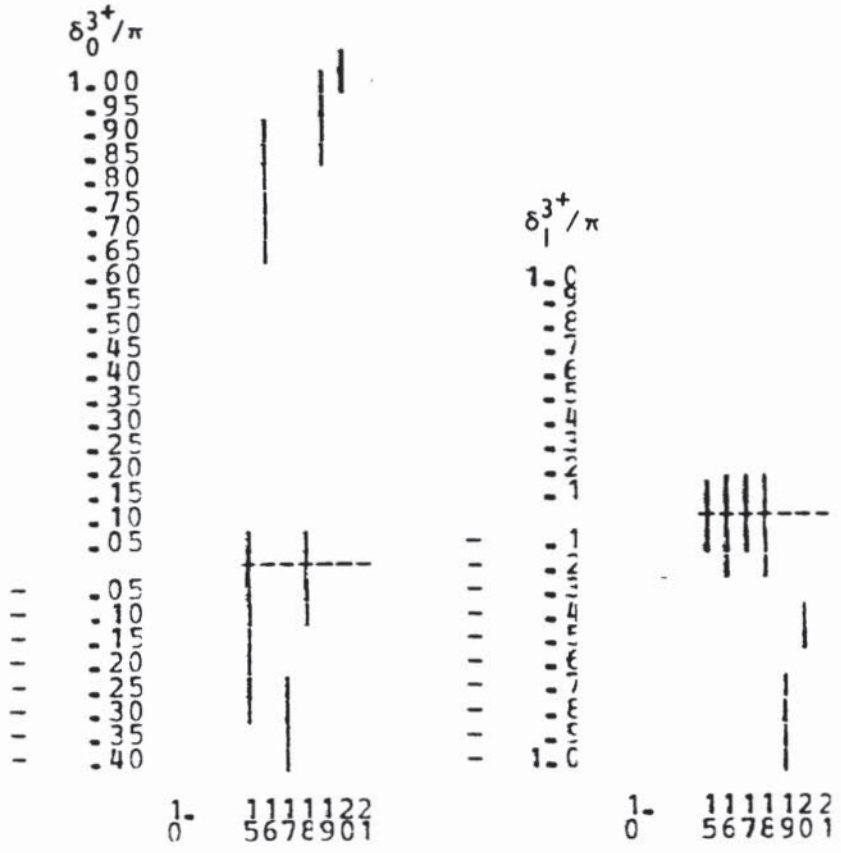

Figure 7.21: Fitted parameters $\delta_1^{1+} - \delta_1^{3+}$

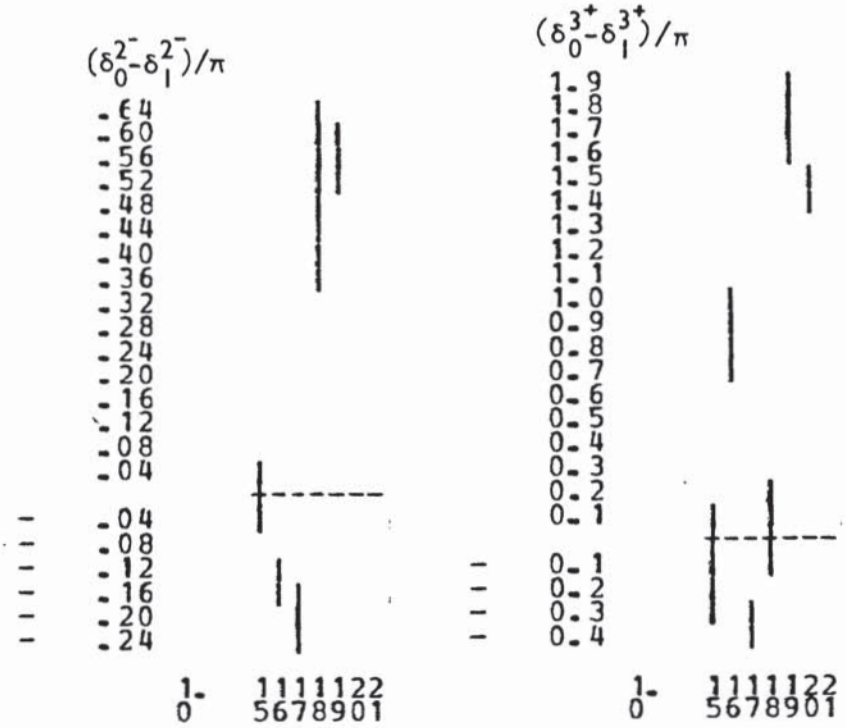

Figure 7.22: Relative decay phases

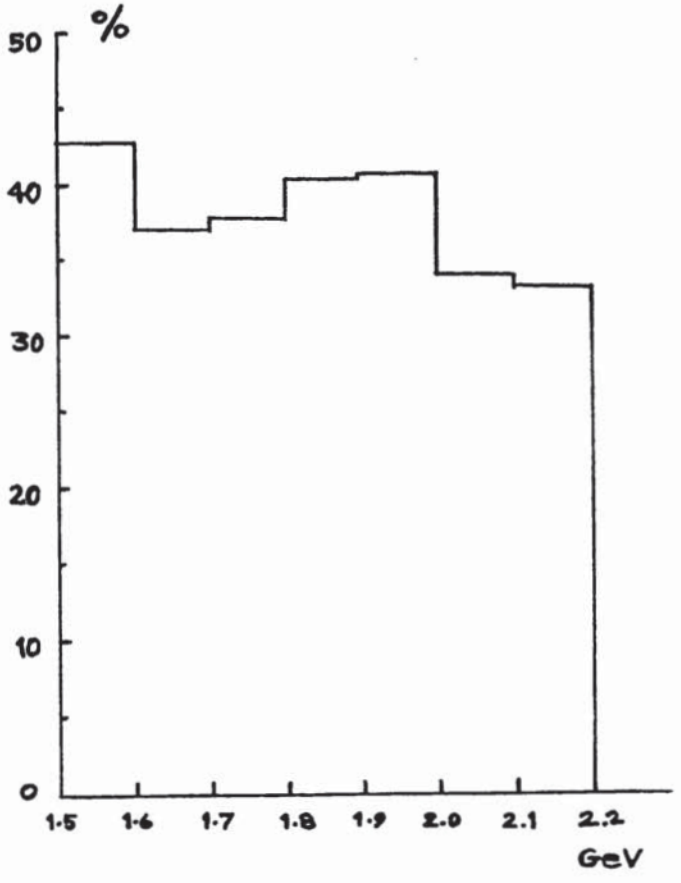

Figure 7.23: Acceptance for ϕK^+

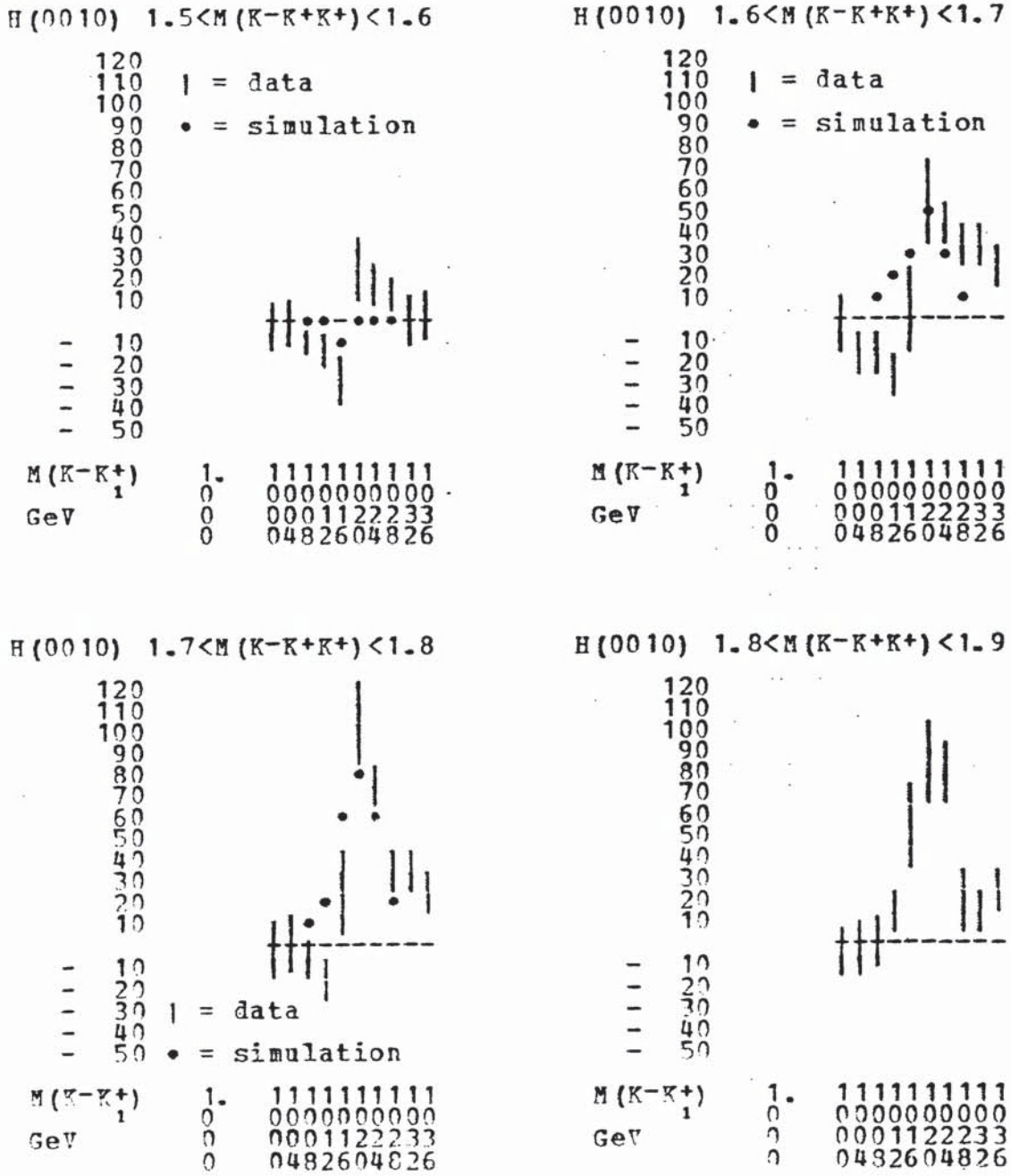

Figure 7.24: Data H(0010)/mass $K^-K^+_1$ for ϕK^+ bins 1-4

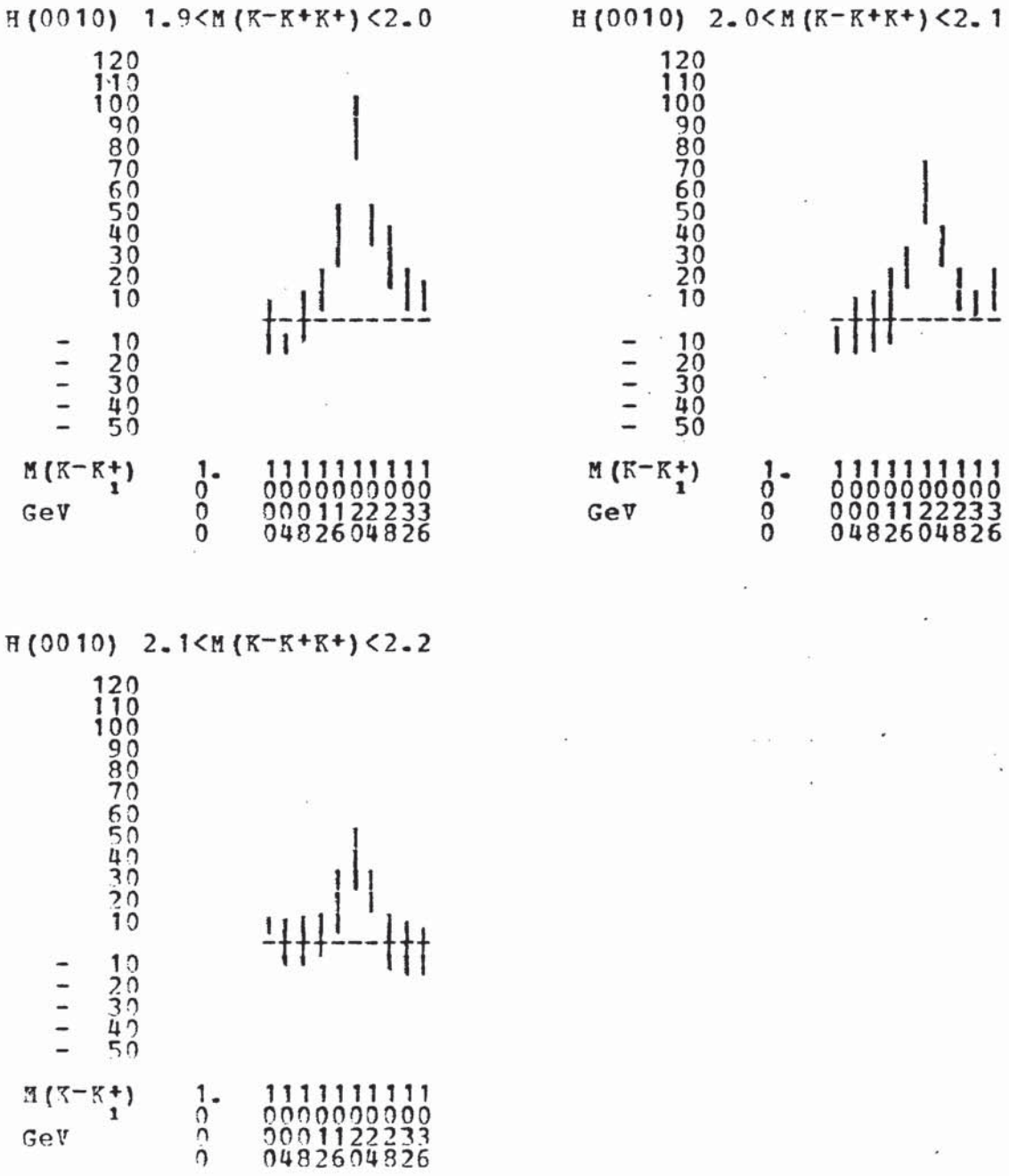

Figure 7.25: Data H(0010)/mass $K^-K^+_1$ for ϕK^+ bins 5-7

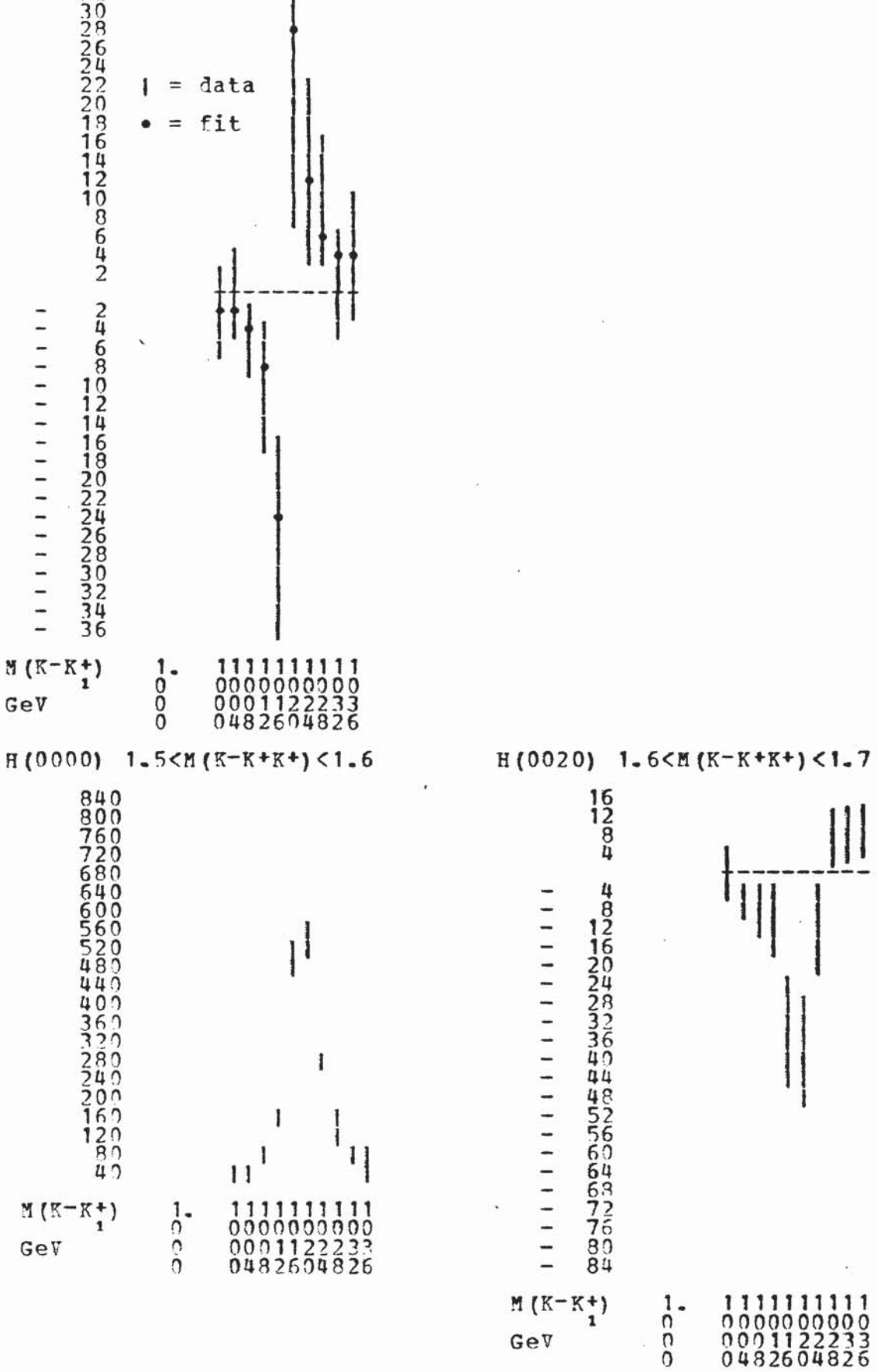

Figure 7.26: Data + fitted H(0010), data H(0000) and H(0020) for ϕK^+ bin 1

Appendix A
SIMULATION OF K^- DECAYS

The probability P that a charged kaon travels a distance greater than d in the laboratory system before decaying is given by

$$P = \exp(-md/pc\tau) \qquad (A.1)$$

where: m = rest mass of kaon (0.4937 GeV)
p = |momentum| of kaon
$c\tau$ = mean life of kaon (370.9 cm)

From reference 2, the main K^- decay mode fractions are:

84% 2-body, including 63% $K^- \rightarrow \mu^- \bar{\nu}$ (A.2)
21% $K^- \rightarrow \pi^- \pi^0$ (A.3)

16% 3-body

yielding muons and pions which could give light in the Cherenkov counter C or have trajectories which could pass through hodoscopes H1 and H2 outside the matrix correlation.

For a K^- which had been generated by the modelling program described in Chapter IV and then tracked through the spectrometer, the following method was used to simulate the effect of the particle decaying:

1. A decay point along the track length was determined using

$$d = -p \ln(P)/(m/c\tau) \qquad (A.4)$$

with a probability P chosen uniformly between 0 and 1. If the simulated decay took place beyond H2, the event was accepted.

2. A random number r1 was chosen uniformly between 0 and 1 to determine whether the decay proceeded by a two-body ($r1 > 0.16$) or three-body ($r1 < 0.16$) mode. It was assumed that all three-body decays were rejected by the trigger.

3. A random number r2 was chosen uniformly between 0 and 1 to determine whether the decay products included a μ^- (r2 > 0.33) or a π^- (r2 < 0.33).
4. If the decay point lay inside the spark chambers, the event was rejected.
   The direction of the track outside the Omega field was determined from its intersections with the hodoscopes H1 and H2.
   If the decay point lay inside the field, but beyond the spark chambers: the linear part of the track outside the field was intersected with the edge of the field and, using an average field value to follow the circular part of the track inside the field, the direction of the track at the decay point was determined.
5. The K^- was decayed in its rest frame such that a μ^- or π^- as required was produced uniformly in solid angle. The decay particle was transformed into the laboratory system, and its momentum components calculated. A decay particle produced inside the field was tracked to the edge of the field, and its direction found.
6. Intersections of the linear part of the decay track outside the field with H1 and H2 were determined. If the decay track lay outside the H1/H2 matrix correlation, the event was rejected.
7. If the decay track had |momentum| < 3 GeV, the event was accepted.
   If the decay track had |momentum| > 3 GeV, and the Cherenkov mirrors (see figure 2.4) were unable to collect the light produced, the event was accepted.

Appendix B

LPS ANALYSIS, RESONANCE PRODUCTION AND DECAY

B.1 LONGITUDINAL PHASE SPACE ANALYSIS

As suggested by Van Hove [60], the description of multiparticle final states may be simplified by assuming that the transverse momenta of the particles produced are small and are largely independent of the incident beam energy. At high energies therefore, many characteristic features of the final state phase space are manifest in the longitudinal phase space (LPS) distributions of the outgoing particles. Considering an n body final state of total CMS energy W, there are two constraint equations:

$$\sum_1^n q_i = 0, \qquad \sum_1^n \sqrt{(m_i^2+r_i^2+q_i^2)} = W$$

where: m_i = rest mass of particle i

q_i = CMS longitudinal momentum of particle i

r_i = CMS transverse momentum of particle i

If the transverse momenta r_i are neglected in the high energy limit, the final state may be described by (n-2) variables.

When all $q_i^2 >> (m_i^2+r_i^2)$, the second constraint equation becomes

$$\sum_1^n |q_i| = W$$

which defines a polyhedron.

For a three-body final state (n=3), the longitudinal momenta (q_1, q_2, q_3) may be plotted in a plane with axes at 120° to each other. Figure B.1 shows the so-called 'Van Hove plot' which is bounded by a hexagon. The angle ω is chosen as the one variable necessary to describe the final three-body phase space.

Although in practice the transverse momenta and masses of the particles produced in a reaction such as

$$K^+p \rightarrow \bar{\Lambda}(1520)\, p_f\, p_s$$

may not be negligible relative to the longitudinal momenta, the Van Hove plot is still useful in indicating possible correlations between the particles. The event distribution as a function of the angle ω may be of assistance in separating the processes shown in figure B.2.

B.2 BREIT-WIGNER RESONANCE FORMULAE

Following the discussion given in reference 61, the Breit-Wigner shape used to describe the production of a resonance R decaying to particles D_1 and D_2 was

$$BW = m^2\Gamma_o\Gamma/((m^2-m_o^2)^2+\Gamma^2 m_o^2) \qquad (B.1)$$

where: m = mass of D_1 and D_2

m_o = mass of R

$\Gamma = \Gamma_o (q/q_o)^{2l+1}$

where: Γ_o = width of R

q = momentum of D_1 or D_2 in the rest frame of D_1 and D_2

q_o = value of q at $m = m_o$

l = angular momentum of decay

The resonant phase shift δ was given by

$$\tan\delta = m_o\Gamma/(m_o^2-m^2) \qquad (B.2)$$

The true shape of a resonance is modified by the experimental resolution (see appendix C). If the resolution can be described by an analytic function ER(m) with some width Γ_r, the resonance shape BW'(m) observed experimentally is then given [28] by the convolution integral

$$BW'(m) = \int_{-\infty}^{+\infty} BW(m')\ ER(m-m')\ dm' \qquad (B.3)$$

Assuming the presence of a polynomial background term, the observed mass distribution I(m) is described by:

$$I(m) = rBW'(m) + a + bm + cm^2 + \ldots \qquad (B.4)$$

where: r = fraction of resonance present

a,b,c = fractions of background terms present

The parameters $\{m_o, \Gamma_o\}$ of a resonance were determined by using the program MINUIT [59] to fit the experimental mass spectrum in the resonance region to the above expression. The parameters $\{m_o, \Gamma_o, \Gamma_r, r, a, b, c..\}$ were varied and the values determined for which the chi-squared function given by

$$\chi^2 = \sum_{\substack{\text{bins} \\ k}} (I(m) - n_k)^2 / e_k^2$$

where: n_k = number of events observed in mass bin k

e_k = error on number of events observed in bin k (usually $\sqrt{n_k}$)

was a minimum.

B.3 DECAY ANGULAR DISTRIBUTIONS

Consider the production and decay of a resonance R of spin J in the process shown in figure B.3. The resonance R (helicity Λ) decays to two particles a and b (helicities λ_a, λ_b), and the particle or combination of particles produced opposite R in the overall CMS is denoted by c. The decay angles (θ, ϕ) of R in the t-channel helicity (TCH) or Jackson [62,61] frame for R are defined in figure B.3, where the particle a has been chosen as analyser. Note that the vectors shown correspond to the momenta of particles in the rest frame of R, and in particular that the incident beam direction and the normal to the production plane define the z and y-axes respectively.

The decay angular distribution $W(\theta, \phi)$ may be calculated [62,63] by summation over the helicity states of the resonance and the decay products thus:

$$W(\theta,\phi) = \left(\frac{2J+1}{4\pi}\right) \sum_{\substack{\Lambda\Lambda' \\ \lambda_a\lambda_b}} \rho_{\Lambda\Lambda'} \, D^{J}_{\Lambda\lambda}(\phi,\theta,0) \, D^{J}_{\Lambda'\lambda}(\phi,\theta,0) \, |F_{\lambda_a\lambda_b}|^2 \qquad (B.5)$$

where: $\lambda = \lambda_a - \lambda_b$

$\rho_{\Lambda\Lambda'}$ are the elements of the spin density matrix of the resonance R [64]

$D^{J}_{\Lambda\lambda}$ are the elements of the rotation matrix [65]

$F_{\lambda_a\lambda_b}$ are the helicity decay amplitudes [65]

$F(\theta,\phi)$ is a normalised distribution if

$$\sum_{\Lambda} \rho_{\Lambda\Lambda} = 1, \qquad \sum_{\lambda_a\lambda_b} |F_{\lambda_a\lambda_b}|^2 = 1$$

The decay angular distributions for the following parent and decay product spins have been calculated using equation B.5 (see also [62,61]):

$\underline{J = 1 \rightarrow 0 + 0}$

$$W(\theta,\phi) = \frac{3}{4\pi}\{\tfrac{1}{2}(1-\rho_{00}) + \tfrac{1}{2}(3\rho_{00}-1)\cos^2\theta - \rho_{1-1}\sin^2\theta\cos 2\phi - \sqrt{2}\,\mathrm{Re}\,\rho_{10}\sin 2\theta\cos\phi\} \qquad \text{(B.6)}$$

$\underline{J = 2 \rightarrow 0 + 0}$

$$W(\theta,\phi) = \frac{15}{16\pi}\{3\rho_{00}(\cos^2\theta-\tfrac{1}{3})^2 + 4\rho_{11}\sin^2\theta\cos^2\theta + \rho_{22}\sin^4\theta - 2\cos\phi\sin 2\theta[\mathrm{Re}\,\rho_{21}\sin^2\theta + \sqrt{6}\,\mathrm{Re}\,\rho_{10}(\cos^2\theta-\tfrac{1}{3})] - 2\cos 2\phi\sin^2\theta[2\rho_{1-1}\cos^2\theta - \sqrt{6}\,\mathrm{Re}\,\rho_{20}(\cos^2\theta-\tfrac{1}{3})] + 2\,\mathrm{Re}\,\rho_{2-1}\cos 3\phi\sin^2\theta\sin 2\theta + \rho_{2-2}\cos 4\phi\sin^4\theta\} \qquad \text{(B.7)}$$

$\underline{J = 3/2 \rightarrow 1/2 + 0}$

$$W(\theta,\phi) = \frac{3}{4\pi}\{\tfrac{1}{6}(1+4\rho_{33}) + \tfrac{1}{2}(1-4\rho_{33})\cos^2\theta - \tfrac{2}{\sqrt{3}}\mathrm{Re}\,\rho_{3-1}\sin^2\theta\cos 2\phi - \tfrac{2}{\sqrt{3}}\mathrm{Re}\,\rho_{31}\sin 2\theta\cos\phi\} \qquad \text{(B.8)}$$

where: $\rho_{11} \equiv \rho_{\frac{1}{2}\frac{1}{2}}$, etc.

The properties of the density matrix arising from positivity, hermiticity and parity conservation in the production plane are, respectively [50]:

$$\begin{cases} |\rho_{\Lambda\Lambda'}|^2 \le \rho_{\Lambda\Lambda}\rho_{\Lambda'\Lambda'} \\ \rho_{\Lambda\Lambda'} = \rho^*_{\Lambda'\Lambda} \\ \rho_{\Lambda\Lambda'} = (-1)^{\Lambda-\Lambda'}\rho_{-\Lambda-\Lambda'} \end{cases}$$

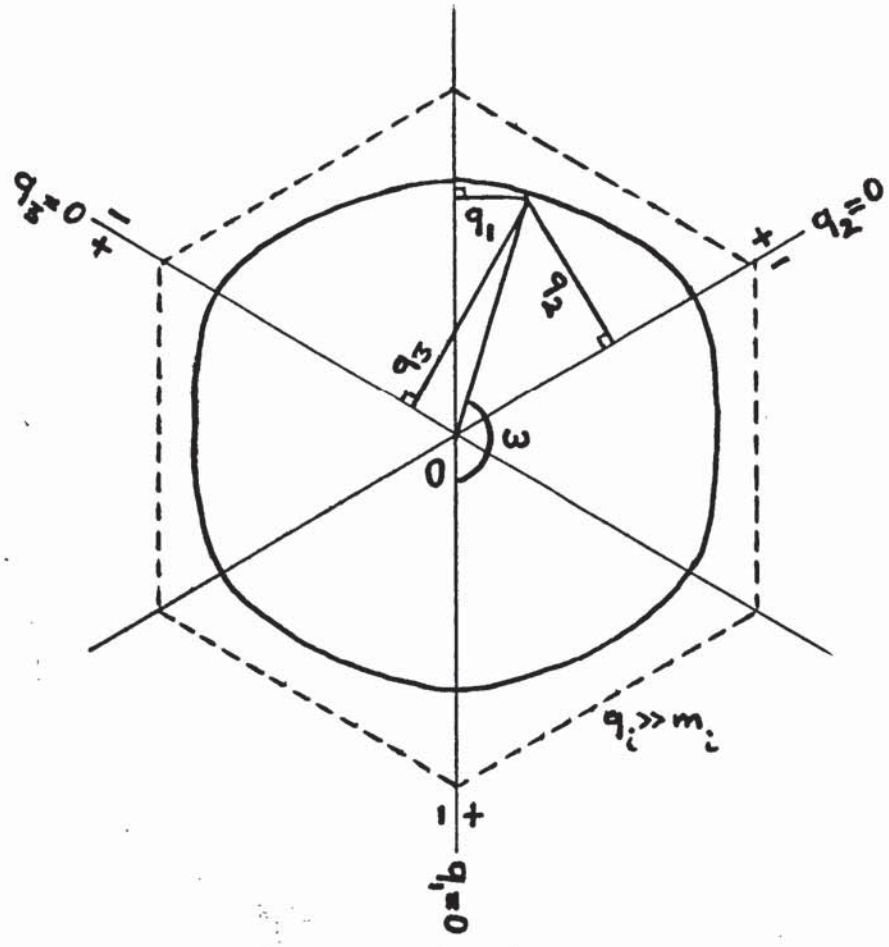

Figure B.1: Van Hove plot for 3-body final state

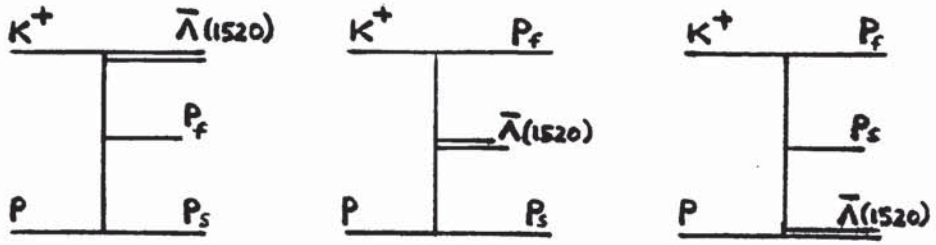

Figure B.2: Production of $\bar{\Lambda}(1520)\, p_f\, p_s$ final state

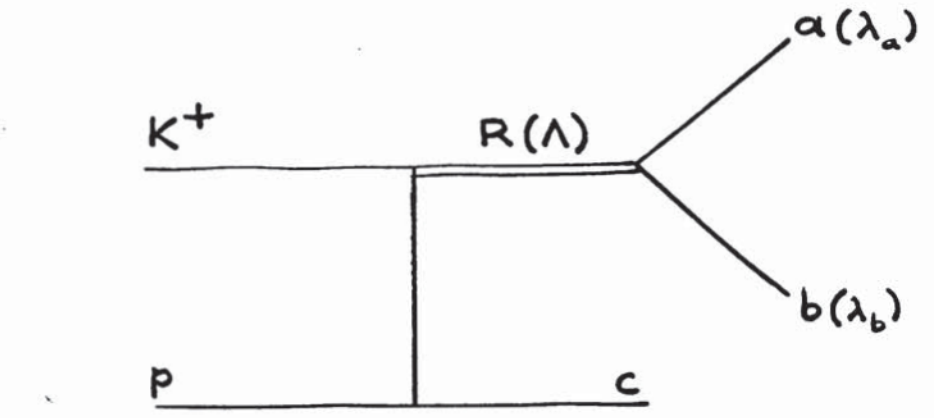

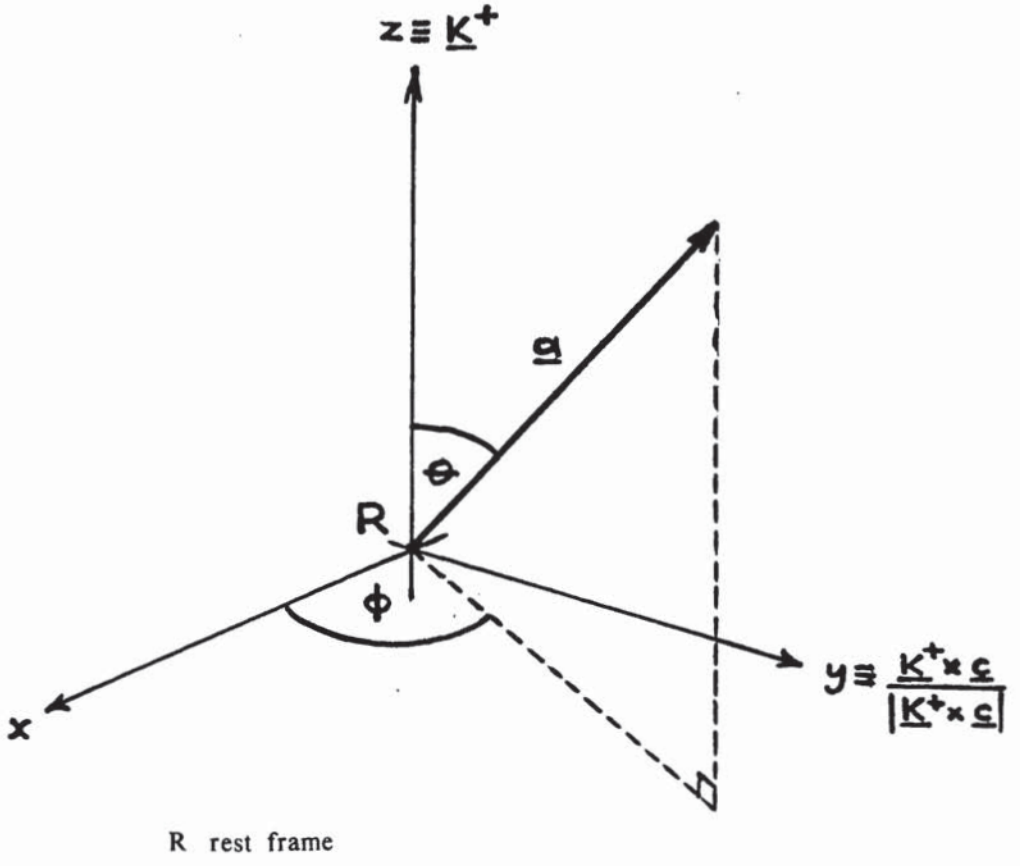

R rest frame

Figure B.3: Decay angles in t-channel helicity frame

Appendix C
EFFECTIVE MASS RESOLUTION

A knowledge of the experimental resolution is essential when searching effective mass spectra for narrow resonant states such as narrow baryonia ($qq\bar{q}\bar{q}$) with widths anticipated to be of the order of a few tens of MeV. True resonance widths and cross-section limits can only be determined if the effects of resolution on the data are measured.

In the discussion which follows, the 'resolution', Γ_r, will be defined as the full width at half maximum (FWHM) of the resolution function, whether the resolution function is known analytically or not.

C.1 DETERMINATION FROM EXPERIMENTAL ERRORS

C.1.1 Method

The following procedure was used to determine the average resolution function width Γ_r, inputing only the track parameters and their associated errors provided by the pattern recognition and geometrical reconstruction program ROMEO (see chapter III):

> For each event i with a mass m_i lying within the region of interest, the error Δm_i on the mass was calculated using a method detailed later. Each Δm_i was taken as the standard deviation of a normal distribution centred on zero, and a value $\Delta m_i'$ was then chosen within this distribution. The width of the resulting distribution of all $\Delta m_i'$ was measured and defined as Γ_r, the 'resolution'.

This method was originally devised by D.Frame (see also [66]). The author was responsible for the calculation of the error on effective or missing mass.

C.1.2 Example of $\bar{\Lambda}(1520) \rightarrow \bar{p}K^+$

As an illustration of the above technique, the distribution of $\Delta m_i'$ for the $\bar{p}K^+$ mass combination in the $\bar{\Lambda}(1520)$ resonance region (1.50 - 1.54 GeV) is plotted in figure C.1. The shape is well fitted by a Breit-Wigner function of width

$$\Gamma_r = 1.9 \pm 0.1 \text{ MeV} \qquad (C.1)$$

Using the known mass and width of the $\bar{\Lambda}(1520)$ resonance ($m = 1519.4 \pm 1.0$ MeV, $\Gamma = 15.6 \pm 1.0$ MeV [2]), and the experimental mass error spectrum, a $\bar{\Lambda}(1520)$ peak was simulated by the following method:

> For each event i generated, a mass m_i was chosen according to the true Breit-Wigner resonance shape, and an error Δm_i selected according to the experimental error distribution. A shifted mass value m_i' was chosen according to the normal distribution defined by taking m_i as the mean and Δm_i as the standard deviation. The distribution of all m_i' then gave the simulated resonance peak.

The simulated peak for the $\bar{\Lambda}(1520)$ is shown in figure C.2, and the Breit-Wigner function fitted to the data $\bar{\Lambda}(1520)$ peak is shown superimposed. It may be seen that the simulated width is narrower than the experimental width:

$$16.8 \pm 2.7 \text{ MeV} \quad cf. \quad 20.6 \pm 2.5 \text{ MeV}$$

C.1.3 Discussion

According to reference 66, if both the true resonance peak and the resolution function have Breit-Wigner shapes of widths Γ and Γ_r repectively, the width Γ_{obs} of the peak observed in the data is given by the linear relationship:

$$\Gamma_{obs} = \Gamma + \Gamma_r \qquad (C.2)$$

Hence, the predicted resolution width for the $\bar{\Lambda}(1520)$ region is:

$$\Gamma_r = (20.6 \pm 2.5) - (15.6 \pm 1.0) = 5.0 \pm 2.7 \text{ MeV}$$

which is in rather poor agreement with the Γ_r value determined previously (C.1).

The width Γ_r of the proton (missing mass)^2 signal for the hypothesis $K^-(p)K^+K^+$ was predicted from the experimental errors, and found to be ~ 0.6 x the width observed in the data.

From the above examples, and from the investigation of other resonance peaks, it was concluded that the Γ_r determined from the experimental mass errors should be regarded as a lower limit to the width of the resolution function. As has already been pointed out by P.W.Minto ([23], see also [67]), the track covariance matrix elements supplied by ROMEO are realistic only insofar as the initial error estimates input to the program are realistic. However, the resolution width predicted by equation C.2 is determined directly from the data. Assuming that the resolution function derived from the experimental mass errors can be described by a Breit-Wigner shape, and that the width of the resonance under study is well known, a reasonable estimate of the resolution can be made by using the relationship C.2.

C.1.4 Error on mass

The variance of a function $y = y(x_1, x_2, \ldots, x_m) = y(\underline{x})$ may be estimated [66] by evaluating

$$V(y(\underline{x})) = \sum_{i=1}^{m}\sum_{j=1}^{m}(\partial y/\partial x_i)(\partial y/\partial x_j)V_{ij}(\underline{x})$$

where: $V(y(\underline{x}))$ = variance of y

$V_{ij}(\underline{x})$ = element of the covariance matrix of $\underline{x}$

Considering the variance of a quantity which is a function of the ROMEO parameters $\{1/p,\lambda,\phi\}$ for n tracks, with no covariance between tracks:

$$y = y(1/p_1, \lambda_1, \phi_1, 1/p_2, \lambda_2, \phi_2, \ldots, 1/p_n, \lambda_n, \phi_n) \quad \text{and}$$

$$V(y) = \sum_{i=1}^{n}\{(\partial y/\partial(1/p_i))^2 V_{1/p_i 1/p_i} + (\partial y/\partial\lambda_i)^2 V_{\lambda_i\lambda_i} + (\partial y/\partial\phi_i)^2 V_{\phi_i\phi_i}$$
$$+ 2[(\partial y/\partial(1/p_i))(\partial y/\partial\lambda_i)V_{1/p_i\lambda_i} + (\partial y/\partial(1/p_i))(\partial y/\partial\phi_i)V_{1/p_i\phi_i}$$
$$+ (\partial y/\partial\lambda_i)(\partial y/\partial\phi_i)V_{\lambda_i\phi_i}]\}$$

If y is taken to be the squared effective mass or missing mass m^2, then

$$m^2 = \left(\sum_{i=1}^{n} s_i e_i\right)^2 - \left(\sum_{i=1}^{n} s_i \underline{p}_i\right)^2 \qquad \text{and}$$

$$\partial m^2/\partial(1/p_i) = 2s_i p_i (Xp_{x_i} + Yp_{y_i} + Zp_{z_i} - (Ep_i^2/e_i))$$

$$\partial m^2/\partial\lambda_i = 2s_i [((Xp_{x_i} p_{x_i} + Yp_{z_i} p_{y_i})/\cos\lambda_i) - Zp_i^2\cos\lambda_i]/p_i$$

$$\partial m^2/\partial\phi_i = 2s_i (Xp_{y_i} - Yp_{x_i})$$

where: s_i = ±1 for effective or missing mass as required

$p_{x_i} = p_i \cos\lambda_i \cos\phi_i$

$p_{y_i} = p_i \cos\lambda_i \sin\phi_i$

$p_{z_i} = p_i \sin\lambda_i$

$e_i = \sqrt{(m_i^2 + p_i^2)}$

$X = \sum_{i=1}^{n} s_i p_{x_i}$

$Y = \sum_{i=1}^{n} s_i p_{y_i}$

$Z = \sum_{i=1}^{n} s_i p_{z_i}$

$E = \sum_{i=1}^{n} s_i e_i$

The variance of the mass m may then be deduced from the variance of m^2 thus:

$$V(m^2) = (2m)^2 V(m)$$

A program was written to calculate the error ($\sqrt{\text{variance}}$) on the effective mass(²) of, or the missing mass(²) to, a combination of tracks in an event, using the covariance matrix elements for the tracks provided by ROMEO.

C.2 DETERMINATION BY OTHER METHODS

C.2.1 Example of $K^+ \rightarrow \pi^-\pi^+\pi^+$

Resolution may be determined by measuring the experimentally observed width of some 'stable' particle which has zero intrinsic width, for example:

$$K^+ \rightarrow \pi^-\pi^+\pi^+ \qquad (\tau\text{-decay of } K^+).$$

The kinematic configuration of the decay products should closely resemble that of the particles which form the mass combination under study.

With a view to estimating the resolution of the $K^-K^+K^+$ system in the $K^-K^+K^+p$ final state, and knowing that the average proton momentum was small, the width of the K^+ beam τ-decay mass spectrum was measured. The τ-decays were selected from run 1 three-prong data taken with non-standard trigger conditions, and were identified by having small missing transverse momentum ($\Delta p_T < 50$ MeV). A decay point reconstructed inside the target was also required. The $\pi^-\pi^+\pi^+$ effective mass distribution is shown in figure C.3, and indicates a three-track resolution (FWHM) of ~ 12 MeV.

C.2.2 Fitting with normal resolution function

Before the resolution functions derived from experimental mass errors had been found to be Breit-Wigner in shape, resonances observed in the data were fitted using the convolution integral technique (equation B.3, appendix B) with a normal resolution function of standard deviation $\sigma_r = 0.424\Gamma_r$.

The true width of the $\bar{\Lambda}(1520)$ resonance and the resolution determined by this method were:

$$\Gamma = 14.6 \pm 3.5 \text{ MeV}, \quad \sigma_r = 5.0 \pm 1.5 \text{ MeV}$$

respectively. The width obtained is therefore in good agreement with the accepted value (see above).

(For completeness, we note that if both the true resonance peak and the resolution have normal shapes of standard deviations σ and σ_r repectively, the standard deviation σ_{obs} of the peak observed in the data is given [66] by the quadratic relationship:

$$\sigma_{obs}^2 = \sigma^2 + \sigma_r^2 \quad)$$

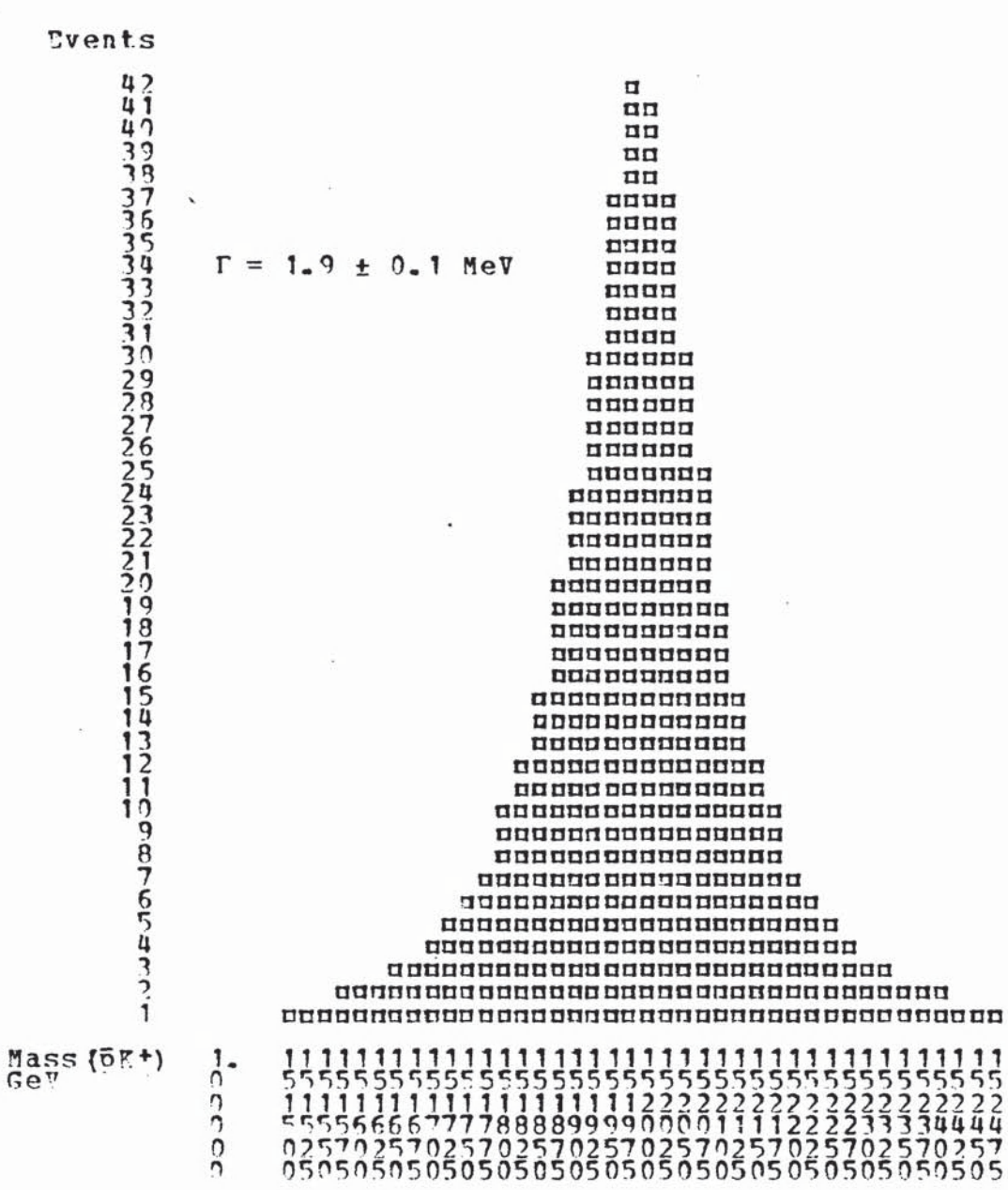

Figure C.1: $\bar{\Lambda}(1520)$ mass resolution function from experimental errors

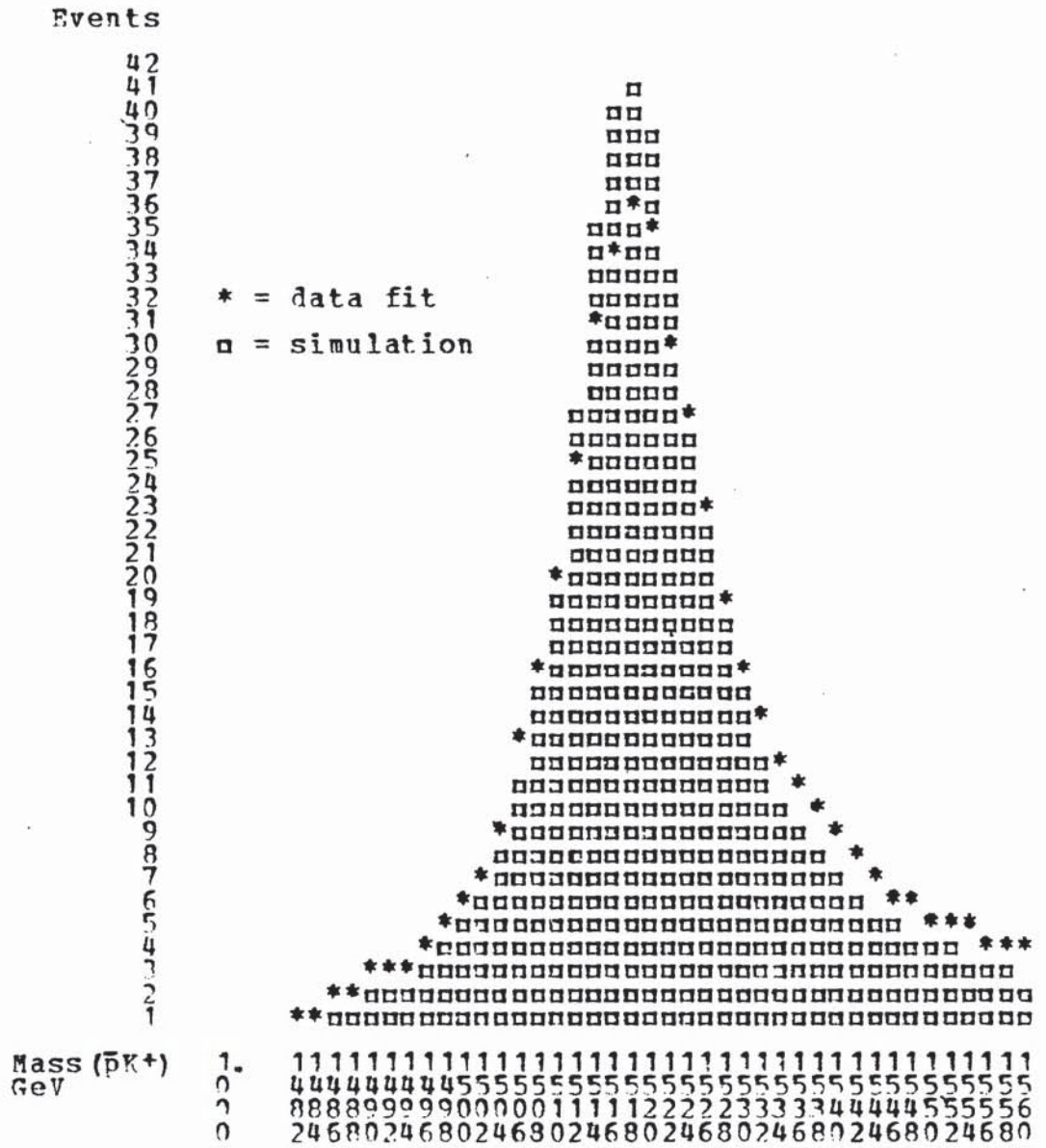

Figure C.2: Simulated $\bar{\Lambda}(1520)$ peak with data Breit-Wigner fit superimposed

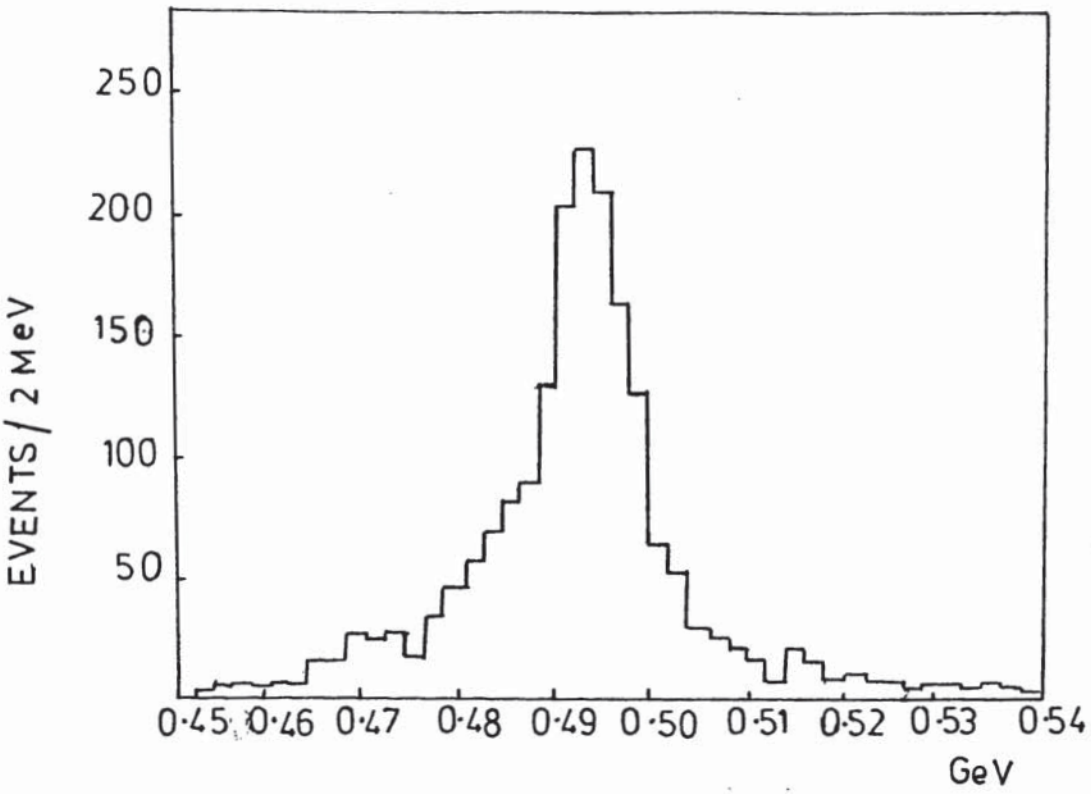

Figure C.3: Mass $\pi^-\pi^+\pi^+$ from K^+ beam τ-decays

REFERENCES

1. Omega Project Working Group, CERN/NP 68-11 (1968).
2. Particle Data Group, Rev. Mod. Phys. 111B (1982).
3. R.Zitoun, paper to the International Conference on High Energy Physics, Lisbon, July 1981, CERN-EP 81-114.
4. High-Energy Reactions Analysis Group, CERN-HERA 79-02 (1979).
5. Citron et al., Nucl. Instrum. Methods 155 (1978) 93.
6. Colley et al., Nucl. Phys. B50 (1972) 1.
7. Lissauer et al., Nucl. Phys. B18 (1970) 491.
8. F.E.Close, An Introduction to Quarks and Partons, Academic Press, (1979).
9. Al-Harran et al., Phys. Lett. 101B (1981) 357.
10. Armstrong et al., Phys. Lett. 110B (1982) 77.
11. Proceedings of the Daresbury Study Weekend, February 1975, Daresbury Laboratory DL/R34.
12. Bosetti et al., Nucl. Phys. B101 (1975) 304.
13. Daum et al., Nucl. Phys. B187 (1981) 1.
14. R.T.Deck, Phys. Rev. Lett. 13 (1964) 169.
15. E.L.Berger and J.T.Donohue, Phys. Rev. D15 (1977) 790.
16. Delfosse et al., paper to the International Conference on High Energy Physics, Lisbon, July 1981, UGVA-DPNC 1981/06-105.
17. Baubillier et al., Nuovo Cimento 70A (1982) 471.
18. Armstrong et al., paper to the XXI International Conference on High Energy Physics, Paris, July 1982, CERN/EP 82-95.

19. D.B.Lichtenberg and J.G.Willis, Phys. Rev. Lett. 35 (1975) 1055.

20. D.P.Stanley and D.Robson, Phys. Rev. 21D (1980) 3180.

21. C.H.Mo and H.Høgaasen, Phys. Lett. 72B (1977) 121.

22. Frame et al., Proceedings of the 5th European Symposium on Nucleon Anti-nucleon Interactions, Bressanone, June 1980.

23. P.W.Minto, Ph.D. thesis, University of Glasgow (1981).

24. Armstrong et al., Phys. Lett. 77B (1978) 447.

25. Frame et al., Phys. Lett. 107B (1981) 301.

26. Baubillier et al., Nucl. Phys. B183 (1981) 1.

27. Cleland et al., Nucl. Phys. B184 (1981) 1.

28. D.Frame, Ph.D. thesis, University of Glasgow (1976).

29. P.Fleury and B.Grossetete, Omega 'Geometry 2' Layout, CERN (1972).

30. Bizeau et el., CERN OM/SPS/85 (1974).

31. E.Byckling and K.Kajantie, Particle Kinematics, Wiley (1973).

32. Carney et al., Phys. Lett. 55B (1975) 117.

33. Armstrong et al., Proceedings of International Conference on High Energy Physics, Palermo, June 1975.

34. Armstrong et al., Nucl. Phys. B157 (1979) 365.

35. D.Frame, private communication.

36. C.Palazzi-Cerrina, CERN WA40 collaboration internal communication.

37. P.W.Minto, private communication.

38. I.T.Wilkie, Ph.D. thesis, University of Glasgow (1983).

39. P.J.Harper, M.Sc. thesis, University of Birmingham (1980).

40. R.Ehrlich, R.J.Plano and J.B.Whittaker, Phys. Rev. Lett. 20 (1968) 686.

41. Barnham et al., Nucl. Phys. B28 (1971) 291.

42. Cohen et al., Phys. Rev. D8 (1973) 2772.

43. F.James, Function Minimization, CERN 72-21 (1972).

44. Proceedings of the 1965 Easter School for Physicists, CERN 65-24 (1965).

45. Proceedings of the Meeting on Exotic Resonances, Hiroshima 1978, HUPD-7813.

46. Otter et al., Nucl. Phys. B89 (1975) 201.

47. Feynman et al., Phys. Rev. 3D (1971) 2706.

48. Armstrong et al., Nucl. Phys. B202 (1982) 1.

49. A.D.Martin and C.Nef, Nucl. Phys. B181 (1981) 61.

50. R.L.Sekulin, Nucl. Phys. B56 (1973) 227.

51. S.M.Flatte, CERN EP Internal Report 76-12 (1976).

52. Otter et al., Nucl. Phys. B181 (1981) 1.

53. Ascoli et al., Phys. Rev. D7 (1973) 669.

54. Hansen et al., Nucl. Phys. B81 (1974) 403.

55. S.U.Chung, Phys. Rev. 169 (1968) 1342.

56. Chung et al., Phys. Rev. D11 (1975) 2426.

57. Aguilar-Benitez et al., CERN/EP 81-54 (1981).

58. Grayer et al., Nucl. Phys. B75 (1974) 189.

59. MINUIT, Cern Program Library D506/D516.

60. L.Van Hove, Nucl. Phys. B9 (1960) 331.

61. J.D.Jackson, Nuovo Cimento 34 (1964) 1644.

62. J.D.Jackson, Nuovo Cimento 33 (1964) 309.

63. S.U.Chung, Spin Formalisms, CERN 71-8 (1971).

64. U.Fano, Rev. Mod. Phys. 29 (1957) 74.

65. A.D.Martin and T.D.Spearman, Elementary Particle Theory, North-Holland (1970).

66. A.G.Frodesen, O.Skjeggestad and H.Tøfte, Probability and Statistics in Particle Physics, Universitetsforlaget (1979).

67. Townsend, ROMEO Information Note No.3, CERN OM/SPS/76/12 (1976).